



Universiteit
Leiden
The Netherlands

The metallophilic interaction between cyclometalated complexes: photobiological applications

Zhou, X.

Citation

Zhou, X. (2021, May 26). *The metallophilic interaction between cyclometalated complexes: photobiological applications*. Retrieved from <https://hdl.handle.net/1887/3158746>

Version: Publisher's Version

License: [Licence agreement concerning inclusion of doctoral thesis in the Institutional Repository of the University of Leiden](#)

Downloaded from: <https://hdl.handle.net/1887/3158746>

Note: To cite this publication please use the final published version (if applicable).

Cover Page



Universiteit Leiden



The handle #<https://hdl.handle.net/1887/3158746> holds various files of this Leiden University dissertation.

Author: Zhou, X.

Title: The metallophilic interaction between cyclometalated complexes: photobiological applications

Issue Date: 2021-04-08

The Metallophilic Interaction between Cyclometalated Complexes: Photobiological Applications

Proefschrift

ter verkrijging van
de graad van doctor aan de Universiteit Leiden,
op gezag van rector magnificus prof.dr.ir. H. Bijl,
volgens besluit van het college voor promoties

te verdedigen op donderdag 8th April 2021
klokke 11:15 uur

Xuequan Zhou

Geboren te Xianning (Hubei), China

In 1990

Samenstelling promotiecomissie

Promotores

Prof. dr. Sylvestre Bonnet

Prof. dr. Elisabeth Bouwman

Overige leden

Prof. dr. Hermen Overkleeft (Leiden University)

Dr. Luis J. Cruz (Leiden University Medical Center)

Prof. dr. Mario van der Stelt (Leiden University)

Prof. dr. Luisa De Cola (Strasbourg University, France)

Prof. dr. Luigi Messori (University of Florence, Italy)

Table of Contents

Chapter 1	Introduction	4
Chapter 2	The two isomers of a cyclometalated palladium sensitizer show distinct photodynamic properties in cancer cells	22
Chapter 3	The self-assembly of a cyclometalated palladium photosensitizer into proteins-stabilized nanorods triggered drug uptake in vitro and in vivo.....	38
Chapter 4	Intracellular dynamic assembly of deep-red emitting supramolecular nanostructures based on Pt...Pt metallophilic interaction.....	74
Chapter 5	Self-assembling cyclopalladated photosensitizers for photodynamic therapy: tumor accumulation and anti-tumor activity in a skin melanoma xenograft....	100
Chapter 6	Nitrogen coordination vs. rollover cyclometalation in tetrapyrrolyl anticancer gold(III) complexes	122
Chapter 7	Summary & General discussion & Outlook	

APPENDICES

Appendix I	Supporting information for chapter 2.....	158
Appendix II	Supporting information for chapter 3	163
Appendix III	Supporting information for chapter 4	173
Appendix IV	Supporting information for chapter 5	182
Appendix V	Supporting information for chapter 6	189

1

Introduction

1.1 Anticancer metallodrugs

Metal-based materials have been on the basis of technology in the history of mankind. In recent decades, they have also shown important applications as therapeutics or for diagnostics, notably for cancer.^{1, 2} Cancer is a general term encompassing many different diseases that all involve uncontrolled cell growth; it is one of the main health problems all over the world.³ In 2017, the death of 9.6 million people was due to various forms of cancer.⁴ This situation stimulates researchers to develop diverse methods for the treatment of cancer. In many aspects, metallodrugs have played a unique role in these developments. Cisplatin is a widely used chemotherapy medication against various types of cancer in clinical use since 1978.⁵ Its success but also its limitations prompted the development of several alternative platinum-based anticancer drugs, including carboplatin, oxaliplatin, nedaplatin and heptaplatin (Figure 1.1a).⁶ Cisplatin induces cancer cell death via binding to the purine bases of DNA (N7 of guanine and adenine), forming stable cross-links that bend duplex DNA and block its replication and transcription (Figure 1.1b).^{5, 7}

Many metal ions and complexes have a natural aptitude for interacting with anionic DNA, because of their cationic characteristics, the properties of their coordination spheres, and their tunable redox, ligand-releasing, and photophysical properties.^{8, 9} The first X-ray structure proving the binding of cisplatin to DNA was reported by the group of Lippard in 1995.¹⁰ Cisplatin shows a specific mechanism, *i.e.* it binds to DNA through one or two coordination bonds. Besides coordination, metal-based anticancer drugs also may have other modes of interaction with DNA, for example, intercalation. Intercalators usually have a planar structure that can insert between the DNA base pairs, thus stabilizing the metallodrug-DNA complex via π - π stacking. Square-planar metal complexes for example can intercalate between DNA base pairs, while octahedral complexes often achieve partial intercalation via planar aromatic heterocyclic ligands, or interact with several DNA bases by groove binding. For example, metal complexes derived from the ligand dppz (dipyrido[2,3-a:3',2'-c]phenazine) and its derivatives, are considered as standard DNA intercalators.¹¹ Barton's group established impressive work based on this ligand. In particular, they developed a series of metal-containing intercalators that specifically interact with mismatched DNA in cancer cells.¹²⁻¹⁴ The Salder and Dyson groups also developed many organometallic anticancer complexes, especially based on the piano-stool scaffold, as DNA intercalators.¹⁵⁻¹⁷

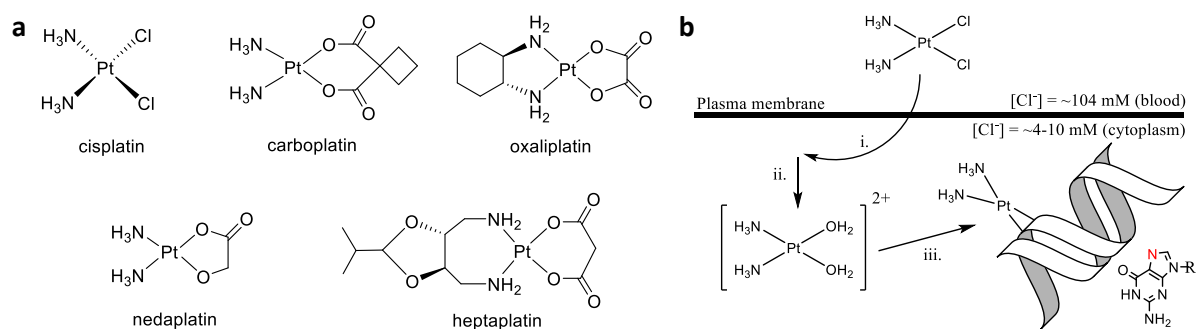


Figure 1.1 (a) Platinum(II) complexes clinically used as cancer chemotherapy agents. (b) Classical view on the uptake (i), hydrolysis (ii) and DNA-binding of cisplatin.

DNA-targeting metallodrugs show significant anticancer ability. However, the poor selectivity of metal complexes for coordination to or intercalating into DNA, results in various off-target effects.^{18, 19} Proteins, the main executors of the cell activity, often are alternative targets, which generates side effects. The combination of various metal ions with different coordination spheres, and the diversity and richness of available organic protein inhibitors, have generated a new era in the field of anticancer metallodrugs.^{6, 20} Platinum and gold complexes have been studied first due to their optimal rate of ligand substitution reaction in biological environments; it even appeared possible to use them as multi-targeted anticancer agents.^{21, 22} For example ethacraplatin, a Pt(IV) prodrug bound to two molecules of ethacrynic acid, a glutathione-S-transferase inhibitor, releases one molecule of cisplatin and two equivalents of ethacrynic acid after cellular uptake and intracellular reduction, which kills cancer cells via two different modes of action.²³ Gold(III) compounds can also be used that are usually reduced to gold(I) upon cellular uptake. These species show strong binding affinity to the thiol groups of many key biomolecules and enzymes inside a cell, such as glutathione (GSH), thioredoxin reductase (TrxR) or trypanothione reductase (TR), which are overexpressed in cancer cells because they control the redox balance of cells (Figure 1.2a).²⁴⁻²⁶ Thus, many gold anticancer compounds disturb the redox level of cancer cells. In particular gold–NHC (N-heterocyclic carbene) complexes have attracted great attention for their stability under physiological conditions and their specific reactivity with TrxR proteins.^{22, 27} Besides, Casini *et al.* also reported several gold(III) complexes showing selective inhibition of human aquaporins, which are positively correlated with tumor proliferation, migration, and angiogenesis.^{28, 29} Altogether, these reports provide strong indications that gold complexes have high potential as anticancer (pro)drugs.

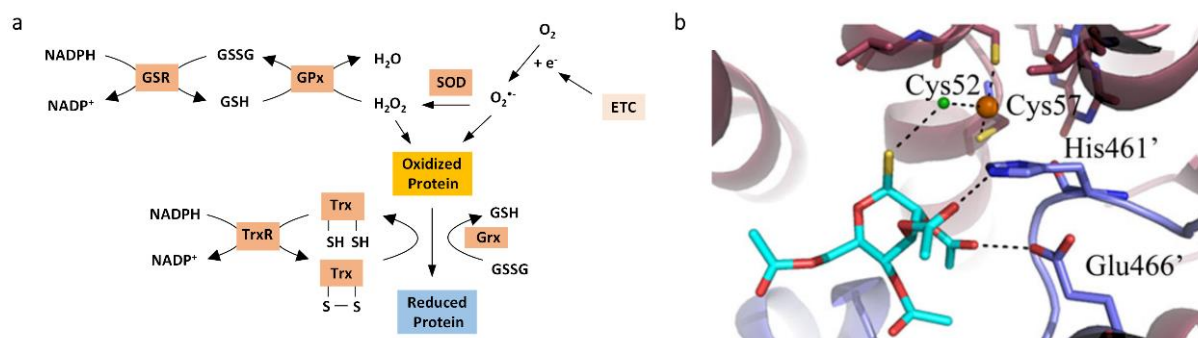


Figure 1.2 (a) Scheme of the thioredoxin (TRx) system including substrate.²⁴ (b) CysS-Au(I)-SCys bond in TR-gold(I) adduct crystals (gold source auranofin).²⁶ The gold, chloride and sulfur ions are indicated in orange, green and yellow, respectively. The Cys52, Cys57, His461', Glu466' residues and the thiosugar moiety are represented as sticks.

1.2 Light in cancer treatment

The cytotoxicity and mode-of-action of DNA- or protein-targeting metal complexes have been thoroughly studied in the last few decades. However, many of the compounds tested in animals or humans still show toxicity to healthy tissues, because the biological molecules they target are also present in healthy cells, even if at a lower level than in cancer cells. Photodynamic therapy (PDT) is an alternative, non-invasive treatment developed to overcome the harmfulness of chemotherapy, radiation therapy, immunotherapy, or surgery, to healthy tissues.³⁰ In PDT, a photosensitizer (PS) is injected into human body. The PSs are designed to be non-toxic in the dark, but they can be activated upon accurate light irradiation at the tumor site. Upon absorption of light inside the cancer cells, the PS generates cytotoxic reactive oxygen species (ROS) that destroy the tumor structures and blood vessels via either a so-called Type I mechanism, which is more or less independent from the partial pressure of O₂ (pO₂) in the irradiated tissues, or via a Type II mechanism, which is highly dependent on pO₂ (Figure 1.3).³¹⁻³³ The first step of type I and type II mechanisms are the same, *i.e.* the PS is excited to a singlet excited state ¹PS* upon photon absorption, which interconverts to a triplet excited state ³PS* via intersystem crossing (ISC). In type I PDT, electron transfer happens between the triplet state ³PS* and substrate biomolecules, with the generation of free radicals and ROS in the sequential reaction chains.³⁴ In type II PDT, energy transfer occurs via triplet-triplet annihilation (TTA) between the triplet state ³PS* and the triplet ground state of dioxygen, ³O₂, to specifically produce singlet oxygen (¹O₂, excited state).³⁵ ¹O₂ is a highly reactive molecule that oxidizes proteins, lipids, and nucleic acids, which also generates ROS and ultimately causes cell death. Whether the PDT mechanism is type I or II, in PDT the precise irradiation at the tumor site generates an anticancer effect due

to massive ROS generation, while avoiding activation of the PS in the healthy tissues, and in parallel stimulating a systemic anti-cancer immune response.^{36, 37}

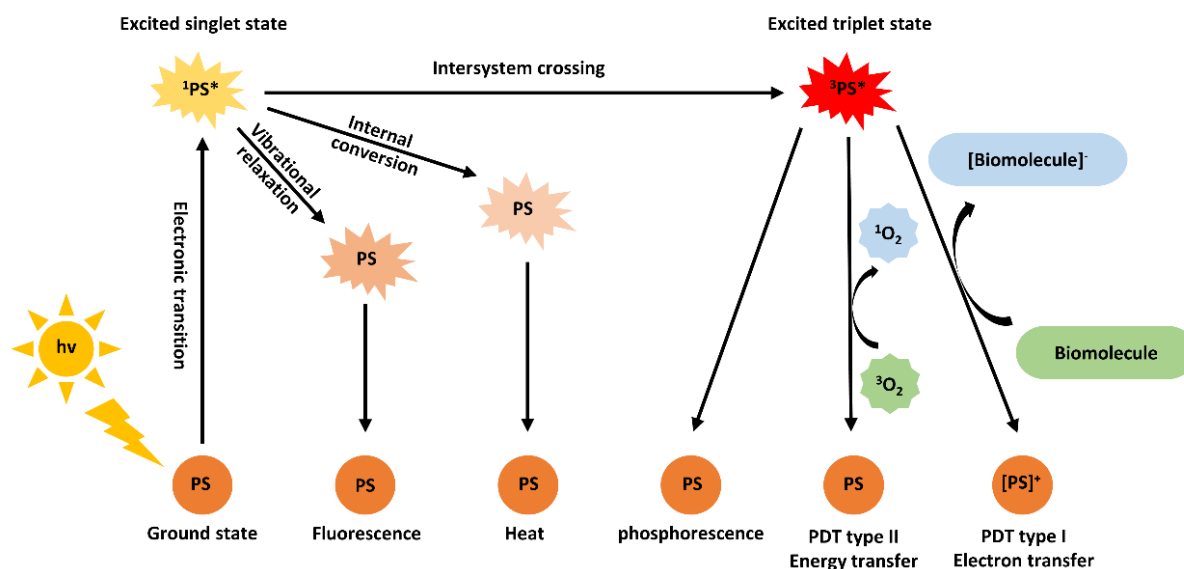


Figure 1.3 Energy scheme and PDT mechanism of the photosensitizer (PS).

PDT treatment of cancer dates back to Ancient Egypt, India, and China, and it was reintroduced into modern society when the first PDT drug, Photofrin[®] (porfimer sodium) was approved by the U.S. Food and Drug Administration (FDA) in the 1990s.³⁸ In the last three decades, PDT has had a rapid development, with several new PSs being approved on the market. Photofrin[®] and HpD (Hematoporphyrin derivative), which belongs to the family of organic porphyrin compounds, are known as the first generation photosensitizers, characterized by high 1O_2 quantum yields (Φ_Δ).³⁹ The second-generation PSs have settled with lowering of the dark cytotoxicity, poorer light absorption in the visible region of the spectrum, and stronger light absorption in the far red or near infra-red region of the spectrum; they are still composed of organic molecules, such as chlorins, pheophorbides, *etc.*⁴⁰ Noticeably, introducing metal ions in the formula of the PS has emerged as a new design principle for the development of new and more efficient PDT agents.⁴¹ Introduction of a heavy atom in a photosensitizer molecule generally facilitates intersystem crossing and improves the 1O_2 quantum yield.⁴² Palladium-based bacteriopheophorbide photosensitizer, WST09 (TOOKAD[®]) and WST11 (TOOKAD[®] soluble, Figure 1.4a), have been approved for prostate cancer treatment, and are in clinical trial for other forms of cancer; they show deeper tissue penetration and minimum skin photosensitivity compared with their organic analogues.⁴³ McFarland's group reported the ruthenium complex TLD1433 (Figure 1.4a), as the first Ru-based PDT agent that successfully completed phase Ib clinical trial.^{41, 44} A recent report also demonstrated that several ruthenium

complexes could be active *in vivo* as two-photon PDT agents.⁴⁵ Those efforts make metal-based PSs a new generation of PDT agents.

The controlled ligand photosubstitution of d^6 metal complexes has brought a new type of light-induced anticancer phototherapy, called photoactivated chemotherapy (PACT, Figure 1.4b).⁴⁶⁻⁴⁸ In PACT, the biological effects of a cytotoxic moiety are inhibited in the dark by “caging” with a photocleavable protecting group. Upon irradiation with light, the photo-cleavable protecting group is released, for example via photosubstitution, which recovers the cytotoxicity of the anticancer moiety. PACT agents can be designed in three different ways: a non-toxic ligand is bound to a bioactive metal complex, the cancer-targeted cytotoxic ligand is bound to a non-active metal complex, or both the ligand and the metal complex are toxic after photosubstitution, which generates a dual mode of action.^{49, 50} Our group recently synthesized a ruthenium-based PACT agent $[\text{Ru}(\text{tpy})(\text{bpy})(\text{STF-31})]\text{Cl}_2$ based on STF-31, an organic enzyme inhibitor; this compound showed significantly increased cytotoxicity upon red-light triggered substitution of the STF31 inhibitor.⁵¹ On the other hand, there are many PACT examples in which the toxic properties are attributed to the photogenerated metal complexes. Glazer and co-workers reported many ruthenium complexes, such as $[\text{Ru}(\text{bpy})_2(\text{dmbpy})]\text{Cl}_2$ (Figure 1.4b), that after irradiation, release dmbpy to generate the supposedly cytotoxic species $\text{cis-}[\text{Ru}(\text{bpy})_2(\text{OH}_2)_2]^{2+}$; the activated ruthenium complex then binds with DNA, which when occurring in cells, leads to a significant change of the half-maximal effective concentration (EC_{50}) of the compound, from 136 μM in the dark to 1.1 μM after light irradiation in A549 cancer cells.⁵²

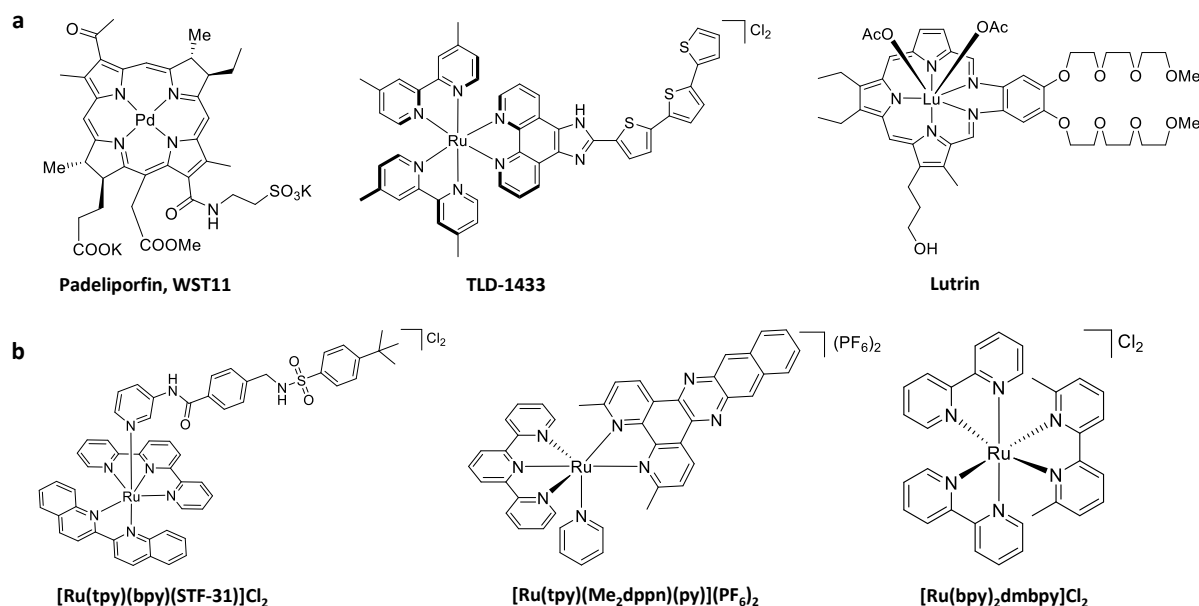


Figure 1.4 (a) Three inorganic photosensitizers for PDT currently in clinical trial: padeliporfin (WST-11), TLD-1433, and lutetium texaphyrin (lutrin).⁴⁶ (b) Three reported PACT ruthenium complexes.

1.3 Cyclometalated complex in cancer treatment

Cyclometalation is defined as the transition metal center activates a C-R bond of organic ligand to form a metallacycle including a new metal-carbon σ bond.⁵³ This family of metal complexes emerges as extremely promising for catalytic, biochemical, and photochemical applications.⁵⁴ Cyclometalated complexes of the platinum group metals comprising Ru, Os, Rh, Ir, Pd, and Pt, have received the most attention.⁵⁶ The M-C bond involves a negatively charged carbon center that has strong σ -donating character, which makes it often stronger than classical M-X coordination bonds involving π -donating or π -accepting ligands based on heteroatoms (X = nitrogen, oxygen, sulfur, phosphorus, or halogen). This stronger coordination of cyclometalated ligands usually results in more stable complexes in (aqueous) physiological conditions, which is particularly relevant for metal-based drugs. Cyclometalation also lowers the overall charge of a metal complex, resulting in increased lipophilicity and thus usually in higher cellular uptake.⁵⁷ Based on these advantages, cyclometalated complexes have attracted considerable attention for anticancer treatment.⁵⁸ Chao *et al.* reported a thorough comparison between polypyridyl ruthenium(II) complexes and their cyclometalated analogs, by testing their anticancer activities against 2D and 3D cancer models.⁵⁷ This study demonstrated that compared with their polypyridyl analogs, cyclometalated ruthenium(II) complexes exhibit higher lipophilicity and better cellular uptake, with a much lower EC_{50} in 2D and 3D cancer models.

In PDT before a photon can excite the photosensitizer *in vivo*, it has to penetrate human tissues. It is well-known that light with a longer wavelength has better tissue penetration.⁴³ The presence of an M-C bond in principle lowers the HOMO-LUMO gap of metal complexes, leading to a bathochromic shift of their absorption spectrum to reach the photodynamic window (600-900 nm),⁵⁹ which is the key for PDT and PACT applications.⁶⁰⁻⁶² Cyclometalated iridium and Platinum complexes derived from polypyridyl ligands are particularly attractive for their low-energy metal-to-ligand charge-transfer (MLCT) excited states, which makes them good absorbers of visible light (Figure 1.5).⁶² Peter and coworkers reported a cyclometalated iridium complex that showed photoredox catalysis in cancer cells upon blue light irradiation with an oxygen-independent mechanism of action.⁶³ The group of Mao reported a series of cyclometalated iridium complexes that acted as lysosome-targeted photodynamic anticancer and real-time tracking agents, presenting cyclometalated complexes as a new kind of theranostic compounds.⁶⁴ Huang *et al.* introduced a coumarin group into a cyclometalated ruthenium complex, thereby affording an efficient type I PDT agent active under white light activation.⁶⁵ Our group synthesized a heteroleptic cyclometalated ruthenium complex that underwent selective photosubstitution of a bidentate ligand, indicating that a cyclometalated complex may be developed with interesting PACT properties.⁶⁶ There are also many cyclometalated platinum-, palladium- and gold-based photosensitizers for PDT.^{42, 67, 68} Sarli *et al.* combined the cyclic peptide c(RGDyK) with a cyclometalated platinum scaffold to successfully achieve PDT treatment of rat bladder cancer cells.⁶⁹ The Zou groups recently reported that cyclometalated gold(III)-hydride complexes act as potent photoactivated anticancer agents based on their visible-light-induced thiol reactivity.⁷⁰ In conclusion, the advantageous properties of cyclometalated complexes bring a new era of bioinorganic chemistry with respect to anticancer treatment.

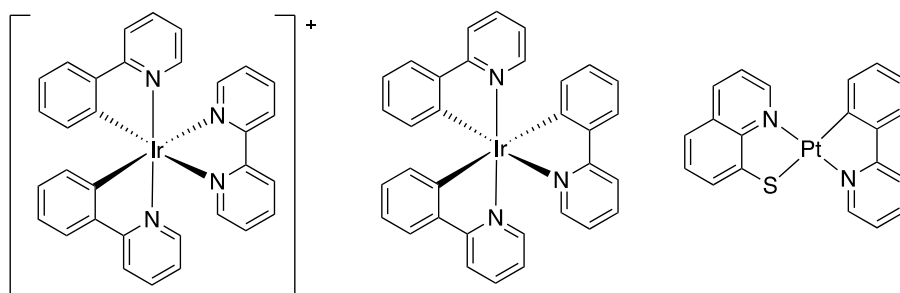


Figure 1.5 The structures of three cyclometalated photosensitizers used in PDT.⁶⁷

1.4 Metallophilic interactions

Several transition metals (M) can be engaged in metallophilic M...M interaction resulting in subsequent self-assembly behavior,⁵⁵ which has brought several fascinating studies in supramolecular bioinorganic chemistry. The metallophilic interaction typically occurs for d^8 and d^{10} square-planar or linear transition metal complexes. It drives molecules to self-assemble into aggregates that minimize the metal...metal distances below 3.5-4.0 Å. This self-assembly dramatically modifies the properties of the metal compound compared to the non-aggregated monomer, for example by enhancing its luminescence, increasing its excited-state lifetime, or reducing its chemical reactivity.⁷¹ This phenomenon has allowed for the creation of a new category of light-emitting self-assembled materials.⁵⁵ Meanwhile, the versatility in ligand structures and metal coordination spheres has facilitated the making of a large range of self-assembled nanostructures and molecular topologies based on metal complexes showing metallophilic interactions (Figure 1.6).⁷² To assess the existence of this interaction, the most direct method is X-ray crystal structure determination, which shows the distance between metal centers. If the metal...metal distance is shorter than the sum of van der Waals radius of the metal cations, it is reasonable to assume the existence of metal...metal interaction. Another common method is to compare the spectroscopic properties of the metal complex in its self-assembled polymeric and monomeric states, which usually resemble the spectra of their solid and solution states, respectively.⁷³

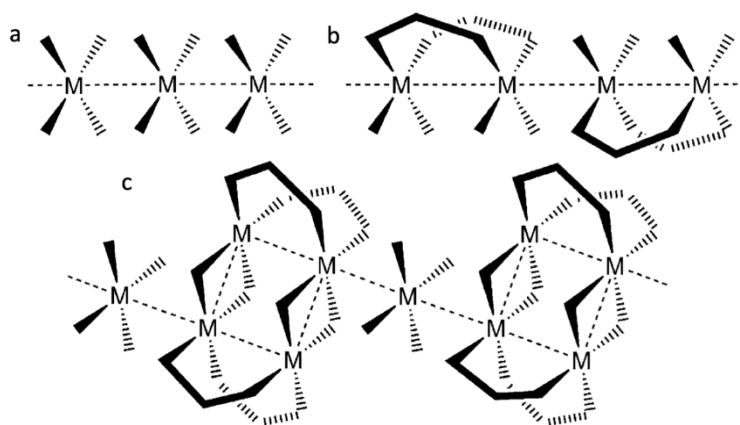


Figure 1.6 Schematic drawing of metal complexes showing a metallophilic interaction. (a) linear chain composed of square planar molecules. (b) linear chain composed of paddlewheel molecules. (c) mixture motifs.⁷²

The most simple self-assembly *via* metallophilic interaction is obtained when the metal complexes form a linear infinite chain of molecules directly interacting with two neighboring

metal centers.⁷⁴ Typical examples of such systems are formed by d^8 transition metal complexes, especially Pt(II) complexes.^{71, 75} The square-planar coordination geometry provided by Pt(II) and the attractive spectroscopic and photophysical properties of complexes based on this metal have been well documented; besides, these complexes are particularly prone to generating intermolecular Pt...Pt interaction.⁷⁶ Specifically, the Pt...Pt interaction is attributed to the closed-shell electronic overlap between the axial d_z^2 orbitals, often combined with π - π stacking of the flat aromatic ligands coordinated to platinum. The orbital interaction between the d_z^2 orbitals induces a new d_z^2 hybridization in the polymeric form, leading to a change of the highest occupied molecular orbital (HOMO). While the stabilized bonding combination of the d_z^2 orbital on both metal centers usually ends up in lower, 2-electron filled molecular orbitals, their destabilized anti-bonding combination, often mixed with π orbital of the ligand(s), gives rise to a new HOMO molecular orbital, while the LUMO is formed by combinations of π^* orbitals of the ligand(s). The resulting low-energy optical transition, from the metal $d\sigma^*$ HOMO to the ligand π^* orbitals LUMO, leads to metal-metal-to-ligand charge transfer (MMLCT) excited states and a lower HOMO-LUMO gap, compared to the either ligand-centered (LC) or metal-to-ligand charge transfer (MLCT) transitions usually observed with the parent monomer molecules (Figure 1.7a).⁷⁵ For platinum complexes, this new transition translates into low-energy absorbance and emission bands, typically in the red or even near-infrared region of the spectrum. A common self-assembly system is the cyclometalated cationic pincer-type Pt(II) complexes (Figure 1.7b).⁷⁷ Cyclometalation lowers the electrostatic repulsion between the Pt(II) centers, while the planar structure of the ligand prevents steric hindrance to occur, which allows π - π stacking to occur and altogether results in short Pt...Pt distances and rather strong Pt-Pt interactions. The occurrence of self-assembly with such complexes is typically accompanied by the generation of nanorods or nanofibers in mixed solvent systems, and deep-red emission in the aggregated form.^{78, 79} The de Cola group established a system where the self-assembly of luminescent Pt(II) complexes could be controlled, which allowed the authors to achieve diagnostic and biosensing functions in such systems.⁸⁰

Palladium is in the same group as platinum in the periodic table of the elements, and Pd(II) thus has similar d^8 square-planar structures. Indeed, several cyclometalated cationic pincer-type Pd(II) complexes were shown to exhibit metallophilic interactions and to form similar self-assembled nanostructures as that obtained with Pt analogs (Figure 1.7b).^{81, 82} However, also being a lighter metal center, Pd(II) usually makes complexes with a fainter phosphorescence because of the less efficient inter-system crossing (ISC) and slower T_1 - S_0 radiative decay.⁸³ As

a result, limited attention has been paid to Pd(II)-based light-emitting materials.⁸⁴ Au(III) complexes, which are isoelectronic to those of Pt(II) or Pd(II), have recently been reported to show self-assembly via aurophilic interaction, thereby introducing a new molecular building block capable of developing metallophilic interactions (Figure 1.7c).⁸⁵ However, the applications based on these new self-assembled nanostructures are still in a primary exploration stage.

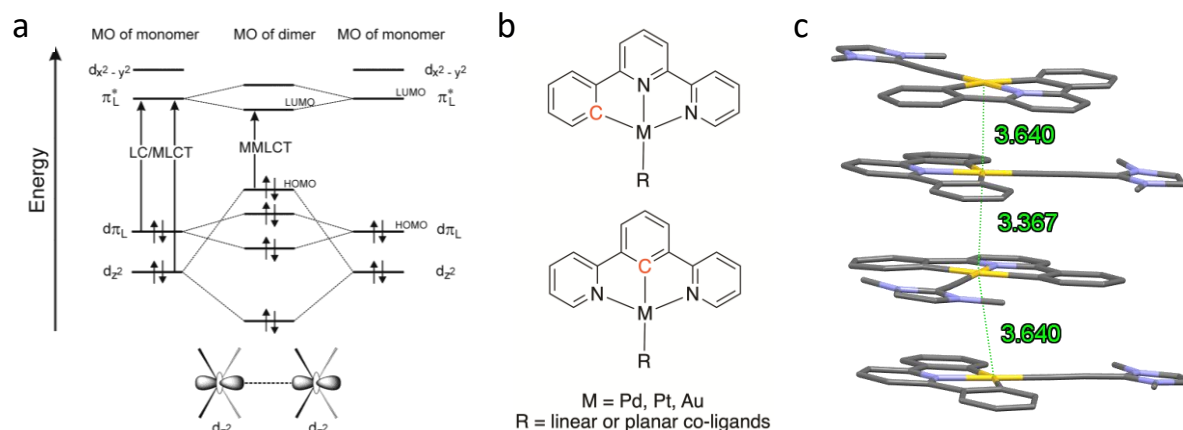


Figure 1.7 (a) Simplified MO diagram of two interacting square-planar platinum(II) complexes, showing the overlap of the d_{z^2} orbital of each metal fragment, and its influence on the energy of the molecular orbital levels of the dimer.⁷¹ (b) Typical molecular structures of self-assembling systems based on the metallophilic interaction. (c) A unidirectional supramolecular chain as an example of an Au(III) complex involved in aurophilic interaction (distance unit Å).⁸⁵

1.5 Metals in nanomedicine

In 2002, the US National Institutes of Health (NIH) started a new research program to apply nanoscience and nanotechnology in medicine, leading to the emergence of a new field called nanomedicine.⁸⁶ Nanomedicine aims to achieve diagnosis and treatment of diseases via the specific properties of nanomaterials.⁸⁷ Cancer therapy is one of the main research areas of the previously unimaginable development of modern nanomedicine. Researchers found that many nanoparticles (NPs) exhibit the so-called “enhanced permeation and retention” (EPR) effect, which makes them more efficiently taken up in tumor tissues than in normal tissues.^{88, 89} The blood vessel at the tumor microenvironment is leakier than that of healthy tissues,⁹⁰ making nanoparticles cross the tumor blood vessels in a high opportunity compared with the healthy tissues. Moreover, The nanostructures may also protect the drug from recognition and clearance before reaching the target,⁹¹ thus providing long circulation times that may be accompanied by

an efficient delivery to the target. The EPR effect has stimulated the application of NPs as drug delivery systems to solid tumors,⁹² However, EPR effect has also been recently discussed extensively in the literature for application in human medicine.⁹³⁻⁹⁵ A recent research convinces that the active process through endothelial cells, instead of the tumor blood vessels gaps, is majorly responsible for the entry of nanoparticles into solid tumors, which challenges the conventional rationale of EPR effect for developing cancer nanomedicine.⁹³

Nanoparticles have been used in studies concerning bioimaging, drug delivery and phototherapy.⁹⁶ Many simple molecules, although they may have excellent photophysical properties for PDT as monomers, are often too hydrophobic to be used in medicine without chemical modification, as they typically aggregate in serum or tumor cells into PDT-inactive aggregates. The conjugation of PDT molecules to NPs has been proposed for solving these problems. The NP coating strategy can easily generate PDT drugs uniformly distributed in aqueous solutions. Based on this research, Hsiao *et al.* developed a Fe₃O₄/SiO₂ core/shell nanocomposite that conjugated a functionalized iridium photosensitizer for cell imaging and anticancer PDT treatment.⁹⁷ Recently, the Chen group reviewed the development of ruthenium complexes from single-molecule compounds to nanoparticles.⁹⁸ The Gasser group has developed several polymers encapsulated metal complexes with significant PDT effect, suggesting a promising future for the nanoconjunction of metal complexes..^{88, 99}

Many nanoparticles include metal centers (Figure 1.8).¹⁰⁰ A well-known category of such NPs comprise gold nanoparticles (AuNPs), which are made by fully reduced Au⁰ atoms.¹⁰¹ Generally, AuNPs are stabilized using thiolate moieties that form strong Au–S bond between the soft Lewis acid Au and the soft thiolate Lewis base (S). One of the specificities of AuNPs is that they have a significant surface plasmon resonance (SPR) mode in the visible region of the spectrum if one of their dimensions is much smaller than the wavelength of the light used to excite them.¹⁰² Light irradiation at the SPR wavelength of AuNPs is usually followed by fast conversion of the photon energy into heat.¹⁰² The SPR absorption of many AuNPs is matching ideally with the first phototherapy window (650-900 nm), making AuNPs highly promising photothermal therapy (PTT) materials in cancer treatment.¹⁰³ On the imaging side, many nanoparticles bound specifically to gadolinium complexes have been investigated as contrast agents (CAs) in magnetic resonance imaging (MRI).¹⁰⁴ Ample works have also focussed on the use of Ln³⁺-doped upconversion nanoparticles (Ln-UCNPs) both for diagnostic sensing (bioimaging), disease treatment (therapy), or both (theranostic). The upconversion properties of these Ln-UCNPs is based on the specific properties of 4f electronic levels in lanthanoid metal

centers; many dedicated reviews have been written on this well-developed chemistry.¹⁰⁵⁻¹⁰⁷ Ln-UCNPs have received particular attention in the field of optical imaging for their high resistance to photobleaching and near-infrared (NIR) excitation, which results in deeper penetration of the exciting light into biological tissues, compared to traditional organic dyes that require visible or UV excitation.¹⁰⁸ Our group has developed a UCNP nanosystem combining lanthanoid upconversion with photocleavable ruthenium complexes, to achieve NIR activation of the ruthenium prodrugs.¹⁰⁹ Overall, these efforts suggest that metal atoms and complexes play an important contribution to the development of nanomedicine.

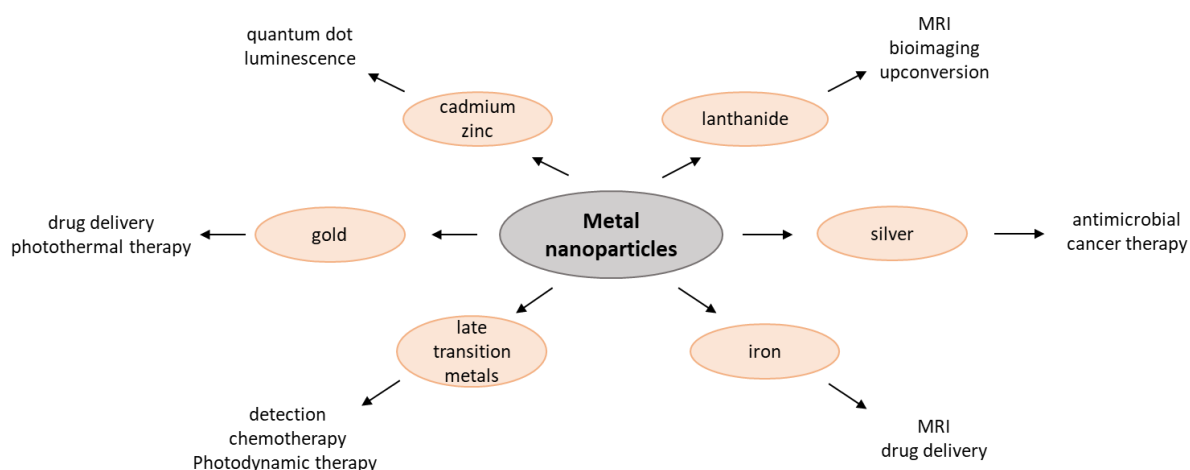


Figure 1.8 Different types of metal nanoparticles and their biological application.

1.6 Aim and outline of this thesis

The studies described above give a short overview of the use of metals in cancer treatment, from metallodrugs to metal-based photosensitizers for PDT and metal-based nanomedicine platforms. However, so far limited research has been dedicated to the self-assembly of molecular photosensitizers into well-defined nanoparticles, and on the evaluation of these aggregates as anticancer compounds. The goal of the research described in this thesis is the exploration of the molecular and supramolecular chemistry of d^8 metal-based PDT sensitizers, and specifically those based on the tetradentate cyclometalating ligands shown in Figure 1.9.

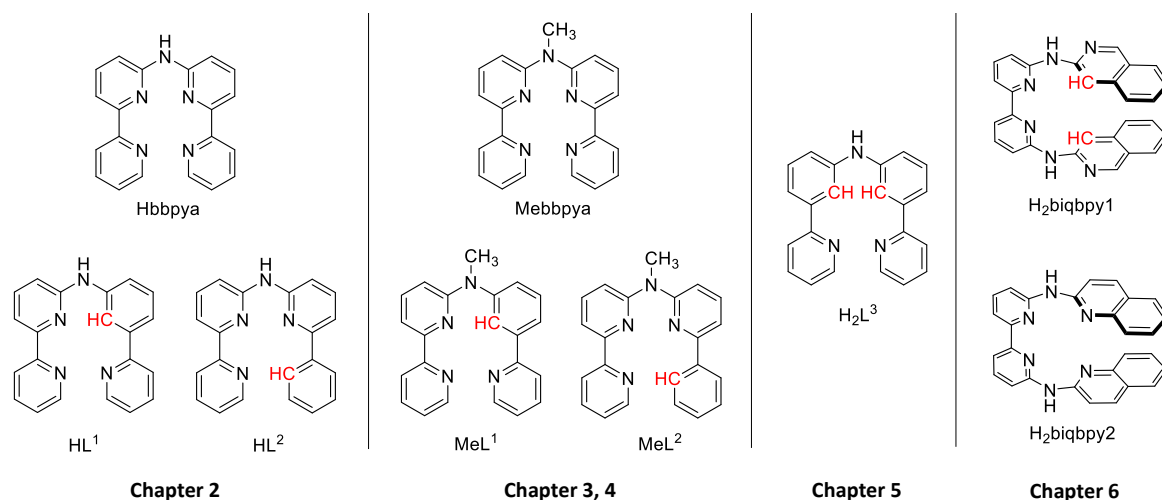


Figure 1.9 The chemical structures of tetrapyridyl and cyclometalating tetradentate ligands described in this thesis.

In **chapter 2**, the chemistry and photochemistry of two isomeric cyclometalated palladium complexes based on the **HL**¹ and **HL**² ligands are described. In particular, blue-light PDT properties were discovered for only one of these isomers, and the role of the position of the Pd-C bond on the photochemical properties of these complexes is discussed in more details using a combination of experiments and theoretical calculations.

In **chapter 3**, the non-coordinated N bridge of the **HL**¹ and **HL**² ligands studied in **chapter 2**, was methylated and the resulting ligands **MeL**¹ and **MeL**² coordinated to palladium(II). By doing so, the NH deprotonation described in **chapter 2**, was made impossible, which allowed for exploring in more detail the self-assembly of these cyclometalated complexes, and to compare it to that of their tetrapyridyl analogue complex based on the Hbbpya ligand (Figure 1.9). The photophysical, photochemical, and photobiological properties of these three molecules were found to highly depend on their self-assembly in biological conditions, which depended dramatically on the presence of proteins in the aqueous medium. Their applications as PDT agents are compared in *in vitro* and *in vivo* cancer models.

In **chapter 4**, the **MeL**¹ and **MeL**² described in **chapter 3** were coordinated to platinum(II), and the photophysical, photochemical, supramolecular, and (photo)biological properties of the resulting two isomer complexes, were studied in detail. Contrary to the palladium complexes studied in **chapter 3**, which were good PDT agents but poor emitters, these platinum-based cyclometalated complexes were found to be weak PDT agents, but very interesting emitters. The self-assembly observed due to the Pt...Pt interaction indeed stimulated red absorption and deep-red emission, which allowed us to monitor in time and space the uptake and distribution

of the nanostructures generated by these complexes in cancer cells. This study brings new perspectives to a new type of theranostic nanoplatform that targets mitochondria.

In **chapter 5**, a biscyclometalated analogue palladium complex, related to the one described in **chapter 2** and using the ligand **H₂L³**, is reported. This complex showed particularly efficient green-light-activated PDT properties not only under normoxia but also in hypoxic cancer cells, as characterized by high photoindex (PI) *in vitro* and excellent antitumor effects in a mice model of skin melanoma. The combination of the excellent PDT properties of this complex and its self-assembly into nanoparticles *via* the metallophilic interaction, results in a new tumor-targeting strategy for PDT that uses a molecular PS to generate nanoparticles *in vivo*, without a need for chemical conjugation to known tumor-targeting nanoplatforms. To name this new strategy we propose the term “molecular photosensitizer self-assembled nanoparticles”, or MoPSAN; in this chapter it was used to achieve hypoxia tumor inhibition.

In **chapter 6**, a gold(III) biscyclometalated complex was serendipitously obtained *via* the so-called “rollover” effect during the coordination of the tetrapyrrolyl ligand **H₂biqbpy1**. Rollover cyclometalation is a specific coordination reversal of polypyridyl ligands, from the common M-N bond coordination to the meta M-C bond in the same heterocyclic ring, which becomes deprotonated. This effect is strongly dependent on the structure of the ligand, as an isomer of the ligand, **H₂biqbpy2**, led to the expected tetrapyrrolyl gold(III) complex. The cytotoxicity of both complexes towards different types of cancer cells was investigated, and rationalized by looking at their reactivity towards thiol-containing compounds, their TrxR inhibition properties, and their potassium channel binding affinity.

Finally, in **chapter 7**, a summary is presented for the main findings described in this thesis, followed by a general discussion, and an outlook for further research.

1.7 References

1. K. H. Thompson and C. Orvig, *Science*, 2003, **300**, 936-939.
2. K. J. Franz and N. Metzler-Nolte, *Chem. Rev.*, 2019, **119**, 727-729.
3. R. L. Siegel, K. D. Miller and A. Jemal, *CA Cancer J. Clin.*, 2019, **69**, 7-34.
4. M. Naghavi, A. A. Abajobir, A. D. Lopez and C. J. L. Murray, *Lancet*, 2017, **390**, 1151-1210.
5. S. Dasari and P. Bernard Tchounwou, *Eur. J. Pharmacol.*, 2014, **740**, 364-378.
6. R. G. Kenny and C. J. Marmion, *Chem. Rev.*, 2019, **119**, 1058-1137.
7. C. R. Rocha, M. M. Silva, A. Quinet, J. B. Cabral-Neto and C. F. Menck, *Clinics*, 2018, **73**.
8. L. J. K. Boerner and J. M. Zaleski, *Curr. Opin. Chem. Biol.*, 2005, **9**, 135-144.
9. A. C. Komor and J. K. Barton, *Chem. Commun.*, 2013, **49**.
10. P. M. Takahara, A. C. Rosenzweig, C. A. Frederick and S. J. Lippard, *Nature*, 1995, **377**, 649-652.
11. A. W. McKinley, P. Lincoln and E. M. Tuite, *Coord. Chem. Rev.*, 2011, **255**, 2676-2692.

12. A. N. Boynton, L. Marcélis and J. K. Barton, *J. Am. Chem. Soc.*, 2016, **138**, 5020-5023.
13. K. M. Boyle and J. K. Barton, *J. Am. Chem. Soc.*, 2018, **140**, 5612-5624.
14. H. Song, J. T. Kaiser and J. K. Barton, *Nat. Chem.*, 2012, **4**, 615-620.
15. H. K. Liu and P. J. Sadler, *Acc. Chem. Res.*, 2011, **44**, 349-359.
16. Y. K. Yan, M. Melchart, A. Habtemariam and P. J. Sadler, *Chem. Commun.*, 2005, **38**, 4764-4776.
17. Z. Ma, G. Palermo, Z. Adhireksan, B. S. Murray, T. V. Erlach, U. R. Paul J. Dyson and C. A. Davey., *Angew. Chem. Int. Ed.*, 2016, **55**, 7441-7444.
18. A.-M. Florea and D. Büsselberg, *Cancers*, 2011, **3**, 1351-1371.
19. C. Santini, M. Pellei, V. Gandin, M. Porchia, F. Tisato and C. Marzano, *Chem. Rev.*, 2013, **114**, 815-862.
20. D.-L. Ma, D. S.-H. Chan and C.-H. Leung, *Acc. Chem. Res.*, 2014, **47**, 3614-3631.
21. T. C. Johnstone, K. Suntharalingam and S. J. Lippard, *Chem. Rev.*, 2016, **116**, 3436-3486.
22. M. Mora, M. C. Gimeno and R. Visbal, *Chem. Soc. Rev.*, 2019, **48**, 447-462.
23. W. H. Ang, I. Khalaila, C. S. Allardyce, L. Juillerat-Jeanneret and P. J. Dyson, *J. Am. Chem. Soc.*, 2005, **127**, 1382-1383.
24. K. Nakao, N. Minato and S. Uemoto, *Innovative medicine: basic research and development*, Springer Nature, 2015.
25. T. Zou, C. T. Lum, C.-N. Lok, J.-J. Zhang and C.-M. Che, *Chem. Soc. Rev.*, 2015, **44**, 8786-8801.
26. A. Ilari, P. Baiocco, L. Messori, A. Fiorillo, A. Boffi, M. Gramiccia, T. Di Muccio and G. Colotti, *Amino Acids*, 2012, **42**, 803-811.
27. J. L. Hickey, R. A. Ruhayel, P. J. Barnard, M. V. Baker and S. J. Berners-Price, *J. Am. Chem. Soc.*, 2008, **130**, 12570-12571.
28. A. de Almeida, A. F. Mosca, D. Wragg, M. Wenzel, P. Kavanagh, G. Barone, S. Leoni, G. Soveral and A. Casini, *Chem. Commun.*, 2017, **53**, 3830-3833.
29. B. Aikman, A. de Almeida, S. M. Meier-Menches and A. Casini, *Metallomics*, 2018, **10**, 696-712.
30. P. Agostinis, K. Berg, K. A. Cengel, T. H. Foster, A. W. Girotti, S. O. Gollnick, S. M. Hahn, M. R. Hamblin, A. Juzeniene, D. Kessel, M. Korbelik, J. Moan, P. Mroz, D. Nowis, J. Piette, B. C. Wilson and J. Golab, *CA Cancer J. Clin.*, 2011, **61**, 250-281.
31. F. Hu, S. Xu and B. Liu, *Adv. Mater.*, 2018, **30**.
32. J. Li and K. Pu, *Chem. Soc. Rev.*, 2019, **48**, 38-71.
33. A. Gorman, J. Killoran, C. O'Shea, T. Kenna, W. M. Gallagher and D. F. O'Shea, *J. Am. Chem. Soc.*, 2004, **126**, 10619-10631.
34. S. Kwiatkowski, B. Knap, D. Przystupski, J. Saczko, E. Kędzierska, K. Knap-Czop, J. Kotlińska, O. Michel, K. Kotowski and J. Kulbacka, *Biomed. Pharmacother.*, 2018, **106**, 1098-1107.
35. L. B. Josefsen and R. W. Boyle, *Met. Based Drugs*, 2008, **2008**, 1-23.
36. F. Anzengruber, P. Avci, L. F. de Freitas and M. R. Hamblin, *Photochem. Photobiol. Sci.*, 2015, **14**, 1492-1509.
37. I. Beltran Hernandez, Y. Yu, F. Ossendorp, M. Korbelik and S. Oliveira, *J. Clin. Med.*, 2020, **9**.
38. A. B. Ormond and H. S. Freeman, *Materials*, 2013, **6**, 817-840.
39. S. K. Pushpan, S. Venkatraman, V. G. Anand, J. Sankar, D. Parmeswaran, S. Ganesan and T. K. Chandrashekar, *Anti-Cancer Agents Med. Chem.*, 2002, **2**, 187-207.
40. H. Kataoka, H. Nishie, N. Hayashi, M. Tanaka, A. Nomoto, S. Yano and T. Joh, *Ann. Transl. Med.*, 2017, **5**, 183.
41. S. Monro, K. L. Colón, H. Yin, J. Roque, P. Konda, S. Gujar, R. P. Thummel, L. Lilge, C. G. Cameron and S. A. McFarland, *Chem. Rev.*, 2018, **119**, 797-828.
42. M. Obata, S. Hirohara, R. Tanaka, I. Kinoshita, K. Ohkubo, S. Fukuzumi, M. Tanihara and S. Yano, *J. Med. Chem.*, 2009, **52**, 2747-2753.
43. A. E. O'Connor, W. M. Gallagher and A. T. Byrne, *Photochem. Photobiol. Sci.*, 2009, **85**, 1053-1074.
44. P. Kaspler, S. Lazic, S. Forward, Y. Arenas, A. Mandel and L. Lilge, *Photochem. Photobiol. Sci.*, 2016, **15**, 481-495.

45. J. Karges, S. Kuang, F. Maschietto, O. Blacque, I. Ciofini, H. Chao and G. Gasser, *Nat. Commun.*, 2020, **11**, 3262.
46. S. Bonnet, *Dalt. Trans.*, 2018, **47**, 10330-10343.
47. V. H. S. van Rixel, B. Siewert, S. L. Hopkins, S. H. C. Askes, A. Busemann, M. A. Siegler and S. Bonnet, *Chem. Sci.*, 2016, **7**, 4922-4929.
48. V. H. S. van Rixel, V. Ramu, A. B. Auyeung, N. Beztsinna, D. Y. Leger, L. N. Lameijer, S. T. Hilt, S. E. Le Devedec, T. Yildiz, T. Betancourt, M. B. Gildner, T. W. Hudnall, V. Sol, B. Liagre, A. Kornienko and S. Bonnet, *J. Am. Chem. Soc.*, 2019, **141**, 18444-18454.
49. J. A. Cuello-Garibo, M. S. Meijer and S. Bonnet, *Chem. Commun.*, 2017, **53**, 6768-6771.
50. J. D. Knoll, B. A. Albani and C. Turro, *Chem. Commun.*, 2015, **51**, 8777-8780.
51. L. N. Lameijer, D. Ernst, S. L. Hopkins, M. S. Meijer, S. H. C. Askes, S. E. Le Dévedec and S. Bonnet, *Angew. Chem. Int. Ed.*, 2017, **56**, 11549-11553.
52. B. S. Howerton, D. K. Heidary and E. C. Glazer, *J. Am. Chem. Soc.*, 2012, **134**, 8324-8327.
53. M. Albrecht, *Chem. Rev.*, 2010, **110**, 576-623.
54. D. Ma, T. Tsuboi, Y. Qiu and L. Duan, *Adv. Mater.*, 2017, **29**.
55. V. W. Yam, V. K. Au and S. Y. Leung, *Chem. Rev.*, 2015, **115**, 7589-7728.
56. M. Albrecht, *Chem. Rev.*, 2010, **110**, 576-623.
57. H. Huang, P. Zhang, H. Chen, L. Ji and H. Chao, *Chem. Eur. J.*, 2015, **21**, 715-725.
58. P. Zhang and P. J. Sadler, *J. Organomet. Chem.*, 2017, **839**, 5-14.
59. S. Bonnet, *Comment Inorg. Chem.*, 2014, **35**, 179-213.
60. P. G. Bomben, K. C. Robson, P. A. Sedach and C. P. Berlinguette, *Inorg. Chem.*, 2009, **48**, 9631-9643.
61. X. Q. Zhou, A. Busemann, M. S. Meijer, M. A. Siegler and S. Bonnet, *Chem. Commun.*, 2019, **55**, 4695-4698.
62. S. L. Higgins and K. J. Brewer, *Angew. Chem. Int. Ed.*, 2012, **51**, 11420-11422.
63. H. Huang, S. Banerjee, K. Qiu, P. Zhang, O. Blacque, T. Malcomson, M. J. Paterson, G. J. Clarkson, M. Staniforth, V. G. Stavros, G. Gasser, H. Chao and P. J. Sadler, *Nat. Chem.*, 2019, **11**, 1041-1048.
64. L. He, Y. Li, C.-P. Tan, R.-R. Ye, M.-H. Chen, J.-J. Cao, L.-N. Ji and Z.-W. Mao, *Chem. Sci.*, 2015, **6**, 5409-5418.
65. Z. Lv, H. Wei, Q. Li, X. Su, S. Liu, K. Y. Zhang, W. Lv, Q. Zhao, X. Li and W. Huang, *Chem. Sci.*, 2018, **9**, 502-512.
66. J. A. Cuello-Garibo, C. C. James, M. A. Siegler, S. L. Hopkins and S. Bonnet, *Chem. Eur. J.*, 2019, **25**, 1260-1268.
67. X. Jiang, N. Zhu, D. Zhao and Y. Ma, *Sci. China Chem.*, 2015, **59**, 40-52.
68. N. M. Shavaleev, H. Adams, J. Best, R. Edge, S. Navaratnam and J. A. Weinstein, *Inorg. Chem.*, 2006, **45**, 9410-9415.
69. T. Chatzisideri, S. Thysiadis, S. Katsamakas, P. Dalezis, I. Sigala, T. Lazarides, E. Nikolakaki, D. Trafalis, O. A. Gederaas, M. Lindgren and V. Sarli, *Eur. J. Med. Chem.*, 2017, **141**, 221-231.
70. H. Luo, B. Cao, A. S. C. Chan, R. W. Sun and T. Zou, *Angew. Chem. Int. Ed.*, 2020, **59**, 11046-11052.
71. M. Mauro, A. Aliprandi, D. Septiadi, N. S. Kehr and L. De Cola, *Chem. Soc. Rev.*, 2014, **43**, 4144-4166.
72. X. Yin, S. A. Warren, Y. T. Pan, K. C. Tsao, D. L. Gray, J. Bertke and H. Yang, *Angew. Chem. Int. Ed.*, 2014, **126**, 14311-14315.
73. K. Li, G. S. Ming Tong, Q. Wan, G. Cheng, W.-Y. Tong, W.-H. Ang, W.-L. Kwong and C.-M. Che, *Chem. Sci.*, 2016, **7**, 1653-1673.
74. T. W. Thomas and A. E. Underhill, *Chem. Soc. Rev.*, 1972, **1**, 99-120.
75. A. Aliprandi, D. Genovese, M. Mauro and L. De Cola, *Chem. Lett.*, 2015, **44**, 1152-1169.
76. Q. Wan, W.-P. To, X. Chang and C.-M. Che, *Chem*, 2020, **6**, 1-23.
77. M.-Y. Yuen, V. A. L. Roy, W. Lu, S. C. F. Kui, G. S. M. Tong, M.-H. So, S. S.-Y. Chui, M. Muccini, J. Q. Ning, S. J. Xu and C.-M. Che, *Angew. Chem. Int. Ed.*, 2008, **47**, 9895-9899.
78. C.-N. Lok, T. Zou, J.-J. Zhang, I. W.-S. Lin and C.-M. Che, *Adv. Mater.*, 2014, **26**, 5550-5557.
79. J. Zhao and M. H. Stenzel, *Polym. Chem.*, 2018, **9**, 259-272.

80. S. Sinn, L. Yang, F. Biedermann, D. Wang, C. Kübel, J. J. L. M. Cornelissen and L. De Cola, *J. Am. Chem. Soc.*, 2018, **140**, 2355-2362.
81. P.-K. Chow, W.-P. To, K.-H. Low and C.-M. Che, *Chem. Asian J.*, 2014, **9**, 534-545.
82. Q. Wan, W.-P. To, C. Yang and C.-M. Che, *Angew. Chem. Int. Ed.*, 2018, **57**, 3089-3093.
83. S. W. Lai, T. C. Cheung, M. C. Chan, K. K. Cheung, S. M. Peng and C. M. Che, *Inorg. Chem.*, 2000, **39**, 255-262.
84. C. Zou, J. Lin, S. Suo, M. Xie, X. Chang and W. Lu, *Chem. Commun.*, 2018, **54**, 5319-5322.
85. Q. Wan, J. Xia, W. Lu, J. Yang and C.-M. Che, *J. Am. Chem. Soc.*, 2019, **141**, 11572-11582.
86. R. A. Freitas, *Nanomedicine*, 2005, **1**, 2-9.
87. B. Y. Kim, J. T. Rutka and W. C. Chan, *N. Engl. J. Med.*, 2010, **363**, 2434-2443.
88. K. Greish, *Enhanced permeability and retention (EPR) effect for anticancer nanomedicine drug targeting*, Cancer nanotechnology, Humana Press, 2010.
89. Y. Shi, R. van der Meel, X. Chen and T. Lammers, *Theranostics*, 2020, **10**, 7921-7924.
90. J. A. Nagy, S. H. Chang, A. M. Dvorak and H. F. Dvorak, *Br. J. Cancer*, 2009, **100**, 865-869.
91. M. Chidambaram, R. Manavalan and K. Kathiresan, *J. Pharm. Pharmaceut. Sci.*, 2011, **14**, 67-77.
92. U. Prabhakar, H. Maeda, R. K. Jain, E. M. Sevick-Muraca, W. Zamboni, O. C. Farokhzad, S. T. Barry, A. Gabizon, P. Grodzinski and D. C. Blakey, *Cancer Res.*, 2013, **73**, 2412-2417.
93. S. Sindhwani, A. M. Syed, J. Ngai, B. R. Kingston, L. Maiorino, J. Rothschild, P. MacMillan, Y. Zhang, N. U. Rajesh, T. Hoang, J. L. Y. Wu, S. Wilhelm, A. Zilman, S. Gadde, A. Sulaiman, B. Ouyang, Z. Lin, L. Wang, M. Egeblad and W. C. W. Chan, *Nat. Mater.*, 2020, **19**, 566-575.
94. Y. Y. Chen, A. M. Syed, P. MacMillan, J. V. Rocheleau and W. C. W. Chan, *Adv. Mater.*, 2020, **32**, e1906274.
95. E. C. Cho, Q. Zhang and Y. Xia, *Nat. Nanotechnol.*, 2011, **6**, 385-391.
96. T. L. Doane and C. Burda, *Chem. Soc. Rev.*, 2012, **41**.
97. C.-W. Lai, Y.-H. Wang, C.-H. Lai, M.-J. Yang, C.-Y. Chen, P.-T. Chou, C.-S. Chan, Y. Chi, Y.-C. Chen and J.-K. Hsiao, *Small*, 2008, **4**, 218-224.
98. L. Zeng, P. Gupta, Y. Chen, E. Wang, L. Ji, H. Chao and Z.-S. Chen, *Chem. Soc. Rev.*, 2017, **46**, 5771-5804.
99. J. Karges, O. Blacque, H. Chao and G. Gasser, *Inorg. Chem.*, 2019, **58**, 12422-12432.
100. J. J. Giner-Casares, M. Henriksen-Lacey, M. Coronado-Puchau and L. M. Liz-Marzán, *Mater. Today*, 2016, **19**, 19-28.
101. E. Boisselier and D. Astruc, *Chem. Soc. Rev.*, 2009, **38**.
102. V. Amendola, R. Pilot, M. Frascioni, O. M. Maragò and M. A. Iatì, *J. Condens. Matter Phys.*, 2017, **29**.
103. L. R. Hirsch, R. J. Stafford, J. A. Bankson, S. R. Sershen, B. Rivera, R. E. Price, J. D. Hazle, N. J. Halas and J. L. West, *Proc. Natl. Acad. Sci. U.S.A.*, 2003, **100**, 13549-13554.
104. A. Narmani, B. Farhood, H. Haghi-Aminjan, T. Mortezaazadeh, A. Aliasgharzadeh, M. Mohseni, M. Najafi and H. Abbasi, *J. Drug Deliv. Sci. Technol.*, 2018, **44**, 457-466.
105. H. Dong, S. R. Du, X. Y. Zheng, G. M. Lyu, L. D. Sun, L. D. Li, P. Z. Zhang, C. Zhang and C. H. Yan, *Chem. Rev.*, 2015, **115**, 10725-10815.
106. B. Chen and F. Wang, *Acc. Chem. Res.*, 2020, **53**, 358-367.
107. Y. Liu, X. Meng and W. Bu, *Coord. Chem. Rev.*, 2019, **379**, 82-98.
108. Y. Liu, D. Tu, H. Zhu and X. Chen, *Chem. Soc. Rev.*, 2013, **42**, 6924-6958.
109. M. S. Meijer, M. M. Natile and S. Bonnet, *Inorg. Chem.*, 2020, **59**, 14807-14818.

2

The two isomers of a cyclometalated palladium sensitizer show distinct photodynamic properties in cancer cells

This report demonstrates that changing the place of the carbon-metal bond in a polypyridyl cyclopalladated complex, i.e. going from PdL^1 ($\text{N}^{\wedge}\text{N}^{\wedge}\text{C}^{\wedge}\text{N}$) to PdL^2 ($\text{N}^{\wedge}\text{N}^{\wedge}\text{N}^{\wedge}\text{C}$), dramatically influences the photodynamic therapeutic ability of the complex in cancer cells. This effect is attributed to the significant difference in absorbance and singlet oxygen quantum yields of the two isomers.

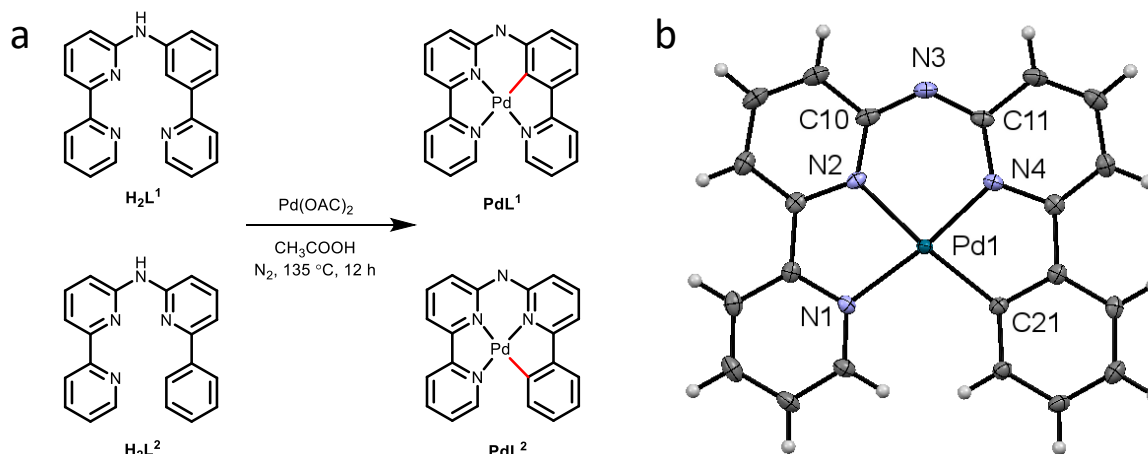
This chapter was published as a communication: X.-Q. Zhou, A. Busemann, M. Meijer, M. A. Siegler and S. Bonnet*, *Chem. Comm.*, 2019, **55**, 4695-4698.

2.1 Introduction

The success of cisplatin, a milestone drug in the treatment of cancers, stimulated the generation of many platinum-based anticancer drugs,¹⁻³ three of which (carboplatin, oxaliplatin and nedaplatin) are approved worldwide. However, the unselective covalent binding of cisplatin with DNA in cancer cells and healthy cells results in serious side effects and drug resistance, which has encouraged the development of anticancer drugs based on alternative metals.⁴⁻⁹ In this regards, palladium(II) complexes have been proposed as potential metal-based anticancer drugs for their similar d^8 coordination sphere and square-planar structure, compared to platinum(II) complexes.^{10, 11} One of them, called padeliporfin or WST11, was recently approved for photodynamic therapy (PDT) of prostate cancer.¹² PDT is a form of light-activated cancer therapy. It emerges as a more patient-friendly approach due to the controlled toxicity effect and low invasiveness of light irradiation.¹³⁻¹⁷ In PDT, a photosensitizing agent (PS) is irradiated by visible light at the tumor site, where it generates cytotoxic reactive oxygen species (ROS), which induce cancer cell death.¹⁸ Polypyridyl metal complexes typically form excellent PDT sensitizers, provided they strongly absorb visible light.^{19,20} The light absorption properties of such complexes can be tuned by changing the metal or the ligands. Critically, good photosensitizers should be photostable, which demands on the strong coordination bonds of multidentate ligands.

Recently, bioactive pincer palladium complexes with tridentate N-heterocyclic carbene ligands showed strong metal-carbon bonds and tunable physicochemical properties.^{10, 21-24} However, the intracellular substitution of remaining monodentate ligand makes speciation in biological medium and mode-of-action complicated to understand. In addition, due to the smaller ionic radius of Pd^{2+} ions, Pd-ligand bonds are longer and more labile than their Pt-ligand analogues,²⁵ so that anticancer drugs based on palladium(II) are still comparatively rare.⁶ To overcome these drawbacks, we investigated the design and properties of palladium(II) PDT sensitizers built from single tetradentate cyclometalating ligands, which are expected to be more stable in biological medium compared with the tridentate N-heterocyclic carbene ligands. Cyclometalation was considered for different reasons. First, the strong Pd-C bond can stabilize these compounds in biological medium. Second, the lower charge introduced by the cyclometalated ligand can improve the lipophilicity and cellular uptake of the metal complexes.^{7, 26} Third, the presence of a Pd-C bond should in principle lead to a bathochromic shift of the visible absorption bands of the metal complex, which is key for PDT applications.²⁷ In polypyridyl metal complexes, introducing a metal-carbon bond usually generates a series of

isomers that might have different properties. Herein we investigated two novel cyclopalladated palladium isomers **PdL¹** (**H₂L¹** = N-(3-(pyridin-2-yl)phenyl)-[2,2'-bipyridin]-6-amine) and **PdL²** (**H₂L²** = N-(6-phenylpyridin-2-yl)-[2,2'-bipyridin]-6-amine) (Scheme 2.1a). In **PdL¹**, the Pd-C bond was introduced in a pyridyl group that is adjacent to the non-bonded nitrogen bridge of the ligand, while in **PdL²** it is introduced in one of the terminal aromatic rings.



Scheme 2.1 (a) Synthesis of **PdL¹** and **PdL²**; (b) Displacement ellipsoid plot (50% probability level) of **PdL²** at 110(2) K (bond distance: Pd-N1 2.060(3) Å, Pd-N2 2.028(4) Å, Pd-N4 1.988(3) Å, Pd-C21 2.017(4) Å); angle: N4-Pd1-C21 81.99(15)°, N4-Pd1-N2 92.66(16)°, C21-Pd1-N2 174.65(18)°, N4-Pd1-N1 172.2(2)°, C21-Pd1-N1 105.02(17)°, N2-Pd1-N1 80.33(13)°).

2.2 Results and discussion

The ligands **H₂L¹** and **H₂L²** were synthesized by Buchwald–Hartwig coupling reactions (Scheme AI.1).^{28–30} Palladation of the ligands was obtained in more than 90% yield by reacting in acetic acid the corresponding ligands with palladium(II) acetate (Scheme AI.1). ¹H NMR spectra of both Pd complexes, as well as their infrared spectra (IR, Figure AI.1), did not show any peak or vibration mode characteristic for a secondary amine bridge, which altogether suggested deprotonation upon coordination. According to ¹³C-APT NMR, the ligands **H₂L¹** and **H₂L²** have six quaternary carbon peaks, while their palladium complexes have seven, demonstrating that cyclometallation did occur. Altogether **PdL¹** and **PdL²** appear to be neutral complexes; their identical HRMS data also demonstrated they are coordination isomers.

Vapor diffusion of diethyl ether into a methanol solution of **PdL²** was used to yield the red rectangular crystals suitable for X-ray structure determination (Table AI.1 and Scheme 1b). **PdL²** crystallized in the centrosymmetric $P2_1/n$ monoclinic space group. Three nitrogen and one carbon were coordinated to the palladium(II) cation, with bond lengths in the range

1.988(3)-2.028(4) Å for the three Pd-N bonds, and a Pd-C bond distance of 2.017(4) Å. The coordination sphere was slightly distorted, with a torsion angle N1-N2-N4-C21 of 2.33°. τ_4 , a structural parameter calculated by $(360^\circ - (\alpha + \beta)) / (141^\circ)$, where α and β are the two greatest valence angles of the coordination sphere,³¹ was 0.093 in the structure of **PdL**², which is typical of an essentially square planar complex. Deprotonation of the nitrogen bridge was evidenced by the shorter distance between the amine nitrogen atoms and the adjacent pyridine carbon atoms (C10-N3 = 1.353(4) Å and C11-N3 = 1.349(4)), compared to that found in metal complexes with protonated nitrogen bridges (N-C distances in the range 1.36 Å to 1.39 Å).^{29, 30} Also, unlike for [Fe(Hbbpya)(NCS)₂] complex,³² no residual electron density was found near the bridging N atom in the structure of **PdL**². Finally, the asymmetric unit contained no counter-ions. In summary, X-ray crystallography confirmed NMR and IR data, showing that **PdL**¹ and **PdL**² are neutral species because of the deprotonation of the nitrogen bridge upon coordination.

The absorption spectrum of both complexes in PBS:DMSO (1:1) solution at 310 K (Figure AI.2) presented no significant changes over 24 hours, suggesting that the complexes were thermally stable in such conditions. Similar results were obtained in cell-growing medium (Figure AI.3), demonstrating good stability in such conditions. The partition coefficients ($\log P_{ow}$) of the palladium complexes were determined by the shake-flask method (Table AI.2). $\log P_{ow}$ was lower for **PdL**¹ (-0.64) than for **PdL**² (+0.046), confirming the higher solubility of the former, compared to the latter. Their cytotoxicity was tested in lung (A549) and skin (A431) cancer cell lines, both in the dark and upon blue light activation. Low doses of blue light were chosen (455 nm, 5 min, 10.5 mW cm⁻², 3.2 J cm⁻²) which have by themselves no effect on cell growth.³³ The cell growth inhibition effective concentrations (EC₅₀) of **PdL**¹ and **PdL**² are reported in Table 1, and the dose-response curves are shown in Figure 2.1 and Figure AI.4. In the dark both compounds showed significant anticancer activity, with EC₅₀ around 10 µM for **PdL**¹ and **PdL**² in A549 cells, respectively. After blue light activation, **PdL**¹ showed a notable 13- or 4.0-fold increase in cytotoxicity in A549 and A431, respectively; while **PdL**² showed negligible photoindex (PI = EC_{50,dark}/EC_{50,light}) of 1.3 or 1.4, respectively.

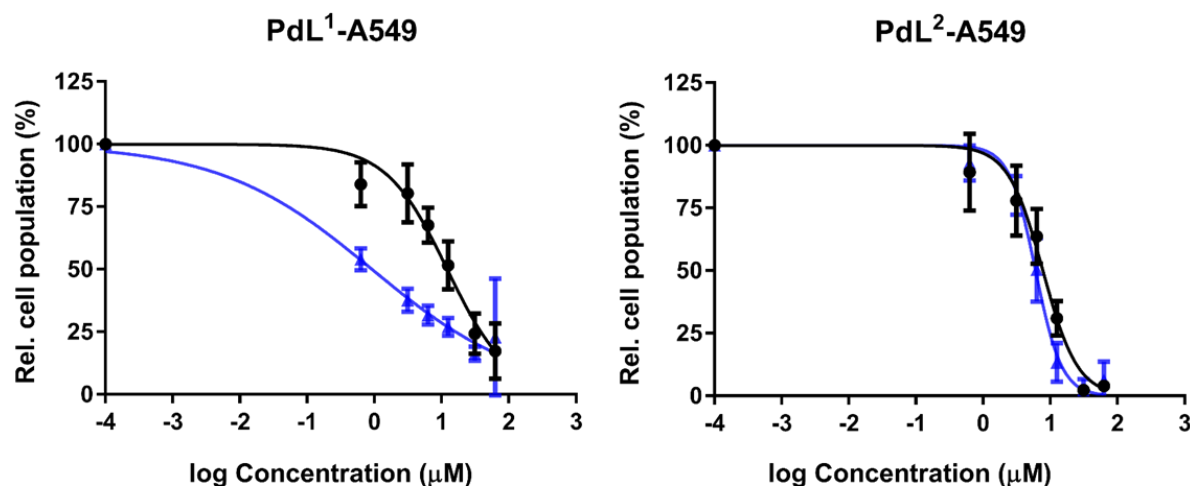


Figure 2.1 Dose-response curves for A549 cells incubated with palladium complexes and irradiated 5 min with blue light (blue data points), or in the dark (black data points).

Table 2.1 The cell growing inhibition effective concentrations (EC_{50} in μM) of **PdL¹** and **PdL²** towards A549 and A431 human cancer cell lines. 95% confidence interval (CI in μM) and photoindex ($PI = EC_{50, \text{dark}}/EC_{50, \text{light}}$) are also indicated.

Complexes		EC_{50} (μM)			
		A549	$\pm CI$	A431	$\pm CI$
PdL¹	Dark	12	+3.0 -3.0	20	+4.0 -3.0
	Light	0.9	+0.8 -0.5	5.0	+2.0 -1.0
PI		13		4.0	
PdL²	Dark	8.0	+2.0 -1.0	14	+2.0 -1.0
	Light	6.0	+0.8 -0.7	10	+1.0 -1.0
PI		1.3		1.4	

irradiation condition: 455 nm blue light, 5 min, 10.5 mW cm^{-2} , 3.2 J cm^{-2} . Data is the mean over three independent experiments.

The difference in photocytotoxicity between the two coordination isomers was quite intriguing. To investigate the reason for such difference, we first measured spectroscopically the singlet oxygen (1O_2) generation quantum yield (ϕ_Δ) of these two isomers in CD_3OD . ϕ_Δ was more than twice higher for **PdL¹** (0.89) than for **PdL²** (0.38, Figure 2.2b and Table AI.3), and higher than the reference **[Ru(bpy)₃]Cl₂** (0.73).³⁴ However, **PdL²** was still a decent 1O_2 generator. In methanol, the absorbance spectra of both complexes (Figure 2.2) were similar in the 270-300 nm region; however, **PdL¹** had a much higher absorption in the blue region with $\lambda_{\text{max}}^{\text{abs}} = 422 \text{ nm}$, compared to **PdL²** that absorbed in the near-UV region ($\lambda_{\text{max}}^{\text{abs}} = 347 \text{ nm}$, Figure 2.2a). In

this solvent the molar absorptivity at 455 nm for **PdL**¹ and **PdL**² was 2004 M⁻¹ cm⁻¹ and 133 M⁻¹ cm⁻¹, respectively, indicating a 15-fold enhanced absorption of **PdL**¹ in the blue region, compared with **PdL**². Considering their similar lifetime (0.271 vs. 0.333 ns for the main component of their biexponential decay, Table AI.3 and Figure AI.5), the difference in ¹O₂ generation efficiency is probably a consequence of the higher phosphorescence quantum yield for **PdL**¹ (0.0017) vs. **PdL**² (0.00084, Table AI.3), which points to the slower non-radiative decay pathways for the former, compared to the latter. Altogether, the dramatically higher phototoxicity of **PdL**¹, compared to **PdL**², seems to result from the much better absorption of blue light of **PdL**¹, coupled to its higher phosphorescence quantum yield, which leads to higher ¹O₂ generation efficiency. Although different log P_{ow} values may lead to different cell uptake and subcellular localization for both isomers, the better photobiological properties of **PdL**¹ depend, at least in part, on the much better photodynamic properties of **PdL**¹, compared to its isomer **PdL**².

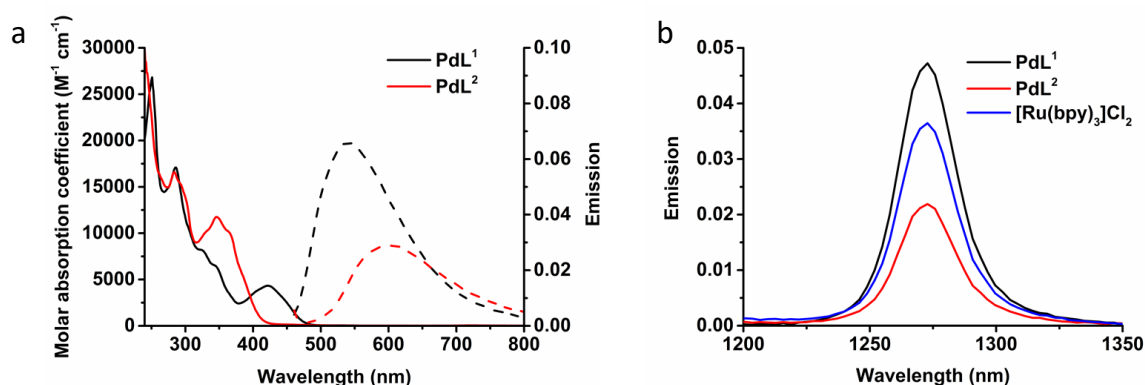


Figure 2.2 (a) The molar absorption coefficient (solid line) and emission spectra (dash line) of **PdL**¹ (black), **PdL**² (red) in CH₃OH. (b) Singlet oxygen emission spectra of [Ru(bpy)₃]Cl₂ (standard, blue), **PdL**¹ (black), **PdL**² (red) in CD₃OD irradiated with blue light (λ_{ex} = 450 nm, 50 mW, 200 ms).

Density functional theory (DFT) calculations were performed to understand why **PdL**¹ exhibited higher absorption in the blue domain than its isomer **PdL**². The nature of the highest occupied molecular orbital (HOMO) and lowest unoccupied molecular orbitals (LUMO) is highly relevant to predict the photophysical properties of metal complexes.³⁵⁻³⁷ As shown in Figure 2.3, the HOMO and LUMO orbitals of both isomers **PdL**¹ and **PdL**² had π symmetry and were centered on the ligand, with a negligible contribution of the palladium(II) center. The bridged secondary amine is the major contributor to the HOMO of both Pd complexes, attributing for 20.4% (**PdL**¹) and 21.8% (**PdL**²) of the electron density. The rest of the HOMO

orbital density was located in the aromatic rings directly connected to the nitrogen bridge. By contrast, the LUMO orbitals for both complexes were centered on the bipyridyl fragment. This suggested that the lowest energy absorption band of both palladium complexes should be of ligand-to-ligand charge transfer character, from the amine to the bipyridyl.

The calculated energies of HOMOs, LUMOs and energy gaps are listed in Table S4. The HOMO of **PdL¹** was significantly higher in energy than that of **PdL²**, indicating the higher electron-donating effect of the negatively charged carbon atom of **PdL¹**, compared with that of **PdL²** which is further away from the nitrogen bridge. By contrast, the LUMO energy levels of both Pd complexes were similar, because LUMO orbitals are located on the almost equivalent bipyridyl fragments. Such lower energy gap of **PdL¹** suggested better absorption of low-energy light, which explains the observed differences in the UV-vis spectra of the two isomers. These results were confirmed by time-dependent density functional theory calculations (TDDFT) for both complexes in methanol, using COSMO to simulate solvent effects (Fig. S14 left). The calculated spectrum of **PdL¹** (Figure AI.6, left) showed lower energy (515 nm) for the HOMO-LUMO transition, compared to **PdL²** (449 nm). These transition energies were decreased (404 and 367 nm, respectively) by protonation of the nitrogen bridge (Figure AI.6, right), which may happen in the slightly acidic environment of cancer cells; however, the trend between [**PdHL¹**]⁺ and [**PdHL²**]⁺ was identical to that seen for **PdL¹** and **PdL²**. Overall, calculations clearly demonstrated that a change of the position of the carbon-metal bond had a strong influence on the HOMO-LUMO energy gaps of these cyclometalated palladium complexes.

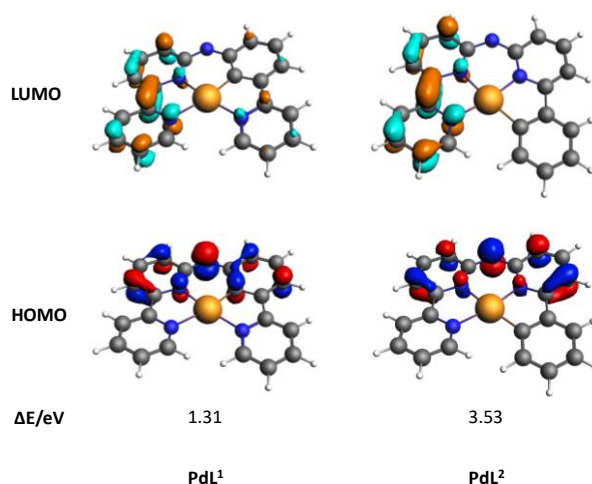


Figure 2.3 DFT calculation of HOMOs (bottom) and LUMOs (top) orbitals of **PdL¹** and **PdL²**; occupied orbitals (HOMO) have red and blue lobes, and unoccupied orbitals (LUMO) brown and cyan lobes. Element colour code: grey = C; orange = Pd; blue = N; white = H.

2.3 Conclusion

In summary, the new cyclopalladated complex **PdL¹** showed good absorbance in the blue region of the spectrum, low phosphorescence, and excellent singlet oxygen quantum yield (0.89), which altogether translated into high photoindex in human cancer cells. By contrast, its isomer **PdL²** had low absorption and low singlet oxygen quantum yield (0.38), resulting in negligible activation by blue light *in vitro*. DFT calculation showed that the higher absorption in the blue region of **PdL¹**, and thus its lower HOMO-LOMO energy gap, was due to the closer proximity between the electron-rich cyclometalated aromatic cycle and the nitrogen bridge of the ligand, while in **PdL²** both aromatic rings adjacent to the N bridge are electron-poor pyridine rings, which lowers the HOMO energy. To the best of our knowledge, this study is the first report that two isomers of organometallic prodrugs have distinct photobiological properties. These results demonstrate that changing the position of the carbon-metal bond in the coordination sphere of photoactive organometallic prodrugs can be used to tune the energy gap between their frontier orbitals, and hence their absorption in the visible region of the spectrum.

2.4 Experimental section

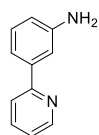
2.4.1 materials and methods

All syntheses were performed in a dinitrogen atmosphere. All the chemical compounds were purchased from Sigma-Aldrich. All reactants and solvents were used without further purification. All ¹H NMR, ¹³C attached-proton-test NMR (¹³C-APT NMR) were recorded on a Bruker DPX-300 or DMX-400 spectrometers. Chemical shifts are indicated in ppm relative to the residual solvent peak. Electrospray ionization mass spectra (ESI-MS) were recorded by using a MSQ Plus Spectrometer positive ionization mode. High-resolution mass spectra (HRMS) of two palladium complexes were recorded on Waters XEVO-G2 XSQ-TOF) mass spectrometer equipped with an electrospray ion source in positive mode (source voltage 3.0 kV, desolvation gas flow 900 L/hr, temperature 250 °C) with resolution R = 22000 (mass range m/z = 50-2000) and 200 pg/uL Leu-enkephalin (m/z = 556.2771) as a “lock mass”. Uv-vis spectra were recorded on a Cary 50 spectrometer from Varian. The singlet oxygen spectra and phosphorescence quantum yield were measured on a special custom-built setup which was described previously. The phosphorescence lifetime of complexes in methanol was measured by LifeSpec-II from Edinburgh Instruments, with excitation source of 375 nm pulsed diode lasers. The partition coefficient log P_{ow} was measured by ICP-OES using a Vista-MPX CCD Simultaneous ICP-OES. The DFT calculations were carried out using the Amsterdam Density

Functional software (ADF2017) from SCM, the PBE0 functional, a triple zeta basis set (TZP), and COSMO to simulate the solvents effects in methanol. Human cancer cell line A549 (human lung carcinoma) and A431 (human skin carcinoma) were purchased from Sigma Aldrich, distributed by the European Collection of Cell Cultures (ECACC). Dulbecco's Modified Eagle Medium (DMEM, with and without phenol red, without glutamine), Glutamine-S (GM; 200 mm), tris(hydroxymethyl)aminomethane (Tris base), trichloroacetic acid (TCA), glacial acetic acid, and sulfo-rhodamine B (SRB) were purchased from Sigma Aldrich. The measurements of complexes on photocytotoxicity were performed according to the literature.

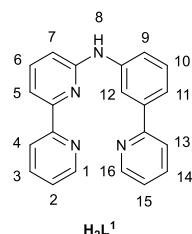
2.4.2 Synthesis

2-(3-Aminophenyl)pyridine.



This compound was synthesized according to a modified literature procedure.³ To a suspension of 2-bromopyridine (0.8 mL, 8.2 mmol), 3-aminophenylboronic acid (1.1 g, 7.7 mmol), anhydrous K₂CO₃ (2.1 g, 15.4 mmol) and Pd(PPh₃)₄ (431 g, 0.4 mmol) in 1,2-dimethoxyethane (19 mL) under N₂, ethanol (6 mL) and water (13 mL) were added. The mixture was refluxed under N₂ at 95 °C for 24 h. It was allowed to cool and filtered, then water (100 mL) and EtOAc (100 mL) were added. The phases were separated and the aqueous phase was extracted with EtOAc (100 mL) three times. The combined organic phases were dried over Na₂SO₄ and the solvent was rotary evaporated. The crude product obtained was purified by silica chromatography using pentane-EtOAc mixtures (2:1, R_f = 0.35) as eluent, to afford 1.0 g of the target compound (yield: 77%, 5.9 mmol). **ESI-MS** (cation): m/z calcd 171.1 (C₁₁H₁₀N₂ + H⁺), found 171.1. **¹H NMR** (300 MHz, CDCl₃): δ 8.69 (1 H, dt, *J* = 4.9, 1.4 Hz), 7.72 – 7.64 (2 H, m), 7.40 (1 H, t, *J* = 2.0 Hz), 7.36 (1 H, dt, *J* = 7.6, 1.4 Hz), 7.26 (1 H, s), 7.22 – 7.18 (1 H, m), 7.17 (0 H, d, *J* = 2.8 Hz), 6.73 (1 H, ddd, *J* = 7.9, 2.5, 1.1 Hz), 3.89 (2 H, s).

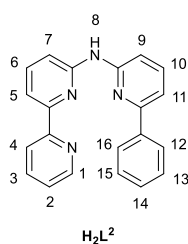
H₂L¹ (N-(3-(pyridin-2-yl)phenyl)-[2,2'-bipyridin]-6-amine).



A mixture of 6-bromo-2,2'-bipyridine (665 mg, 2.8 mmol), Pd(dba)₂ (30 mg, 0.5 mmol), racemic 2,2'-bis(diphenylphosphino)-1,1'-binaphthyl (BINAP, 61.4 mg, 0.098 mmol) and KO^t-Bu (997 mg, 8.9 mmol) was partially dissolved in dry toluene (53 mL) under N₂ atmosphere.⁴ The mixture was stirred for 10 min, then 2-(3-Aminophenyl)pyridine (484 mg, 2.8 mmol) was added, followed by heating the reaction mixture to 85 °C. After 3 days stirring, the brown mixture was cooled down. Demi water (75.0 mL) was added and the mixture was stirred for 1 h. The mixture was then filtered, but no solids were obtained. The H₂O layer was separated from the toluene

layer. Extracted the H₂O layer with EtOAc (100 mL) for three times and combined the toluene and EtOAc layers, followed by rotary evaporation of the solvents. The crude product obtained was purified by silica chromatography using pentane-EtOAc mixtures (2:1, R_f = 0.25) as eluent, to afford 67.1 mg of the target compound **H₂L¹** (yield: 73%, 0.21 mmol). **ESI-MS** (cation): m/z calcd 325.1 (C₂₁H₁₆N₄ + H⁺), found 325.4. **¹H NMR** (300 MHz, DMSO-*d*₆): 9.40 (1 H, s, H⁸), 9.03 (1 H, t, J = 2.0 Hz, H¹²), 8.75 (1 H, ddd, J = 4.8, 1.8, 1.0 Hz, H¹), 8.68 (1 H, ddd, J = 4.7, 1.9, 0.9 Hz, H¹⁶), 8.61 (1 H, dt, J = 8.0, 1.1 Hz, H⁴), 8.01 – 7.97 (1 H, m, H¹⁴), 7.96 (1 H, d, J = 1.4 Hz, H¹³), 7.91 (1 H, td, J = 7.6, 1.8 Hz, H³), 7.84 (1 H, dd, J = 7.5, 0.9 Hz, H⁵), 7.74 (1 H, t, J = 7.8 Hz, H⁶), 7.68 (1 H, ddd, J = 8.1, 2.3, 1.0 Hz, H⁹), 7.60 (1 H, dt, J = 7.9, 1.2 Hz, H¹¹), 7.48 – 7.44 (1 H, m, H¹⁰), 7.43 (1 H, d, J = 4.5 Hz, H⁵), 7.41 – 7.35 (1 H, m, H²), 6.93 (1 H, dd, J = 8.2, 0.9 Hz, H⁷). **¹³C-APT NMR** (75 MHz, DMSO-*d*₆), δ 156.9, 156.2, 155.8, 153.6, 150.0, 149.6, 142.6, 139.6, 138.7, 137.6, 129.5, 124.3, 123.1, 121.0, 120.6, 119.0, 118.9, 116.6, 112.2, 111.6.

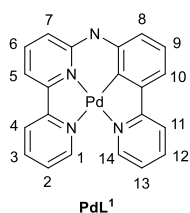
H₂L² (N-(6-phenylpyridin-2-yl)-[2,2'-bipyridin]-6-amine).



A mixture of 6-bromo-2,2'-bipyridine (665 mg, 2.8 mmol), Pd(dba)₂ (30 mg, 0.5 mmol), racemic BINAP (61 mg, 0.1 mmol) and KO^{*t*}-Bu (997 mg, 8.9 mmol) was partially dissolved in 53 mL dry toluene under N₂ atmosphere.⁴ The mixture was stirred for 10 min, then 2-Amino-6-phenylpyridine (484 mg, 2.8 mmol) was added, followed by heating the reaction mixture to 85 °C. After

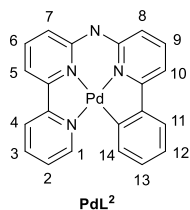
3 days of stirring, the brown mixture was cooled down with an ice bath. Demi water (75.0 mL) was added and the mixture was stirred for 1 h. The mixture was filtered, but no solids were obtained. The H₂O layer was separated from the toluene layer. Extracted the H₂O layer with EtOAc (100 mL) three times and combined the toluene and EtOAc layers, followed by the evaporation of solvents. The residues were dissolved in EtOAc and recrystallized at -20 °C, to get 596 mg of the target compound **H₂L²** (yield: 65%, 1.8 mmol). **ESI-MS** (cation): m/z calcd 325.1 (C₂₁H₁₆N₄ + H⁺), found 325.5. **¹H NMR** (400 MHz, DMSO-*d*₆) 9.86 (1 H, s, H⁸), 8.69 (1 H, ddd, J = 4.7, 1.8, 0.9 Hz, H¹), 8.38 (1 H, dt, J = 7.9, 1.1 Hz, H⁴), 8.13 – 8.07 (2 H, m, H¹³, H¹⁴), 7.99 (1 H, td, J = 7.7, 1.8 Hz, H³), 7.95 – 7.79 (5 H, m, H¹⁰, H⁹, H⁷, H¹⁶, H⁵), 7.54 – 7.41 (5 H, m, H², H⁶, H¹¹, H¹², H¹⁵). δ **¹³C-APT NMR** (101 MHz, DMSO-*d*₆) δ 155.6, 154.4, 154.09, 154.0, 153.4, 149.3, 139.0, 138.8, 138.7, 137.3, 129.0, 128.8, 126.6, 124.1, 120.4, 112.8, 112.5, 112.4, 110.7.

PdL¹



A mixture of **H₂L¹** (36 mg, 0.1 mmol) and Pd(OAc)₂ (25 mg, 0.1 mmol) in a glacial acetic acid was refluxed for 12 h at 135 °C under N₂ atmosphere to give a yellowish green solution. Then the solvent was rotary evaporated. The resulted yellow solid was washed with EtOAc, ether and dried in vacuum to get 43 mg of pure **PdL¹** complex (yield: 92%, 0.1 mmol). **HRMS** (cation): *m/z* calcd 429.0326 (C₂₁H₁₄N₄Pd + H⁺), found 429.0339. **¹H NMR** (400 MHz, Methanol-*d*₄) δ 8.34 (1 H, d, *J* = 5.4 Hz, H¹), 8.20 (1 H, d, *J* = 8.1 Hz, H⁴), 8.14 (1 H, d, *J* = 5.6 Hz, H¹⁴), 8.12 – 8.05 (1 H, m, H³), 7.93 (1 H, td, *J* = 7.9, 1.4 Hz, H¹²), 7.72 (2 H, dd, *J* = 8.1, 6.1 Hz, H⁶, H¹¹), 7.58 (2 H, d, *J* = 7.3 Hz, H², H⁵), 7.26 (1 H, t, *J* = 6.5 Hz, H¹³), 7.15 (1 H, d, *J* = 7.4 Hz, H¹⁰), 7.08 (1 H, t, *J* = 7.6 Hz, H⁹), 7.02 (1 H, d, *J* = 8.5 Hz, H⁷), 6.73 (1 H, d, *J* = 7.7 Hz, H⁸). **¹³C NMR** (101 MHz, Methanol-*d*₄) δ 165.9 (**Pd-C**), 155.6, 153.3, 149.7, 148.7, 147.6, 146.4, 141.1, 140.7, 138.7, 137.1, 134.6, 127.8, 127.3, 124.5, 124.0, 121.2, 119.9, 118.4, 117.6, 115.2. **Elemental analysis** calcd for **PdL¹** + 2H₂O + CH₃COOH: C, 52.63; H, 4.23; N, 10.67; Found for **PdL¹** + 2H₂O + CH₃COOH: C, 52.21; H, 4.42; N, 10.43.

PdL²



The synthesis of complex **PdL²** was similar to that of **PdL¹**, except that ligand **H₂L²** was used. A mixture of **H₂L²** (32 mg, 0.1 mmol) and Pd(OAc)₂ (22 mg, 0.1 mmol) in a glacial acetic acid was refluxed for 12 h at 135 °C under N₂ atmosphere to give a yellowish green solution. Then the solvent was rotary evaporated. The resulted yellow solid was washed with EtOAc, ether and dry in vacuum to get 41 mg of pure **PdL²** complex (yield: 95%, 0.1 mmol). The red rectangular single crystal of **PdL²** was obtained by slow evaporation of ether into a saturated methanol solution of **PdL²**. **HRMS** (cation): *m/z* calcd 429.0326 (C₂₁H₁₄N₄Pd + H⁺), found 429.0337. **¹H NMR** (400 MHz, Methanol-*d*₄) δ 8.05 (1 H, d, *J* = 5.6 Hz, H¹), 7.80 – 7.65 (2 H, m, H³, H⁴), 7.53 (1 H, t, *J* = 7.9 Hz, H⁶, H⁹), 7.45 (1 H, t, *J* = 7.8 Hz, H⁵), 7.25 (1 H, d, *J* = 7.5 Hz, H²), 7.17 (1 H, t, *J* = 6.3 Hz, H¹¹), 6.99 (1 H, d, *J* = 7.6 Hz, H¹⁰), 6.87 (1 H, d, *J* = 7.6 Hz, H⁷), 6.80 (2 H, t, *J* = 7.2 Hz, H¹²), 6.74 – 6.65 (1 H, m, H¹³), 6.55 (1 H, d, *J* = 8.2 Hz, H⁸), 6.49 (1 H, d, *J* = 7.6 Hz, H¹⁴). **¹³C NMR** (101 MHz, Methanol-*d*₄) δ 162.27 (**Pd-C**), 156.0, 154.3, 149.4, 148.8, 146.7, 145.7, 145.6, 139.1, 138.8, 138.8, 129.9, 128.4, 125.8, 124.8, 123.4, 122.8, 116.4, 114.9, 112.7, 111.2. **Elemental analysis** calcd for **PdL²** + H₂O + MeOH: C, 55.18; H, 4.21; N, 11.70; Found for **PdL²** + H₂O + MeOH: C 55.13; H 4.22; N 11.15.

2.4.3 Single-crystal X-ray crystallography

All reflection intensities were measured at 110(2) K using a SuperNova diffractometer (equipped with Atlas detector) with Mo $K\alpha$ radiation ($\lambda = 0.71073 \text{ \AA}$) under the program CrysAlisPro (Version CrysAlisPro 1.171.39.29c, Rigaku OD, 2017). The same program was used to refine the cell dimensions and for data reduction. The structure was solved with the program SHELXS-2014/7 (Sheldrick, 2015) and was refined on F^2 with SHELXL-2014/7. Numerical absorption correction based on gaussian integration over a multifaceted crystal model was applied using CrysAlisPro. The temperature of the data collection was controlled using the system Cryojet (manufactured by Oxford Instruments). The H atoms were placed at calculated positions using the instructions AFIX 43 with isotropic displacement parameters having values 1.2 U_{eq} of the attached C atoms. The structure is disordered. The whole Pd complex is disordered over two orientations as both orientations may have the same space filling requirement. The occupancy factor of the major component of the disorder refines to 0.835(3).

2.4.4 Partition coefficients ($\log P_{ow}$) of palladium complexes

The partition coefficients of palladium complexes were determined by the shake-flask method. Briefly, each palladium complex was dissolved (0.8 mM) in octanol-saturated water and ultrasonicated for 1 h. After filtering with 0.2 μM membrane filters, aliquots of the stock solutions (0.2 mL) were transferred to 15 mL centrifuge tubes and diluted up to 6.0 mL. Then 6.0 mL of water-saturated octanol was added to one of the tubes and the mixture was shaken in a IKA Vibrax shaker for 24 h at 2200 rpm. The mixture was then centrifuged for 20 min at 4300 rpm to separate the water phase. For each of the samples, a 5.5 mL aliquot of the aqueous layer was taken using a syringe and 65% HNO_3 (vol) was added to it to give diluted samples with 5% HNO_3 final concentration. The palladium concentrations $[\text{Pd}]_{aq}$ (in ppm) of the samples were determined by ICP-OES using a Vista-MPX CCD Simultaneous ICP-OES. Partition coefficients $\log P_{ow}$ was calculated using the equation below:

$$\log P_{ow} = \log ([\text{Pd}]_{oct}/[\text{Pd}]_{aq}) = \log ([\text{Pd}]_{total} - [\text{Pd}]_{aq}) / [\text{Pd}]_{aq}$$

where $[\text{Pd}]_{total}$ is the concentration of palladium in the sample that was not extracted with octanol, and $[\text{Pd}]_{aq}$ is the concentration of palladium in the aqueous layer after octanol addition, as a mean of three replicates.

2.4.5 Cell culturing

Cells were thawed and at least passaged twice before starting photocytotoxicity experiments. Cells were cultured in DEMEM complete medium (Dulbecco's Modified Eagle Medium

(DMEM) with phenol red, supplemented with 8.0% v/v fetal calf serum (FCS), 0.2% v/v penicillin/streptomycin (P/S), and 0.9% v/v Glutamine), under humidified normoxic conditions, 37 °C atmosphere, 21% O₂ and 7.0% CO₂ in 75 cm² flasks. They were sub-cultured upon reaching 70-80% confluence, approximately once per week. Cells were passaged never more than 8 weeks.

2.4.6 Cytotoxicity assay

The cell irradiation system consists of a Ditabis thermostat (980923001) fitted with two flat-bottom microplate thermoblocks (800010600) and a 96-LED array fitted to a standard 96-well plate. The 455 nm LED (FNL-U501B22WCSL), fans (40 mm, 24 V DC, 9714839), and power supply (EA-PS 2042-06B) were ordered from Farnell. Full description of the cell irradiation setup is given in Hopkins et al.² The cytotoxicity of **PdL**¹ and **PdL**² were assayed in normoxic conditions (21 % O₂) against two human cancer cell lines (A549 and A431) according to a published protocol. Briefly, 24 h after seeding, the cells were treated with **PdL**¹ and **PdL**² with a range of 6 different concentrations (0, 0.625, 3.125, 6.25, 12.5, 31.25, 62.5 μM, maximum 0.5% DMSO was used in each well). After 24 h incubation, one plate was irradiated with blue light (455 nm, 5 min, 10.5 mW cm⁻², 3.2 J cm⁻²) while the other was left in the dark. Cell viability was then assayed 96 h after seeding using standard sulforhodamine B (SRB) assay. Half maximal effective concentrations (EC₅₀) for cell growth inhibition were calculated by fitting the curves using a non-linear regression function for the dose-response curves of treated vs. non-treated wells via Graphpad prism 5.

$$100/(1 + 10^{\log_{10}EC_{50}-X) \times Hill\ Slope})$$

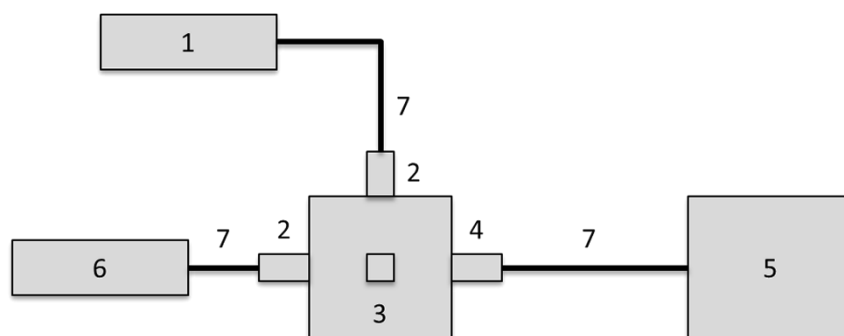
2.4.7 Singlet oxygen generation and phosphorescence quantum yield

The quantum yields of singlet oxygen generation and phosphorescence were determined in a custom-built setup shown in Scheme S2. All optical parts were connected with optical fibers from Avantes, with a diameter of 200–600 μm. The sample, consisting of the compound in deuterated methanol (500 μL), was added to a 104F-OS semi-micro fluorescence cuvette from Hellma Analytics, and placed in a CUV-UV/VIS-TC temperature-controlled cuvette holder (Avantes). The sample was allowed to equilibrate at 298 K for 5 minutes. Emission spectroscopy was performed with a 450 nm fiber-coupled laser (LRD-0450, Laserglow), which was set to 50 mW at the cuvette (4 mm beam diameter; 0.4 W·cm⁻²) at a 90° angle with respect to the spectrometer. The excitation power was measured using a S310C thermal sensor connected to a PM100USB power meter (Thorlabs). The emission spectra were recorded using

two separate spectrometers for the UV-Vis and NIR emission, *i.e.* from 300 nm to 1000 nm for the phosphorescence of the complex (Avantes 2048L StarLine spectrometer) and from 1000 nm to 1700 nm for the phosphorescence of singlet oxygen ($^1\Delta_g$) around 1275 nm (Avantes NIR256-1.7TEC spectrometer, detector set to $-12\text{ }^\circ\text{C}$). The infrared emission spectrum was acquired within 9 seconds, after which the laser was turned off directly. Similarly, the visible emission spectrum was acquired within 2 seconds. UV-Vis absorption spectra before and after emission spectroscopy were measured using an Avalight-DHc halogen-deuterium lamp (Avantes) as light source (turned off during emission spectroscopy) and the before mentioned UV-Vis spectrometer as detector, both connected to the cuvette holder at a 180° angle. All spectra were recorded using Avasoft 8.5 software from Avantes and further processed using Microsoft Office Excel 2010 and Origin Pro 9.1 software. The quantum yields of phosphorescence and singlet oxygen production were calculated using the relative method with $[\text{Ru}(\text{bpy})_3]\text{Cl}_2$ as the standard ($\Phi_\Delta = 0.73$, $\Phi_P = 0.015$ in MeOD), according to Equation below:

$$\Phi_{\text{sam}} = \Phi_{\text{std}} \times \frac{A_{\text{std}}^{450}}{A_{\text{sam}}^{450}} \times \frac{E_{\text{sam}}}{E_{\text{std}}}$$

where Φ is the quantum yield, A^{450} is the absorbance at 450 nm (always kept below 0.1 for a 4 mm path length), E is the integrated emission peak of singlet oxygen at 1270 nm or the integrated phosphorescence emission peak between 520 and 950 nm, and *sam* and *std* denote the sample and standard, respectively.



Scheme 2.2 Setup used for Φ_Δ and Φ_P determination. (1) 450-nm CW laser light source, (2) collimating lens, (3) temperature-controlled cuvette holder, (4) double collimator, (5) UV-Vis (300-1000 nm) or NIR (1000-1700 nm) CCD spectrometer, (6) UV-Vis halogen-deuterium light source, and (7) optical fibers.

2.5 Acknowledgement

X. Zhou gratefully acknowledges the China Scholarship Council (CSC) for a personal grant (No. 201606200045). This work is supported by an ERC Starting Grant to S. Bonnet.

2.6 References

1. T. C. Johnstone, K. Suntharalingam and S. J. Lippard, *Chem. Rev.*, 2016, **116**, 3436-3486.
2. L. Kelland, *Nat. Rev. Cancer*, 2007, **7**, 573-584.
3. D. Wang and S. J. Lippard, *Nat. Rev. Drug Discovery*, 2005, **4**, 307-320.
4. L. Ma, N. Wang, R. Ma, C. Li, Z. Xu, M. K. Tse and G. Zhu, *Angew. Chem. Int. Ed.*, 2018, **57**, 1-6.
5. S. Medici, M. Peana, V. M. Nurchi, J. I. Lachowicz, G. Crisponi and M. A. Zoroddu, *Coord. Chem. Rev.*, 2015, **284**, 329-350.
6. N. Cutillas, G. S. Yellol, C. de Haro, C. Vicente, V. Rodriguez and J. Ruiz, *Coord. Chem. Rev.*, 2013, **257**, 2784-2797.
7. L. Zeng, P. Gupta, Y. Chen, E. Wang, L. Ji, H. Chao and Z. S. Chen, *Chem. Soc. Rev.*, 2017, **46**, 5771-5804.
8. F. E. Poynton, S. A. Bright, S. Blasco, D. C. Williams, J. M. Kelly and T. Gunnlaugsson, *Chem. Soc. Rev.*, 2017, **46**, 7706-7756.
9. H. Huang, P. Zhang, H. Chen, L. Ji and H. Chao, *Chem. Eur. J.*, 2015, **21**, 715-725.
10. T. T. Fong, C. N. Lok, C. Y. Chung, Y. M. Fung, P. K. Chow, P. K. Wan and C. M. Che, *Angew. Chem. Int. Ed.*, 2016, **55**, 11935-11939.
11. M. Fanelli, M. Formica, V. Fusi, L. Giorgi, M. Micheloni and P. Paoli, *Coord. Chem. Rev.*, 2016, **310**, 41-79.
12. A.-R. Azzouzi, S. Vincendeau, E. Barret, A. Cicco, F. Kleinclauss, H. G. van der Poel, C. G. Stief, J. Rassweiler, G. Salomon, E. Solsona, A. Alcaraz, T. T. Tammela, D. J. Rosario, F. Gomez-Veiga, G. Ahlgren, F. Benzaghrou, B. Gaillac, B. Amzal, F. M. J. Debruyne, G. Fromont, C. Gratzke and M. Emberton, *Lancet Oncol.*, 2017, **18**, 181-191.
13. H. Cao, L. Wang, Y. Yang, J. Li, Y. Qi, Y. Li, Y. Li, H. Wang and J. Li, *Angew. Chem. Int. Ed.*, 2018, **57**, 7759-7763.
14. Y. Ma, X. Li, A. Li, P. Yang, C. Zhang and B. Tang, *Angew. Chem. Int. Ed.*, 2017, **56**, 13752-13756.
15. S. H. Askes, A. Bahreman and S. Bonnet, *Angew. Chem. Int. Ed.*, 2014, **53**, 1029-1033.
16. S. L. Higgins and K. J. Brewer, *Angew. Chem. Int. Ed.*, 2012, **51**, 11420-11422.
17. H. Bi, Y. Dai, P. Yang, J. Xu, D. Yang, S. Gai, F. He, B. Liu, C. Zhong, G. An and J. Lin, *Small*, 2018, **14**, e1703809.
18. H. Bi, Y. Dai, P. Yang, J. Xu, D. Yang, S. Gai, F. He, G. An, C. Zhong and J. Lin, *Chem. Eng. J. (Lausanne)*, 2019, **356**, 543-553.
19. J. D. Knoll and C. Turro, *Coord. Chem. Rev.*, 2015, **282-283**, 110-126.
20. F. Heinemann, J. Karges and G. Gasser, *Acc. Chem. Res.*, 2017, **50**, 2727-2736.
21. J.-Y. Lee, J.-Y. Lee, Y.-Y. Chang, C.-H. Hu, N. M. Wang and H. M. Lee, *Organometallics*, 2015, **34**, 4359-4368.
22. S. M. Ray, R.; Singh, J. K.; Samantaray, M. K.; Shaikh, M. M; Panda, D.; Ghosh, P, *J. Am. Chem. Soc.*, 2007, 15042-15053.
23. S. G. Churusova, D. V. Aleksanyan, E. Y. Rybalkina, O. Y. Susova, V. V. Brunova, R. R. Aysin, Y. V. Nelyubina, A. S. Peregudov, E. I. Gutsul, Z. S. Klemenkova and V. A. Kozlov, *Inorg. Chem.*, 2017, **56**, 9834-9850.
24. W. Liu and R. Gust, *Chem. Soc. Rev.*, 2013, **42**, 755-773.
25. J. Ruiz, V. Rodriguez, C. de Haro, A. Espinosa, J. Perez and C. Janiak, *Dalton Trans.*, 2010, **39**, 3290-3301.
26. G. Gasser, I. Ott and N. Metzler-Nolte, *J. Med. Chem.*, 2011, **54**, 3-25.
27. S. Bonnet, *Comments Inorg. Chem.*, 2014, **35**, 179-213.
28. Z. Fan, J. Ni and A. Zhang, *J. Am. Chem. Soc.*, 2016, **138**, 8470-8475.
29. V. H. S. van Rixel, B. Siewert, S. L. Hopkins, S. H. C. Askes, A. Busemann, M. A. Siegler and S. Bonnet, *Chem. Sci.*, 2016, **7**, 4922-4929.
30. E. M. Hernández, S. Zheng, H. J. Shepherd, D. S. Yufit, K. Ridier, S. Bedoui, W. Nicolazzi, V. Velázquez, S. Bonnet, G. Molnár and A. Bousseksou, *J. Phys. Chem. C*, 2016, **120**, 27608-27617.
31. L. Yang, D. R. Powell and R. P. Houser, *Dalton Trans.*, 2007, **0**, 955-964.
32. S. Zheng, N. R. Reintjens, M. A. Siegler, O. Roubeau, E. Bouwman, A. Rudavskyi, R. W. Havenith and S. Bonnet, *Chem. Eur. J.*, 2016, **22**, 331-339.

33. S. L. Hopkins, B. Siewert, S. H. Askes, P. Veldhuizen, R. Zwier, M. Heger and S. Bonnet, *Photochem. Photobiol. Sci.*, 2016, **15**, 644-653.
34. M. C. DeRosa and R. J. Crutchley, *Coord. Chem. Rev.*, 2002, **233-234**, 351-371.
35. X. Li, J. Zhang, Z. Zhao, L. Wang, H. Yang, Q. Chang, N. Jiang, Z. Liu, Z. Bian, W. Liu, Z. Lu and C. Huang, *Adv. Mater.*, 2018, **30**, e1705005.
36. F. F. Hung, S. X. Wu, W. P. To, W. L. Kwong, X. Guan, W. Lu, K. H. Low and C. M. Che, *Chem. Asian J.*, 2017, **12**, 145-158.
37. J. Fernandez-Cestau, B. t. Bertrand, A. Pintus and M. Bochmann, *Organometallics*, 2017, **36**, 3304-3312.

3

The self-assembly of a cyclometalated palladium photosensitizer into proteins-stabilized nanorods triggered drug uptake in vitro and in vivo

Enhanced passive diffusion is usually considered as the primary cause for the enhanced cellular uptake of cyclometalated drugs, because cyclometalation lowers the charge of a metal complex and increases its lipophilicity. However, in this work, the monocationic cyclometalated palladium complexes [1]OAc ($N^+N^+C^-N$) and [2]OAc ($N^+N^+N^+C^-$) were found to self-assemble, in aqueous solutions, into soluble supramolecular nanorods, while their tetrapyrrolyl dicationic analogue [3](OAc)₂ ($N^+N^+N^+N^+$) dissolved as isolated molecules. These nanorods formed via metallophilic Pd...Pd interaction and π - π stacking, and were stabilized in cell medium by serum proteins, in absence of which the nanorods precipitated. In cell cultures these protein-stabilized self-assembled nanorods were responsible for the improved cellular uptake of the cyclometalated compounds, which took place via endocytosis, i.e. an active uptake pathway. In addition to triggering self-assembly, cyclometalation in [1]OAc also led to dramatically enhanced photodynamic properties under blue light irradiation. These combined penetrations and photodynamic properties were observed in multicellular tumor spheroids and a mice tumor xenograft, demonstrating that protein-stabilized nanoaggregation of cyclometalated drugs such as [1]OAc allows efficient cellular uptake also in 3D tumor models. Overall, serum proteins appear as a major element of drug design, as they strongly influence the size and bioavailability of supramolecular drug aggregates, and hence their efficacy in vitro and in vivo.

This chapter has been accepted for publication as a full paper and front cover: X.-Q. Zhou, M. Xiao, V. Ramu, J. Hilgendorf, X. Li, P. Papadopoulou, M. A. Siegler, A. Kros, W. Sun* and S. Bonnet*, *J. Am. Chem. Soc.*, 2020, **142**, 23, 10383-10399.

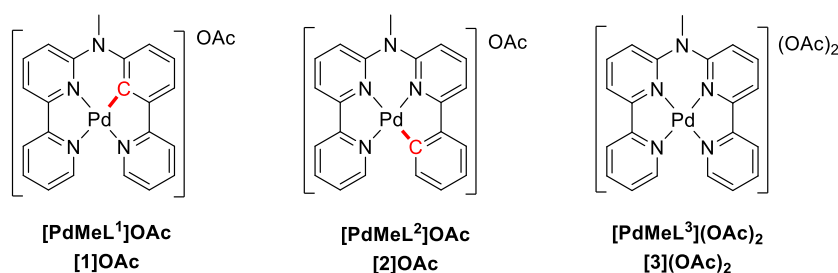
3.1 Introduction

Research on metal-based anticancer drugs has been encouraged for many years by the clinical success of cisplatin, carboplatin, oxaliplatin, and nedaplatin, four metal-based drugs used in the treatment of cancer.¹⁻³ However, the similar mode of action of these platinum-based compounds, where aquation of some of the leaving groups by intracellular water leads to nonselective covalent binding of platinum to DNA, results in significant side effects and drug resistance.³⁻¹⁰ Several strategies have been developed to overcome these drawbacks, in particular photodynamic therapy (PDT). PDT is a fast-developing cancer treatment modality because it shows reduced systemic cytotoxicity to cancer patients.¹¹⁻¹³ In PDT, a photosensitizing agent (PS) is injected, and upon light at the tumor site, cytotoxic reactive oxygen species (ROS) are generated via a so-called type I (electron transfer) mechanism, or via a type II (energy transfer) pathway.¹⁴⁻¹⁹ These two competing pathways may also occur simultaneously, and the ratio between these processes depends on many parameters such as the type of PS used, the concentrations of substrate, and dioxygen (O₂), the localization of the photosensitizer.^{14, 16} In the design of new PSs, metal complexes derived from heterocyclic ligands, especially polypyridyl ligands, have attracted a great amount of attention due to their tunable photophysical properties and their visible light absorption, which greatly improve the light penetration of biological tissues compared to that of UV-light-sensitive molecules.^{13, 20-24} Short-wavelength (blue or green) PDT agents, although traditionally considered to be academic curiosities due to the low tissue penetration of this type of visible light, are regaining interest for certain cancers of thin organs, such as skin and bladder, because the thickness of the tumors in such cancers matches the penetration depth of blue light and green light well.²⁵

More particularly, cyclometalated metal complexes, in which a metal-nitrogen bond is replaced by a metal-phenylene bond, have been considered to be a way to improve the efficiency of metal-based PDT sensitizers. Cyclometalated complexes are indeed known for the significant red-shift of their absorption maxima compared to that of polypyridyl analogues, enhanced stability in solution, and improved cellular uptake.²⁶ The latter is usually claimed to be due to their decreased charge and increased lipophilicity compared to those of polypyridyl analogues.^{20, 26} However, little is known for the fate of cyclometalated metal complexes in cell medium, which is a complex mixture of many small biological molecules and proteins.²⁷ These biomolecules might interact with cyclometalated complexes to generate either new molecular species or supramolecular aggregates, resulting in modified cellular uptake and biological properties.^{28, 29} Recently, Thomas's group reported a series of cyclometalated [Ir^{III}Ru^{II}]³⁺

luminescent DNA imaging probes that were prevented to penetrate the nuclei of cancer cells by reaction with the serum albumin present in cell growing medium, while their polypyridyl analogue $[\text{Ir}^{\text{III}}\text{Ru}^{\text{II}}]^{4+}$ retained nuclear staining properties in serum-containing medium.³⁰ Che's group also reported a self-assembled platinum/gold system for controlled drug release and accumulation in tumors.³¹ Coincidentally, many cyclometalated complexes in the literature have been shown to produce fluorescent dots in the cytoplasm and not to reach the nucleus,³¹⁻³³ an organelle that selectively sorts out particles of small sizes.³⁴

Palladium(II) complexes have been proposed as possible analogues of antitumor platinum complexes for their similar d^8 coordination sphere and tetradentate square-planar structure. Recently, two palladium-based PDT sensitizers, Padoporfin and its derivative Padeliporfin, have been clinically approved to treat prostate cancer, which demonstrates the potential of palladium complexes for PDT.^{15, 35} Encouraged by these developments, our group recently studied the influence of the position of the Pd-C bond in cyclometalated palladium complexes based on tetrapyridyl ligand Hbbpya (N,N-bis(2,2'-bipyrid-6-yl)amine), with respect to their photodynamic properties.³⁶ The isomer characterized by a Pd-C bond on the side of the noncoordinated NH bridge of this ligand shows better blue-light absorption and a better singlet oxygen generation ability, compared to the isomer where the Pd-C bond lies further from the NH bridge. However, in these complexes the deprotonation of the noncoordinated NH bridge becomes easy upon palladation of the ligand, resulting in insoluble neutral metal complexes, thus limiting their application for cancer treatment *in vivo*. In this work, we methylated this NH bridge and synthesized three analogous palladium complexes: cyclometalated isomers **[1]OAc** ($\text{N}^{\wedge}\text{N}^{\wedge}\text{C}^{\wedge}\text{N}$ coordination) and **[2]OAc** ($\text{N}^{\wedge}\text{N}^{\wedge}\text{N}^{\wedge}\text{C}$ coordination), and the reference tetrapyridyl complex **[3](OAc)₂** ($\text{N}^{\wedge}\text{N}^{\wedge}\text{N}^{\wedge}\text{N}$ coordination, Scheme 3.1). All palladium complexes, prepared with acetate counterion, were water-soluble. With this new series of complexes at hand, it was possible to address the influences of cyclometalation and isomerism on the aggregation and fate of these metal complexes *in vitro* and *in vivo* and to study how proteins present in serum influenced their speciation and uptake.



Scheme 3.1 Structures of the metal complexes.

3.2 Results

3.2.1. Synthesis and characterization. The three titled palladium complexes $[1]^+$ - $[3]^{2+}$ were synthesized as acetate salts by reacting methylated ligands **MeL**¹, **MeL**², and **MeL**³ with palladium acetate (Scheme AII.1). All complexes were obtained in high yield without chromatography and were characterized by NMR, HRMS, elemental analysis, and single-crystal X-ray diffraction (APPENDIX II). The acetate counteranion provided good water solubility and similar log P_{ow} values of -1.88, -1.92, and -1.71, respectively. These values suggested similar cellular uptake efficacy if the three molecules would remain as monomers in aqueous solutions. It is noteworthy that the ¹H NMR spectra of cyclometalated complexes $[1]^+$ and $[2]^+$ showed significant differences at low and high concentrations, while $[3]^{2+}$ did not show this effect (Figure AII.1). Thus, NMR suggested that cyclometalation may promote aggregation in this type of complex.^{37, 38}

Single crystals of $[1]PF_6$, $[2]PF_6$, and $[3](BF_4)_2$, were obtained by the slow evaporation of a MeCN/EtOAc solution or by vapor diffusion from diethyl ether to a MeCN/EtOAc solution. The crystals were analyzed by single-crystal X-ray diffraction. Crystallographic data and a selection of interatomic distances and angles are shown in Table AII.1 and Table 3.1, respectively. All three complexes crystallized in the triclinic *P*-1 space group. As shown in Figure 3.1a, $[1]PF_6$ and $[2]PF_6$ were coordination isomers, with three nitrogen atoms and one carbon atom coordinated to the palladium(II) cation and bond lengths in the range 1.9786(18)-2.1086(17) Å. Four nitrogen atoms are coordinated to palladium in reference complex $[3](BF_4)_2$. The coordination sphere of these three complexes was slightly distorted, as shown by the small dihedral angle in complexes $[1]PF_6$ (N1-N2-C17-N4 = 3.96°), $[2]PF_6$ (N1-N2-N4-C22=2.91°), and $[3](BF_4)_2$ (N1-N2-N4-N5=5.42°). τ_4 , a structural parameter used to distinguish square-planar from tetrahedral coordination complexes ($\tau_4=360^\circ-(\alpha+\beta)/(141^\circ)$, where α and β are the two greatest valence angles of the coordination sphere),³⁹ was 0.112 for $[1]PF_6$, 0.109 for $[2]PF_6$, and 0.097 for $[3](BF_4)_2$, suggesting that these complexes are essentially square planar. The two cyclometalated, monocationic palladium complexes, also showed clear π - π^* stacking and short Pd-Pd distances (3.275 Å-4.316 Å), suggesting the occurrence of Pd...Pd metallophilic interaction.⁴⁰ In contrast, the reference complex $[3](BF_4)_2$ had higher Pd...Pd distances (6.814 Å-8.373 Å) that were almost twice as long, indicating the absence of Pd...Pd interaction in this dicationic compound (Figure 3.1b). Interestingly, these metal-metal interactions stimulate the cyclometalated complexes $[1]PF_6$, $[2]PF_6$ to self-assemble.⁴¹⁻⁴³

Overall, X-ray crystallography was consistent with NMR results and suggested that Pd...Pd metallophilic interaction may occur both in solution and in the solid state.

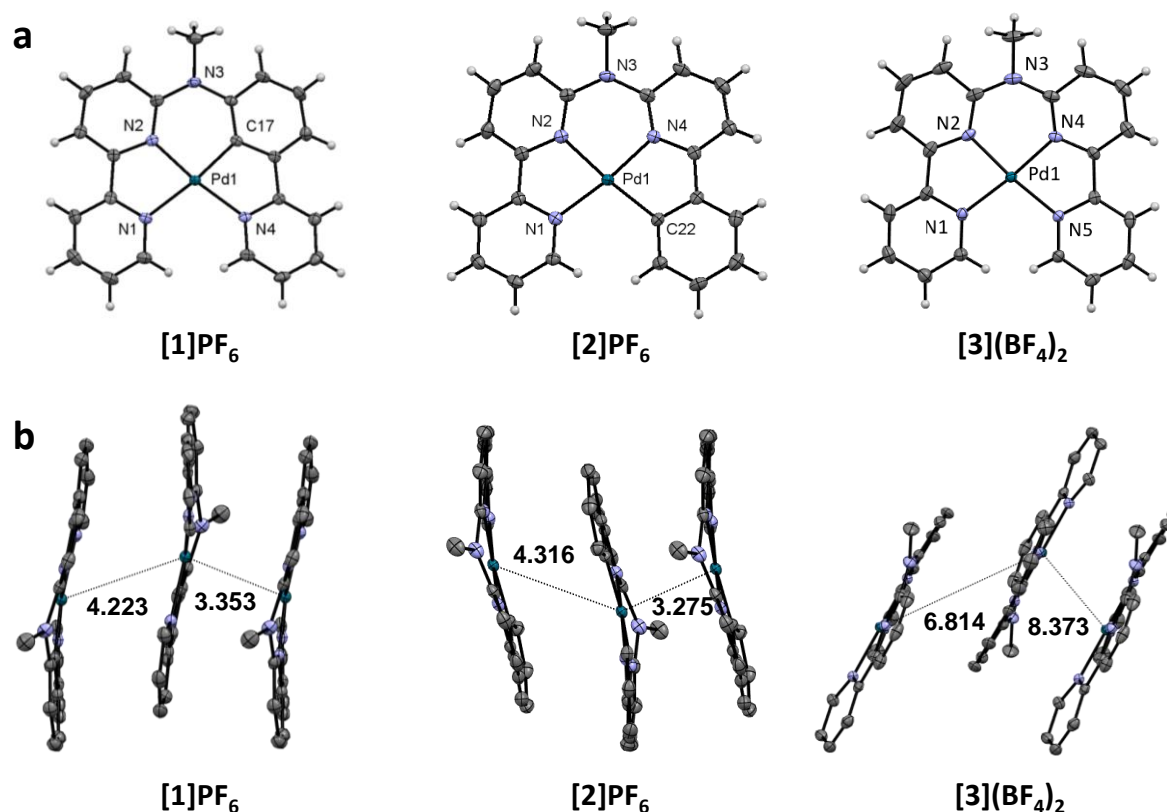


Figure 3.1 Molecular view of the cationic complexes (a) and their stacking (b) in the crystal structures of [1]PF₆, [2]PF₆, and [3](BF₄)₂. Displacement ellipsoids are shown at the 50% probability level. Pd...Pd distances are indicated in angstroms. Counterions and disorder have been omitted for clarity.

Table 3.1 Selected bond distance (angstroms) and angles (degrees) of [1]PF₆, [2]PF₆ and [3](BF₄)₂.

[1]PF ₆		[2]PF ₆		[3](BF ₄) ₂	
Pd-N1	2.1086(17)	Pd-N1	2.0544(18)	Pd-N1	2.048(2)
Pd-N2	1.9860(19)	Pd-N2	2.0435(18)	Pd-N2	1.979(2)
Pd-C17	1.9786(18)	Pd-N4	2.0096(18)	Pd-N4	1.983(2)
Pd-N4	2.0912(18)	Pd-C22	2.019(2)	Pd-N5	2.034(2)
Pd-Pd	4.223, 3.353	Pd-Pd	4.316, 3.275	Pd-Pd	6.814, 8.373
N1-Pd-N2	81.00(7)	N1-Pd-N2	80.88(7)	N1-Pd-N2	81.75(9)
N2-Pd-C17	92.19(8)	N2-Pd-N4	92.04(7)	N2-Pd-N4	92.97(9)
C17-Pd-N4	80.94(7)	N4-Pd-C22	82.33(8)	N4-Pd-N5	81.67(9)
N4-Pd-N1	105.77(7)	C22-Pd-N1	104.52(8)	N5-Pd-N1	103.64(9)

3.2.2. Photophysical characterization and frontier orbitals. The photophysical properties of **[1]OAc-[3](OAc)₂** in water are shown in Figure 3.2 and Table 3.2. Importantly (see below), under such conditions none of the molecules aggregate. Both complexes **[2]⁺** and **[3]²⁺** showed intense absorbance essentially in the ultraviolet range (300-400 nm), but a bathochromically-shifted absorption band was observed for **[1]⁺**, characterized by an absorption maximum at 428 nm. As a result, in pure water the molar absorptivity values at 455 nm for the three complexes were 1500, 37 and 56 M⁻¹ cm⁻¹, respectively, indicating that while **[2]⁺** or **[3]²⁺** are bad blue light PDT sensitizers, **[1]⁺** may be good at it. The difference in blue light absorption can be explained by the different HOMO-LUMO orbital energy gaps of the three compounds. According to DFT at the PBE0/TZP/COSMO level (Figure AII.2, Table AII.2) the HOMO and LUMO orbitals of all three complexes have π symmetry and have a very low (5.55% for **[1]⁺**) to zero (for **[2]⁺** and **[3]²⁺**) contribution of the palladium centers. The HOMO is centered on the noncoordinated amine bridge NMe of the ligand, and in the two cyclometalated complexes, its energy is strongly affected by how close the electron-rich Pd-C⁻ bond is to NMe (E_{HOMO} = -6.24 eV for **[1]⁺**, -6.58 eV for **[2]⁺**). On the other hand, the LUMO is based on the bipyridine fragment of the ligand and its energy is hence essentially independent of the position of the electron-rich Pd-C⁻ bond (E_{LUMO} = -2.41 eV for **[1]⁺**, -2.46 eV for **[2]⁺**). For **[3]²⁺**, the HOMO was slightly stabilized compared to that of **[2]⁺** due to the more electron-poor nature of the tetrapyrrolyl ligand, compared to its cyclometalated version (Table AII.2). The resulting HOMO-LUMO energy gaps of the three complexes follow the series **[1]⁺** (3.83 eV) << **[2]⁺** (4.11 eV) < **[3]²⁺** (4.13 eV), which explains the better absorption of **[1]⁺** in the blue region of the spectrum. These results were confirmed by time-dependent density functional theory calculations (TDDFT, see Figure AII.3). Compounds **[1]⁺**-**[3]²⁺** showed their lowest-energy transitions at 412, 368 and 369 nm, respectively, and these lowest-energy transitions corresponded to 97.5%, 95.2% and 98.1%, respectively, for the HOMO→LUMO transition. The excited states of these complexes, which must be of triplet multiplicity considering the heavy nature of the palladium atom and the efficient formation of ¹O₂ (see below), hence have intraligand charge transfer character (³ILCT). The phosphorescence emission from these states was similarly weak and very short in aerated Milli-Q solutions (Figure 3.2a), with quantum yields (ϕ_{p}) lower than 0.5% and lifetimes between 150 and 310 ps (Table 3.2, Figure AII.4). However, their quantum yields for ¹O₂ generation (ϕ_{Δ}), which were measured under 450 nm excitation by direct detection of the 1274 nm infrared emission of ¹O₂ in CD₃OD, were very different (Figure 3.2b, Table 3.2). **[1]⁺** showed the best ¹O₂ quantum yield (0.78, compared to 0.73 for the reference **[Ru(bpy)₃]Cl₂]**,⁴⁴ followed by **[2]⁺** (0.052) and finally **[3]²⁺** (0.009).

Overall, $[1]^+$ shows excellent properties for blue-light PDT, including good light absorption around 450 nm and excellent $^1\text{O}_2$ generation efficiency in air, while $[2]^+$ is only slightly better than $[3]^{2+}$, which has negligible photodynamic properties.

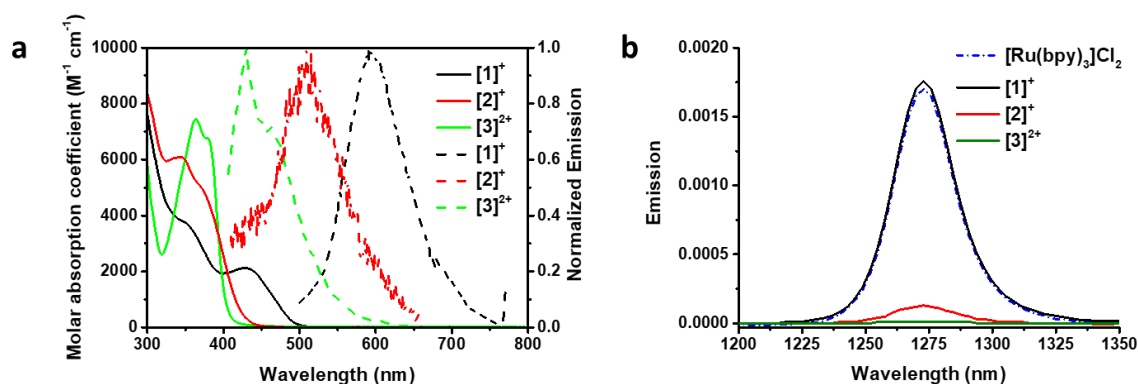


Figure 3.2 (a) Absorption (solid line, left axis) and normalized emission spectra (dashed line, right axis) of $[1]\text{OAc}$ - $[3](\text{OAc})_2$ in water (50 μM , 350 nm excitation). (b) Singlet oxygen emission for solutions of $[1]^+$ - $[3]^{2+}$ in CD₃OD (450 nm excitation, $A_{450} = 0.1$).

Table 3.2 Photophysical data for complexes $[1]\text{OAc}$ - $[3](\text{OAc})_2$.

Complex	λ_{abs} , nm ($\epsilon \times 10^3$ M ⁻¹ cm ⁻¹) ^a		λ_{em} (nm) ^a	ϕ_{P}	Lifetime (ns) ^{a,d}			ϕ_{Δ} ^e
					τ_1	τ_2		
$[1]\text{OAc}$	428 (2.12), (1.50)	455	593	0.0029 ^b	0.159 0.003	\pm —		0.78 ^f 0.73 ^g
$[2]\text{OAc}$	344 (6.10), (0.037)	455	509	0.00038 ^b	0.211 0.008	\pm —		0.052 ^f
$[3](\text{OAc})_2$	364 (7.45), (0.056)	455	430	0.0038 ^c	0.309 0.003 (87%)	\pm (13%)	4.17 \pm 0.08	0.009 ^f

^a Measurements were carried out in Milli-Q water. ^b Phosphorescence quantum yield measurements of $[1]^+$ - $[2]^+$ were carried out at a 390 nm excitation wavelength in aerated water, using $[\text{Ru}(\text{bpy})_3]\text{Cl}_2$ ($\phi_{\text{P}} = 0.028$) as the standard.⁴⁵ ^c Phosphorescence quantum yield measurement of $[3]^{2+}$ was carried out at 350 nm excitation wavelength in aerated ethanol, using 9,10-diphenylanthracene ($\phi_{\text{P}} = 0.885$) as the standard.⁴⁵ ^d Excitation wavelength 375 nm. ^e Excitation wavelength 450 nm, air atmosphere. The absorption of each complex at 450 nm was adjusted to 0.1 to avoid the generation of excimer. ^f In CD₃OD by spectroscopic detection at 1270 nm; $[\text{Ru}(\text{bpy})_3]\text{Cl}_2$ was used as the standard ($\phi_{\Delta} = 0.73$).⁴⁶ ^g In Opti-MEM complete using 9,10-anthracenediyl-bis(methylene)dimalonic acid as the $^1\text{O}_2$ probe; $[\text{Ru}(\text{bpy})_3]\text{Cl}_2$ was used as standard ($\phi_{\Delta} = 0.14$; see Figure AII.2).

3.2.3 Aggregation of the metal complexes in cell culture medium. In this family of palladium complexes, cyclometalation of dicationic complex $[3]^{2+}$ lowers its charge from +2 to +1, which

influences the supramolecular interaction of the metal complexes with itself and with other charged biomolecules. The NMR and crystallographic studies discussed above stimulated us to compare the behavior of complexes $[1]^+$ - $[3]^{2+}$ at 5 or 50 μM in a series of biomimetic solvents: H_2O , PBS, Opti-MEM cell medium with 2.5% fetal calf serum (FCS; this mixture is hereafter Opti-MEM complete), and Opti-MEM without FCS. The formation of nanoaggregation in the biomimetic solvents was studied with dynamic light scattering (DLS). All three palladium complexes dissolved well in water and PBS solution, as shown by the low DLS derived count rate (in kcps), indicating that no aggregation occurred under these conditions (Figure 3.3a, Table AII.5). In contrast, in the presence of Opti-MEM cell medium with or without FCS, cyclopalladated complexes $[1]^+$ - $[2]^+$ aggregating into particles, with a 35-fold (5 μM) or 102-fold (50 μM) increase in the derived count rate values. However, the derived count rate for $[3]^{2+}$ in all biomimetic solvents remained at a low level. The different behavior of complexes $[1]^+$ - $[3]^{2+}$ in Opti-MEM demonstrates the significant influence of cyclometalation and complex charge on the aggregation properties of these palladium complexes. Besides, the size of the aggregates made in the $[1]^+$ - $[2]^+$ in medium utterly depended on the presence of serum proteins (Figure 3.3b, AII.5). In the medium with FCS, the particle distribution maximum was 458 nm and 396 nm at 50 μM concentration (Figure 3.3b). In the absence of FCS, microparticles (hydrodynamic diameter > 1000 nm) were formed, resulting in precipitation (Figure 3.3c). Upon increasing the palladium complex concentration from 5 to 50 μM , the nanoparticles around 10-100 nm, which belong to the FCS proteins, almost disappeared and were replaced by micrometer-sized particles (Figure AII.5). For the dicationic complex $[3]^{2+}$ no significant changes occurred in the DLS analysis when the concentration was varied from 5 μM to 50 μM in all solutions, showing the absence of aggregation for this dicationic compound (Figure 3.3, AII.5). Meanwhile, the acidic nature of cancer cells⁴⁷ stimulated us to observe the aggregation behavior of $[1]\text{OAc}$ in cell medium at different pH values (3.30-7.64). As shown in Figure AII.6, $[1]^+$ still formed nanoaggregates (100-1000 nm) while the size distribution maximum slightly increased with pH, suggesting possible aggregation of this compound in the more acidic environment of cancer cells or lysosome.

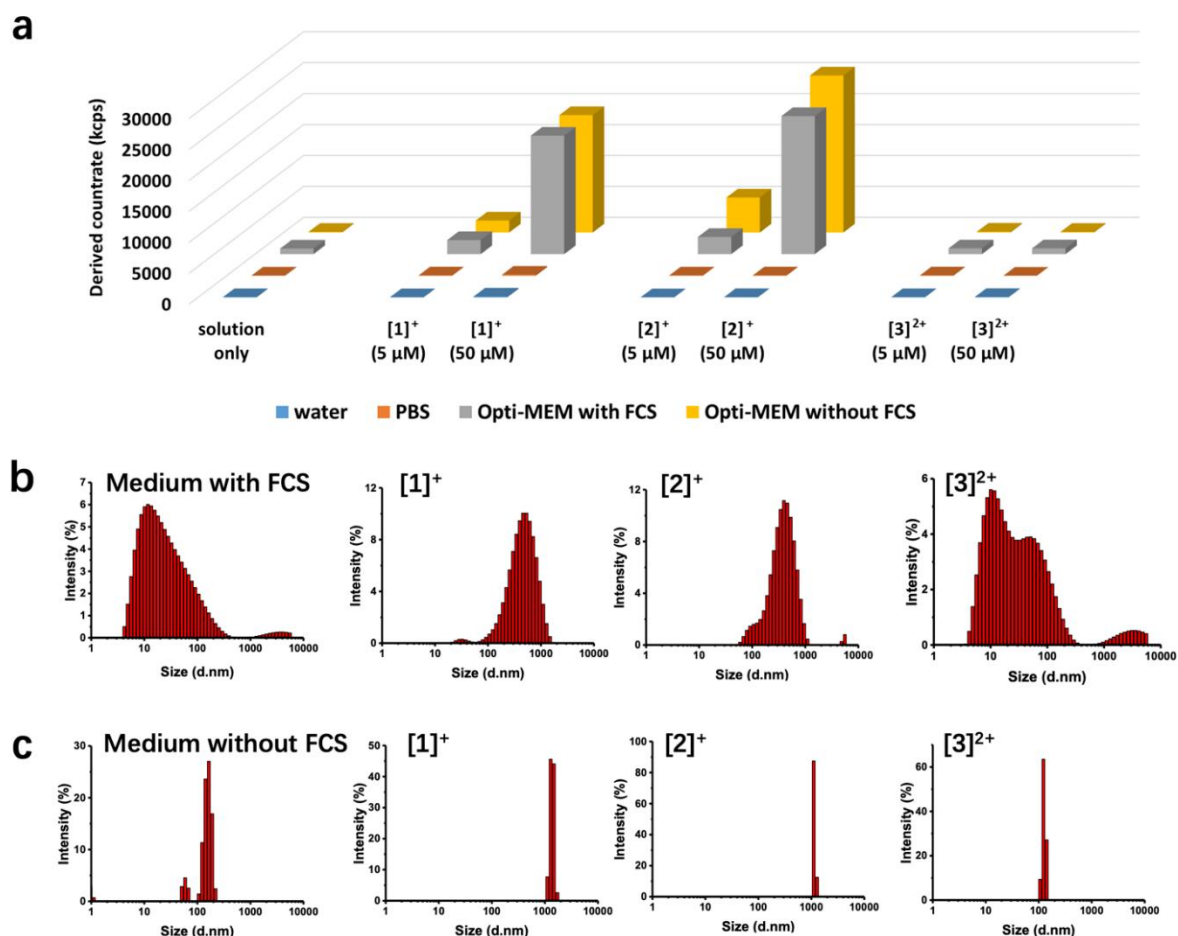


Figure 3.3 (a) Dynamic light scattering derived count rate of $[1]^+$ - $[3]^{2+}$ at 5 or 50 μ M in pure water, PBS, and Opti-MEM medium with or without FCS (2.5% v/v); Size distribution of the DLS analysis of solutions of $[1]^+$ - $[3]^{2+}$ (50 μ M) in Opti-MEM medium with (b) or without (c) FCS. The X-axis is the hydrodynamic diameter (in nm); the Y-axis is intensity (%).

Another view of the chemical stability and aggregation behavior of these complexes in the different media was provided by following in time the absorbance spectra of solutions of $[1]^+$ - $[3]^{2+}$ in H₂O, PBS, and Opti-MEM cell medium with or without FCS (Figure AII.7). All complexes were stable in water and PBS solutions for 24 h, confirming that the tetradentate nature of the ligand prevents the coordination of water or chloride ligands to the metal center. In addition, the complexes were stable in the presence of GSH and ascorbic acid (Figure AII.7), showing that palladium(II) was not reduced under such conditions. In cell medium with FCS, $[1]^+$ - $[2]^+$ showed significant increases in the baseline absorbance over 24 h, which can be attributed to increased scattering by the nanoparticles forming in solutions.⁴⁸ In contrast, in the medium without FCS the absorbance decreased quickly during the first 15 min and remained essentially constant in a second step, which can be assigned to precipitation. For $[3]^{2+}$, the

absorbance did not vary significantly in the medium without FCS, confirming the higher solubility of the dicationic complex. However, in FCS-containing medium a dramatic change was observed, characterized by an isosbestic point at 358 nm, indicating a chemical reaction between $[3]^{2+}$ and one of the components of FCS. These results matched the observations made by DLS (*i.e.* $[1]^+-[2]^+$ precipitated in medium without FCS but generated ~400 nm hydrodynamic diameter nanoparticles when FCS was added to the cell medium). This result suggests that the proteins present in FCS play a dramatic role in the aggregation state of cyclopalladated compounds $[1]^+-[2]^+$, while for tetrapyrridyl complex $[3]^{2+}$ this role is much less pronounced. We can hence expect a different mechanism of cell uptake for monocationic complexes $[1]^+-[2]^+$ compared with dicationic compound $[3]^{2+}$ because many cell uptake pathways, including endocytosis, depend on the size of drugs.^{49, 50} Besides, the aggregation of $[1]^+-[2]^+$ in an FCS-containing medium suggests that upon injection into the bloodstream of a mammal these types of cyclometalated compounds may generate protein-capped nanoparticles, which may influence the tumor uptake and biological half-time of cyclometalated compounds compared to nonaggregated small molecules such as $[3]^{2+}$.

3.2.4 Supramolecular polymerization of cyclometalated complexes. If the data above demonstrated that nanoaggregates were stabilized in FCS-containing medium, it was not clear yet as to whether the palladium complex or proteins abundant in serum, such as albumin, were responsible for aggregate formation. As $[1]OAc-[3](OAc)_2$ do not form aggregates in pure water, and form them too quickly in Opti-MEM complete, we changed their counteranion to hexafluorophosphate by reprecipitation with KPF_6 to make them less hydrophilic, which allowed for observing the kinetics of the formation of the nanorods. Supramolecular live polymerization of $[1]PF_6$, and $[2]PF_6$ was observed in $H_2O/MeCN$ solution (100 μM , 9:1, v/v) via UV-vis absorption spectroscopy.⁴² As shown in Figure 3.4a, b, d, for $[1]PF_6$ and $[2]PF_6$ the baseline of the absorbance spectrum increased quickly (within 6 to 7 min), suggesting increasing light scattering; it then stabilized until the end of the experiment ($t=30$ min). By contrast, the absorbance of $[3](PF_6)_2$ showed only negligible variations (Figure 3.4c, d). At the end of these UV-vis experiments, each solution was deposited on a TEM grid to observe the morphology of the nanoaggregates by TEM. Complexes $[1]PF_6$ and $[2]PF_6$ showed beautiful nanorod morphologies, while $[3](PF_6)_2$ showed random aggregates reminiscent of a precipitate. These data clearly show that the cyclometalated complexes $[1]^+-[2]^+$ themselves can self-assemble into nanorods most probably due to the Pd...Pd interaction observed in the solid state.

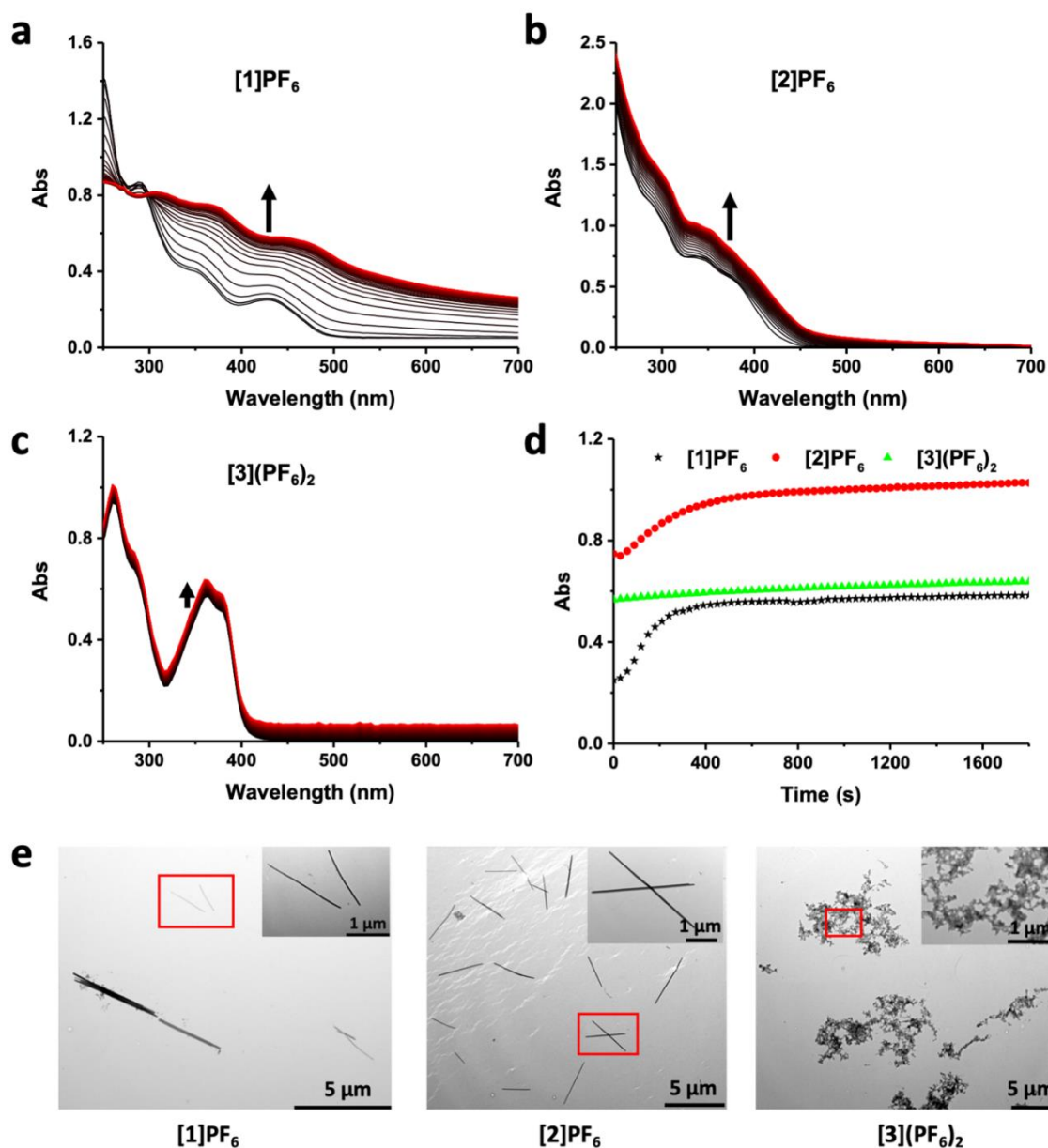


Figure 3.4 Time evolution of the absorption spectra of the H₂O/MeCN solution (100 μM, 9:1, v/v) of complexes [1]PF₆ (a), [2]PF₆ (b), and [3](PF₆)₂ (c) at 298 K for 30 min; (d) Time evolution of the absorption at 428 nm (black stars, [1]PF₆), 332 nm (red dots, [2]PF₆), 360 nm (green triangles, [3](PF₆)₂) of these solutions. The absorption spectra were measured every 30 s. (e) TEM images of [1]PF₆ (a), [2]PF₆ (b), and [3](PF₆)₂ after aggregation in the H₂O/MeCN solution (100 μM, 9:1, v/v) for 30 min (scale bar 5 μm, inset 1 μm).

3.2.5 Cryo-TEM measurements in Opti-MEM medium. Compounds [1]OAc-[3](OAc)₂ dissolve well in water with a low derived count rate according to DLS (Figure 3.3a). TEM gives a higher-contrast picture: while samples of [1]OAc-[2]OAc prepared from a Milli-Q water solution (50 μM) showed rectangular nanorods with an average length of around 139 and 203

nm, respectively, samples of $[3](\text{OAc})_2$ at the same concentration showed random shapes characteristic of a precipitate (Figure AII.8). In both cases, the observed particulates were artifacts due to the evaporation of solvent before TEM imaging. Cryo-TEM, on the contrary, allows for observing nanostructures directly as they are in solution (*i.e.* in their native state). Cryo-TEM images of a 50 μM solution of $[1]\text{OAc}$ - $[3](\text{OAc})_2$ under different conditions were hence recorded. As shown in Figure 3.5 and Figure AII.9, the two cyclometalated compounds $[1]\text{OAc}$ - $[2]\text{OAc}$ in Opti-MEM did generate nanorods characterized by a width of ~ 20 nm. In the presence of FCS, these nanorods were nicely dispersed on the grid or were forming aggregates of about 500 nm, while in the absence of FCS they aggregated in much larger aggregates of micrometer size. Compound $[3](\text{OAc})_2$, on the contrary, did not show such nanorods. Interestingly, when $[1]\text{OAc}$ (50 μM) was dispersed in pure FCS solution, bent nanofibers were observed, indicating that the proteins contained in FCS also played a role in the generation of nanostructures. Overall, all cryo-TEM images were fully consistent with the DLS results. From these data, it appears that FCS stabilized nanorods in the cell medium for cyclometalated compounds $[1]\text{OAc}$ - $[2]\text{OAc}$ while in the absence of FCS the nanorods aggregate with each other into larger clusters that end up precipitating out of solution.

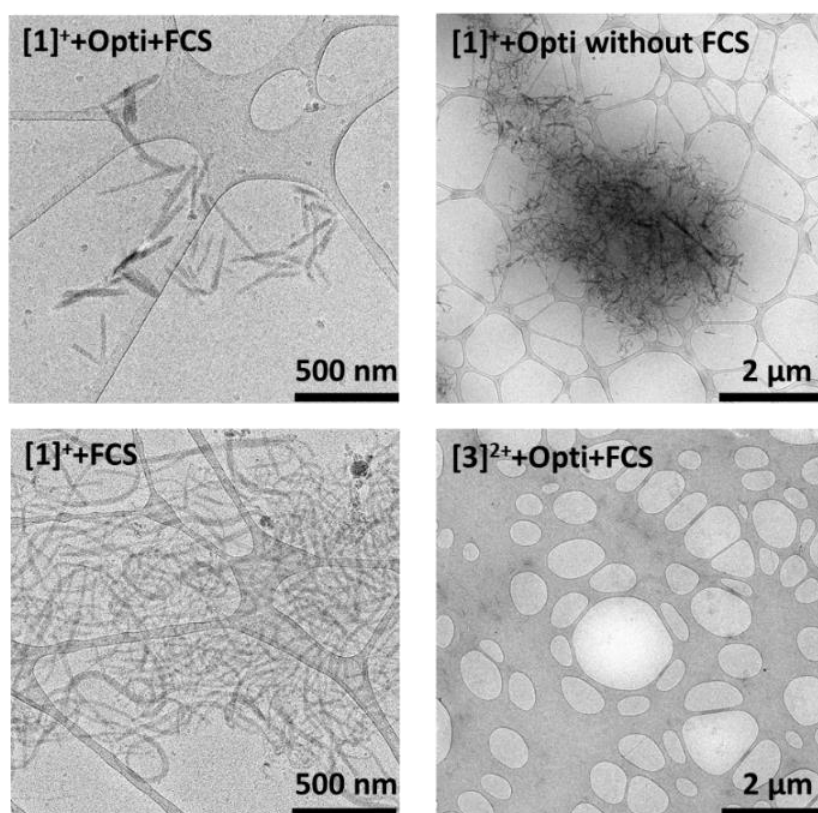


Figure 3.5 Cryo-TEM images of complexes $[1]\text{OAc}$ and $[3](\text{OAc})_2$ (50 μM) in Opti-MEM medium with or without FCS or pure FCS solution.

3.2.6 Influence of the charge on the supramolecular interaction. In order to understand why $[1]^+$ and $[2]^+$ self-assemble and not $[3]^{2+}$, we first minimized by DFT at the PBE0/TZP/COSMO level in water a supramolecular dimer of $[1]^+$ and $[2]^+$ (Figure AII.10, Table AII.6). Minimization converged with a local minimum characterized by Pd...Pd distances of 3.18 and 3.20 Å, respectively, which qualitatively fits the experimental distance observed in the crystal structure (3.35 Å and 3.27 Å, respectively; see Figure 3.1b). This minimum demonstrates that for two isolated molecules of cyclometalated, monocationic complex $[1]^+$ or $[2]^+$, electrostatic repulsion is low enough to be compensated for the metallophilic Pd...Pd interaction, coupled to π - π stacking of the flat polyaromatic ligands. By contrast, a similar minimization run from a dimer of $[3]^{2+}$, assembled by hand at a short (3.18 Å) Pd...Pd distance, saw the Pd...Pd distance increase steadily to > 6.5 Å during the energy minimization, without converging (*data not shown*). This result demonstrated that for $[3]^{2+}$ the charge and hence the intermolecular electrostatic repulsion are too high to be compensated for the metallophilic interaction and the π - π stacking that may occur at short Pd...Pd distances. Thus, the supramolecular assembly of $[1]^+$ and $[2]^+$ seems to be modulated by the environment of the complex in solution (solvent, counteranions, and the presence of proteins), but it is an inherent property of these cyclometalated metal complexes. It originates from the strong and attractive combination between the metallophilic interaction and π - π stacking between the ligands at short Pd...Pd distances, combined with low electrostatic repulsion. For $[3]^{2+}$, the latter is too strong to lead to supramolecular assembly.

3.2.7 Photophysical and photochemical properties of [1]OAc in Opti-MEM complete medium. As in a cell cytotoxicity assay, the cyclometalated complexes will be added in Opti-MEM complete medium and not in water or methanol, and they will form aggregates rather than monomers. It is hence important to determine whether aggregation modifies the photophysical and photochemical properties of [1]OAc, compared to the monomer. The absorbance (Figure AII.11) of [1]OAc in the medium, for example, showed on top of a broader and more intense absorption band between 350 and 500 nm, a baseline increasing with decreasing wavelengths, which is typical for light scattering by nanoaggregates. Blue light absorption was enhanced for the aggregates compared to that for the monomer. The weak emission peak at 593 nm for [1]OAc in water (Figure AII.11) was quenched in Opti-MEM complete medium and replaced by a new stronger peak with a maximum at 469 nm. This new peak was located in a similar region compared to the emission peak of Opti-MEM complete medium itself, but it was more intense. The exact nature of the emitters responsible for this new

band remains unknown; in particular, it is unclear whether this peak might be attributed to supramolecular associations between **[1]OAc** and endogenous fluorophores in the medium. All in all, the emission properties of the supramolecular aggregates of **[1]OAc** were still too low to be observed *in vitro* by emission microscopy.

In terms of the $^1\text{O}_2$ generation quantum yield (ϕ_Δ), direct spectroscopic detection of the 1270 nm emission of $^1\text{O}_2$, which was used for determining ϕ_Δ of the monomer in CD_3OD , could not be used in nondeuterated aqueous cell-growing medium, where the intensity of this NIR emission band was too low. Hence, to determine the value of ϕ_Δ of aggregates of **[1]OAc** in Opti-MEM medium, a specific water-soluble $^1\text{O}_2$ probe was used (*i.e.*, 9,10-anthracenediyl-bis(methylene)dimalonic acid (ABMDMA)). In the dark, this dye absorbs light at around 378 nm, but in presence of photogenerated $^1\text{O}_2$, it forms an endoperoxide that leads to a loss of conjugation and thus a decrease in the absorbance at 378 nm.⁵¹ When **[1]OAc** (50 μM) was mixed with ABMDMA (100 μM) in Opti-MEM complete, the absorbance remained stable in the dark; however, upon 450 nm light irradiation the absorbance of ABMDMA dramatically decreased (Figure 3.6), showing the good $^1\text{O}_2$ production of the aggregates of **[1]OAc**. A high quantum yield of 0.73 was obtained by a quantitative comparison of the slope obtained with **[1]OAc** with the slope obtained with a reference sample of **[Ru(bpy)₃]Cl₂** (50 μM , $\phi_{\Delta\text{ref}} = 0.14$, see Figure AII.12 and details in Appendix II).⁵² Overall, **[1]OAc** retains excellent $^1\text{O}_2$ generation properties in the aggregated state and its blue light absorption properties are enhanced (*i.e.*, its blue light PDT properties are improved in cell growing medium).

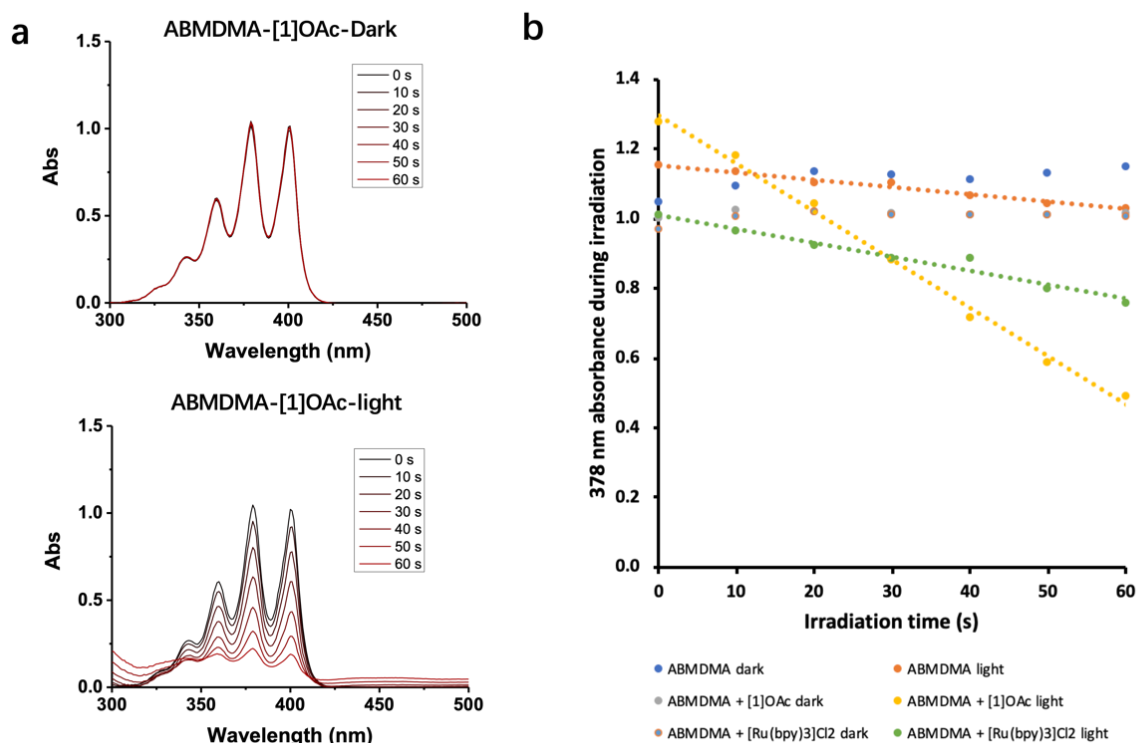


Figure 3.6 Singlet oxygen generation of aggregates of [1]OAc in Opti-MEM complete medium. (a) The absorbance change of ABMDMA (100 μM) in Opti-MEM complete in the presence of [1]OAc (50 μM) in the dark (top) or upon blue light irradiation (bottom). (b) Evolution of the absorbance at 378 nm vs irradiation time of ABMDMA (100 μM) in Opti-MEM complete medium in the absence or presence of [1]OAc (50 μM) or [Ru(bpy)₃]Cl₂ (50 μM) in the dark or under blue light irradiation. Irradiation conditions: 298 K, 450 nm, 5.23 mW cm⁻², and 1 min.

3.2.8 Phototoxicity assay in normoxic and hypoxic conditions. Considering the good photodynamic properties of [1]⁺ under blue light irradiation and its FCS-stabilized nanoaggregation behavior, the anticancer activities of [1]⁺-[3]²⁺ were studied first in vitro, both in the dark and following a low dose of blue light (1.7 J cm⁻²). A dose-response curve was obtained in two human cancer cell lines A549 (lung cancer) and A431 (skin cancer) grown in 2D under normoxia (21% O₂) and using FCS-containing medium. The sulforhodamine B (SRB) assay was used as an end-point assay to quantify cell viability in treated vs untreated wells, and cisplatin was used as the positive control. The half-maximal effective concentrations (EC₅₀), defined as the compound concentration necessary to divide cell growth by a factor of 2, compared to untreated wells, and the photoindexes (PI), defined as EC_{50,dark}/EC_{50,light}, are reported in Table 3.3 In A549 all three complexes showed significant anticancer abilities in the

dark ($EC_{50} < 10 \mu M$), comparable to that of cisplatin, while in A431 $[3]^{2+}$ was much more toxic than $[1]^+$ - $[2]^+$. This result suggests that the cyclopalladated complexes, unlike $[3]^{2+}$, might have a form of cell toxicity in the dark that is cell-specific. Upon blue light irradiation, complex $[1]^+$ showed a 6.7- and 9.4-fold increase in cytotoxicity toward A549 and A431 cancer cells, respectively, to reach 330 nM cytotoxicity for A549 cells, which is 9.4 more toxic than cisplatin (3.1 μM in dark). These results are in line with the excellent singlet oxygen generation properties of this compound under blue light irradiation, and they were comparable, at such low doses of light ($< 2 J.cm^{-2}$), to the photoindeces obtained with the clinically approved 5-ALA control ($PI = 9.8$ in normoxic A431 cells, see Table 3). Meanwhile, compounds $[2]^+$ - $[3]^{2+}$ did not show any significant photocytotoxicity, which is consistent with their very low blue light absorption.

The excellent singlet oxygen generation properties of $[1]OAc$ in both monomeric and aggregated forms and its clear blue light activation in normoxic cells suggested that this compound may work via a type II PDT mechanism (*i.e.*, via energy transfer from the 3ILCT states of the complex to 3O_2). When the cytotoxicity experiment was repeated in the same cancer cells grown under hypoxia (1% O_2 , Figure AII.13-15), the phototoxicity of $[1]^+$ indeed showed a 3-fold decrease. However, it was not fully quenched, because the photoindeces of 4.6 and 6.7 in A549 and A431, respectively, were smaller compared to 6.7 and 9.4 under only normoxia, but far from unity. By contrast, two well-known PDT type II photosensitizers, 5-ALA and rose bengal, when used as the positive control, showed good PDT effect ($PI < 10$) under normoxic conditions but no phototoxicity at all under hypoxic conditions, as expected for PDT type II photosensitizers. These results suggest that PDT type I may also occur with $[1]^+$, as observed with other metal-based sensitizers.¹⁴ Finally, the higher EC_{50} obtained in the dark for $[1]^+$ - $[3]^{2+}$ under hypoxic conditions can be rationalized by the different microenvironments and gene expression usually found in hypoxic cancer cells, which are known to overexpress resistance mechanisms compared to normoxic cells.

Table 3.3 Half maximal effective concentrations (EC_{50} in μM) of $[1]^+$ - $[3]^{2+}$, cisplatin, 5-ALA and Rose bengal for A549 and A431 cancer cells in the dark and under blue light irradiation in normoxic (21% O_2) and hypoxic (1% O_2) conditions. 95% confidence interval (CI in μM) and photoindeces ($PI = EC_{50,dark}/EC_{50,light}$) are also indicated.

Complex		EC_{50} (μM)							
		Normoxic condition				Hypoxic condition			
		A549	$\pm CI$	A431	$\pm CI$	A549	$\pm CI$	A431	$\pm CI$
$[1]^+$	Dark	2.2	+0.4	45	+13	6	+3	100	+70

PI			-0.4		-9		-2		-28
	Light	0.33	+0.15 -0.11	4.8	+0.9 -0.8	1.3	+0.3 -0.3	15	+2 -2
		6.7		9.4		4.6		6.7	
[2]⁺	Dark	2.7	+0.7 -0.6	12	+4 -3	4	+1 -1	29	+38 -13
	Light	2.5	+0.7 -0.6	7	+2 -1	3	0.9 -0.8	22	+18 -8
		1.1		1.4		1.3		1.3	
[3]²⁺	Dark	5	+2 -2	7	+2 -2	23	+8 -5	21	+2 -1
	Light	4.4	+0.9 -0.9	6	+1 -1	15	+4 -3	21	+3 -3
		1.1		1.2		1.5		1.0	
cisplatin	Dark	3.1	+0.6 -0.5	2.5	+0.4 -0.4	24	+11 -5	13	+4 -3
	Light	3.9	+0.8 -0.7	2.9	+0.5 -0.4	20	+8 -4	8	+2 -2
		0.79		0.86		1.2		1.6	
5-ALA	Dark	390	+620 -270	11000	+2200 -1900	13300	+3400 -2700	16800	+2800 -2400
	Light	170	+250 -110	1200	+1900 -850	14400	+3500 -2900	19200	+4500 -3700
		2.3		9.2		0.9		0.9	
Rose bengal	Dark	63	+13 -11	57	+28 -18	76	+18 -16	70	+22 -21
	Light	21	+6 -4	8	+1 -1	81	+24 -19	74	+20 -19
		3.0		7.1		0.9		0.9	

^a Irradiation condition: normoxic 455 nm, 5 minutes, 5.66 mW cm⁻², 1.7 J cm⁻²; hypoxic 455 nm, 8 min, 3.54 mW cm⁻², 1.7 J cm⁻². Data is the mean of three independent biological experiments.

3.2.9 Cellular uptake, subcellular fractionation, and uptake inhibition studies with A549 cells. Usually, nanoaggregates are taken up by endocytosis and end up either in the endosome or lysosome.⁵³ In order to check this hypothesis, A549 cells were first treated for 1 h with sodium azide (15.4 mM) or dynasore (80 μM), which inhibited active uptake and dynamin-dependent endocytosis, respectively.⁵⁴ Then, the cells were incubated with the three palladium complexes (5 μM) for a short time (*i.e.*, 3 h). The Pd contents of the cells were finally determined by ICP-MS. As shown in Figure 3.7a, in the control group without any inhibitors drug uptake of cyclometalated compounds **[1]⁺**-**[2]⁺** was 3 times higher than that of tetrapyrrolyl analogue **[3]²⁺**. In addition, samples pretreated with NaN₃ or dynasore showed significant inhibition efficiency for the uptake of **[1]⁺**-**[2]⁺**, while no inhibition was observed for **[3]²⁺**. These results demonstrated that **[1]⁺**-**[2]⁺** were taken up in the cell via active, dynamin-

dependent endocytosis, while $[3]^{2+}$ went into the cells by energy-independent uptake, possibly passive diffusion. This assay confirmed that $[1]^+-[2]^+$ entered the cells as nanoaggregates and that cyclometalation dramatically changed the mechanism of cellular uptake.

In a second experiment aimed at determining the intracellular localization, at longer incubation times for these nonemissive palladium complexes, A549 cells were treated with complexes $[1]OAc-[3](OAc)_2$ (1 μ M) for 24 h and then trypsinized and fractionated into four fractions: cytosol, membranes, nuclei, and cytoskeleton. The membrane fractions include not only the cell membrane, but also the membranes in the mitochondria, endosomes, and lysosomes. In principle, nanoaggregates of $[1]^+-[2]^+$ were expected to end up in the membrane fraction. The results (Figure 3.7b, Table AII.7) did not fit such expectations. $[1]^+-[2]^+$ were found neither in the membrane nor in the nuclear fractions, but almost exclusively (94.3% and 89.1%, respectively) in the cytoskeleton fraction. In contrast, $[3]^{2+}$ was distributed among the cytoskeleton (61.1%), the membrane fraction (15.5%), and the cytosol (23.3%). Besides, as at shorter times the total amount of palladium found in the cells was more than 10 times higher for cyclometalated complexes $[1]^+-[2]^+$ (19 and 14 ng Pd/million cells, respectively) than for $[3]^{2+}$ (1.7 ng Pd/million cells). Overall, these combined ICP-MS results confirmed previous reports that cyclometalated compounds are more efficiently taken up than their polypyridyl analogue. However, they also shed new light on the reason for such enhanced uptake: considering their similar log P_{ow} values but very different aggregation behavior in the FCS-containing cell medium, it is the nanoaggregation of cyclometalated compounds $[1]^+-[2]^+$, stabilized by FCS, that leads to enhanced cellular uptake, rather than passive uptake by diffusion through the cell membrane. In addition, the supramolecular nature of the interactions leading to aggregate formation seems weak enough to allow for a redistribution of the palladium complex after endocytosis, as palladium ends up in the cytoskeleton fraction, rather than in the endosome or lysosome. According to this study, the mode of action of $[1]^+-[2]^+$ is very unlikely to be related to nuclear DNA damage, suggesting that these compounds may overcome chemotherapy resistance originating from DNA damage repair.

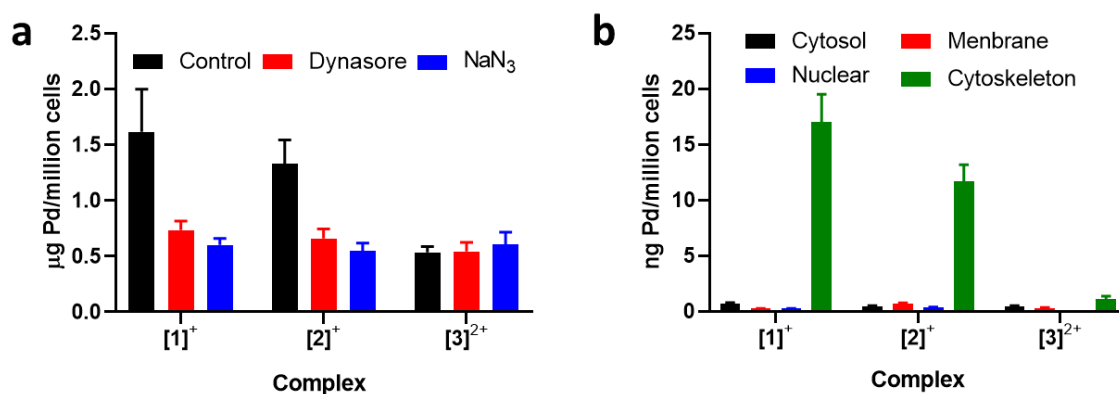


Figure 3.7 (a) Pd contents (expressed in $\mu\text{g Pd/million cells}$) of A549 cells after treatment with NaN_3 or dynasore for 1 h and compounds $[1]^+$ - $[3]^{2+}$ ($5 \mu\text{M}$) for 3 h. (b) Distribution (expressed in $\text{ng Pd/million cells}$) of palladium compounds $[1]^+$ - $[3]^{2+}$ in the cytosol (black), membranes (red), nucleus (blue), and cytoskeleton (green) of A549 cells after treatment at $1 \mu\text{M}$ for 24 h.

3.2.10 Intracellular ROS determination and apoptosis. The generation of ROS in cancer cells usually induced cell death via apoptosis.⁵⁵ 2,7-Dichlorodihydrofluorescein diacetate (DCFH-DA) is an excellent sensor for intracellular ROS, which generates green-emissive metabolite dichlorofluorescein (DCF). ROS levels were hence measured in A549 cells using flow cytometry after treatment with $[1]^+$ - $[3]^{2+}$ ($5 \mu\text{M}$) followed or not by blue light irradiation (455 nm , 5 min , 5.66 mW cm^{-2} , 1.7 J cm^{-2} , Figure 3.8a). In the dark, cyclometalated complexes $[1]^+$ - $[2]^+$ showed significant ROS levels, even higher than that for the positive control ($400 \mu\text{M H}_2\text{O}_2$). Upon 455 nm irradiation, the ROS levels in all groups increased, especially for complex $[1]^+$, with a 3.5-fold enhancement and the highest ROS level of all samples. This experiment confirmed the photodynamic character of light-induced cell killing with $[1]^+$. The ROS level found for $[2]^+$ under blue light irradiation was close to the sum of the ROS levels found in cells treated with only blue light and that of cells treated with $[2]^+$ and left in the dark, indicating the weak light-induced ROS generation ability of complex $[2]^+$. Unexpectedly, $[3]^{2+}$ inhibited ROS generation, compared with cells treated with $[3]^{2+}$ but kept in the dark or cells irradiated with blue light in the absence of any compound. The cytotoxicity difference between cyclometalated complexes $[1]^+$ - $[2]^+$ and $[3]^{2+}$ is the ability of the former to generate ROS in the dark, and the ability of $[1]^+$ to absorb blue light to increase ROS generation.

The cell death mode triggered by such ROS formation in A549 cells was determined by flow cytometry using the Annexin V-FITC/propidium iodide double staining assay (Figure AII.16). After 24 h of incubation with each complex, the A549 cells were irradiated with blue light or left in the dark and incubated for another 24 h and then harvested and treated with both dyes

for FACS analysis. The percentage of live cells (Annexin -, PI -), early apoptotic (Annexin +, PI -), later apoptotic (Annexin +, PI +), and necrotic (Annexin -, PI +) cells, are shown in Figure 8b. Clearly, in the dark $[1]^+$ - $[3]^{2+}$ provoke cell death via apoptosis. Under blue light irradiation, the percentage of apoptotic cells induced by complex $[1]^+$ increased by 21% (from 71 to 92%), while the other two complexes increased by only 4.3% ($[2]^+$) and 7.1% ($[3]^{2+}$). Overall, in A549 cells $[1]^+$ kills cells via apoptosis in the dark by generating ROS near the cytoskeleton; this action is dramatically enhanced by low doses of blue light irradiation.

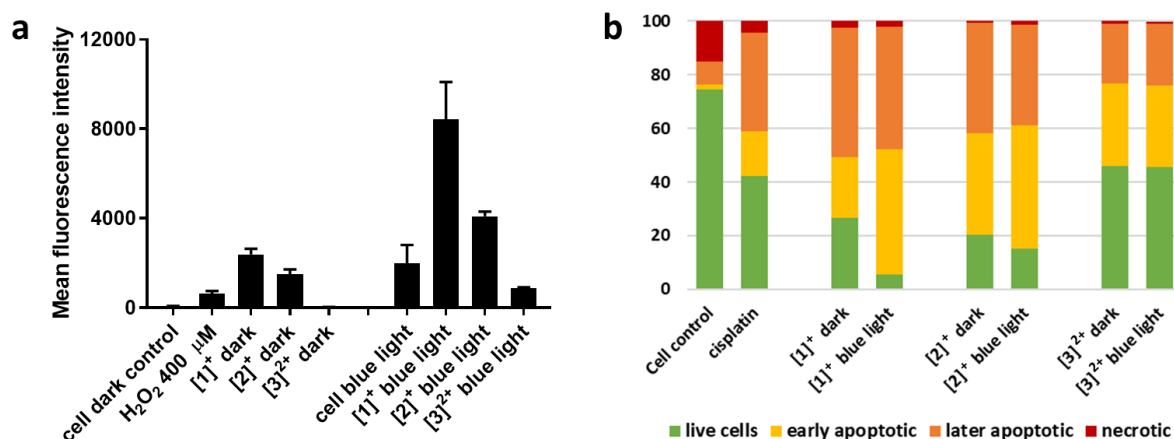


Figure 3.8 (a) Mean fluorescence intensity of cells treated first with $[1]\text{OAc}-[3](\text{OAc})_2$ (5 μM , 24 h) and then with DCFDA (20 μM , 30 min), and analyzed by flow cytometry; (b) Flow cytometry quantification of alive (Annexin -, PI -), early apoptotic (Annexin +, PI -), later apoptotic (Annexin +, PI +), and necrotic (Annexin -, PI +) A549 cells after treatment with $[1]^+$ - $[3]^{2+}$ (15 μM) or cisplatin (15 μM) in the dark or after irradiation for 5 min with blue light (455 nm, 5.66 mW cm⁻², 1.7 J cm⁻²).

3.2.11 Photocytotoxicity of $[1]\text{OAc}$ in 3D tumor spheroids. In 2D cell monolayers, the physical access of the drug to the cancer cells is not an issue and light optimally and equally bathes all cells, which represents a poor model of in vivo tumor treatment with PDT. By contrast, 3D multicellular tumor spheroid models provide a more accurate biological evaluation of the physical penetration of PDT drugs, nanoparticle-based drug delivery systems, and light.⁵⁶ The cytotoxicity of $[1]^+$ in FCS-containing medium was hence tested in 3D tumor spheroids using a CellTiter-Glo 3D cell viability end-point assay to quantify the ATP concentration.⁵⁷ As shown in Figure 3.9, it was possible to fully eradicate the tumor spheroids in the dark, suggesting that the nanoaggregates of $[1]^+$ and FCS either well penetrated the spheroid to kill simultaneously all cell layers including the center, or destroyed the outer layers of the spheroids first to move toward the center and kill the cells there. Upon blue light activation (455 nm, 10 min, 3.48 mW

cm^{-2} , 2.1 J cm^{-2}) the EC_{50} value of 3D tumor spheroids decreased by 6.2-fold, from 13 to $2.1 \mu\text{M}$, and here as well full eradication of ATP production could be achieved. Such a photoindex is surprisingly similar to the one measured in normoxic 2D cell monolayers (6.7), which again suggests that sensitizer penetration is not an issue here. These results not only confirm the excellent potential of $[1]^+$ as a blue light PDT agent, but also highlight its ability to penetrate, as a nanoaggregate, to the core of tumor spheroids, and to kill all cancer cells by a combination of a chemical (dark toxicity) and photochemical (blue-light activation) effect.

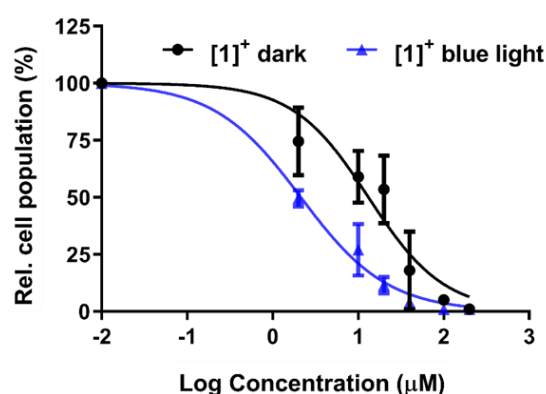


Figure 3.9 Dose-response curves for A549 3D tumor spheroids incubated with complex $[1]^+$ irradiated for 10 min with blue light (in blue) or kept in the dark (in black). $\text{EC}_{50,\text{dark}} = 13 \mu\text{M}$ (95% confidence intervals $+7.7 \mu\text{M}$, $-6.0 \mu\text{M}$), $\text{EC}_{50,\text{light}} = 2.1 \mu\text{M}$ (95% confidence intervals $+0.7 \mu\text{M}$, $-0.7 \mu\text{M}$), $\text{PI} = 6.2$.

3.2.12 In vivo experiments. The penetration of blue light well matches the depth of skin cancers in the human body. Considering the excellent dark cytotoxicity of $[1]\text{OAc}$ *in vitro* and its good photodynamic properties in hypoxic cancer cells and 3D tumor spheroids, the *in vivo* antitumor property of compound $[1]\text{OAc}$ was evaluated, in the dark or upon blue light irradiation (450 nm), in 4T1 breast tumor xenografts in Balb/c female mice. This model is a commonly used subcutaneous tumor model in mice, which is better suited for blue light PDT *in vivo* than orthotopic xenografts models because of the short irradiation wavelength used. In general, intravenous tail injection is the main injection method for *in vivo* antitumor experiments because it best mimics the mode of administration of PDT sensitizers in clinical trials. However, in this work the higher dark cytotoxicity of the palladium complexes, compared to clinically approved PDT sensitizers, led us to consider paracancerous injection and a short drug-to-light interval of 1 h as a more efficient method for maximizing the drug concentration near the tumor and hence the PDT effect, while minimizing toxicity to the mice. Compound $[2]\text{OAc}$ was also tested as a control complex that also forms nanoparticles in the presence of proteins, but does

not absorb blue light at that wavelength. The mice (N=3) were divided into six groups when the tumor volume reached around 40 mm³: dark vehicle control, blue light-irradiated vehicle control, and injection of [1]OAc or [2]OAc (40 μM, 100 μL) either with or without blue light irradiation in a 60 J cm⁻² light dose. The mice were treated twice, at days 0 and day 2. One hour after compound injection, the mice were irradiated with blue light for 20 min. The tumor volume of each mouse (Figure 3.10a), and the body weight (Figure AII.17) were measured and recorded over 10 days following treatment. On day 10, the mice were sacrificed, and tumors were isolated to compare the volume scale of tumor spheres. All mice showed similar body weight at the end of the treatment (around 20 g), meaning that the mice were healthy and the complexes were not very toxic to the mice themselves. At day 10, the tumor of dark vehicle control and blue light-irradiated vehicle control groups showed similar (and highest) volumes, followed by the mice group treated with [2]⁺ (dark) > [2]⁺ (450 nm) > [1]⁺ (dark) > [1]⁺ (450 nm). In the dark, the tumor volumes of mice were gradually growing with the treatment of complex [1]⁺ and [2]⁺ from day 0 to day 8 and then significantly increased on day 10. When treated with [1]⁺ and irradiated with blue light on days 0 and 2, no obvious growth of the tumor occurred over 10 days (Figure 3.10a), demonstrating the excellent photodynamic therapy properties of [1]⁺ under these conditions.

As a side note, when the intravenous tail injection of a PDT sensitizer is chosen, longer drug-to-light intervals are typically used (4-24 h) in order to wait for the PDT sensitizer to accumulate in the tumor, in particular, for sensitizer nanoformulations relying on the enhanced permeability and retention (EPR) effect to enter the tumor. By contrast, paracancerous injection is a quicker and more direct method of concentrating the sensitizer (here the Pd nanoaggregates) near the tumor site. Also, it is better than intratumoral injection because paracancerous injection still holds the possibility of blood circulation of the drug to occur. On the other hand, a longer drug-to-light interval could lead to further transport of the drug to the rest of the body and unwanted toxicity to occur. Thus, a rather short drug-to-light time of 1 h was chosen. The final results suggest that 1 h is indeed a reasonable time setting and that under such conditions [1]⁺ penetrates well enough into the tumor to serve as a PDT sensitizer.

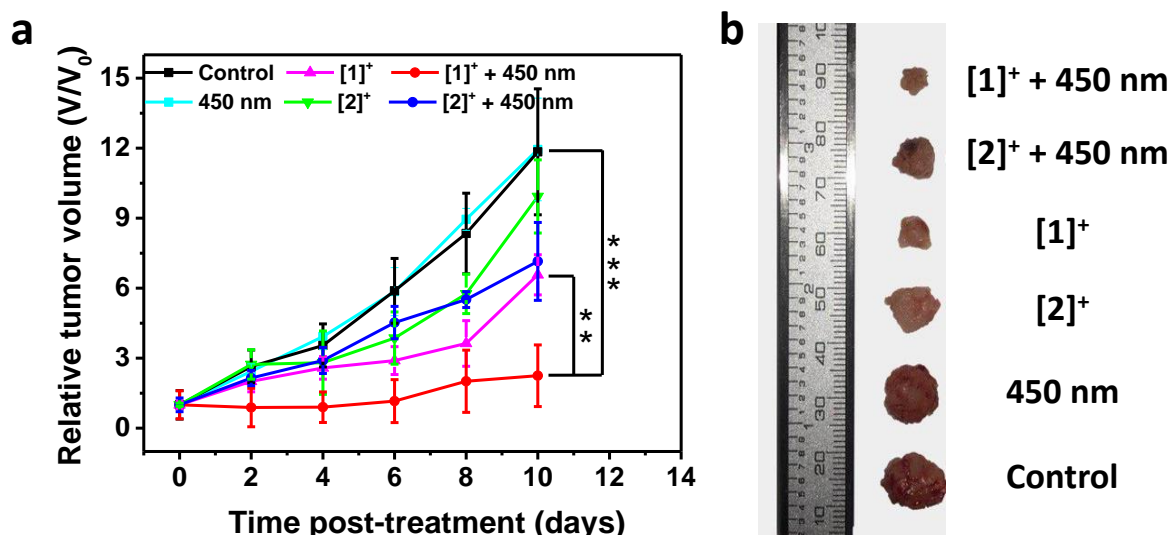


Figure 3.10 (a) Relative 4T1 breast tumor volumes of Balb/c mice and (b) visual tumor sizes at day 10 of Balb/c mice treated with vehicle control, [1]⁺, or [2]⁺ at day 0 and left in the dark or irradiated with blue light. Mice were treated on days 0 and 2 and irradiated with blue light (450 nm, 50 mW cm², 20 min, 60 J cm⁻²) 1 h after injection. Statistical significance was set to $p < 0.01$ (**) and 0.001 (***).

3.3 Discussion

Traditionally, a vast majority of the PDT literature argues that because light penetration is better with red light than with blue light, blue light PDT is not relevant *in vivo*. Recently, however, research compared blue light vs. red light for the 5-aminolevulinic acid (ALA) photodynamic therapy of basal cell carcinoma patients.^{58, 59} 5-ALA is transformed selectively by tumors into protoporphyrin IX, which can be excited either in the Soret band using blue light or in the Q band using red light. In this study, blue light showed statistically noninferior efficacy compared to red light, and a lower light fluence rate could be used with blue light due to the better light absorption of the Soret band, which generated less pain for the patients.⁵⁸ These results suggested that blue light PDT should be studied and optimized further to evaluate its potential as an effective nonscarring anticancer treatment option in, for example skin, eye, or bladder cancer. In cancers of superficial tissues indeed, short-wavelength (blue or green) PDT agents are interesting because short-wavelength light potentially reduces the damage to deeper healthy tissues. For skin cancer, for example, skin contains two layers: the cuticular layer (~0.08-0.27 mm thickness) and the derma (~2.1-5.9 mm thickness).⁶⁰ As in skin tissue the penetration depth for blue, red, and NIR light is 1-2 mm, 4-5 mm, and > 5 mm, respectively,⁶¹ hence blue light may reduce photodynamic damage to the derma. It is known that the cuticular tissue can recover

soon after damage, but for the derma, tissue recovery is sometimes difficult. Thus, in the treatment of skin diseases, it is beneficial to reduce damage to the derma. Similar strategies are being developed in bladder cancer patients, where the green light PDT sensitizer (TLD1433) is currently in clinical phase II trial¹³, to alleviate the phototoxicity issues experienced with red light PDT using photofrin at the end of the 1990s.⁶² Recently, Lilge's group reported a method to formulate TLD1433 with transferrin, which improved molar extinction coefficients in the visible domain of the spectrum, ROS production by the photosensitizer, cellular uptake, and the *in vivo* PDT efficacy.⁶³ These results provide an inspiring example of how to further improve the photoactivity of cyclometalated PDT compounds such as **[1]**⁺.

In the present study, **[1]**⁺ stands out for two reasons. First, it is an excellent singlet oxygen generator under blue light irradiation, while **[2]**⁺ and **[3]**²⁺ have negligible absorption and singlet oxygen generation properties at such wavelengths. The bathochromically shifted absorbance of **[1]**⁺ is a consequence of the lower HOMO-LUMO gap in this compound due to (i) the presence and (ii) the position of the Pd-C bond with respect to the noncoordinated amine bridge.³⁶ The photodynamic properties of **[1]**⁺ were observed in both normoxic and hypoxic 2D cell monolayers, suggesting that **[1]**⁺ can serve for both PDT type II (normoxia) and type I (hypoxia). Second, the self-aggregation properties of **[1]**⁺ and **[2]**⁺ cause them efficiently penetrate into cancer cells via endocytosis where it is distributed to the cytoskeleton, while **[3]**²⁺ is taken up in smaller amounts and codistributed in the membranes and cytosol. These self-assembly properties are a direct consequence of the lower charge of the cyclometalated complexes, of their extended, flat aromatic ligand, of the presence of a palladium(II) atom in the center of the complexes, which generates Pd...Pd metallophilic interaction,^{43, 64, 65} and of the stabilization of the self-assembled nanorods in a biological medium by serum proteins. One should also note that although aggregation is often detrimental to the photodynamic properties of porphyrin sensitizers for example, with cyclometalated palladium compounds such as **[1]**⁺ self-assembly leads to nanostructures without quenching the blue-light photoreactivity. Of course, aggregation of the Pd complex as nanorods in the cell medium suggests that aggregation may also occur in the blood, and that sensitizer uptake by the tumor may partially rely on the enhanced permeability and retention (EPR) effect via the trans-endothelial pathways. However, at that stage these hypotheses remain speculations. Altogether, the excellent uptake, localization, and photodynamic properties of **[1]**⁺ make it an interesting blue-light-activated tumor killer not only in the 3D spheroid model, but also in 4T1 breast tumor xenografts in mice.

3.4 Conclusion

For metal-based anticancer drugs and photosensitizers, achieving cytotoxicity requires efficient cellular uptake. The most common method for increasing cellular uptake, which consists of increasing the lipophilicity of the compounds, allows for a better crossing of the lipophilic phospholipid bilayer of cells. Cyclometalation is one way to enhance the lipophilicity of metal complexes, and it almost systematically significantly improves cellular uptake. On the other hand, such a strategy is usually detrimental to the selectivity of the uptake, because healthy cells also have a membrane, too. Our work offers a new perspective on the effects of cyclometalation on cell uptake beyond a simple increase in molecular lipophilicity. First, the octanol-water partition coefficient ($\log P$) is always measured in the absence of serum protein, so similar $\log P$ values do not necessarily allow for predicting the solubility and aggregation properties of a drug candidate in cell growing medium or blood. Second, when the balance between hydrophobicity and self-assembly properties is just right, cyclometalated complexes such as palladium complexes **[1]**⁺ and **[2]**⁺ can generate nanoaggregates. Our results unambiguously demonstrate that the colloidal stability of these aggregates critically depends on the presence of the protein component (FCS) of the cell-growth medium and that in the presence of serum, cellular uptake *in vitro* is greatly enhanced, compared to that of nonaggregated compounds such as **[3]**²⁺. Endocytosis probably plays a critical role here; however, it should be noted that the compound was finally detected in the cytoskeleton rather than in the endosome or lysosome, which suggests that the supramolecular nature of the interaction responsible for the aggregation (*i.e.*, Pd...Pd metallophilic interaction) may be reversible in the cell and allow for the compound to escape the endocytic pathway. Protein-controlled self-assembly in aqueous solution via Pd...Pd metallophilic interaction has not been documented before. It suggests that (pro)drug self-assembly in serum may offer straightforward strategies for improving drug uptake without a sophisticated drug delivery system and that such strategies may work not only *in vitro*, but also *in vivo*.

3.5 Experimental Section

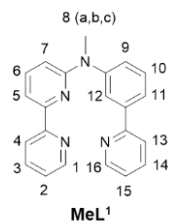
3.5.1 Compounds preparations. The starting materials and precursors **HL**¹-**HL**³ were prepared according to literature methods.³⁶ The preparation details of ligands **MeL**¹, **MeL**², and **MeL**³ and corresponding metal complexes **[PdMeL**¹]**OAc** (**[1]**⁺), **[PdMeL**²]**OAc** (**[2]**⁺), and **[PdMeL**³](**OAc**)₂ (**[3]**²⁺) are given in the below. All solvents and reagents were purchased from commercial vendors and used without purification. All synthesis was performed in a dinitrogen atmosphere. The metal complexes were synthesized and purified without column

chromatography in high yields. In the subsequent report, the complexes are all in the CH_3COO^- counterion unless otherwise specified.

3.5.1.1 Synthesis of ligand MeL^1 , MeL^2 , and MeL^3

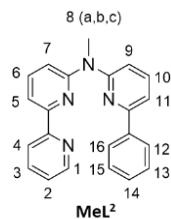
The three ligands were synthesized in the same reaction conditions. The synthesis of MeL^1 is described in detail below as an example.

MeL^1



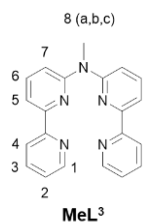
A mixture of its precursor HL^1 (324.0 mg, 1.0 mmol), KOtBu (448.4 mg, 2.0 mmol), and CH_3I (282.0 mg, 0.1 mL, 2.0 mmol), was dissolved in DMF (10 mL) and stirred for 24 h at room temperature under an N_2 atmosphere. Then the reaction solution was extracted with ethyl acetate (EtOAc) and water. NH_4Cl was added to the extracting solution for a good separation of the two layers. The crude product collected from the EtOAc layer was purified by silica gel chromatography using Pentane: EtOAc 4:1 ($R_f = 0.25$) to 2:1 ($R_f = 0.35$) as eluents. MeL^1 was obtained in 47% yield (159.0 mg, 0.47 mmol). **ESI-MS** (cation): m/z calcd 339.2 ($\text{C}_{22}\text{H}_{18}\text{N}_4 + \text{H}^+$), obsd 339.2; **^1H NMR** (400 MHz, Methanol- d_4) δ 8.58 (2 H, dddd, $J = 9.6, 4.9, 1.8, 0.9$ Hz, $\text{H}^1, \text{H}^{12}$), 8.39 (1 H, dq, $J = 8.0, 0.9$ Hz, H^4), 7.92 (1 H, t, $J = 2.0$ Hz, H^{15}), 7.90 – 7.82 (3 H, m, $\text{H}^{16}, \text{H}^3, \text{H}^{14}$), 7.80 (1 H, ddd, $J = 7.7, 1.8, 1.0$ Hz, H^{13}), 7.63 (1 H, dd, $J = 7.4, 0.8$ Hz, H^9), 7.59 – 7.47 (2 H, m, $\text{H}^6, \text{H}^{11}$), 7.43 – 7.27 (3 H, m, $\text{H}^2, \text{H}^5, \text{H}^{10}$), 6.67 (1 H, dt, $J = 8.5, 0.7$ Hz, H^7), 3.61 (3 H, d, $J = 0.6$, H^8). **^{13}C APT-NMR** (101 MHz, Methanol- d_4) δ 159.6, 158.3, 158.1, 154.8, 150.4, 149.7, 148.8, 142.1, 139.0, 138.9, 138.6, 131.2, 128.0, 126.0, 125.2, 124.9, 124.0, 122.7, 122.6, 111.6, 110.7, 38.8.

MeL^2



This ligand was collected from the EtOAc layer and purified by silica gel chromatography using Pentane: EtOAc 4:1 ($R_f = 0.25$) to 2:1 ($R_f = 0.35$) as eluents. Yield 143.4 mg, 0.42 mmol, 42%; **ESI-MS** (cation): m/z calcd 339.2 ($\text{C}_{22}\text{H}_{18}\text{N}_4 + \text{H}^+$), obsd 339.2; **^1H NMR** (300 MHz, Methanol- d_4) 8.62 (1 H, d, $J = 4.9$ Hz, H^1), 8.38 (1 H, d, $J = 8.0$ Hz, H^5), 8.12 – 7.99 (2 H, m, $\text{H}^{12}, \text{H}^{15}$), 7.99 – 7.85 (2 H, m, H^3, H^6), 7.77 (2 H, td, $J = 8.1, 6.8$ Hz, $\text{H}^4, \text{H}^{10}$), 7.53 – 7.33 (6 H, m, $\text{H}^{14}, \text{H}^{13}, \text{H}^{15}, \text{H}^2, \text{H}^{11}, \text{H}^7$), 7.27 (1 H, d, $J = 8.2$ Hz, H^9), 3.79 (3 H, d, $J = 1.7$ Hz, H^8); **^{13}C APT-NMR** (75 MHz, Methanol- d_4) δ 149.9, 139.6, 139.3, 138.7, 128.0, 129.7, 127.8, 125.1, 122.7, 115.6, 114.9, 114.9, 114.4, 36.5.

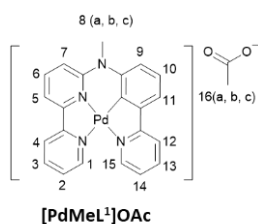
MeL^3



This ligand was purified by alumina column chromatography with eluent Pentane:EtOAc (20:3, R_f = 0.3). Yield 56 mg, 0.17 mmol, 97%; **ESI-MS** (cation): m/z calcd 340.2 ($C_{22}H_{18}N_4 + H^+$), obsd 340.3; **1H NMR** (400 MHz, Methanol- d_4) 8.64 – 8.59 (2 H, m, H^1), 8.36 (2 H, dt, J = 8.0, 1.1 Hz, H^4), 7.94 – 7.88 (4 H, m, H^5 , H^3), 7.80 (2 H, dd, J = 8.3, 7.5 Hz, H^6), 7.44 – 7.34 (4 H, m, H^2 , H^7), 3.80 (3 H, s, H^8). **^{13}C APT-NMR** (101 MHz, Methanol- d_4) δ 157.2, 156.1, 153.9, 148.6, 138.1, 137.3, 123.7, 121.2, 114.5, 113.8, 113.3, 35.0.

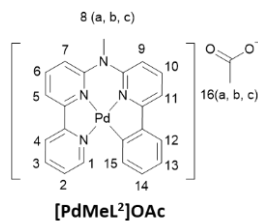
3.5.1.2 Synthesis of palladium complexes

[PdMeL¹]OAc ([1]OAc)



A mixture of ligand **MeL¹** (67.6 mg, 0.20 mmol) and $Pd(OAc)_2$ (44.4 mg, 0.20 mmol) was dissolved in CH_3COOH (50 mL) and heating at 135 °C on N_2 atmosphere for 24 h. The solvent was rotary evaporated to obtain a yellow solid, which was washed with EtOAc (50 mL) and ether (30 mL), and dried under vacuum, to finally obtain (**1**)OAc as analytically pure product (Yield: 86 mg, 0.17 mmol, 86%). **HRMS** (cation): m/z calcd 443.0488 [$C_{22}H_{17}N_4Pd]^+$, obsd 443.0493. **1H NMR** (300 MHz, Methanol- d_4) 8.55 (1 H, d, J = 5.4 Hz, H^1), 8.35 (2 H, t, J = 8.3 Hz, H^4 , H^{15}), 8.18 (1 H, td, J = 8.0, 1.5 Hz, H^3), 8.05 – 7.93 (2 H, m, H^6 , H^{13}), 7.88 (2 H, td, J = 7.4, 1.3 Hz, H^5 , H^{12}), 7.69 (1 H, ddd, J = 7.3, 5.6, 1.2 Hz, H^2), 7.45 – 7.30 (3 H, m, H^7 , H^{11} , H^{14}), 7.25 (1 H, t, J = 7.8 Hz, H^{10}), 7.07 (1 H, dd, J = 8.4, 1.0 Hz, H^9), 3.59 (3 H, s, H^8), 1.90 (3 H, s, H^{16}). **^{13}C APT-NMR** (75 MHz, Methanol- d_4) δ 150.3, 149.4, 141.6, 141.4, 140.4, 124.8, 124.8, 121.5, 120.6, 119.7, 118.3, 116.3, 42.1. Elemental analysis calcd for [**1**]OAc + 6H₂O: C, 47.18; H, 5.28; N, 9.17; Found for [**1**]OAc + 6H₂O: 47.20, 5.22, 9.35.

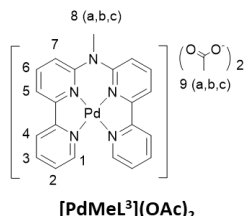
[PdMeL²]OAc ([2]OAc)



[2]OAc was synthesized using the same method as for **[2]OAc**, but starting from ligand **MeL²** (67.6 mg, 0.2 mmol). The yield in **[2]OAc** was 88% (88.7 mg, 0.18 mmol). **HRMS** (cation): m/z calcd 443.0488 [$C_{22}H_{17}N_4Pd]^+$, obsd 443.0490. **1H NMR** (400 MHz, Methanol- d_4) 8.73 (1 H, dd, J = 5.9, 1.4 Hz, H^1), 8.39 – 8.32 (1 H, m, H^4), 8.22 (1 H, td, J = 7.8, 1.5 Hz, H^3), 8.18 – 8.10 (1 H, m, H^6), 8.01 (1 H, d, J = 7.7 Hz, H^5), 7.95 (1 H, t, J = 8.1 Hz, H^{10}), 7.67 (1 H, ddd, J = 7.3, 5.6, 1.4 Hz, H^2), 7.55 (2 H, dd, J = 11.6, 8.1 Hz, H^7 , H^{11}), 7.52 – 7.48 (1 H, m, H^{14}), 7.20 (1 H, d, J = 8.5 Hz, H^9), 7.17 – 7.09 (3 H, m, H^{15} , H^{13} , H^{12}), 3.61 (3 H,

s, H⁸), 1.90 (3 H, s, H¹⁶). **¹³C APT-NMR** (101 MHz, Methanol-*d*₄) δ 165.0, 158.0, 156.5, 152.7, 152.0, 151.8, 151.1, 142.2, 141.8, 141.7, 132.1, 130.5, 128.2, 127.0, 125.8, 125.3, 118.6, 118.1, 115.0, 114.7, 43.6. Elemental analysis calcd for [2]OAc + 2H₂O: C, 53.49; H, 4.49; N, 10.40; Found for [2]OAc + 2H₂O: 53.46, 4.53, 10.38.

[PdMeL³](OAc)₂ ([3](OAc)₂)



The mixture of ligand **MeL³** (23.3 mg, 0.065 mmol) and Pd(OAc)₂ (25.6 mg, 0.065 mmol) was dissolved in MeOH and heated at 65 °C under an N₂ atmosphere for 24 h. The solvent was rotary evaporated to obtain a yellow solid, which was washed with EtOAc (50 mL) and ether (30 mL), dried in vacuum to obtain [3](OAc)₂ as analytically pure product (Yield: 29.3

mg, 0.054 mmol, 80%). **HRMS** (cation): *m/z* calcd 222.5254 [C₂₁H₁₇N₃Pd]²⁺, obsd 222.5255. **¹H NMR** (400 MHz, Methanol-*d*₄) 9.03 (2 H, d, *J* = 5.8 Hz, H¹), 8.75 (2 H, d, *J* = 8.1 Hz, H⁴), 8.52 (6 H, dt, *J* = 16.2, 7.5 Hz, H³, H⁵, H⁶), 8.04 (4 H, dd, *J* = 8.3, 5.2 Hz, H⁷, H²), 4.08 (3 H, s, H⁸), 1.87 (6 H, s, H⁹). **¹³C APT-NMR** (101 MHz, Methanol-*d*₄) δ 158.3, 155.4, 152.2, 151.2, 144.1, 143.8, 129.4, 125.9, 120.4, 119.9, 44.1. Elemental analysis calcd for [3](OAc)₂ + 8H₂O: C, 42.41; H, 5.55; N, 9.89; Found for [3](OAc)₂ + 8H₂O: 42.63, 4.92, 9.98.

3.5.2 Partition coefficients (log P_{ow}) determination. The partition coefficients of palladium complexes were determined by the shake-flask method. In brief, the palladium complexes were dissolved in octanol-saturated water and ultrasonicated for 1 h to prepare 1 mM stock solutions. After filtering with a 0.2 μM membrane filter, aliquots of the stock solutions (0.2 mL) were transferred per duplicate to 15 mL centrifuge tubes and diluted up to 1 mL using octanol-saturated water. Then, 1 mL of water-saturated octanol was added to one of the tubes and the mixtures were shaken in an IKA Vibrax shaker for 24 h at 2200 pm. The mixture was centrifuged for 20 min at 4300 rpm to separate the water phase. An aliquot of the water phase (0.4 mL) was first mixed with 0.8 mL of 65% HNO₃ and then diluted with Milli-Q water (4.8 mL) to make 8.7% HNO₃ solution (6 mL). The palladium content of these samples was determined by ICP-OES using a Vista-MPX CCD simultaneous ICP-OES. Partition coefficient log P_{ow} was calculated using the equation below,

$$\log P_{ow} = \log ([Pd]_{oct}/[Pd]_{aq}) = \log ([Pd]_{total} - [Pd]_{aq})/[Pd]_{aq}$$

where [Pd]_{total} is the concentration of palladium in the control sample (where no water-saturated octanol was added) and [Pd]_{aq} is the concentration of palladium in the aqueous layer.

3.5.3 Single-crystal X-ray diffraction. The CH_3COO^- counterion of $[\mathbf{1}]^+$ and $[\mathbf{2}]^+$ was changed to PF_6^- ion by adding excess KPF_6 to a water solution of the acetato metal complexes, to obtain a precipitate of $[\mathbf{1}]\text{PF}_6$ and $[\mathbf{2}]\text{PF}_6$ that was filtered off and dried. The single crystals suitable for X-ray structure determination were obtained for $[\mathbf{1}]\text{PF}_6$ and $[\mathbf{2}]\text{PF}_6$ via slow evaporation of a solution of the metal complex (PF_6^- counterion) in a MeCN/EtOAc mixture (2:1). Single crystals of $[\mathbf{3}]\text{BF}_4$ were obtained via vapor diffusion from diethyl ether to a MeCN/EtOAc solution of $[\mathbf{3}](\text{OAc})_2$ containing HBF_4 . All reflection intensities were measured at 110(2) K using a SuperNova diffractometer (equipped with an Atlas detector) with Mo $K\alpha$ radiation ($\lambda = 0.71073 \text{ \AA}$) for $[\mathbf{1}]\text{PF}_6$ and $[\mathbf{3}](\text{BF}_4)_2$ and with Cu $K\alpha$ radiation ($\lambda = 1.54178 \text{ \AA}$) for $[\mathbf{2}]\text{PF}_6$ via the program CrysAlisPro program (Version CrysAlisPro 1.171.39.29c, Rigaku OD, 2017). The same program was used to refine the cell dimensions and reduce the data. The structure was solved with the SHELXS-2018/3 program (Sheldrick, 2018) and was refined on F^2 with SHELXL-2018/3 (Sheldrick, 2018). Numerical absorption correction based on Gaussian integration over a multifaceted crystal model was performed using CrysAlisPro. The temperature of the data collection was controlled using the Cryojet system (manufactured by Oxford Instruments). The H atoms were placed at calculated positions (unless otherwise specified) using the AFIX 43 or AFIX 137 instructions with isotropic displacement parameters having value of 1.2 or 1.5 U_{eq} for the attached C atoms. For $[\mathbf{2}]\text{PF}_6$, the H atoms attached to N1 and N21 were found from different Fourier maps, and their coordinates were refined pseudofreely. The H1...H21 distance was set to be found within an acceptable range ($> 1.9 \text{ \AA}$) using the DFIX instructions.

3.5.4 Photophysical properties measurements. Absorption spectra of complexes were recorded on a Cary 50 spectrometer from Varian. The emission spectra and relative phosphorescence quantum yields of metal complexes in aerated water were obtained *via* a FLS900 spectrometer from Edinburgh Instruments Ltd. The phosphorescence lifetime of complexes in aerated water was measured by LifeSpec-II from Edinburgh Instruments, with an excitation source of a 375 nm pulsed diode laser (pulse width $< 90 \text{ ps}$). The relative singlet oxygen quantum yield (ϕ_{Δ}) of complexes was measured in deuterated methanol on a special custom-built setup described previously, with $[\text{Ru}(\text{bpy})_3]\text{Cl}_2$ (Tris(bipyridine)ruthenium(II) chloride) as the standard ($\phi_{\Delta} = 0.73$).^{44, 46}

3.5.5 Calculated values and TDDFT-Calculated spectra of metal complexes. The structures of complexes $[\mathbf{1}]^+$, $[\mathbf{2}]^+$, and $[\mathbf{3}]^{2+}$ were minimized by DFT at the PBE0/TZP level for all atoms including Pd, as implemented in the ADF2017 suite from SCM, using COSMO to simulate

solvent effects (in water), scalar relativistic effects for Pd, no frozen core, and starting from the X-ray structures of **[1]PF₆** and **[2]PF₆**. The 20 first singlet-to-singlet electronic transitions were also calculated with TDDFT using ADF2017 and at the same level of theory, using the Davidson method. Dimer **{[1]⁺}₂** was minimized at the same level of theory as monomer **[1]⁺**.

3.5.6 Aggregation of metal complexes in different aqueous solutions according to DLS.

DLS was chosen to determine the numbers and size of particles in complex solutions (5 and 50 μ M) in H₂O, PBS, Opti-MEM medium with and without FCS (fetal calf serum) proteins, via the ZEN1600 Zetasizer Nano instrument (Malvern Instruments Limited) operating with a 633 nm laser.

3.5.7 TEM measurement of metal complexes in different solutions. The TEM experiments were carried out with a TEM JEOL 1010:100 kV transmission electron microscope using Formvar/carbon-coated copper grid from Polysciences Inc. For the preparation of samples, each drop (15 μ L) of complex solution was deposited on parafilm. The grids were placed on top of the drops for 2 min and then the excess liquid on the grid was removed with filter paper and dried for 2 h for TEM measurement. The TEM measurements were carried out under vacuum conditions.

3.5.8 Cryo-TEM measurements. sample (6 μ L, [complex] = 50 μ M) was applied to a freshly glow-discharged carbon 200 mesh Cu grid (lacey carbon film, Electron Microscopy Sciences, Aurion, Wageningen, The Netherlands). Grids were blotted for 3 s at 99% humidity in a Vitrobot plunge-freezer (FEI VitrobotTM Mark III, Thermo Fisher Scientific). Cryo-TEM images were collected on a Talos L120C (NeCEN, Leiden University) operating at 120 kV. Images were recorded manually at a nominal magnification of 4300 \times or 13500 \times yielding a pixel size at the specimen of 29.9 or 5.9 Å, respectively.

3.5.9 Cell Culture. Cells were thawed and at least passaged twice before starting cytotoxicity experiments. For normoxia experiments cells were cultured in DMEM completed medium (Dulbecco's Modified Eagle Medium with phenol red, supplemented with 8.0% v/v fetal calf serum (FCS), 0.2% v/v penicillin/streptomycin (P/S), and 1% v/v glutamine), under humidified normoxic conditions (37 °C atmosphere, 21% O₂ and 7.0% CO₂) in 75 cm² flasks. They were subcultured upon reaching 70-80% confluence, approximately once per week. Cells were passaged never more than 8 weeks. For the cytotoxicity assay, Opti-MEM complete medium without phenol red was used, supplemented with 2.5% v/v fetal calf serum (FCS), 0.2% v/v penicillin/streptomycin (P/S), and 1% v/v glutamine). For hypoxia cytotoxicity experiments, cells were cultured in DMEM complete medium for at least two weeks in humidified hypoxic

conditions (37 °C atmosphere, 1.0% O₂ and 7.0% CO₂) before starting hypoxic cytotoxicity tests.

3.5.10 Photocytotoxicity assay. The working solutions of the three complexes were typically prepared from 1.0 mM stock solutions of the complex in distilled water. The cell irradiation system consists of a Ditabis thermostat (980923001) fitted with two flat-bottomed microplate thermoblocks (800010600) and a 96-LED array fitted to a standard 96-well plate. The 455 nm LED (FNL-U501B22WCSL), fans (40 mm, 24 V DC, 9714839), and power supply (EA-PS 2042-06B) were ordered from Farnell. A full description of the cell irradiation setup is given in Hopkins et al.⁶⁶ The photocytotoxicity assay was carried out via the sulforhodamine B (SRB) assay reports previously.⁶⁷ Briefly, a certain number of cells (5000 cells for A549, 8000 cells for A431) were seeded in 96-well plates at $t = 0$ in a volume of 100 μ L of Opti-MEM complete medium without phenol red and incubated for 24 h under normoxic (21% O₂) or hypoxic (1% O₂) conditions. The cells were treated with a freshly prepared solution of the complexes in Opti-MEM at different concentrations in triplicate on the same plates at $t = 24$ h. The concentrations of complexes were tuned depending on their cytotoxicity. At $t = 48$ h, the irradiation plates were irradiated with blue light under normoxic (455 nm, 5 min, 5.66 mW cm⁻², 1.7 J cm⁻²) or hypoxic (455 nm, 8 min, 3.54 mW cm⁻², 1.7 J cm⁻²) conditions, while the dark plates were kept nonirradiated. After light irradiation, all plates were incubated in the dark for another 48 h under normoxic or hypoxic conditions, respectively. Then, the cells in each well were fixed with trichloroacetic acid (TCA, 10% w/v), gently washed with distilled water, and stained with 100 μ L of SRB (0.6% w/v in 1% v/v acetic acid/H₂O solution). The SRB dye was then solubilized with Tris base (10 mM, 200 μ L) and the absorbance in each well was read at 510 nm using a M1000 Tecan Reader. Three independent biological replicates were completed for each cell line. The obtained data were analyzed with Graphpad Prism 5 using the dose-response two-parameter Hill-slope equation 1 to obtain the half-maximal effective concentrations EC₅₀ (defined as the concentration of drug that gives a half-maximum effect).

$$100/(1 + 10^{\log_{10}EC_{50}-X) \times Hill\ Slope}) \quad \text{Equation 1}$$

3.5.11 Cellular uptake inhibition. A549 cells (5×10^5 cells) were seeded in six-well plates, incubated for 24 h under normoxic conditions, and then treated with NaN₃ (active uptake inhibitor, 15.4 mM) or dynasore (dynamin-dependent endocytosis inhibitor, 80 μ M) for 1 h; after that, the cells were incubated with one of the three palladium complexes (5 μ M) for 3 h. To remove the surface-bound drug, the cells were first washed three times using ice-cold PBS. Then the cells were counted via a cell-counting board three times, collected by centrifugation,

and 7 mL of cell lysis buffer (RIPA Lysis and Extraction Buffer, Thermo Scientific™) was added. Ultrasonication was then realized for 3 h at 37 °C to afford clear samples. If precipitation was still observed, HNO₃ (65 % 1 mL) was added to the samples, and the sample was heated for 6 h at 100 °C with a parafilm on the top to prevent solution evaporation. Once back at room temperature, each sample was then diluted with Milli-Q water to reach a volume of 10 mL; this solution was finally injected into a PerkinElmer NexION 2000 ICP-MS to measure the Pd concentration.

3.5.12 Cellular uptake and localization. A549 cells (5×10^5 cells) were seeded in T-75 flasks, incubated for 24 h in Optimum medium at 37 °C under 5% CO₂, and then treated with complexes [1]OAc–[3](OAc)₂ (1 μM, 15 mL), and the control groups were treated with equal volumes of medium. After 24 h of incubation under normoxic conditions, the cells were washed with ice-cold PBS (20 mL) three times and then collected in a 15 mL centrifuge tube and diluted to 10 mL with ice-cold PBS. Then the cells were counted via a cell-counting board three times. Then the Pd contents of the cells were determined by ICP-MS using the same protocol as described above. For cellular fractionation, a FractionPREP Cell Fractionation Kit was used according to the supplier's instructions to prepare the cytosol, membranes, nucleus, and cytoskeleton fractions using the other half of the cell lysis solution. The samples in each fraction were used directly to detect the Pd content by ICP-MS

3.5.13 Measurement of intracellular ROS. The generation of ROS (reactive oxygen species) in A549 cells was measured using the ROS fluorescence indicator, 2,7-dichlorodihydrofluorescein diacetate (DCFH-DA).¹⁹ After acetate cleavage by cellular esterases DCFH-DA can be oxidized by ROS to dichlorofluorescein (DCF), which exhibits strong green fluorescence that can be detected by a fluorescent microscopy or flow cytometry. A549 cells (1×10^5) were seeded into 24-well plates and incubated for 6 h in the dark. The cells were then treated with 5 μM complexes and labeled as dark or blue light groups. After 24 h incubation under normoxia, the medium was refreshed, and the cells were treated with DCFH-DA (20 μM) for 30 min at 37 °C. After that, the blue light group was irradiated with 455 nm blue light for 5 min (5.66 mW cm^{-2} , 1.7 J cm^{-2}). Then the cells were washed with PBS twice, harvested, and centrifuged (3 min \times 2000 rpm) to remove supernatant. The cells were resuspended in 200 μL PBS per well in 96-well plate. Untreated cells were maintained as negative controls, whereas a 400 μM H₂O₂ solution in Opti-MEM complete was administered to another set of three wells for 1 h as a positive control for ROS. The levels of intracellular ROS were examined using the Guava easyCyte HT flow cytometer. Gates were applied over

forward scattering, side scattering, and forward scattering area measurements when possible to remove cellular debris and select only for singlet whole cells for further statistical analysis. The GRN-B parameter (488 nm excitation, 525/30 nm emission) was used for fluorescence measurements given its close proximity to the known excitation/emission wavelengths of DCF (498/522 nm, respectively). All flow cytometry data were processed using FlowJo10.

3.5.14 Apoptosis determination. The apoptosis of A549 cells induced by metal complexes was determined with an Annexin V-FITC/propidium iodide double-staining assay. The assay was performed according to the manufacturer's (Bio-Connect BV) protocol. A549 cells were seeded in 6-well plates with 2 mL of Opti-MEM complete medium (2×10^5 cells/well), incubated for 6 h, then treated with the three complexes (15 μ M) and cisplatin (15 μ M) for 24 h in the dark and under normoxia. Then one plate treated with complexes was irradiated for 5 min with 455 nm blue light (5.66 mW cm⁻², 1.7 J cm⁻²), named as the blue light group. The cells were all further incubated in the dark for 24 h under normoxia, after which cells were harvested and then resuspended in 200 μ L 1 \times annexin binding buffer (purchased from Sanbio B.V.). The resulting cell suspension (200 μ L) was stained with 5 μ L of Annexin-V-FITC and 5 μ L of propidium iodide (purchased from Sanbio B.V) for 15 min at room temperature in the dark, and then detected by flow cytometry immediately. GRN-B Parameter (488 nm excitation, 525 \pm 30 nm emission) and RED-B Parameter (488 nm excitation, 661 \pm 15 nm emission) were used for fluorescence measurements given their proximity to the known excitation/emission wavelengths of Annexin V-FITC (494/518 nm) and propidium iodide (535/617 nm). All flow cytometry data were processed using FlowJo10.

3.5.15 3D tumor spheroids viability assay. The cytotoxicity of complex [1]⁺ in 3D tumor spheroids was determined with a CellTiter-Glo 3D cell viability assay.⁵⁷ A549 cells (500 cells/200 μ L per well) were added to a 96-well round-bottomed Corning spheroid plate microplate and centrifuged for 6 min at 800 g to produce tiny tumor spheroid cores that were incubated under normoxia for 120 h to generate 3D tumor spheroids (658 \pm 52 μ m diameter). At $t = 120$ h, 100 μ L of medium was carefully pipetted out from each well while avoiding the pipetting of spheroids; then the spheroids were immediately treated with 100 μ L of an Opti-MEM complete medium solution of complex [1]⁺ with a range of concentrations to reach final concentrations in the wells of 0, 2, 10, 20, 40, 100, and 200 μ M. Each concentration was repeated in technical triplicate on the same plate. The spheroids were incubated further under normoxia. At $t = 144$ h, one plate was irradiated with blue light under air (455 nm, 10 min, 3.48 mW cm⁻², 2.1 J cm⁻²), and the other was left in the dark in a normoxic incubator. The spheroids

were further incubated under normoxia in the dark. At $t = 192$ h, a CellTiter Glo 3D solution (100 μL /well) was added to each well to stain the 3D tumor spheroids. After 30 min of shaking on an IKA Vibrax shaker at 500 rpm at room temperature, the luminescence in each well was measured with a Tecan microplate reader. Half-maximal effective concentrations (EC_{50}) for 3D tumor spheroid growth inhibition were calculated by fitting the CellTiter Glo3D dose-response curves using the same non-linear regression function as in 2D (Equation 1) as implemented in Graphpad Prism 5.

3.5.16 *In vivo* experiments. Tumor-bearing female BALB/c mice were originally purchased from Vital River Laboratory Animal Center (Beijing, China). The mice were kept under specific pathogen-free conditions with free access to standard food and water. This study was conducted in accordance with the Guide for the Care and Use of Laboratory Animals published by the U.S. National Institutes of Health (8th edition, 2011). All protocols for animal studies conformed to the Guide for the Care and Use of Laboratory Animals. All animal experiments were performed following guidelines approved by the ethics committee of Peking University. The tumor model was established by injecting 1×10^7 of 4T1 breast cells suspended in 100 μL of PBS into the right flank region of each mouse to obtain a mouse 4T1 breast tumor implant. The tumor volume (V) can be calculated with equation $V = L/2 \times W^2$ after measuring the tumor length (L) and width (W) using a vernier caliper.⁶⁸ The mice were randomly divided into six groups (control, 450 nm light, [1]⁺ dark, [2]⁺ dark, [1]⁺ + 450 nm light, and [2]⁺ + 450 nm light groups) when the tumor volume reached about 40 mm^3 . The mice were treated through paracancerous injection with saline (control and 450 nm light groups), [1]⁺ (40 μM , 100 μL , 0.01 mg/kg) and [2]⁺ (40 μM , 100 μL , 0.01 mg/kg). One hour after injection, 450 nm irradiation (50 mW cm^{-2} , 20 min, 60 J cm^{-2}) was then carried out in 450 nm irradiation, [1]⁺ + 450 nm, and [2]⁺ + 450 nm groups. The tumor volume and body weight of each mouse were measured and recorded, and the average tumor volume and body weight were calculated ($N=3$) over a period of 10 days.

3.6 References

1. P. Štarha, J. Vančo and Z. Trávníček, *Coord. Chem. Rev.*, 2019, **380**, 103-135.
2. S. Dilruba and G. V. Kalayda, *Cancer Chemother. Pharmacol.*, 2016, **77**, 1103-1124.
3. X. Wang and Z. Guo, *Chem. Soc. Rev.*, 2013, **42**, 202-224.
4. R. J. Browning, P. J. T. Reardon, M. Parhizkar, R. B. Pedley, M. Edirisinghe, J. C. Knowles and E. Stride, *ACS Nano*, 2017, **11**, 8560-8578.
5. S. Dasari and P. B. Tchounwou, *Eur. J. Pharmacol.*, 2014, **740**, 364-378.
6. B. Li, Z. Meng, Q. Li, X. Huang, Z. Kang, H. Dong, J. Chen, J. Sun, Y. Dong, J. Li, X. Jia, J. L. Sessler, Q. Meng and C. Li, *Chem. Sci.*, 2017, **8**, 4458-4464.
7. K. S. Lovejoy and S. J. Lippard, *Dalton Trans.*, 2009, 10651-10659.

8. E. Petruzzella, R. Sirota, I. Solazzo, V. Gandin and D. Gibson, *Chem. Sci.*, 2018, **9**, 4299-4307.
9. R. Oun, Y. E. Moussa and N. J. Wheate, *Dalton Trans.*, 2018, **47**, 6645-6653.
10. L. Galluzzi, L. Senovilla, I. Vitale, J. Michels, I. Martins, O. Kepp, M. Castedo and G. Kroemer, *Oncogene*, 2012, **31**, 1869-1883.
11. J. N. Liu, W. Bu and J. Shi, *Chem. Rev.*, 2017, **117**, 6160-6224.
12. S. Mallidi, S. Anbil, A. L. Bulin, G. Obaid, M. Ichikawa and T. Hasan, *Theranostics*, 2016, **6**, 2458-2487.
13. S. Monro, K. L. Colon, H. Yin, J. Roque, 3rd, P. Konda, S. Gujar, R. P. Thummel, L. Lilge, C. G. Cameron and S. A. McFarland, *Chem. Rev.*, 2019, **119**, 797-828.
14. A. P. Castano, T. N. Demidova and M. R. Hamblin, *Photodiagn. Photodyn. Ther.*, 2004, **1**, 279-293.
15. P. Agostinis, K. Berg, K. A. Cengel, T. H. Foster, A. W. Girotti, S. O. Gollnick, S. M. Hahn, M. R. Hamblin, A. Juzeniene, D. Kessel, M. Korbelik, J. Moan, P. Mroz, D. Nowis, J. Piette, B. C. Wilson and J. Golab, *CA: Cancer J. Clin.*, 2011, **61**, 250-281.
16. T. He, C. Ren, Y. Luo, Q. Wang, J. Li, X. Lin, C. Ye, W. Hu and J. Zhang, *Chem. Sci.*, 2019, **10**, 4163-4168.
17. T. L. Lam, K. C. Tong, C. Yang, W. L. Kwong, X. Guan, M. D. Li, V. Kar-Yan Lo, S. Lai-Fung Chan, D. Lee Phillips, C. N. Lok and C. M. Che, *Chem. Sci.*, 2019, **10**, 293-309.
18. Z. Dong, L. Feng, Y. Hao, M. Chen, M. Gao, Y. Chao, H. Zhao, W. Zhu, J. Liu, C. Liang, Q. Zhang and Z. Liu, *J. Am. Chem. Soc.*, 2018, **140**, 2165-2178.
19. Z. Lv, H. Wei, Q. Li, X. Su, S. Liu, K. Y. Zhang, W. Lv, Q. Zhao, X. Li and W. Huang, *Chem. Sci.*, 2018, **9**, 502-512.
20. H. Huang, P. Zhang, H. Chen, L. Ji and H. Chao, *Chem. Eur. J.*, 2015, **21**, 715-725.
21. F. Heinemann, J. Karges and G. Gasser, *Acc. Chem. Res.*, 2017, **50**, 2727-2736.
22. L. Salassa, *Eur. J. Inorg. Chem.*, 2011, **2011**, 4931-4947.
23. K. Arora, M. Herroon, M. H. Al-Afyouni, N. P. Toupin, T. N. Rohrabough, L. M. Loftus, I. Podgorski, C. Turro and J. J. Kodanko, *J. Am. Chem. Soc.*, 2018, **140**, 14367-14380.
24. T. J. Whittemore, A. Millet, H. J. Sayre, C. Xue, B. S. Dolinar, E. G. White, K. R. Dunbar and C. Turro, *J. Am. Chem. Soc.*, 2018, **140**, 5161-5170.
25. M. Clement, G. Daniel and M. Trelles, *J. Cosmet. Laser. Ther.*, 2005, **7**, 177-189.
26. G. Ghosh, K. L. Colon, A. Fuller, T. Sainuddin, E. Bradner, J. McCain, S. M. A. Monro, H. Yin, M. W. Hetu, C. G. Cameron and S. A. McFarland, *Inorg. Chem.*, 2018, **57**, 7694-7712.
27. A. Notaro, G. Gasser and A. Castonguay, *ChemMedChem*, 2020, **15**, 345-348.
28. J. L. Tsai, T. Zou, J. Liu, T. Chen, A. O. Chan, C. Yang, C. N. Lok and C. M. Che, *Chem. Sci.*, 2015, **6**, 3823-3830.
29. K. Suntharalingam, J. J. Wilson, W. Lin and S. J. Lippard, *Metallomics*, 2014, **6**, 437-443.
30. A. Wragg, M. R. Gill, L. McKenzie, C. Glover, R. Mowll, J. A. Weinstein, X. Su, C. Smythe and J. A. Thomas, *Chem. Eur. J.*, 2015, **21**, 11865-11871.
31. C. N. Lok, T. Zou, J. J. Zhang, I. W. Lin and C. M. Che, *Adv. Mater.*, 2014, **26**, 5550-5557.
32. K. Qiu, Y. Chen, T. W. Rees, L. Ji and H. Chao, *Coord. Chem. Rev.*, 2019, **378**, 66-86.
33. P. Wu, E. L. Wong, D. L. Ma, G. S. Tong, K. M. Ng and C. M. Che, *Chem. Eur. J.*, 2009, **15**, 3652-3656.
34. L. Shang, K. Nienhaus and G. U. Nienhaus, *J. Nanobiotechnol.*, 2014, **12**, 1-11.
35. A.-R. Azzouzi, S. Vincendeau, E. Barret, A. Cicco, F. Kleinclauss, H. G. van der Poel, C. G. Stief, J. Rassweiler, G. Salomon, E. Solsona, A. Alcaraz, T. T. Tammela, D. J. Rosario, F. Gomez-Veiga, G. Ahlgren, F. Benzaghrou, B. Gaillac, B. Amzal, F. M. J. Debruyne, G. Fromont, C. Gratzke and M. Emberton, *Lancet Oncol.*, 2017, **18**, 181-191.
36. X. Q. Zhou, A. Busemann, M. S. Meijer, M. A. Siegler and S. Bonnet, *Chem. Comm.*, 2019, **55**, 4695-4698.
37. K. T. Chan, G. S. M. Tong, Q. Wan, G. Cheng, C. Yang and C. M. Che, *Chem. Asian J.*, 2017, **12**, 2104-2120.
38. J. M. Hope, J. J. Wilson and S. J. Lippard, *Dalton Trans.*, 2013, **42**, 3176-3180.
39. J.-L. Li, L. Jiang, B.-W. Wang, J.-L. Tian, W. Gu, X. Liu and S.-P. Yan, *New J. Chem.*, 2015, **39**, 529-538.
40. C. Zou, J. Lin, S. Suo, M. Xie, X. Chang and W. Lu, *Chem. Comm.*, 2018, **54**, 5319-5322.

41. A. Aliprandi, M. Mauro and L. De Cola, *Nat. Chem.*, 2016, **8**, 10-15.
42. Q. Wan, J. Xia, W. Lu, J. Yang and C. M. Che, *J. Am. Chem. Soc.*, 2019, **141**, 11572-11582.
43. X. Yin, S. A. Warren, Y. T. Pan, K. C. Tsao, D. L. Gray, J. Bertke and H. Yang, *Angew Chem. Int. Ed.*, 2014, **53**, 14087-14091.
44. M. C. DeRosa and R. J. Crutchley, *Coord. Chem. Rev.*, 2002, **233-234**, 351-371.
45. A. M. Brouwer, *Pure Appl. Chem.*, 2011, **83**, 2213-2228.
46. J. A. Cuello-Garibo, M. S. Meijer and S. Bonnet, *Chem. Comm.*, 2017, **53**, 6768-6771.
47. P. Swietach, R. D. Vaughan-Jones, A. L. Harris and A. Hulikova, *Philos. Trans. R. Soc. B*, 2014, **369**, 20130099.
48. J.-Y. Lee, M.-C. Tsai, P.-C. Chen, T.-T. Chen, K.-L. Chan, C.-Y. Lee and R.-K. Lee, *J. Phys. Chem. C*, 2015, **119**, 25754-25760.
49. S. Zhang, J. Li, G. Lykotrafitis, G. Bao and S. Suresh, *Adv. Mater.*, 2009, **21**, 419-424.
50. L. Kou, J. Sun, Y. Zhai and Z. He, *Asian J. Pharm. Sci.*, 2013, **8**, 1-10.
51. M. S. Meijer, V. S. Talens, M. F. Hilbers, R. E. Kieltyka, A. M. Brouwer, M. M. Natile and S. Bonnet, *Langmuir*, 2019, **35**, 12079-12090.
52. J. Karges, P. Goldner and G. Gasser, *Inorganics*, 2019, **7**.
53. J. Zhao and M. H. Stenzel, *Polym. Chem.*, 2018, **9**, 259-272.
54. J. Yang, J. Tu, G. E. M. Lamers, R. C. L. Olsthoorn and A. Kros, *Adv. Healthc. Mater.*, 2017, **6**.
55. P. Mroz, A. Yaroslavsky, G. B. Kharkwal and M. R. Hamblin, *Cancers*, 2011, **3**, 2516-2539.
56. G. Lazzari, P. Couvreur and S. Mura, *Polym. Chem.*, 2017, **8**, 4947-4969.
57. M. Zanoni, F. Piccinini, C. Arienti, A. Zamagni, S. Santi, R. Polico, A. Bevilacqua and A. Tesei, *Sci. Rep.*, 2016, **6**, 19103.
58. E. V. Maytin, U. Kaw, M. Ilyas, J. A. Mack and B. Hu, *Photodiagn. Photodyn. Ther.*, 2018, **22**, 7-13.
59. P. Gholam, I. Bosselmann, A. Enk and C. Fink, *J. Dtsch. Dermatol. Ges.*, 2018, **16**, 711-717.
60. P. Oltulu, B. Ince, N. Kokbudak, S. Findik and F. Kilinc, *Turk. J. Plast. Surg.*, 2018, **26**.
61. C. Ash, M. Dubec, K. Donne and T. Bashford, *Lasers Med. Sci.*, 2017, **32**, 1909-1918.
62. H. Zheng, *Technol. Cancer Res. T.*, 2005, **4**, 283-293.
63. P. Kaspler, S. Lazic, S. Forward, Y. Arenas, A. Mandel and L. Lilge, *Photochem. Photobiol. Sci.*, 2016, **15**, 481-495.
64. Q. Wan, W. P. To, C. Yang and C. M. Che, *Angew Chem. Int. Ed.*, 2018, **57**, 3089-3093.
65. M. Wehner and F. Würthner, *Nat. Rev. Chem.*, 2019, **4**, 38-53.
66. S. L. Hopkins, B. Siewert, S. H. Askes, P. Veldhuizen, R. Zwier, M. Heger and S. Bonnet, *Photochem. Photobiol. Sci.*, 2016, **15**, 644-653.
67. V. Vichai and K. Kirtikara, *Nat. Protoc.*, 2006, **1**, 1112-1116.
68. W. Sun, J. Fan, S. Wang, Y. Kang, J. Du and X. Peng, *ACS Appl. Mater. Interfaces*, 2018, **10**, 7832-7840.

4

Intracellular dynamic assembly of deep-red emitting supramolecular nanostructures based on Pt...Pt metallophilic interaction

Many nanoparticle drug delivery systems end up in the endosome or lysosome because they are made of covalent or kinetically trapped self-assembled systems (e.g. liposomes) that cannot escape the membrane of the endo-lysosomal intracellular vesicles after endocytic uptake. To be able to reach other organelles, nanoparticles would hence need to either be made from a kinetically labile interaction that allows re-assembly of the nanoparticles inside the cell following uptake, or, to be taken up by a mechanism that short-circuits the classical endocytosis pathway. In this work, we studied the intracellular fate of nanorods generated by self-assembly via the Pt...Pt metallophilic interaction of cyclometalated platinum(II) compounds. Outside cells, these deep-red emissive nanostructures (638 nm excitation, ~ 700 nm emission) are stabilized by proteins in cell medium. Once in contact with A549 lung cancer cells, they cross the cell membrane via dynamin- and clathrin-dependent endocytosis. However, time-dependent confocal colocalization and cellular electron microscopy demonstrated that they directly move to the mitochondria without passing by the lysosomes. Altogether, this study suggests that the Pt...Pt interaction is strong enough to generate emissive, aggregated nanoparticles inside the cell, but labile enough to allow these nanostructures to reach the mitochondria without being trapped, or passing by, the lysosomes. These findings open a new venue for the development of supramolecular theranostic nanoplatforms based on the Pt...Pt interaction.

This chapter has been submitted as a full paper: X-Q Zhou, M. Mytiliniou, J. Hilgendorf, Y. Zeng, P. Papadopoulou, Y. Shao, E. Bos, M. A. Siegler, F. Buda, A. Kros, R. I. Koning, D. Heinrich, S. Bonnet*, **Advanced Materials**.

4.1 Introduction

The metallophilic M...M interaction, which is based on d orbital overlap, has been described for planar d^8 and d^{10} metals, such as gold(I), nickel(II), palladium(II) and platinum(II) complexes.¹⁻⁴ It affords fascinating supramolecular aggregated systems with unique optical or properties such as “organic” light-emitting diodes or biosensors.⁵⁻¹² The emissive properties arising when the Pt...Pt interaction takes place are attributed to low-energy metal-metal-to-ligand charge-transfer (MMLCT) or ligand-to-metal-metal charge-transfer (LMMCT) transitions, which also generate good absorbance in the visible region of the spectrum.^{11, 13} These bands are attributed to the low HOMO-LUMO gap arising when platinum(II) centers come close enough for their d_{z^2} orbitals to interact; this interaction is typically facilitated by π - π stacking of the ligands bound to platinum, which counter-balance the electrostatic repulsion exerted by the positively charged metal centers.¹⁴ Overall, red light absorbance and deep-red luminescence are both particularly important for intracellular imaging and phototherapeutic compounds, where light penetration of tissues is critical.^{15, 16}

Independently from their ability to engage in metallophilic interaction, phosphorescent platinum complexes show several advantages for live-cell imaging, compared with organic dyes, such as large Stokes shift, reduced photobleaching, and long excited state lifetimes.^{6, 17-21} In parallel, the clinical success of cisplatin has stimulated research towards new platinum-based anticancer drugs and bioinorganic applications of platinum-organic compounds.²²⁻²⁴ Many reports focus on pincer-like platinum complexes based on tridentate polypyridyl ligands because of their tunable photophysical properties, the existence of various mechanisms inducing cytotoxicity, and supramolecular assembly derived from the Pt...Pt metallophilic interaction.^{14, 24-28} Che *et al.* reported a series of complexes generating supramolecular polymers based on the Pt...Pt interaction can show pH-dependent emission in the lysosome of cells.¹⁸ Meanwhile, the role of proteins in the self-assembly of Pt compounds is very diverse; for example, Cola *et al.* reported that cell medium prevented some platinum complexes to be internalized by the cells.¹⁷ Overall, little is known about the morphology of supramolecular polymers based on the Pt...Pt interaction in cell medium or inside cells, their mechanism of cellular uptake, and the dynamics of their intracellular distribution.

These questions have become particularly relevant because of the emergence of nanomaterials as functional delivery platforms for the imaging and therapy of cancer.²⁹⁻³¹ Many types of organic and inorganic theranostic nanosystems have been developed, derived from *e.g.* lipid-based nanoparticles, polymers, lanthanide fluorides, or silica nanoparticles.³¹⁻³⁵ Endocytosis is

considered to be the major cellular uptake mechanism for nanoparticles, as a consequence of which they typically end up in the endosome or lysosome.³⁶ The lysosome, in particular, is responsible for the digestion of extracellular substances, and it generates for this aim abundant hydrolytic enzymes and an acidic environment, which limits many nano-drug delivery systems by preventing drug release into the cytosol.^{37,38} Thus, nanoparticles capable of endo-lysosomal escape or avoiding lysosomes are of great interest. In this work, we were able to generate self-assembled nanoparticles based on the Pt...Pt interaction that can move from the cell membrane to mitochondria directly with exceptional uptake efficiency, without the assistance of lysosome. These nanoparticles are built from a molecularly well-defined cyclometalated platinum complex, which makes these nanomaterials particularly easy to prepare in a reproducible manner. Because of the aggregation-induced red absorption and deep-red emission of these nanostructures, their low photobleaching, and the high electron density generated by the platinum centers, it is possible to monitor in cells their morphology, fate, and dynamic reorganization by a combination of confocal microscopy, cell electron microscopy, and flow cytometry, effectively demonstrating cellular uptake by endocytosis, endosomal escape, and relocation into the mitochondria.

4.2 Results

4.2.1 Synthesis and characterization of two cyclometalated platinum(II) complexes. Two isomeric complexes $[\text{PtMeL}^1]\text{OAc}$ ($[1]\text{OAc}$) and $[\text{PtMeL}^2]\text{OAc}$ ($[2]\text{OAc}$, Figure 4.1) were prepared by cyclometalation of the known tetradentate ligands HMeL^1 and HMeL^2 ,³⁹ using platinum(II) acetylacetonate in boiling acetic acid. The compounds $[1]^+$ and $[2]^+$ differ by the position of the platinum-carbon bond: in $[1]^+$ it is closer to the bridging NMe group than in $[2]^+$. The ^1H NMR spectra obtained for each complex were different at low (2 mg/mL MeOD) vs. high (7 mg/mL MeOD) concentration (Figure AIII.1), which suggested some form of supramolecular assembly in this solvent. The crystal structure of $[2]\text{PF}_6$ confirmed this tendency: The crystal packing of $[2]\text{PF}_6$ (Figure 4.1b) clearly identified one short (3.3216(5) Å) and one long (4.2572(6) Å) intermolecular Pt...Pt distance. The short Pt...Pt distance also corresponded to short distances between the aromatic rings of the parallel cyclometalated ligand (the shortest distance around 3.5 Å), demonstrating strong π - π stacking as well. Altogether the crystal suggested the formation of supramolecular dimers in the solid state.

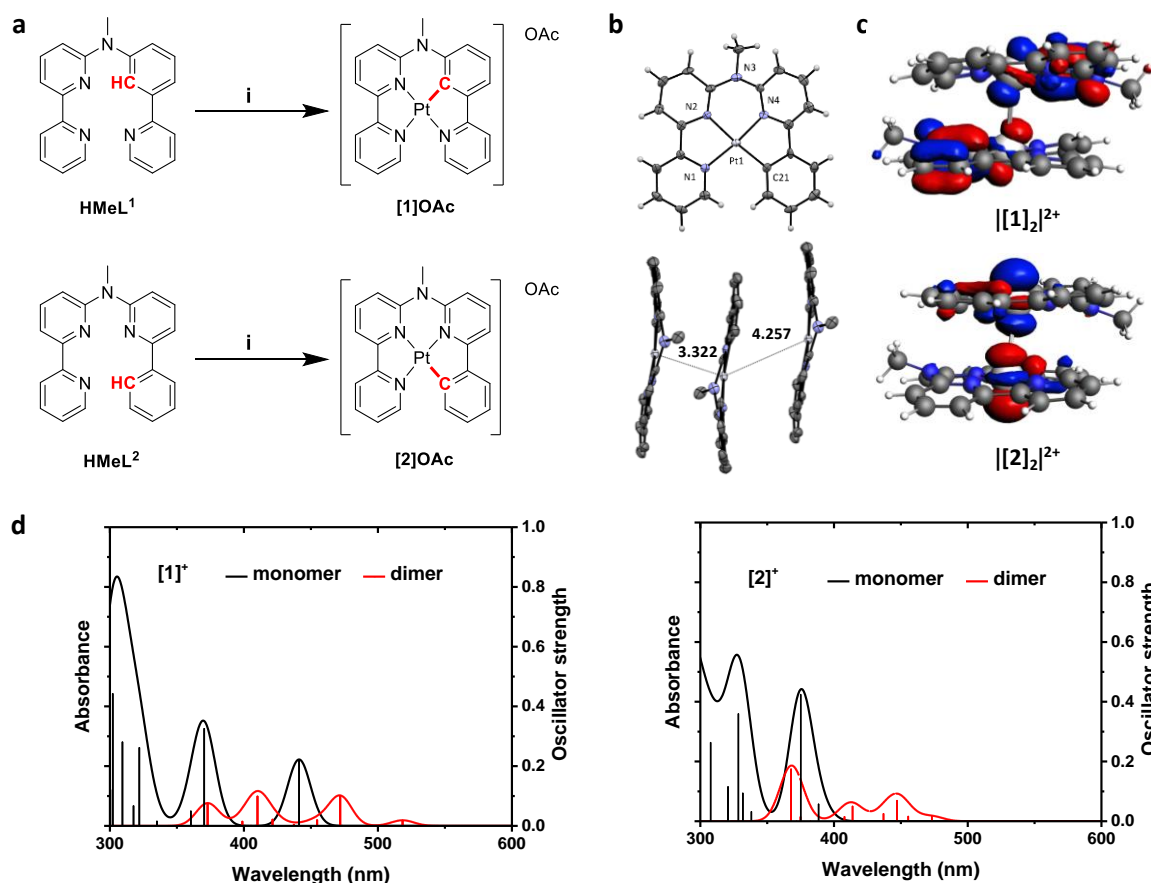


Figure 4.1 (a) Synthesis of [1]OAc and [2]OAc. Reaction condition: i) Platinum(II) acetylacetonate (1 eq.), tetrabutylammonium acetate, CH₃COOH, N₂, 135 °C, 6 days; 32% yield for [1]OAc and 93% yield for [2]OAc. (b) Displacement ellipsoid plot (50% probability level) and packing of [2]PF₆ at 110(2K). Element color code: gray = C, blue = N, white = Pt and H; anion has been omitted for clarity; Pt...Pt distances are given in Å. (c) HOMO of [1]₂²⁺ and [2]₂²⁺ showing the d_z² overlap, calculated by DFT at the PBE0/TZP/COSMO level in water. Element color code: gray = C, blue = N, white = Pt and H. (d) Excitation spectra of [1]⁺ and [2]⁺ in the monomeric and dimeric states according to TDDFT calculations.

According to density functional theory (DFT) and time-dependent density functional theory calculations (TDDFT) run at the PBE0/TZP/COSMO level for both monomolecular complexes in water, the calculated HOMO-LUMO transition of [1]⁺ is at much lower energy (441 nm) than that of [2]⁺ (375 nm, Table AIII.1). As the HOMO is based on the lone pair of the NMe bridge, and the LUMO is essentially located on the bipyridine part of the ligand, the HOMO in [1]⁺ is more destabilized by the closer, electron-rich cyclometalated bond, than the HOMO in [2]⁺, while both bpy-based LUMOs are essentially at the same energy level. The dimers of complexes were also modeled by DFT. According to these calculations, dimers form despite

the electrostatic repulsion exerted by the monocationic complexes. Their HOMO is composed of the two d_{z^2} orbitals on the platinum centers interacting in an antibonding fashion, with an additional contribution from π orbitals of the ligands (Figure 4.1c). The calculated Pt...Pt distance was short (3.34 Å for **[1]**⁺ and 3.26 Å for **[2]**⁺), confirming that in such dimers the metallophilic interaction is strong, and occurs as a result of a combination of d_{z^2} axial overlap and π - π stacking. Besides, the HOMO-LUMO energy gaps of both complexes significantly decreased in the dimer state compared with the monomer (Figure AIII.2), especially for **[2]**⁺, from 4.13 eV (monomer) to 3.39 eV (dimer). Further TDDFT calculation demonstrated that the dimer of both complexes shows a lower-energy absorbance band than their monomer, which can be attributed to a transition from the σ^* orbital on the Pt...Pt axis to π^* ligand-based orbitals, corresponding to an MMLCT excited state. These results indicated that the aggregates of these complexes might be excited at a longer wavelength than the monomers.

4.2.2 Photophysical properties of platinum(II) complexes in the monomeric and aggregated states. The absorbance and normalized emission spectra of **[1]OAc** and **[2]OAc** (50 μ M) in methanol, water, and Opti-MEM complete cell medium (2.5% V/V fetal calf serum (FCS)), are shown in Figure 4.2. The distinct absorbance of both isomers around 450 nm in MeOH solution can be attributed to their different HOMO-LUMO gap (Figure AIII.2), which critically depends on the proximity between the Pt-C bond and the non-bonding electron pair on the NMe bridge.⁴⁰ At low concentration in methanol (50 μ M), both complexes showed a weak phosphorescence around 600 nm, characterized by low quantum yields (below 0.001, Table 4.1). The emission peaks at 588 nm (**[1]OAc**) and 616 nm (**[2]OAc**) in methanolic solution, which according to TDDFT can be assigned to ligand-to-ligand charge-transfer (LLCT) transitions with a small triplet metal-to-ligand charge-transfer (³MLCT) character. They also showed, in the same conditions, moderate quantum yields in generating singlet oxygen (ϕ_{Δ} = 0.44 for **[1]OAc**, 0.11 for **[2]OAc**), suggesting sub-optimal photodynamic properties in this solvent.

Spectroscopic measurements were then carried out in Milli-Q water (50 μ M) to determine whether Pt...Pt interaction might occur in aqueous solution. In such conditions, moderate bathochromic shifts of the absorbance spectra of both compounds were found, which are typical indications for the formation of low-energy ³MMLCT states derived from the Pt...Pt interaction (Figure 4.2a).^{5, 6} This bathochromic shift of the absorbance was strongly enhanced when either compound (50 μ M) was dissolved in Opti-MEM complete, and for **[2]OAc** a new absorption maximum appeared at 540 nm. The emission of both compounds was also red-shifted in pure

water with maxima at 655 and 691 nm for **[1]OAc**, 651 and 687 nm for **[2]OAc**, which are attributed to mixed $^3\text{MLCT}$ and $^3\text{MMLCT}$ transitions emission, probably from a mixture of monomers, oligomers, and polymers. In Opti-MEM complete, only the deep-red emission was observed (705 nm for **[1]OAc**, 699 nm for **[2]OAc**), which is the clear spectroscopic signature from $^3\text{MMLCT}$ transitions.⁶ The singlet oxygen quantum yields in aqueous solutions were measured using the $^1\text{O}_2$ chemical sensor 9,10-anthracenediyl-bis(methylene)dimalonic acid (ABMDMA).³⁹ The value found for **[1]OAc** was lower (0.19) in the aggregated state in Opti-MEM complete medium, compared to the monomeric state in CD_3OD (0.44), while that of **[2]OAc** remained at a comparably low level (0.10) (Table 4.1, Figure AIII.3). The phosphorescence lifetime of both isomers in aerated MeOH, water, and Opti-MEM complete, showed biexponential decay (Figure AIII.4). The main component of the decay showed significant increase when changing the solvent from methanol to water to medium (Table 4.1). Meanwhile, the deep-red emission obtained in cell medium matched well, in terms of emission maximum, with the emission of the complexes in the solid state (Figure AIII.5). Interestingly, in the solid state, **[2]OAc** showed a much higher emission intensity than **[1]OAc**, which might be partially ascribed to the shorter Pt...Pt distance of **[2]OAc** and its comparatively stronger Pt...Pt interaction as demonstrated by DFT calculations (Pt...Pt distance: 3.34 Å for **[1]**⁺ and 3.26 Å for **[2]**⁺), and partially by different crystal structures. In conclusion, the red shifted absorbance and emission of both cyclometalated complexes in water and Opti-MEM solutions could be attributed to the formation of soluble nanoaggregates via Pt...Pt interaction, and it is similar to the spectroscopic signature of the solid state.

The strong deep-red emission of the platinum complexes as a solid or nanoparticle is attributed to the aggregation of the molecules via the Pt...Pt interaction, which represents a new mechanism for aggregation-induced emission (AIE) based on the metallophilic interaction. Up to now, the generally accepted mechanism of luminescence induction in AIE luminogens (AIEgens) is based on the restriction of intramolecular rotations and vibrations in supramolecular aggregates that, in the monomer, quench emission by vibronic coupling.⁴¹⁻⁴⁴ Rare cases of metal complexes that can generate luminescence in aggregated condition via metallophilic interaction, have lately attracted much interest.^{23, 45-49} To demonstrate the aggregation-induced character of the Pt...Pt interaction, the emission spectrum was measured in methanol/diethylether mixtures containing 10-90 vol% ether. For both complexes upon the increase of the ether fraction from 10 to 60%, the emission gradually increased, indicating AIE was taking place (Figure 4.2b). However, above 60% of both complexes followed different

patterns. For **[2]OAc**, the luminescence at 700 nm increased suddenly at an ether fraction of 90%, which corresponds well with the strong red emission of the bulk solid state. For **[1]OAc**, the emission suddenly decreased and slightly red-shifted, which also indicated the formation of the bulk solid, which is a poorly emissive material (Figure AIII.5). This experiment confirmed the AIE property of these two complexes: the nanoaggregation taking place via Pt...Pt interaction leads to increased emission as long as the particles stay small enough to be solvated; upon precipitation at a high ether content, **[1]OAc** becomes poorly emissive while **[2]OAc** becomes more emissive, which corresponds to the bulk emission properties of the solids.

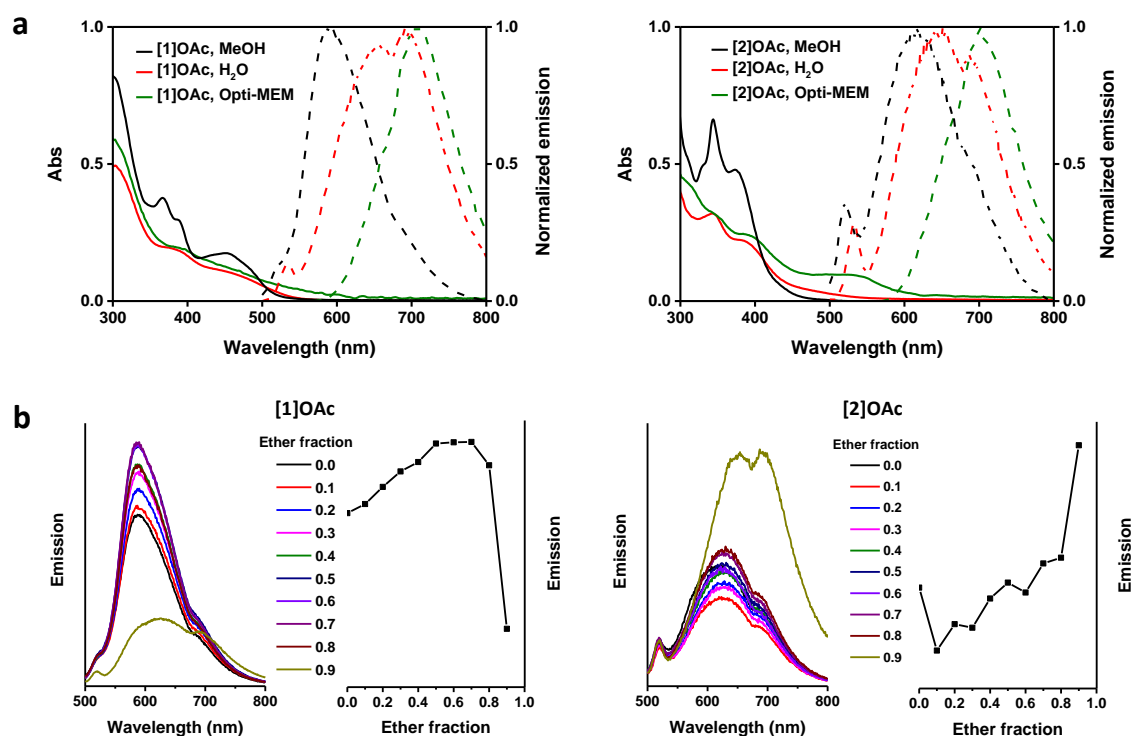


Figure 4.2 (a) The absorbance (solid lines) and emission spectra (dashed lines) of **[1]OAc** and **[2]OAc** in methanol (black), water (red) and Opti-MEM complete medium (green) (Concentration 50 μ M, excitation 450 nm). (b) The emission spectra and emission intensity at 587 nm of **[1]OAc** (left) and **[2]OAc** (right) in methanol with different diethylether ratio (concentration 50 μ M, excitation 450 nm).

Table 4.1 Photophysical data for **[1]OAc** and **[2]OAc**.

complex		[1]OAc	[2]OAc
λ_{abs} , nm ($\epsilon \times 10^3 \text{ M}^{-1} \text{ cm}^{-1}$)	H ₂ O	303 (8.9), 382 (3.4), 552 (0.25)	343 (6.1), 383 (4.2), 552 (0.22)
	MeOH	588	616
λ_{em} , nm ^a	H ₂ O	655, 691	651, 687
	Opti-MEM	705	699
	solid	727	721

ϕ_p^b	MeOD		0.00125		0.00051
	H ₂ O		0.00080		0.00030
ϕ_Δ	MeOD ^c		0.44		0.11
	Opti-MEM ^d		0.19		0.10
Lifetime (ns) ^e	MeOH	τ_1	2.6±0.2 (19%)		0.61±0.05 (10%)
		τ_2	11±1 (81%)		5.7±0.5 (90%)
	H ₂ O	τ_1	0.5±0.2 (2%)		1.54±0.06 (13%)
		τ_2	23.7±0.5 (98%)		10.5±0.3 (87%)
	Opti-MEM	τ_1	3.96±0.07 (12%)		3.3±0.3 (9%)
		τ_2	29.6±0.3 (88%)		33.9±0.5 (91%)

^a The emission spectra were measured in air condition. Excitation 450 nm, complex concentration 50 μ M ^b Phosphorescence quantum yield measurements of **[1]OAc**-**[2]OAc** were carried out at 390 nm excitation wavelength in aerated water, or MeOD, using **[Ru(bpy)₃]Cl₂** (ϕ_p = 0.028 in water, 0.015 in MeOD) as standard. ^c Excitation wavelength 450 nm, air atmosphere. The absorption of each complex at 450 nm was adjusted to 0.1 to avoid the generation of excimer.³⁹ In CD₃OD by spectroscopic detection at 1270 nm; **[Ru(bpy)₃]Cl₂** was used as standard (ϕ_Δ = 73%). ^d In Opti-MEM complete using ABMDMA as ¹O₂ probe; **[Ru(bpy)₃]Cl₂** was used as standard (ϕ_Δ = 14%).³⁹ ^e Excitation wavelength 375 nm.

4.2.3 Pt...Pt interaction induced supramolecular self-assembly. Interestingly, the aggregation-induced emission via Pt...Pt interaction does not only occur in methanol/ether mixtures, but also in several physiological solutions such as PBS and Opti-MEM medium. The size and number of nanoparticles obtained with platinum complexes **[1]OAc** and **[2]OAc** in water, PBS and Opti-MEM solution with different proteins (FCS, BSA and globulin) were investigated via dynamic light scattering (DLS) and transmission electron microscopy (TEM). In pure water, very few nanoparticles were detected (derived count rate (kcps)<700, Figure 4.3a); in PBS, the complexes showed significant aggregation (higher kcps values, kcps = 7627 and 1373 for **[1]OAc** and **[2]OAc** respectively, Figure 4.3a), indicating that the addition of salts might stimulate the self-assembly of the complexes. However, the time-evolution of the absorbance spectra of PBS solution of the complexes showed a gradual decrease (Figure AIII.6), suggesting slow precipitation (*i.e.* colloidal instability) in such conditions. When dissolved in the Opti-MEM medium with or without proteins, the size of the particles exhibited a large difference. This behavior resembles that of the palladium analogs of **[1]OAc** and **[2]OAc**, which form nanorods stabilized by FCS.³⁹ DLS measurements showed the presence of 100-500 nm nanoaggregates in Opti-MEM solutions containing FCS (v/v 2.5%, Opti-MEM complete), and of much larger aggregates (~1000 nm) indicative of precipitation in Opti-MEM medium deprived of proteins, suggesting that fetal calf serum plays a key role in the stabilization of the nanoaggregates in solution (Figure 4.3a, 4.3b, AIII.7). In the meantime, in Opti-MEM complete

solution the two platinum complexes showed a gradual increase in absorbance with time, which we attributed to increased light scattering due to the formation of nanoparticles; Reversely, the absorbance dramatically decreased when no FCS was present, which indicates fast precipitation (Figure AIII.6). When pure BSA (50 g/L) and globulin (30 g/L), the two main proteins in FCS, were dissolved in Opti-MEM medium and added to solutions of the complexes (50 μ M), DLS indicated that both proteins play a key factor in the stabilization of the nanoparticles of these complexes (Figure 4.3a and AIII.7). TEM images (Figure AIII.8) showed that the aggregates in Opti-MEM complete were irregular round nanoparticles, with an average size of 56 nm for **[1]OAc** and 40 nm for **[2]OAc**, mixed with nanorod structures of 20 nm thickness. TEM also showed that **[2]OAc** resulted in more concentrated nanorod generation than **[1]OAc**, which might be attributed to the stronger Pt...Pt interaction. However, TEM is sub-optimal for determining the structures of self-assembled nanoparticles in solution, since structures are dried during preparation. To alleviate this problem, cryo-EM was carried out, which allows for observing the nanostructures in a vitrified solution state. The cryo-EM images of **[1]OAc** and **[2]OAc** (50 μ M, Figure 4.3c) in Opti-MEM complete medium show clear nanorod structures with a width of around 30 nm, demonstrating the existence of supramolecular assembly via Pt...Pt interaction; specifically, no round particles were observed in cryo-EM images. The nanoparticles of **[1]OAc** were of smaller dimensions than that of **[2]OAc**, which matched with the TEM results. Cryo-EM imaging at higher magnifications for the nanoparticles of **[1]OAc** (Figure 4.3d), clearly revealed a crystalline structure for the nanorods, characterized by a high contrast hexagonal lattice captured in both x and z directions (repeating distance \sim 1.3 nm as indicated by fast Fourier transform). Overall, for both cyclometalated complexes, the Pt...Pt interaction observed in the solid state and solution by different spectroscopy techniques, triggered the self-assembly of platinum complexes into strongly deep-red emissive nanorod-like aggregates that are stabilized by serum proteins in cell medium.

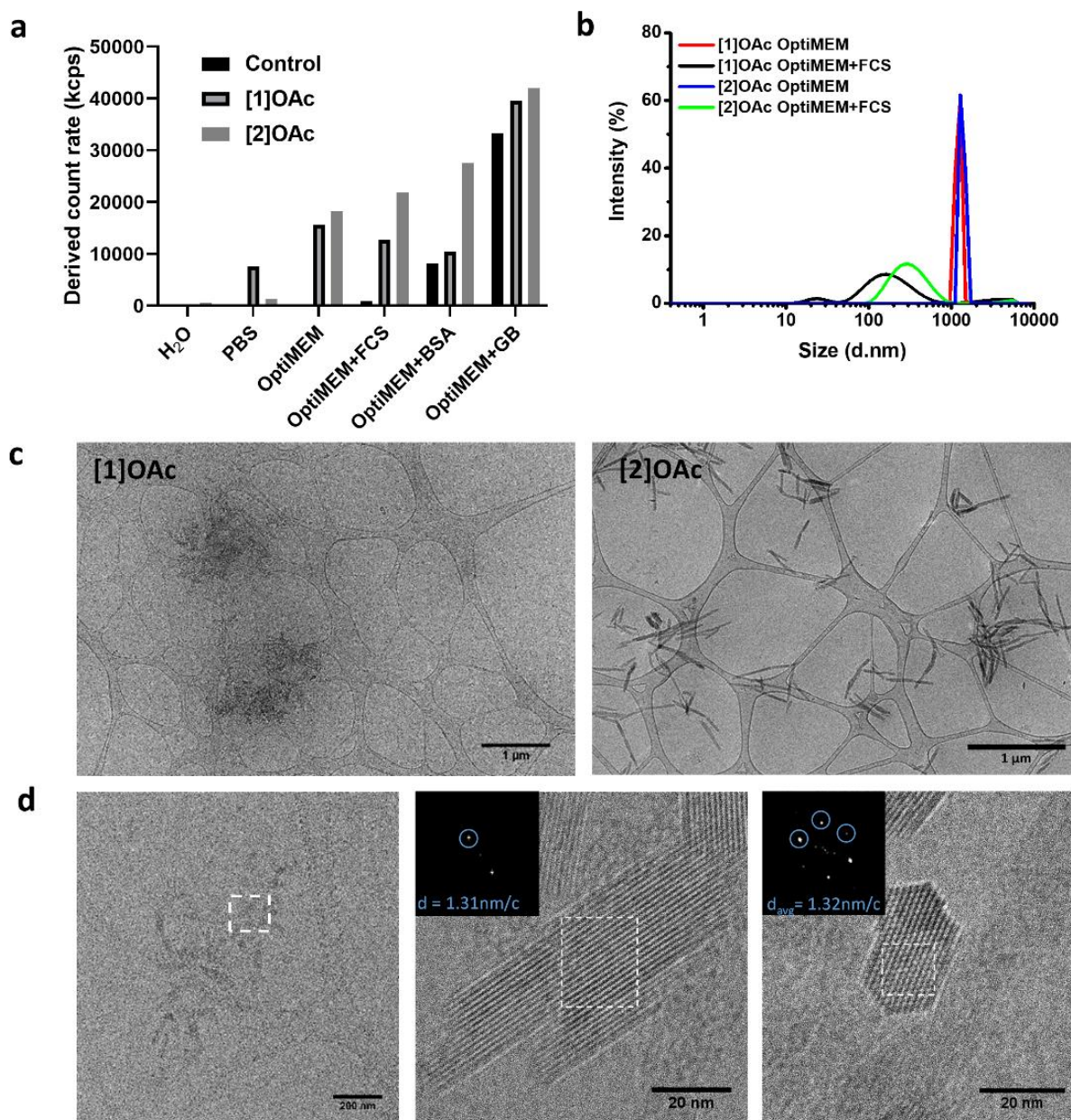


Figure 4.3 (a) DLS mean count rate (kcps) of solutions of [1]OAc or [2]OAc in water (50 μ M), PBS, Opti-MEM, Opti-MEM with fetal calf serum (FCS), serum albumin (BSA) and globulin (GB). (b) size distribution of complexes [1]OAc and [2]OAc (50 μ M) in Opti-MEM medium with and without FCS (X-axis is the hydrodynamic diameter in nm, Y-axis is relative intensity in %). (c) Cryo-EM images of [1]OAc-[2]OAc in Opti-MEM complete medium (50 μ M). (d) High-resolution cryo-EM images of [1]OAc in Opti-MEM complete medium (50 μ M); insert: average repeating distance as indicated by FFT (nm per repeating cycle).

4.2.4 Cytotoxicity and cell imaging of platinum(II) complexes. Considering the emissive properties of the nanoaggregates of [1]OAc and [2]OAc in serum-containing aqueous solutions, their biological properties in human cancer cell lines were further investigated. Both complexes

showed significant cytotoxicity in A549 lung cancer cell lines after 72 h incubation in the dark, with EC_{50} values of 10 μM for **[1]OAc** and 5 μM for **[2]OAc**, but negligible cytotoxicity in A431 human skin carcinoma, with EC_{50} values of 94 μM for **[1]OAc** and 68 μM for **[2]OAc** (Figure 4.4a). None of the complexes showed significant photocytotoxicity under blue light irradiation (455 nm, 5 minutes, 5.7 mW cm^{-2} , 1.7 J cm^{-2}) in normoxic condition (21% O_2 , Figure 4.4a). This absence of light activation is in strong contrast with their palladium analogs, which showed strong photodynamic properties and negligible emission properties in similar conditions.³⁹ After 24 h treatment with 5 μM of **[1]OAc** and **[2]OAc**, a very high platinum cellular uptake observed, as measured with ICP-MS in A549 cells and A431 cells, up to $0.51 \pm 0.03 \mu\text{g Pt/million cells}$ (Figure 4.4b), which is more than 100-fold higher efficiency than that of cisplatin.⁵⁰ This result gives a strong indication that nanoaggregation can significantly improve metallodrug uptake. In contrast with the palladium analogues, A549 cells treated with 5.0 μM of the platinum complexes for 24 h and imaged by confocal microscopy showed strong deep-red luminescence in the 650-750 nm region under 638 nm excitation, which suggested that emissive nanoaggregates similar to those observed in cell-free conditions, are also formed inside the cancer cells (Figure 4.4c). Interestingly, continued confocal imaging for 48 h (Figure AIII.9) demonstrated that the emission of **[1]OAc** does not photobleach or degrade during that period, even upon cells splitting ([Video S2](#)), and thus that nanoaggregates formed via Pt...Pt interaction are not only surviving dioxygen and light, but also cell division.

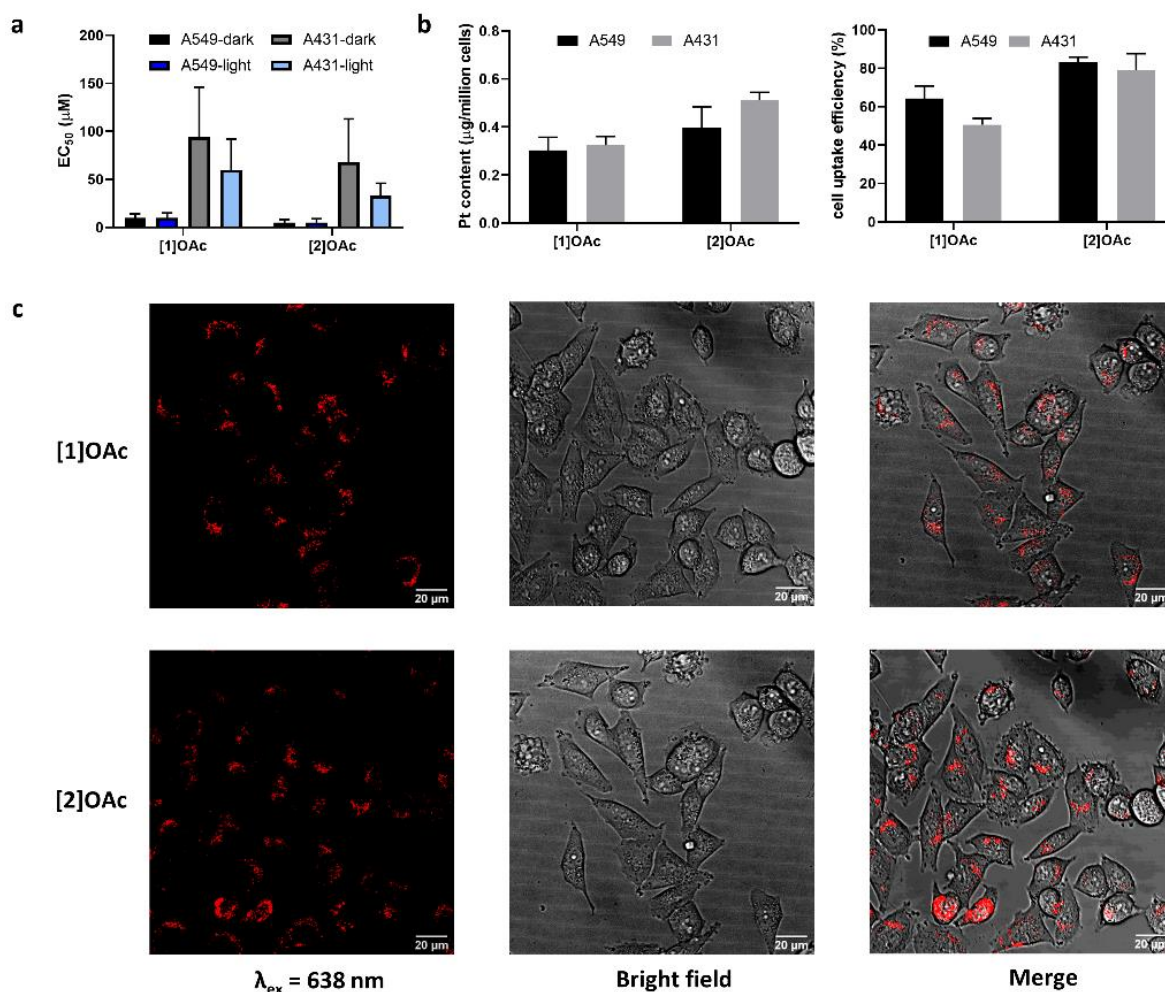


Figure 4.4 (a) EC_{50} values of [1]OAc or [2]OAc in the dark or under blue light irradiation (455 nm, 5 minutes, 5.7 mW cm^{-2} , 1.7 J cm^{-2}). (b) Pt content as measured by ICP-MS and cellular uptake efficiency (cellular Pt content/working solution Pt content $\times 100\%$) for A549 and A431 cells treated with [1]OAc and [2]OAc (concentration $5 \mu\text{M}$). (c) Confocal images of A549 cells (scale bar $20 \mu\text{m}$) after 24 h treatment with [1]OAc and [2]OAc ($5 \mu\text{M}$, $\lambda_{\text{ex}} = 638 \text{ nm}$, $\lambda_{\text{em}} = 650\text{-}750 \text{ nm}$).

4.2.5 Cellular colocalization and uptake mechanism of platinum(II) complexes. Further colocalization imaging experiments were carried out at 552 nm excitation wavelength, where both complexes show a better absorbance compared with 638 nm. A549 cells were first treated with platinum complexes ($5 \mu\text{M}$) for 24 h, then co-stained for 15 min with Hoechst 33342 ($0.1 \mu\text{g/ml}$), a nucleus dye for living cells. The confocal images (Figure AIII.10) showed that [1]OAc-[2]OAc did not localize in the nucleus. More colocalization experiments were performed with green-emitting dyes for different organelles, such as lysosomes, mitochondria, Golgi apparatus, endoplasmic reticulum (ER), and lipid droplets. The overlapping images (Figure AIII.11-12) indicated an anti-correlation of [1]OAc-[2]OAc with the ER, lysosomes

and lipid droplets, suggesting they do not stay in such organelles after 24 h treatment. Though the emission of **[1]OAc** overlapped well with the Golgi apparatus (Pearson's correlation coefficient (PPC) values of 0.5-0.7, see Table AIII.2),⁵¹ the emission characteristics of Golgi dye and metal complexes were significantly different: the former one showed a thread-like emissive pattern, while the platinum complex showed non-consecutive red dots in the cells. Thus it is elusive whether or not **[1]OAc** is present in the Golgi 24 h after treatment. For **[2]OAc**, the best co-localization pattern was obtained for the mitochondria, for which color-dependent pixel intensity curves (Figure 5a,b) and high PPC values (0.2-0.6, Table AIII.2) were obtained. Overall, 24 h after compound addition **[2]OAc** emitted primarily from the mitochondria, while the localization of **[1]OAc** in cells was unclear.

Because of their AIE deep red emission, the cell uptake mechanism of complexes could be monitored via flow cytometry. A549 cells were co-incubated with **[1]OAc** or **[2]OAc** (5 μ M) and different cell uptake inhibitors, after which the variations of the relative fluorescent cell populations at 2 h were assessed by FACS.⁵² The presence of self-assembled nanorods of the complexes in medium inspired us to particularly look into different inhibitors of endocytosis, an active transport mechanism for the uptake of nanoparticles across the cell membrane. Thus we chose a series of endocytosis and active transport inhibitors, including sodium azide (NaN_3 , active transport inhibitor), pitstop 2 (clathrin-dependent endocytosis inhibitor), dynasore (dynamin-dependent endocytosis inhibitor), nocodazole (phagocytosis inhibitor), and wortmannin (macropinocytosis inhibitor).⁵³⁻⁵⁵ As shown in Figure 5c, nocodazole and wortmannin did not result in inhibition of the relative deep-red fluorescent cell populations, thus excluding the role of phagocytosis and micropinocytosis in the drugs uptake. NaN_3 showed slight uptake inhibition for both complexes, suggesting that active transport and clathrin-dependent endocytosis are playing an active but limited role in compound uptake. The strongest response was obtained after treatment with dynasore and Pitstop 2, upon which the percentage of emissive cells was dramatically decreased, compared with the control groups only treated with the complexes. Specifically, pitstop 2 showed a more significant uptake inhibition for **[2]OAc** than **[1]OAc**, suggesting the different endocytic pathways for the isomeric compounds, while dynasore had an equal and large effect on both compounds. Overall, these data indicated that **[1]OAc** and **[2]OAc** enter into cells by dynamin-dependent and clathrin-dependent endocytosis, which is consistent with the hypothesis of uptake as nanoparticles.^{56, 57}

Still, these flow cytometry experiments were based on the aggregation-induced deep red emission, and hence only measured internalization of the aggregated particles, but no detection

of the essentially non-emissive monomeric platinum complexes, which might be uptaken via energy-independent transport. Thus ICP-MS was used to detect the whole Pt content of A549 cells treated with the Pt complex alone at 37 °C (control), the complex alone at 4 °C, to check passive uptake, or the complex co-incubated with dynasore for 2 h. As showed in Figure 5d, dynasore inhibited the cellular uptake of the two Pt complexes, matching well with the flow cytometry analysis. At 4 °C, significant cellular uptake inhibition was observed for both complexes, resulting in 53% and 58% reduction of the Pt content for [1]OAc and [2]OAc, respectively (Table AIII.3), which accounts for the shutting of active uptake processes at low temperatures. On the other hand, there was still significant Pt uptake at low temperature, which means that not all Pt complexes are taken up by active processes. Overall, these results suggest that more than half of the platinum complexes are internalized in A549 cells by energy-dependent, endocytic transport, while a bit less than half of the metal complexes cross the cell membrane via passive diffusion or energy-independent channels.

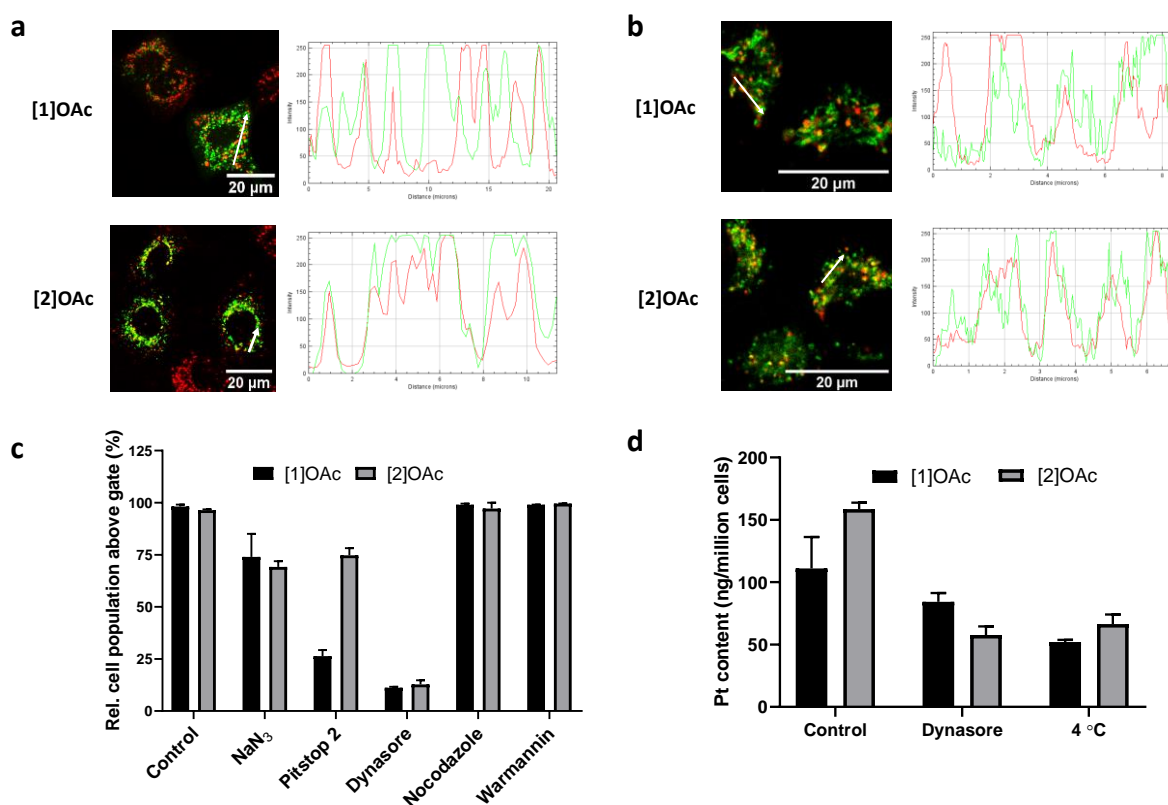


Figure 4.5 Cellular uptake of [1]OAc-[2]OAc in A549 cells. (a)-(b) Overlapping images and pixel intensity curves of A549 cells treated with [1]OAc or [2]OAc (red color, 5 μ M) and (a) Mitochondria Green Fluorescent Protein (GFP, green) or (b) MitoTracker Green FM (green color). (c) Relative fluorescent cell population (%), according to cell flow cytometry (FACS), after treatment of A549 cells with [1]OAc-[2]OAc (5 μ M) and different cellular uptake

inhibitors. (d) Pt content, according to ICP-MS analysis, of A549 cells treated with [1]OAc-[2]OAc (5 μ M) for 2 h at 37 °C, without (control) or with dynasore, or at 4 °C.

4.2.6 Time evolution of [2]OAc inside A549 cells. As [2]OAc showed increased colocalization with mitochondria after 24 h, and its major internalization mechanism was endocytosis, we engaged into investigating the time evolution of its intracellular colocalization with lysosomes and mitochondria upon uptake. Following 3 h incubation with [2]OAc and fluorescent labeling of the lysosomes and mitochondria, fluorescent images of A549 cells were acquired at time points 3.5, 4.5, 5.0, 5.5, 6.0, 21.0 and 45.0 hours (time point zero was set to the time of addition of the compound). Volume-view images of representative cells at 3.5, 6.0, 21.0 and 45.0 hours are shown in Figure 6a. The top row shows the lysosomes (blue), the second row the mitochondria (green), the third row shows the [2]OAc compound (red), and the fourth and fifth row shows the merged fluorescence of [2]OAc (red) with lysosomes (blue) and mitochondria (green), respectively. Lysosomes fluorescence increased with incubation time, whereas mitochondria fluorescence exhibited a peak at 6.0 hours and a subsequent decrease, especially at the time point of 45.0 hours. [2]OAc fluorescence increased at time points 21.0 and 45.0 hours, with bigger aggregates clearly distinguishable inside the cells. An increase in the colocalization of [2]OAc with the mitochondria was observed with increasing time. This observation was confirmed quantitatively by plotting Mander's overlap coefficient vs. time (Figure 6b).⁵⁸ Colocalization of [2]OAc with the lysosomes (grey circles) was rather low (overlap coefficient below 0.15) for all time points, suggesting limited uptake of the nanoaggregated platinum compound by the lysosomes. However, these results conflict with the typical endocytosis mechanism that usually involves endosomes and lysosomes. This conflict may indicate that [2]OAc traffics to mitochondria directly after dynamin- and clathrin-mediated endocytosis, an endocytotic mechanism that is unusual but was reported recently.⁵⁹ Alternatively, the accumulation of emissive nanoparticles in the mitochondria at 24 h could also be the result from passive uptake of the compound as monomer, migration to the mitochondria driven by the negative charge of the mitochondrial membrane ([2]⁺ is monocationic), and re-assembly due to the increased local concentration of the monomer. The decrease in colocalization of [2]OAc with both the lysosomes and the mitochondria after 45.0 hours might be due either to partial degradation of the complex, or to disassembly; this is suggested also by Figure 6c, where the average deep-red fluorescent intensity of [2]OAc per cell shows a slight decrease at 45.0 hours, as compared to that at 21.0 hours. The mean [2]OAc intensity per cell exhibits an increase after 21.0 hours as compared to that for 3.5-6.0 hours, as shown in Figure

6c, probably due to the formation of larger aggregates. Although the increase is statistically significant, the difference is of the same order of magnitude in the intensity scale (a bit more than 6000 AU for 21.0 hours, vs approximately 5000 AU for 3.5-6.0 hours), whereas visually it appears more intense (Figure 6a, third row). This observation may be attributed to a non-linear relationship between the fluorescence intensity observed and the size of [2]OAc aggregates formed.⁶⁰ Altogether, these data confirmed the accumulation of deep-red emissive aggregates of [2]OAc inside the cellular environment already 3 h after treatment, the limited assistance of lysosomes during aggregates internalization, and a tendency of the compound to co-localize with the mitochondria.

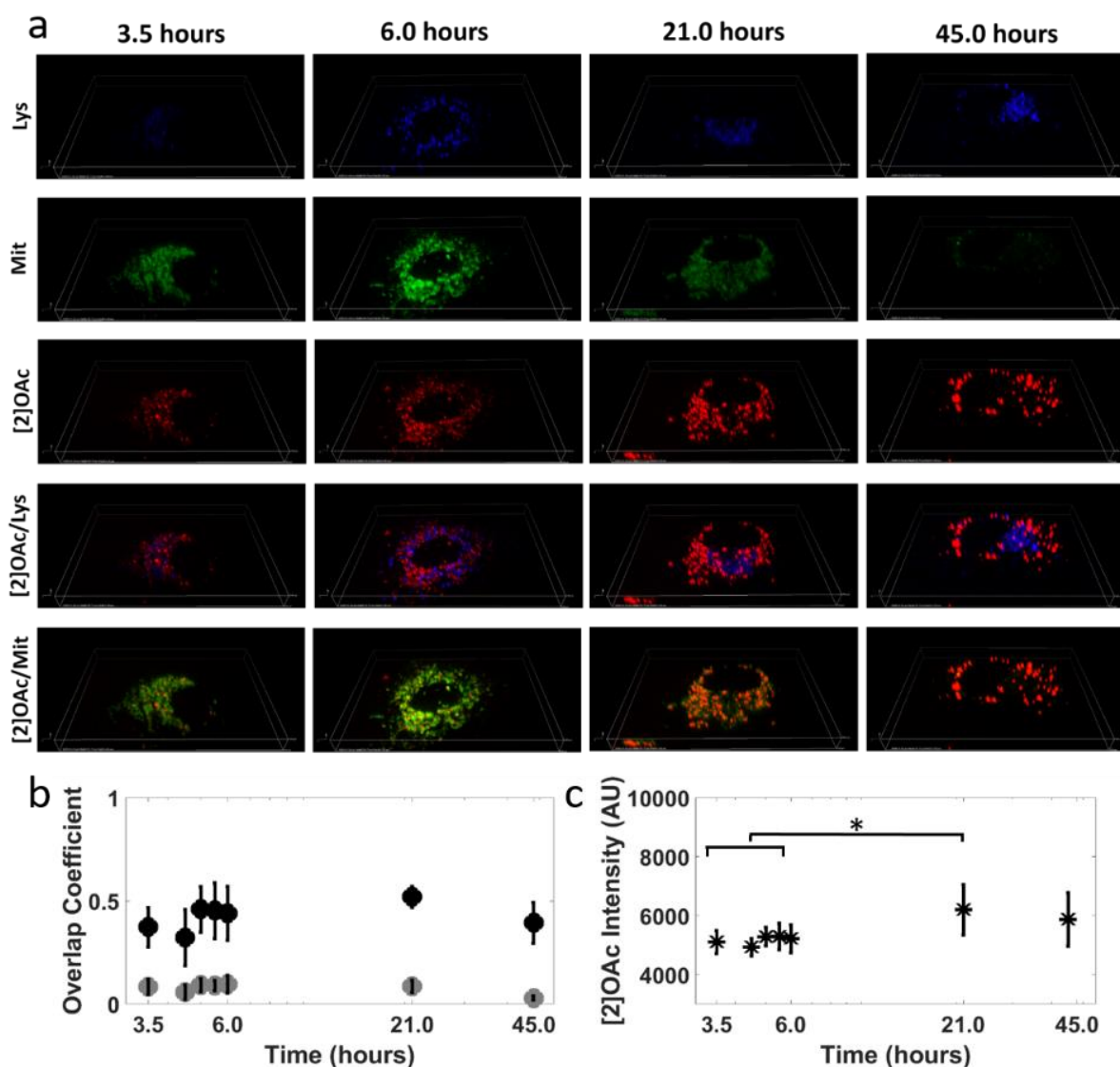


Figure 4.6 (a) Fluorescent images of lysosomes (blue, top row), mitochondria (green, second row), [2]OAc (red) (third row), merged [2]OAc with lysosomes (fourth row) and merged [2]OAc with mitochondria (bottom row), at 3.5, 6.0, 21.0 and 45.0 hours after 3-hours incubation with [2]OAc ($t=0-3$ hours). (b) Quantification of [2]OAc colocalization with

lysosomes (grey) or mitochondria (black) at 3.5, 4.5, 5.0, 5.5, 6.0, 21.0 and 45.0 hours after 3-hours incubation with [2]OAc ($t=0-3$ hours). Overlap coefficients were calculated using Mander's Overlap Coefficient (MOC) with the Nikon Nis Elements Software and are shown as mean values \pm standard deviations of an average of 8-16 cells per time point. (c) [2]OAc mean intensity per cell, at 3.5, 4.5, 5.0, 5.5, 6.0, 21.0 and 45.0 hours. Values are shown as means \pm standard deviations of an average of 6-11 cells per time point. Statistical significance p -values were calculated using the Wilcoxon statistical test * $p \leq 0.05$.

4.2.7 Determining the morphology of [2]OAc in the cell by cell-EM. The limited spatial resolution of confocal microscopy, and the conflicting observations of an endocytosis uptake with limited colocalization with the lysosomes, pushed us to use electron microscopy (EM) imaging to study the fate and morphology of the nanoparticles inside the cells. EM imaging of A549 cells incubated for 3 h, 5 h and 24 h with compound [2]OAc (5 μ M) was performed. No nanoparticles were observed in the untreated cell control group (Figure AIII.13). On the other hand, many dark-contrasted spots were observed in the treated cells, indicative of nanoparticles of [2]OAc (Figure 7a-c). These nanoparticles were located in the mitochondria, which is in agreement with the confocal microscopy data. Note that the apparent morphology of nanoaggregates of [2]OAc in the mitochondria of sectioned cells looked like nanoparticles, which seemed different from the nanorod morphology observed in cell-free medium (Figure 4c). However, nanorods observed in absence of cells by cryo-EM, are not sectioned like in cell-EM, but lie flat in a plane that is essentially perpendicular to the electron beam, hence their length can be systematically imaged. It was hence difficult to distinguish, within the cell environment, the true morphology (*i.e.*, nanoparticles vs. nanorods) of the nanostructures made by [2]OAc. In addition, it was curious to notice that no nanoparticle was observed in the lysosomes or cytoplasm at any time point investigated by cell-EM. Combined with the observed endocytotic uptake mechanism found by FACS analysis and the low co-localization of lysosome-target dyes and aggregated [2]OAc, these results suggested that this compound performed a direct transfer from the dynamine- and clathrin-coated vesicles to the mitochondria, avoiding the classical endosome- and lysosome-assisted endocytosis process.⁵⁹ All in all, the cell-EM images at three different time points fit quite well the time-dependent confocal microscopy images, demonstrating the formation, following endocytosis, of nanostructures of [2]OAc in the mitochondria, without involvement of the endosome or lysosome, and without nanoparticle formation (or migration) in the cytoplasm.

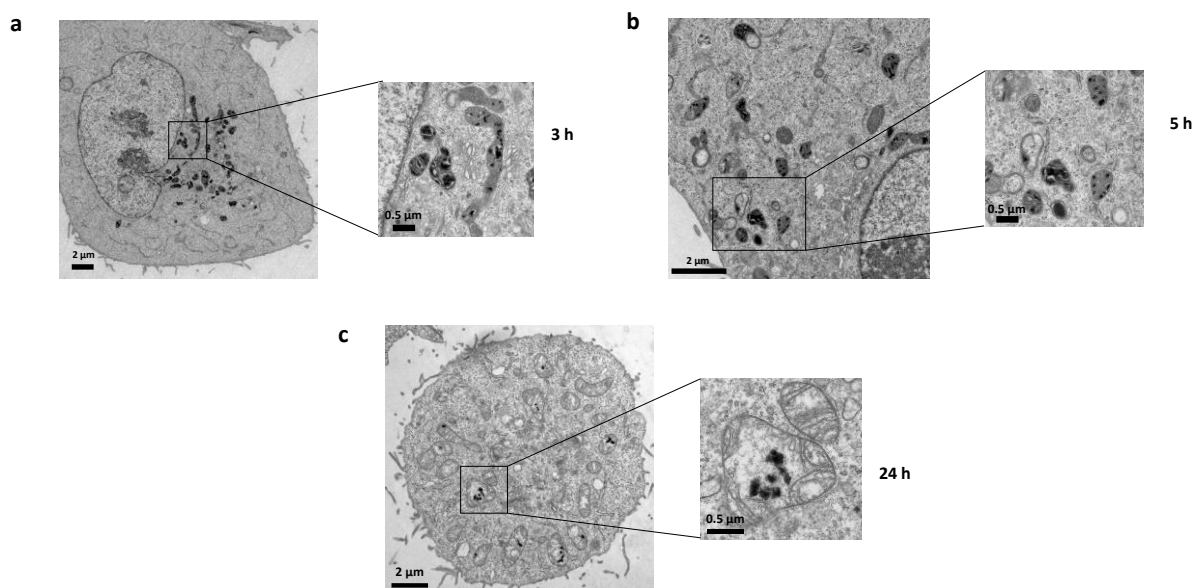


Figure 4.7 EM images of A549 cells 24 h after treatment with [2]OAc (5 μ M) at 3 h (a), 5 h (b) and 24 h (c) (scale bar 2 or 0.5 μ m).

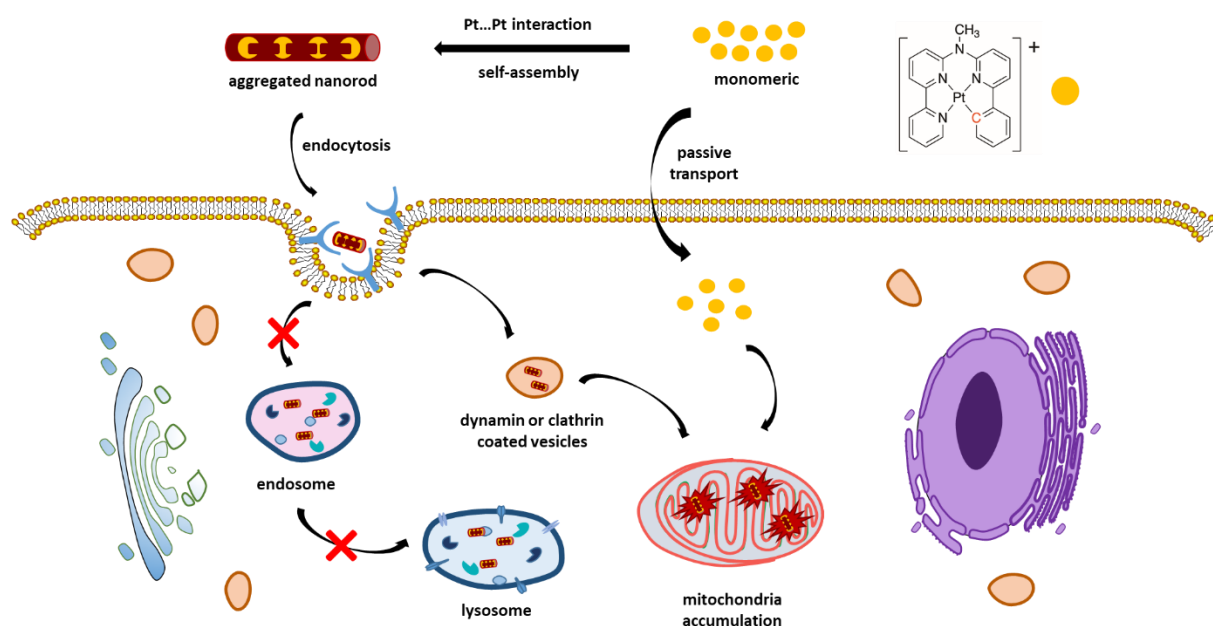
4.3 Discussion

In recent years, the metallophilic interaction has developed as an essential form of supramolecular interaction, with many new applications, *i.e.* from OLED to bioimaging.^{48, 61-64} Our group recently demonstrated that the palladium analog of [1]OAc could serve as a very efficient PDT agent that generated serum-stabilized, phototoxic but not-emissive, nanorods via Pd...Pd metallophilic interactions.³⁹ These nanorods are difficult to study in cells because they are non-emissive. By changing the metal center to platinum, we now demonstrate that similar self-assembly takes place with [1]OAc and [2]OAc. Remarkably, the metallophilic Pt...Pt interaction at the source of the nanorod self-assembly in the serum-containing medium now generates deep-red emission, which allows for studying the uptake and intracellular fate of these nanorods both by confocal microscopy and cellular EM.

The results of the uptake inhibition experiments suggested that dynamin- and (or) clathrin dependent endocytosis, a specific uptake pathway working via dynamin and clathrin proteins, are the main channels for the nanoparticles of [1]OAc and [2]OAc to cross the cell membranes. However, near half of the Pt complexes [1]OAc and [2]OAc were internalized into the cells via passive diffusion (or at least energy-independent channels), suggesting that the platinum complexes might exist both as aggregated nanoparticles and isolated molecules in the cell medium. Importantly, already after 3 h [2]OAc was found to locate in the mitochondria in an aggregated, emissive state. The confocal colocalization and cell-EM experiments excluded the

role of lysosomes in the cellular movement of [2]OAc. These apparently conflicting results can be explained by a recent report that exogenous molecules may also traffic to mitochondria directly from the plasma membrane by clathrin-mediated endocytosis, and entry of the endosome into mitochondria using microtubule-dependent active transport.⁵⁹

Overall, two (co-existing) mechanisms can be proposed to interpret the cellular uptake and time-dependent localization of [2]OAc. First, an energy-dependent mechanism can be proposed (Scheme 1): small nanoaggregates enter into cells *via* endocytosis, and traffic to the mitochondria directly via the clathrin- or dynamine-coated endosomes. These aggregates are small enough not to be detected by EM, but big enough to contribute to the phosphorescence signal detected by FACS. As a side note, this process is very fast and efficient, as it takes place within 3 h and leads to above half of the cellular uptake of the compound. The second mechanism involves passive uptake of [2]OAc as isolated molecules. These isolated molecules are invisible by cell EM and not emissive, but due to their positive charge they diffuse to the negatively charged mitochondrial membrane, where re-assembly occurs, contributing to the accumulation of larger and emissive nanoparticles in the mitochondria.



Scheme 1. Schematically cellular uptake and movement of [2]OAc.

Whatever the mechanism for cellular uptake, Pt nanoparticles were observed in the mitochondria, suggesting that the Pt...Pt interaction is a reliable supramolecular interaction for building theranostic platforms in cells, because it survives cell metabolism and even cell division. This interaction could be used for making supramolecular sensors or devices that can penetrate inside a cell by endocytosis, rearrange, and relocate to perform a specific function

(here mitochondria staining). Importantly, these self-assembled sensors work at high wavelengths that are ideal for bioimaging. In the cell medium, these nanoaggregates are stabilized by plasma proteins, which generates nanorods, while in mitochondria they might have different, particle-like morphologies. Altogether, proteins, as well as salts, appear to play a critical role in balancing the repulsive (electrostatics) and attractive (π - π stacking, d_z^2 overlap) forces at the origin of the metallophilic interaction. The different proteins present in the cell medium, lysosome, cytosol, and mitochondria, may lead to different forms of self-assembly, which contributes to the dynamics of the complex inside the cell.

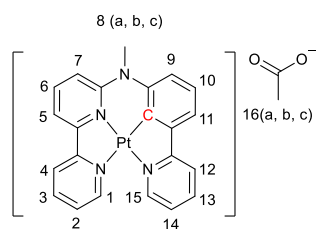
4.4 Conclusion

In summary, this work demonstrated that two cyclometalated platinum complexes generated self-assembled, protein-stabilized nanorods in cell medium via Pt...Pt interaction. Due to their supramolecular aggregation properties, these compounds cross the cell membrane *via* a combination of passive uptake (for the monomers) and dynamin- and clathrin-dependent endocytosis (for the nanoparticles). The nanoparticles directly move to mitochondria *via* the specific dynamin- and clathrin-coated vesicles, and re-assemble inside the mitochondria as deep-red phosphorescent nanoparticles. These nanoparticles survive both in living and dividing cells, while showing very limited phototoxicity. Overall, this set of platinum complexes demonstrate new perspectives for using the metallophilic interaction to build supramolecular nanosystem that, at high concentration, can kill cancer cells, but at low concentration, may be used as deep-red trackers for different organelles – here the mitochondria.

4.5 Experimental section

4.5.1 Compounds preparations. The ligands **HMeL**¹ and **HMeL**² were prepared as described in chapter 3. The platinum complexes **[1]OAc** and **[2]OAc** were synthesized using the methods described in chapter 3, using platinum(II) bis(acetylacetonate) instead of palladium(II) acetate.

[1]OAc

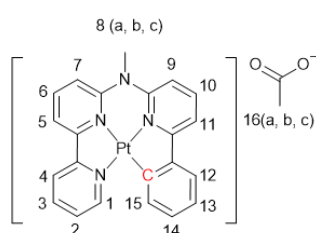


A mixture of the ligand **HMeL**¹ (68 mg, 0.2 mmol), Pt(acac)₂ (79 mg, 0.2 mmol) and tetrabutylammonium acetate (10 mg, 0.04 mmol) was dissolved in CH₃COOH (50 mL) and heated at 135 °C under an N₂ atmosphere for 6 days. The solvent was rotary evaporated to obtain a

yellow solid, which was washed with EtOAc (100 mL) and diethyl ether (50 mL), and dried under vacuum, to finally obtain **[1]OAc** as analytically pure product (Yield: 38 mg, 0.06 mmol, 32%). **HRMS** (cation): *m/z* calcd 532.1101 [C₂₂H₁₇N₄Pt]⁺, obsd 532.1097. **¹H NMR** (400 MHz,

Methanol- d_4) 9.03 (1 H, s, H^1), 8.79 (1 H, d, J 5.6, H^{15}), 8.55 (1 H, d, J 8.2, H^4), 8.32 (1 H, t, J 7.8, H^3), 8.19 (1 H, t, J 8.1, H^6), 8.11 (1 H, t, J 7.7, H^{13}), 8.04 (2 H, t, J 6.8, H^5 , H^{12}), 7.88 (1 H, s, H^2), 7.63 (1 H, d, J 8.7, H^7), 7.54 (1 H, d, J 7.4, H^{11}), 7.48 (1 H, d, J 7.1, H^{14}), 7.37 (1 H, t, J 7.6, H^{10}), 7.30 (1 H, d, J 8.0, H^9), 3.88 (3 H, d, J 1.6, H^8), 1.90 (3 H, d, J 1.5, H^{16}). ^{13}C APT-NMR (101 MHz, MeOD) δ 154.4, 150.0, 148.5, 145.8, 141.3, 140.7, 139.2, 138.4, 128.9, 127.7, 126.6, 124.8, 124.5, 121.4, 120.5, 119.2, 118.8, 116.6, 42.4. Elemental analysis calcd for **[1]OAc** + 2 H_2O : C, 45.93; H, 3.85; N, 8.93; Found for **[1]OAc** + 2 H_2O : C, 46.07; H, 3.97; N, 8.88.

[2]OAc



[2]OAc was synthesized using the same method as for **[PtMeL¹]OAc**, but starting from ligand **HMeL²** (34 mg, 0.1 mmol).

The yield in **[2]OAc** was 93% (55 mg, 0.093 mmol). **HRMS** (cation): m/z calcd 532.1101 [$\text{C}_{22}\text{H}_{17}\text{N}_4\text{Pt}$] $^+$, obsd 532.1093. ^1H NMR (400

MHz, Methanol- d_4) 8.79 (1 H, d, J 5.6, H^1), 8.18 (2 H, d, J 4.3, H^3 ,

H^4), 8.10 (1 H, t, J 8.1, H^6), 7.87 (1 H, t, J 8.1, H^{10}), 7.80 (1 H, d, J 7.7, H^5), 7.55 (1 H, q, J 4.9, H^2), 7.50 (1 H, d, J 8.6, H^7), 7.46 – 7.41 (5 H, m, H^{12}), 7.37 (1 H, d, J 7.7, H^{11}), 7.13 – 7.09 (2 H, m, H^{13} , H^{14}), 7.07 (1 H, d, J 8.5, H^9), 7.01 (1 H, d, J 7.3, H^{15}), 3.52 (3 H, s, H^8), 1.92 (3 H, s, H^{16}). ^{13}C APT-NMR (101 MHz, Methanol- d_4) δ 157.0, 150.6, 149.7, 149.1, 148.0, 145.5, 143.9, 139.8, 139.3, 139.2, 130.8, 129.1, 126.9, 124.8, 124.2, 123.9, 117.5, 117.3, 113.2, 113.0, 42.7. Elemental analysis calcd for **[2]OAc** + 1.5 H_2O : C, 46.60; H, 3.75; N, 9.06; Found for **[2]OAc** + 1.5 H_2O : 46.37, 3.79, 9.01. The CH_3COO^- counter ion of **[2] $^+$** was changed to **PF₆ $^-$** ion by adding excess **KPF₆** to a water solution of the metal acetate complex, to obtain a precipitate of **[2]PF₆** that was collected by filtration and dried. Single crystals of **[2]PF₆** were obtained through vapor diffusion of diethyl ether into a MeOH/DCM solution of **[2]PF₆**. The single X-ray crystallography of **[2]PF₆** was determined via methods described in section 3.5.3. CCDC number of **[2]PF₆** is 2001190.

4.5.2. DFT calculation. The geometries of the monomeric and dimeric complexes were optimized in water solvent with the Amsterdam Density Functional (ADF) software package at the density functional theory (DFT) level employing the PBE0 hybrid density functional⁶³ and the TZP (triple- ζ polarized) Slater-type basis set. The time-dependent DFT (TD-DFT) calculations were then performed at the same level to evaluate the optical properties. The vertical excitation energy was efficiently calculated by the corresponding TD-DFT method. The first 20 excited singlet states were taken into account in the calculations of the absorption

spectra. Solvent effects were included using the continuum solvation model (COSMO) in all calculations to describe the water environment.

4.5.3 TEM measurement of metal complexes in Opti-MEM complete medium. The TEM experiments were carried via TEM JEOL 1010:100 kV transmission electron microscope using Formvar/Carbon coated copper grid from Polysciences Inc. For the preparation of samples, each drop (15 μ L) of complex solutions (50 μ M) was deposited on parafilm. The grids were placed on top of the drops for 2 min, then the excess liquid on the grid was removed by filter paper, and the grid was dried for 2 h before the TEM measurement. The TEM measurements were carried out in vacuum conditions.

4.5.4 Cryo-EM measurement. 6 μ L of sample ([complex] = 50 μ M) was applied to a freshly glow-discharged carbon 200 mesh Cu grid (Lacey carbon film, Electron Microscopy Sciences, Aurion, Wageningen, The Netherlands). Grids were blotted for 3 s at 99% humidity in a Vitrobot plunge-freezer (FEI VitrobotTM Mark III, Thermo Fisher Scientific). Cryo-EM images were collected on a Titan/Krios operating at 300 kV or on a Talos L120C operating at 120 kV (NeCEN, Leiden University). In the case of Titan/Krios, images of [1]OAc were recorded manually at a nominal magnification of 3600x, 33000x or 81000x yielding a pixel size at the specimen of 31.8 \AA , 3.5 \AA or 1.4 \AA , respectively. In the case of Talos L120C, images of [2]OAc were recorded manually at a nominal magnification of 13500x yielding a pixel size at the specimen of 2.3 \AA .

4.5.5 Cell culture and photocytotoxicity experiments. The process for cell culture and photocytotoxicity experiments are described in section 2.4.6 of chapter 2.

4.5.6 Cellular uptake experiments. A549 and A431 cells were seeded in a 12-well plate (2×10^5 cells, 1 mL Opti-MEM complete per well). At $t = 24$ h, the cells were treated with complexes [1]OAc or [2]OAc (5 μ M, 0.5 mL Opti-MEM complete). After 24 h treatment, the cells were harvested by trypsin (5% v/v in PBS), counted via trypan blue, and centrifuged in 15 mL tubes. After removing the supernatant, the cell pellets were lysed by adding 0.5 mL HNO₃ (65%) into the tubes, keeping for 10 min and sonicating for 30 min at room temperature. After that, the cell solution was diluted to 10 mL using milli-Q water, and the Pt content in the solution was determined using ICP-MS (NexION 2000, PerkinElmer). Each experiment was carried out for 3 times.

4.5.7 Confocal experiments in A549 cells. The cell-imaging experiments were carried out using confocal microscopy. In brief, 200 μ L aliquots containing 2×10^4 A549 cells were first

seeded onto a μ -slide 8-well confocal plate (ibidi). At $t = 24$ h, the wells were treated with [1]OAc or [2]OAc (5 μ M). At $t = 47.5$ h, the wells were treated with a chemical dye, unless otherwise stated. A 20X oil immersion objective was used for all imaging, with an additional zoom factor from 1.0X – 3.0X. Control wells were used to set laser and gain intensity such that background signal was eliminated or negligible prior to measurement of target wells. For nucleus staining, A549 cells were treated with Hoechst 33342 (0.1 μ g/mL) for 15 min. For GFP experiments, CellLight™ GFP expression vector solutions were added to wells at $t = 24$ h with the drug compounds under study for a full 24-h incubation before measurement, as directed by the included manufacturer protocol. For MitoTracker™ Green FM (ThermoFisher), a 1 mM stock solution was prepared from dry product, which was diluted in Opti-MEM complete to the desired concentration (100 nM) for treatment and incubation 30 min before measurement. For HCS LipidTOX™ Green neutral lipid stain, LysoTracker™ Green DND-26 and BODIPY™ FL C5-Ceramide complexed to BSA golgi dye (ThermoFisher), the provided stock solutions were similarly diluted and treated according to the manufacturer's protocol. All image analyses were processed using ImageJ. Colocalization measurements were taken using the ImageJ plugin Coloc2 with PSF = 5.0 and verified with Costes' significance test. Linear correlation graphs were created using the RGB Profile Plot plugin.

4.5.8 [1]OAc real-time uptake. Uptake of [1]OAc was captured via live cell imaging, with fluorescence Spinning Disk Confocal Microscopy. 2×10^4 A549 cells were seeded in a μ -slide 8-well confocal plate (ibidi) and allowed to adhere for 24 hours. Cells had been treated with [1]OAc (5 μ M) for 15 minutes when image acquisition started. Fluorescence and bright-field images were acquired at 50 seconds interval for 12 hours. Control wells were used to set laser and gain intensity such as to eliminate the background and exclude signal saturation.

4.5.9 Time-dependent colocalization of [2]OAc with lysosomes and mitochondria. To investigate the colocalization over time of [2]OAc with the lysosomes and the mitochondria, 7×10^4 A549 cells were seeded in a round dish (ibidi) and allowed to adhere for 24 hours, then treated with [2]OAc (5 μ M) for 3 hours after which time the compound was removed. Fluorescence Spinning Disk Confocal 3D images were captured at time points 3.5, 4.5, 5.0, 5.5, 6.0, 21.0 and 45.0 hours after addition of the compound (time=0), for 8-16 cells per time point. At each time point, 3D fluorescent and bright-field images were captured with a step size of 200 nm. Image processing and extraction of the Mander's Overlap Coefficient (MOC) was carried out for each focal plane using the NIS Elements software (Nikon Corporation, Japan). Further data processing was performed with Matlab. Quantification of [2]OAc intensity inside

the cells over time was performed by averaging the mean [2]OAc fluorescence intensity per cell, for 6-11 cells per time point.

4.5.10 Cell uptake inhibition experiment using flow cytometry. At $t = 0$ h, 2.0×10^5 A549 cells (1 mL, Opti-MEM complete) were seeded into flat bottom 24-well plates (Cellstar® F-bottom No.622160). At $t = 21$ h, all wells except controls were treated with inhibitor solutions prepared in Opti-MEM complete unless otherwise noted at the following treatment concentrations: NaN_3 (1 mg / mL), Pitstop 2 (20 μM , Opti-MEM without fetal calf serum or other additives), Dynasore (80 μM), Nocodazole (40 μM), and Wortmannin (250 nM). At $t = 22$ h, stock solutions of drug compounds were added to each well to a final concentration of 5 μM . At $t = 24$ h, all wells were prepared and measured by flow cytometry, with the parameter “RED-B” (488 nm excitation, 661 ± 15 nm emission) for each drug compound. The experiments were carried out in three independent experiments and analyzed via FlowJ 10.

4.5.11 EM imaging in A549 cells. A549 cells (3×10^5 cells/mL, 9 mL, Opti-MEM complete medium) were seeding into 10 cm diameter plate and incubated for 24 h under normoxic condition (21% O_2 , 5% CO_2 , 37 °C). After that, the cells were treated with [2]OAc (5 μM) for another 24 h under normoxic condition. Then cells were fixed for 2 h in 1.5% glutaraldehyde in 0.1M Cacodylate buffer at room temperature and post-fixed first for 1 h in 1% Osmium tetroxide and then for 1 h in 1% Uranyl acetate. The fixed cells were dehydrated through a series of ethanol and flat embedded in Epon. Ultrathin sections (50 nm) of the embedded cells were produced in a Leica UC6 ultra-microtome and transferred to a formvar and carbon coated copper grid. The sections were stained with 7% Uranyl acetate and 1% Lead citrate before imaging in the TEM. Electron microscopy images were recorded using a Tecnai 12 TEM (FEI Company) equipped with an EAGLE 4×4 K digital camera using a magnification of 13,000x.

4.6 Acknowledgments

X.-Q Zhou gratefully acknowledges the China Scholarship Council (CSC) for a personal grant (No. 201606200045). This work is supported by the European Research Council via a Starting Grant to S. Bonnet and Huygens Fellowship Leiden University Grant to P. Papadopolou. Maria Mytiliniou and Doris Heinrich acknowledge funding from the Fraunhofer Attract "3DNanoCell" grant. Dr. S. Zheng is thanked for the ICP-MS measurement. Prof. E. Bouwman is wholeheartedly acknowledged for scientific discussion and support. The cryo-EM measurements benefited from access to the Netherlands Centre for Electron Nanoscopy (NeCEN) at Leiden University.

4.7 References

1. V. W. Yam, V. K. Au and S. Y. Leung, *Chem. Rev.*, 2015, **115**, 7589-7728.
2. A. Diez, J. Fornies, C. Larraz, E. Lalinde, J. A. Lopez, A. Martin, M. T. Moreno and V. Sicilia, *Inorg. Chem.*, 2010, **49**, 3239-3251.
3. Y. S. Wong, M. C. Tang, M. Ng and V. W. Yam, *J. Am. Chem. Soc.*, 2020, **142**, 7638-7646.
4. M. A. Soto, V. Carta, R. J. Andrews, M. T. Chaudhry and M. J. MacLachlan, *Angew. Chem. Int. Ed.*, 2020, **59**, 10348-10352.
5. W. Lu, Y. Chen, V. A. Roy, S. S. Chui and C. M. Che, *Angew. Chem. Int. Ed.*, 2009, **48**, 7621-7625.
6. A. Aliprandi, D. Genovese, M. Mauro and L. De Cola, *Chem. Lett.*, 2015, **44**, 1152-1169.
7. J. Romanova, M. R. Ranga Prabhath and P. D. Jarowski, *J. Phys. Chem.*, 2016, **120**, 2002-2012.
8. M. Y. Yuen, V. A. Roy, W. Lu, S. C. Kui, G. S. Tong, M. H. So, S. S. Chui, M. Muccini, J. Q. Ning, S. J. Xu and C. M. Che, *Angew. Chem. Int. Ed.*, 2008, **47**, 9895-9899.
9. X. Yan, T. R. Cook, P. Wang, F. Huang and P. J. Stang, *Nat. Chem.*, 2015, **7**, 342-348.
10. H. L. Au-Yeung, S. Y. Leung, A. Y. Tam and V. W. Yam, *J. Am. Chem. Soc.*, 2014, **136**, 17910-17913.
11. K. Li, G. S. Ming Tong, Q. Wan, G. Cheng, W. Y. Tong, W. H. Ang, W. L. Kwong and C. M. Che, *Chem. Sci.*, 2016, **7**, 1653-1673.
12. A. Aliprandi, M. Mauro and L. De Cola, *Nat. Chem.*, 2016, **8**, 10-15.
13. H. Xiang, J. Cheng, X. Ma, X. Zhou and J. J. Chruma, *Chem. Soc. Rev.*, 2013, **42**, 6128-6185.
14. M. Mauro, A. Aliprandi, D. Septiadi, N. S. Kehr and L. De Cola, *Chem. Soc. Rev.*, 2014, **43**, 4144-4166.
15. N. A. Smith and P. J. Sadler, *Philos. Trans. R. Soc. A*, 2013, **371**, 20120519.
16. C. Ash, M. Dubec, K. Donne and T. Bashford, *Lasers in Med. Sci.*, 2017, **32**, 1909-1918.
17. D. Septiadi, A. Aliprandi, M. Mauro and L. De Cola, *RSC Adv.*, 2014, **4**, 25709-25718.
18. J. L. Tsai, T. Zou, J. Liu, T. Chen, A. O. Chan, C. Yang, C. N. Lok and C. M. Che, *Chem. Sci.*, 2015, **6**, 3823-3830.
19. C.-K. Koo, B. Lam, S.-K. Leung, M. H.-W. Lam and W.-Y. Wong, *J. Am. Chem. Soc.*, 2006, **128**, 16434-16435.
20. C. Y.-S. Chung, S. P.-Y. Li, M.-W. Louie, K. K.-W. Lo and V. W.-W. Yam, *Chem. Sci.*, 2013, **4**, 2453-2462.
21. L. Y. Liu, H. Fang, Q. Chen, M. H. Chan, M. Ng, K. W. Wang, W. Liu, Z. Tian, J. Diao, Z. W. Mao and V. W. W. Yam, *Angew. Chem. Int. Ed.*, 2020, DOI: 10.1002/anie.202007878.
22. N. Metzler-Nolte and Z. Guo, *Dalton Trans.*, 2016, **45**, 12965-12965.
23. X. Wang, X. Wang, S. Jin, N. Muhammad and Z. Guo, *Chem. Rev.*, 2019, **119**, 1138-1192.
24. N. Cutillas, G. S. Yellol, C. de Haro, C. Vicente, V. Rodríguez and J. Ruiz, *Coord. Chem. Rev.*, 2013, **257**, 2784-2797.
25. S. C. Kui, F. F. Hung, S. L. Lai, M. Y. Yuen, C. C. Kwok, K. H. Low, S. S. Chui and C. M. Che, *Chem. Eur. J.*, 2012, **18**, 96-109.
26. L. J. Chen and H. B. Yang, *Acc. Chem. Res.*, 2018, **51**, 2699-2710.
27. M. L. Saha, X. Yan and P. J. Stang, *Acc. Chem. Res.*, 2016, **49**, 2527-2539.
28. C. N. Lok, T. Zou, J. J. Zhang, I. W. Lin and C. M. Che, *Adv. Mater.*, 2014, **26**, 5550-5557.
29. W. Zhang, M. Wang, W. Tang, R. Wen, S. Zhou, C. Lee, H. Wang, W. Jiang, I. M. Delahunty, Z. Zhen, H. Chen, M. Chapman, Z. Wu, E. W. Howerth, H. Cai, Z. Li and J. Xie, *Adv. Mater.*, 2018, **30**, e1805557.
30. L. Cheng, C. Wang, L. Feng, K. Yang and Z. Liu, *Chem. Rev.*, 2014, **114**, 10869-10939.
31. B. Yang, Y. Chen and J. Shi, *Chem*, 2018, **4**, 1284-1313.
32. H. Kang, S. Hu, M. H. Cho, S. H. Hong, Y. Choi and H. S. Choi, *Nano Today*, 2018, **23**, 59-72.
33. D. M. Samhadaneh, G. A. Mandl, Z. Han, M. Mahjoob, S. C. Weber, M. Tuznik, D. A. Rudko, J. A. Capobianco and U. Stochaj, *ACS Appl. Bio Mater.*, 2020, **3**, 4358-4369.
34. Y. Feng, H. Chen, Y. Wu, I. Que, F. Tamburini, F. Baldazzi, Y. Chang and H. Zhang, *Biomaterials*, 2020, **230**, 119637.
35. M. Buchner, P. Garcia Calavia, V. Muhr, A. Kroninger, A. J. Baeumner, T. Hirsch, D. A. Russell and M. J. Marin,

- Photochem. Photobiol. Sci.*, 2019, **18**, 98-109.
36. J. Zhao and M. H. Stenzel, *Polym. Chem.*, 2018, **9**, 259-272.
 37. J. Chen, J. Li, J. Zhou, Z. Lin, F. Cavalieri, E. Czuba-Wojnilowicz, Y. Hu, A. Glab, Y. Ju, J. J. Richardson and F. Caruso, *ACS Nano*, 2019, **13**, 11653-11664.
 38. S. Behzadi, V. Serpooshan, W. Tao, M. A. Hamaly, M. Y. Alkawareek, E. C. Dreaden, D. Brown, A. M. Alkilany, O. C. Farokhzad and M. Mahmoudi, *Chem. Soc. Rev.*, 2017, **46**, 4218-4244.
 39. X. Q. Zhou, M. Xiao, V. Ramu, J. Hilgendorf, X. Li, P. Papadopoulou, M. A. Siegler, A. Kros, W. Sun and S. Bonnet, *J. Am. Chem. Soc.*, 2020, **142**, 10383-10399.
 40. X. Q. Zhou, A. Busemann, M. S. Meijer, M. A. Siegler and S. Bonnet, *Chem. Commun.*, 2019, **55**, 4695-4698.
 41. L. Zong, Y. Xie, C. Wang, J. R. Li, Q. Li and Z. Li, *Chem. Commun.*, 2016, **52**, 11496-11499.
 42. M. Yamaguchi, S. Ito, A. Hirose, K. Tanaka and Y. Chujo, *Mater. Chem. Front.*, 2017, **1**, 1573-1579.
 43. J. Mei, N. L. Leung, R. T. Kwok, J. W. Lam and B. Z. Tang, *Chem. Rev.*, 2015, **115**, 11718-11940.
 44. H. Qian, M. E. Cousins, E. H. Horak, A. Wakefield, M. D. Liptak and I. Aprahamian, *Nat. Chem.*, 2017, **9**, 83-87.
 45. L. Ravotto and P. Ceroni, *Coord. Chem. Rev.*, 2017, **346**, 62-76.
 46. Y. Ai, Y. Li, H. L. Fu, A. K. Chan and V. W. Yam, *Chem. Eur. J.*, 2019, **25**, 5251-5258.
 47. J. Zhao, Z. Feng, D. Zhong, X. Yang, Y. Wu, G. Zhou and Z. Wu, *Chem. Mater.*, 2018, **30**, 929-946.
 48. Z. Gao, Y. Han, Z. Gao and F. Wang, *Acc. Chem. Res.*, 2018, **51**, 2719-2729.
 49. Y. Zhu, M. Zhang, L. Luo, M. R. Gill, C. De Pace, G. Battaglia, Q. Zhang, H. Zhou, J. Wu, Y. Tian and X. Tian, *Theranostics*, 2019, **9**, 2158-2166.
 50. V. H. S. van Rixel, A. Busemann, M. F. Wissingh, S. L. Hopkins, B. Siewert, C. van de Griend, M. A. Siegler, T. Marzo, F. Papi, M. Ferraroni, P. Gratteri, C. Bazzicalupi, L. Messori and S. Bonnet, *Angew. Chem. Int. Ed.*, 2019, **58**, 9378-9382.
 51. K. W. Dunn, M. M. Kamocka and J. H. McDonald, *Am. J. Physiol. Cell Physiol.*, 2011, **300**, C723-742.
 52. C. A. Puckett, R. J. Ernst and J. K. Barton, *Dalton Trans.*, 2010, **39**, 1159-1170.
 53. J. Yang, J. Tu, G. E. M. Lamers, R. C. L. Olsthoorn and A. Kros, *Adv. Healthc. Mater.*, 2017, **6**, 1700759.
 54. D. Dutta, C. D. Williamson, N. B. Cole and J. G. Donaldson, *PLOS One*, 2012, **7**, e45799.
 55. G. Preta, J. G. Cronin and I. M. Sheldon, *Cell Commun. Signal.*, 2015, **13**, 24.
 56. O. Harush-Frenkel, N. Debotton, S. Benita and Y. Altschuler, *Biochem. Biophys. Res. Commun.*, 2007, **353**, 26-32.
 57. T.-G. Iversen, T. Skotland and K. Sandvig, *Nano Today*, 2011, **6**, 176-185.
 58. E. M. M. Manders, F. J. Verbeek and J. A. Aten, *J. Microsc.*, 1993, **169**, 375-382.
 59. Z. Wei, W. Su, H. Lou, S. Duan and G. Chen, *J. Mol. Cell. Biol.*, 2018, **10**, 539-548.
 60. Z. Zolmajd-Haghighi and Q. S. Hanley, *Biophys. J.*, 2014, **106**, 1457-1466.
 61. Z. Gao, P. A. Korevaar, R. Zhong, Z. Wu and F. Wang, *Chem. Commun.*, 2018, **54**, 9857-9860.
 62. L. Barrientos, S. Miranda-Rojas and F. Mendizabal, *Int. J. Quantum Chem.*, 2018, **119**, e25675.
 63. Q. Wan, W.-P. To, X. Chang and C.-M. Che, *Chem*, 2020, **6**, 945-967.
 64. X. Yin, S. A. Warren, Y. T. Pan, K. C. Tsao, D. L. Gray, J. Bertke and H. Yang, *Angew. Chem. Int. Ed.*, 2014, **53**, 14087-14091.

5

Self-assembling cyclopalladated photosensitizers for photodynamic therapy: tumor accumulation and anti-tumor activity in a skin melanoma xenograft

*Though small-molecule drugs remain the major form of anticancer chemotherapy, they usually show low tumor accumulation and severe side effects. Nanocarriers are considered to be an appealing strategy to increase drug accumulation in the tumor via the enhanced permeability and retention effect. However, many of these nanocarriers are still limited by low drug-loading capacity and tumor accumulation efficiency. In this work, we designed a molecular photosensitizer self-assembly nanosystem (MoPSAN) based on the supramolecular Pd...Pd interaction between cyclometalated palladium (i.e. cyclopalladated) complexes **PdL**. On the one hand the drug loading issue of nanocarriers is overcome because each molecule of the self-assembly is a **PdL** photosensitizer. On the other hand, the photosensitizer is taken up with high efficacy via endocytosis because it is self-assembled into a nanoparticle. As a result, the **PdL** assembly shows low toxicity in the dark, but upon irradiation with green light it generates massive amount of reactive oxygen species, resulting in effective anticancer effect both in vitro and in a skin melanoma tumor xenografts. Overall, the Pd...Pd interactions stimulate high tumor accumulation efficiency in vivo without jeopardy of the phototoxicity of the photosensitizer, suggesting that this form of supramolecular bonds can be used for the efficient tumor delivery of new nanomedicines.*

This chapter will be submitted as a full paper: X.-Q Zhou, W. Sun*, P. Wang, V. Ramu, S. Jiang, S. Abyar, P. Papadopoulou, Y. Shao, M. A Sieglar, F. Buda, A. Kros, S. Bonnet*, *manuscript in preparation*.

5.1 Introduction

Curing cancer is one of the toughest challenges of modern medicine,¹ and chemotherapy remains one of the main tools in oncology: using chemicals to kill cancer cells.² However, the small size of many molecular chemotherapy drugs is also responsible for their main disadvantages: chemotherapy suffers from nonspecific delivery, rapid blood clearance, and low accumulation in tumors, which altogether generates severe side effects for cancer patients.³ To overcome these restrictions, vehicles such as polymer nanoparticles, liposomes, or nanosized inorganic materials, have been developed as drug delivery systems that can be functionalized with molecular chemotherapy drugs.⁴⁻⁶ In a limited number of systems now clinically applied, such conjugation was shown to decrease the drug's systemic toxicity, protect it from blood/renal clearance, and enhance tumor accumulation *via* the enhanced permeability and retention (EPR) effect.^{7, 8} However, many nanocarriers show low drug loading capacity (typically <20%),^{9, 10} while the resulting tumor accumulation remains comparatively low: recent studies showed that a median 0.7% only of the administered nanoformulated drug dose ends up in the solid tumor.^{10, 11} These shortcomings dramatically restrict the promising clinical potential of nano-sized drug delivery systems.

Recently, a new approach was proposed, called drug self-delivery system (DSDS), which consists in using molecular drugs that self-assemble themselves as nanoparticles and accumulate at the tumor site, without the assistance of any specialized nanocarriers.¹² One main advantage of this approach is the high drug-loading capacity of such systems, as the nanoparticles are solely composed of drug molecules. However, this advantage comes with an obvious disadvantage: keeping a low cytotoxicity to healthy organs is more tricky to achieve, as each nanoparticle brings into a cell many toxic molecules. A solution to this problem is proposed here, and consists of using a light-activatable prodrug, or photosensitizer, as the building block for the DSDS. Such molecules are non-toxic or poorly toxic in the dark, but they can help to generate some highly cytotoxic species by *in vivo* light irradiation of the tumor.¹³ This form of prodrugs, called photodynamic therapy (PDT) sensitizers, are currently developed at a high pace in the clinics because of the low side effects experienced by cancer patients.¹⁴⁻¹⁶ At the moment, most clinical PDT photosensitizers work *via* the so-called type II PDT mechanism, which involves the triplet excited state of the photosensitizer (³PS) transferring its energy to triplet ground-state dioxygen (³O₂) to generate cytotoxic singlet dioxygen (¹O₂).¹⁷ Ideally, when a sufficient number of PS molecules, enough light, and enough ³O₂, are present altogether inside the cancer tissue, very efficient cell death occurs. However, this efficacy can

become dramatically lower in hypoxic regions of the tumors, where $^3\text{O}_2$ concentration is low.¹⁸ The photosensitizer used here is of another type: upon light irradiation, its excited triplet state transfers an electron to the surrounding biomolecules, which generates cytotoxic reactive oxygen species (ROS) such as $\text{O}_2^{\cdot-}$, OH^{\cdot} , and H_2O_2 .^{19, 20} This mechanism, called PDT type I, also requires a large amount of photosensitizer molecule to be present inside the irradiated tumor tissue, which can be achieved by self-assembly of the PS into nanoparticles. However, it is much less dependent on the concentration of O_2 . The results presented here, which combine DSDS and type I PDT photosensitizers to make a MoPSAN, provides a highly antitumor active treatment in a skin melanoma xenograft in mice, notably because high phototoxicity is achieved even in hypoxic cancer cells.

The photosensitizer of interest, **PdL** (Figure 1a), contains a palladium(II) metal center, which is also present in the recent clinically approved PDT sensitizers padeliporfin.²¹ In contrast with padeliporfin, however, the bis-cyclometalated palladium compounds presented here self-assembles *via* metallophilic Pd...Pd interactions.²²⁻²⁴ The M-C bond of cyclometalated complexes compensates for the positive charge of the metal ion, which when combined with the strong π - π stacking of the planar aromatic ligand, allows the metal d_z^2 orbitals of nearby complexes to overlap. This orbital overlap generates the supramolecular metal...metal interactions,²⁵ which leads not only to a lower HOMO-LUMO gap than in the monomer, but also to self-assembly in aqueous solution.^{22, 26} We demonstrate in this work that this new palladium photosensitizer **PdL**, not only self-assembles *via* the Pd...Pd interaction in the blood of mice upon intravenous tail injection, but also that it circulates for hours in the body and leads to tumor accumulation and excellent antitumor effect upon light irradiation 12 h after injection.

5.2 Results

5.2.1 Synthesis and characterization of palladium complex. The cyclometalated palladium complex **PdL** was synthesized by boiling the ligand H_2L and $\text{Pd}(\text{OAc})_2$ in acetic acid (Figure 5.1a). The activation of the two C-H bonds of the ligand upon coordination to palladium(II) was unequivocally demonstrated by ESI-MS, ^1H and ^{13}C NMR and X-ray crystal structure determination (Table AIV.1 and Figure 5.1b). The neutral palladium complex crystallized in the centrosymmetric $P2_1/n$ monoclinic space group. The palladium ion is in a square-planar geometry with a dihedral angle N2-C11-C17-N3 of 0.25° , and a low τ value (0.11; this structural parameter characterizes the planar *vs.* tetrahedral geometry of tetracoordinate metal complexes).²⁷ The structure shows head-to-tail dimers that are stabilized by π - π stacking as demonstrated by the short interplanar distance of 3.4 Å, and by metallophilic interaction, as

shown by the short Pd...Pd distance of 3.518 Å (Figure 5.1b). A DFT model of the dimer confirmed its stability, with a converged Pd...Pd distance of 3.52 Å (Figure 5.1c) that matches well with that observed in the crystal lattice. As shown in the DFT model, the Pd...Pd interaction is derived from the hybridization of both palladium d_{4z^2} orbitals and π orbitals of the ligand in the HOMO of the dimer. The HOMO-LUMO gap is decreased from -3.543 eV in the monomer to -3.319 eV in the dimer, suggesting a bathochromic shift should be observed in the absorbance spectrum due to the Pd...Pd interaction. TDDFT calculations confirmed this expectation with HOMO-LUMO transitions at 502 nm for the dimer vs. 383 nm for the monomer (Figure 5.1d, Table AIV.2).

When dissolved in DMSO, **PdL** showed a modest absorption band based on ligand-to-ligand charge transfer states (LLCT) in the range 434-540 nm, with a maximum at 481 nm ($\epsilon = 3700 \text{ M}^{-1} \text{ cm}^{-1}$, Figure 1e and Table AIV.3). At concentrations of 10 μM , 100 μM , or 1000 μM in DMSO, the complex showed a constant emission maximum at 564 nm with low phosphorescence quantum yield and short lifetime (Figure 5.1e, $\phi_p = 0.0008$, $\tau = 0.406 \text{ ns}$, Table AIV.3), characteristic for a monomer **PdL** molecule. However, in a DMSO/H₂O 1:9 volumetric mixture (100 μM), a rapid (<1 min) change of the absorbance spectrum was observed, accompanied by a significant increase of the baseline and the generation of a new absorbance peak at 504 nm, characteristic for the MMLCT states typically from Pd...Pd interaction;²⁸ the absorption spectra then remained constant for as long as the measurement was continued (30 min, Figure 5.1f). The TEM pictures of this solution showed the self-assembly of **PdL** into nanorods and nanocubes (Figure 1f, insert). Usually, the formation of Pd...Pd supramolecular bonds is accompanied by a long-wavelength emission peak.²⁸ As shown in Figure 5.1g, an increase of the H₂O content of DMSO ($\text{fw} = V_{\text{water}}/V_{\text{total}}$) indeed led to a decrease of the monomeric emission peak at 564 nm in pure DMSO ($\text{fw} = 0.0$) and gradual replacement by an emission maximum at 593 nm at $\text{fw} = 0.5$ that evolved into a final band at 610-670 nm ($\text{fw} = 0.9$), concomitant with the formation of a precipitate. In a THF/H₂O solution, similar self-assembly was observed, but with a slower polymerization rate and resulting in different nanostructures as observed with TEM (nanocrystals and nanofibers, Figure AIV.1-2). These results suggest that the structure and size of the nanoparticles derived from **PdL** are highly influenced by the nature of the solvent and the rate of self-assembly.

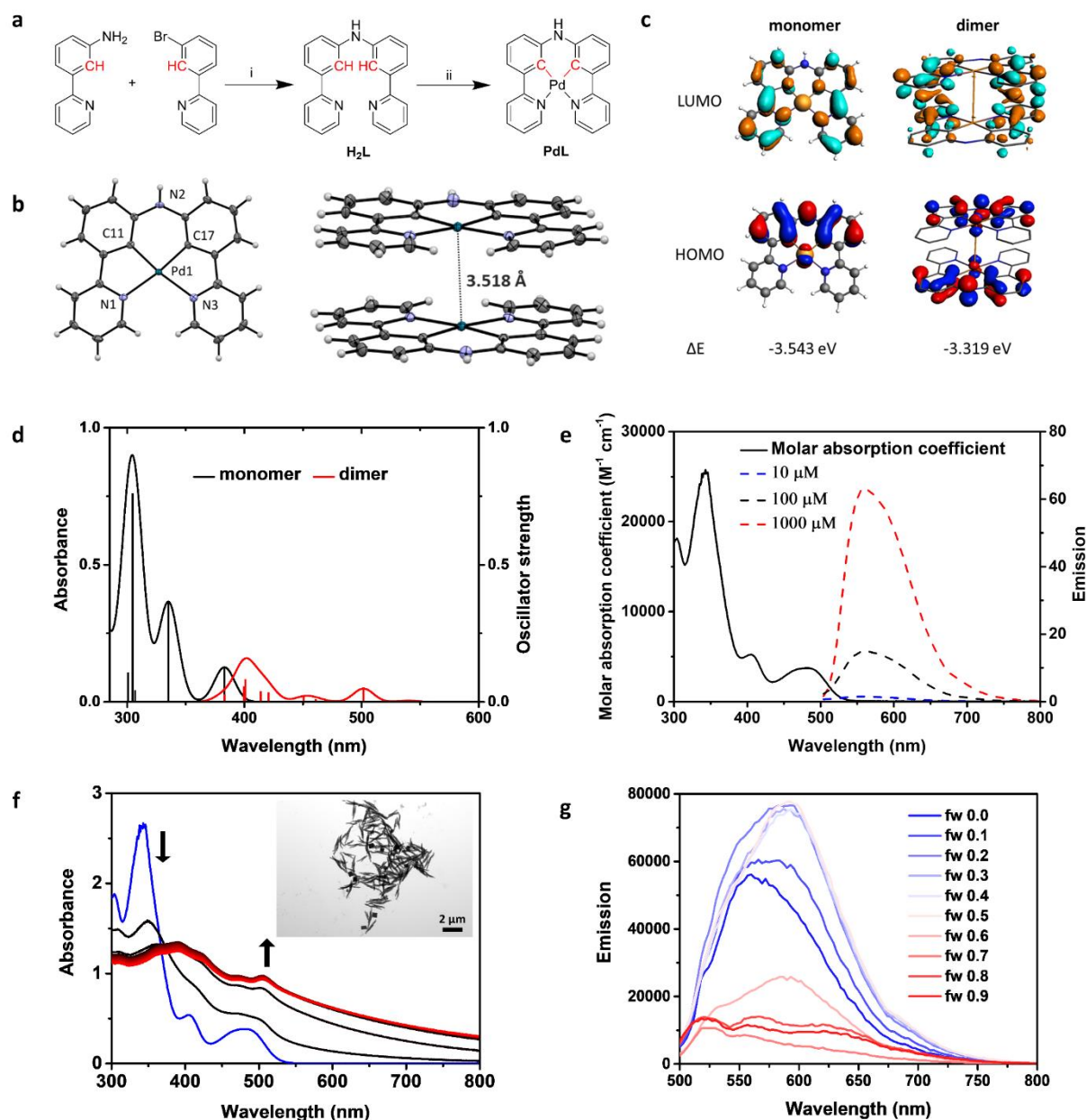


Figure 5.1 (a) Synthesis of **H₂L** and **PdL** ((i) Pd(dba)₂, KOt-Bu, BINAP, Toluene, 95 °C, N₂, 72 h, yield 67%; (ii) Pd(OAc)₂, CH₃COOH, 135 °C, 24 h, yield 56%). (b) Displacement ellipsoid plot (50% probability level) of **PdL** and its stacking structure at 110(2) K. (c) DFT calculation of HOMOs (bottom) and LUMOs (top) orbitals of **PdL** as a monomer or dimer (calculated Pd...Pd distance 3.52 Å). Occupied orbitals (HOMO) have red and blue lobes, and unoccupied orbitals (LUMO) brown and cyan lobes. Element color code: blue = N, grey = C, brown = Pd, white = H. (d) TDDFT-calculated spectra of **PdL** as a monomer (red line) or dimer (black line). Level of theory: TDDFT/PBE0/TZP/COSMO (methanol). (e) The absorption spectrum (black solid line) and emission spectra of **PdL** in pure DMSO solution at different concentrations (blue dash line 10 μ M; black dash line 100 μ M, red dash line 1000 μ M;

excitation 419 nm). (f) Time evolution of the absorption spectra of DMSO/H₂O solution (100 μ M, V/V = 1/9) of **PdL** at 298 K for 30 min (30 s interval, the color of spectra change from black (0 min) to red (30 min); the blue line is the absorbance spectra of **PdL** (100 μ M) in pure DMSO. Inset picture: the TEM images of nanostructures of **PdL** in DMSO/H₂O solution (100 μ M, V/V = 1/9, scale bar 2 μ m) (g) Emission spectra of **PdL** (100 μ M) in H₂O/DMSO mixtures with different volumetric ratios ($f_w = V_{\text{water}}/V_{\text{total}}$).

5.2.2 Self-assembly of PdL in cell-growing medium. Before evaluating the biological properties of the complex **PdL** in cancer cells, an important but often ignored step consists in determining its self-assembly behavior in cell-growing medium, here Opti-MEM complete containing 2.5 vol% of fetal calf serum (FCS). When the complex (25 μ M) was dissolved in medium, aggregation into nanoparticles immediately occurred, as demonstrated by the maximum hydrodynamic diameter of 164 nm determined with dynamic light scattering (DLS, Figure 5.2a). After 30 min, the maximum hydrodynamic diameter of nanoparticles had only slightly shifted (to 190 nm), but the number of particles had increased significantly (Figure AIV.3). The absorption spectrum of **PdL** in medium showed a gradual increase in intensity over 2 h, characteristic for the light-scattering due to self-assembled nanoparticles. After the first 2 h the absorption spectrum remained stable over 24 h, demonstrating the stability of the aggregates for longer time scales (Figure 5.2b). The morphology of the self-assembled nanostructures was then determined using TEM, which showed a stepwise self-assembly process (Figure 5.2c, 50 nm). The structures appeared first as regular hollow nanorods, which gradually lengthened and were surrounded by small nanodots with a much lower thickness-to-length ratio, demonstrating that there might be several nanostructures in medium. According to cryo-EM imaging, the nanofibers had a crystalline structure with a repeating distance of ~ 1.68 nm, as indicated by fast Fourier transform (Figure 5.2d). On the other hand, fewer nanoparticles were detected in the cryo-EM images than in the TEM images, suggesting that **PdL** might exist both as isolated molecules or small oligomers, and larger nanoaggregates in the medium. In summary, DLS, EM, and UV-vis measurements demonstrated the time-dependent self-assembly of **PdL** into nanorods and nanoparticles in cell-growing medium, which probably form *via* the metallophilic Pd...Pd interactions.

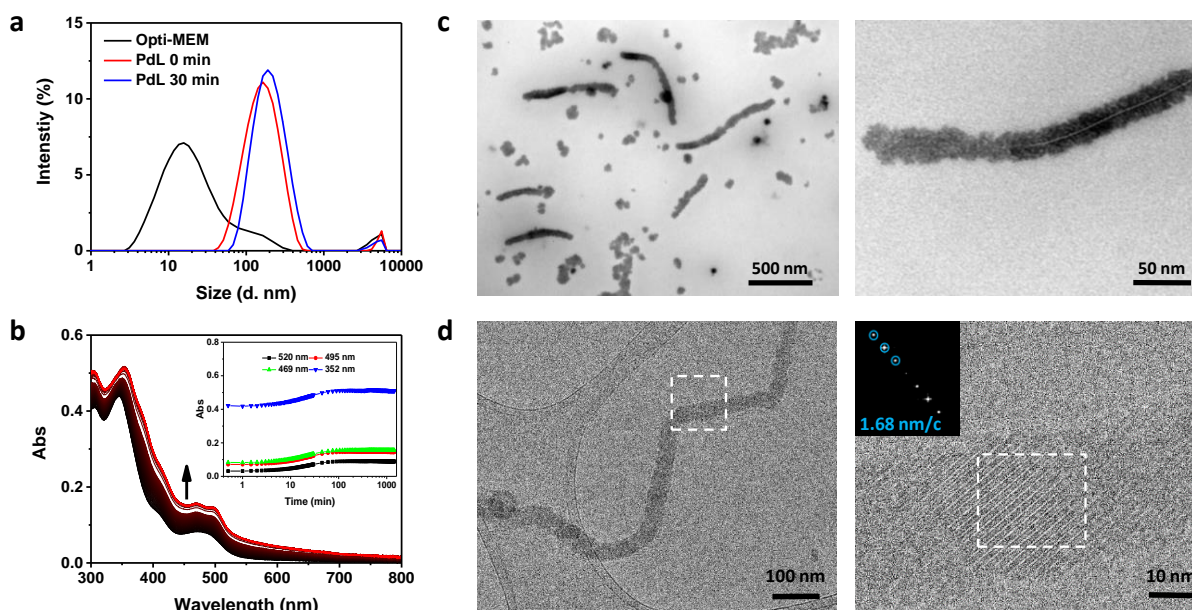


Figure 5.2 (a) Size distribution of Opti-MEM complete medium, and its **PdL** (25 μM) solution at 0 min (red line) or 30 min (blue line) according to DLS analysis at room temperature. (b) Observation of absorbance spectra of **PdL** (25 μM) in Opti-MEM complete medium over 24 h (30 s interval for the first 30 min, 15 min interval for the next 23.5 h). (c, d) TEM images and cryo-EM images of samples prepared from an Opti-MEM complete medium solution of **PdL** (25 μM) at room temperature.

5.2.3 Photodynamic properties of PdL in cell-growing medium. The formation of self-assembled nanostructures may influence the photochemical properties of the palladium complex. As mentioned above, PDT may occur either *via* a type I mechanism (electron transfer) or type II (energy transfer) mechanism. Type II photodynamic properties are straightforward to determine *via* direct detection of the near-infrared emission peak of $^1\text{O}_2$ at 1270 nm, or *via* indirect detection of $^1\text{O}_2$ using chemoselective chemical probes.²⁹ NIR detection of $^1\text{O}_2$ by monomeric **PdL** in MeOD under blue light irradiation (450 nm) showed very low quantum yields for $^1\text{O}_2$ generation ($\phi_{\Delta} = 0.09$, using $[\text{Ru}(\text{bpy})_3]\text{Cl}_2$ as standard, $\phi_{\Delta}^{\text{ref}} = 0.73$, Figure 5.3a, Table AIV.3). To determine the value of ϕ_{Δ} of the nano-aggregated **PdL** in Opti-MEM medium, 9,10-anthracenediyl-bis(methylene)-dimalonic acid (ABMDMA) was used as hydrophilic probe for $^1\text{O}_2$. In the dark, this dye absorbs light at 378 nm, but in the presence of photogenerated $^1\text{O}_2$, it forms an endoperoxide that leads to loss of conjugation and thus a decrease in absorbance at 378 nm. Upon green light irradiation of medium-containing ABMDMA and **PdL** (25 μM), the absorbance of ABMDMA did not decrease significantly (Figure 5.3b), indicating $^1\text{O}_2$ generation was negligible ($\phi_{\Delta} = 0.04$; rose bengal used as

standard, $\phi_{\Delta} = 0.68$, Figure AIV.4).²⁴ Overall, **PdL** was found to be a poor PDT type II sensitizer, both as a monomer and in the polymeric state. By contrast type I PDT sensitizers can be characterized by the generation of superoxide ($O_2^{\cdot-}$) as primary photochemical species, which can further react with many biological substrates to generate other ROS such as HO^{\cdot} or H_2O_2 .³⁰ When a DMSO or Opti-MEM solution of **PdL** (25 μ M) was irradiated with green light (525 nm) in the presence of dihydroethidium (DHE), a chemoselective chemical probe for superoxide, the oxidation product 2-hydroxyethidium was produced efficiently, as shown by its emission at 590-620 nm (Figure 5.3c, **Figure AIV.5**).³¹ The results of these experiments suggest that **PdL** is capable of generating superoxide upon green light irradiation, both in the monomeric and in aggregated states, and that this compound is hence essentially a PDT type I photosensitizer that is almost incapable of generating singlet oxygen.

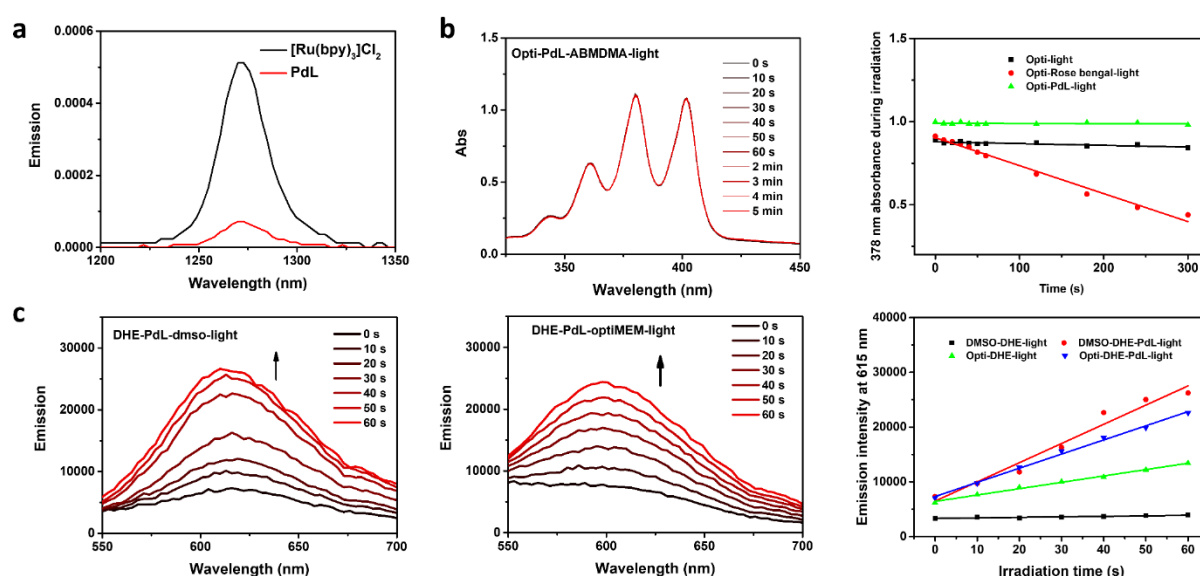


Figure 5.3 (a) Singlet oxygen emission spectra of $[Ru(bpy)_3]Cl_2$ (black) and **PdL** (red) in CD_3OD irradiated with blue light ($\lambda_{ex} = 450$ nm, 50 mW, 0.4 W/cm^2). (b) The absorbance change of ABMDMA Opti-MEM complete solution (100 μ M) in the presence of **PdL** or rose bengal (25 μ M) under green light irradiation (515 nm, 2.0 mW) over 5 min. (c) The emission spectra of a dihydroethidium (DHE) solution (DMSO or Opti-MEM complete) in the presence of **PdL** (25 μ M) under green light irradiation over 60 s.

5.2.4 Photocytotoxicity, cell death mechanism and *in vivo* tumor inhibition. Considering the significant absorption of 520 nm light by **PdL** ($\epsilon = 915$ $M^{-1} cm^{-1}$) and its promising PDT type I properties, its photocytotoxicity in 2D-monolayers of three different human cancer cell lines (lung carcinoma A549, epidermoid carcinoma A431, melanoma (A375) was evaluated *in vitro* using a reported protocol,³² both in the dark and under a low dose of green light (520 nm,

13 J/cm²). **PdL** showed moderate dark cytotoxicity with EC₅₀ above 10 μM for the three cancer cell lines under normoxic growing conditions (21% O₂, 37 °C). By contrast, after green light irradiation (520 nm, 20 min, 10.9 mW/cm², 13 J/cm²), the complex exhibited high photocytotoxicity with sub-micromolar EC₅₀ and a very high photoindex PI = EC_{50,dark}/EC_{50,light} of 72 (Figure 5.4a, **Figure AIV.6** and Table 1). Interestingly, in A375 cells growing in hypoxic conditions (1% O₂) the EC₅₀ of **PdL** also decreased dramatically upon the same dose of green light irradiation, *i.e.* from 15.9 μM in the dark to 0.49 μM after activation with green light, thus demonstrating outstanding PDT efficacy of this complex even at low dioxygen concentrations. The cell death mode resulting from the PDT treatment with **PdL** was determined *via* Annexin V/Propidium iodide double staining experiments using flow cytometry either 2 h, 4 h, or 24 h after irradiation (Figure 5.4b and Figure AIV.7). Clearly, **PdL** (0.5 and 2 μM) showed no or limited cell death in dark conditions. In the irradiated group, no toxicity was observed after 2 h, but after 4 h and 24 h, the number of apoptotic and necrotic cells had increased significantly, suggesting that **PdL** started to induce cancer cell death 4 h after irradiation *via* both cell death mechanisms.

3D multicellular tumor spheroid models provide a more accurate biological evaluation not only of compound toxicity but also of the physical penetration of light, drugs, and nanoparticle-based delivery systems.³³ The photocytotoxicity of **PdL** in A549 and A375 spheroids was hence determined using a CellTiter-Glo end-point viability assay in 96-well round-bottom Corning spheroid plates. In the dark, **PdL** was nearly non-toxic to A549 spheroids (EC_{50, normoxic} > 25 μM), while moderate toxicity was observed for A375 tumor spheroids (EC_{50, normoxic} = 9.19 μM, EC_{50, hypoxic} = 14.3 μM). However, after green light irradiation, **PdL** showed nearly 100-folds increase in cytotoxicity, leading to submicromolar EC₅₀ values (around 0.20 μM), accompanied by the visible collapse of the spheroid cores and dramatic shrinking of the spheroid diameters (Figure 5.4c, AIV.8 and Table 1). A further Hoechst 33342/Propidium iodide double-staining experiment was carried out to compare the morphology and health status of A375 spheroids treated with **PdL** (2 μM) and either kept in the dark or irradiated with green light (520 nm, 32 min, 6.9 mW/cm², 13 J/cm²). Hoechst 33342 results in staining the nucleus of all cells with blue fluorescence, while propidium iodide only stains dead cells with red fluorescence. As shown in Figure 5.4c, in the dark only limited propidium iodide emission was detected, which demonstrated that the tumor spheroid was essentially intact. In the green-light irradiated group, the red fluorescence of propidium iodide significantly increased, accompanied by the obvious collapse of the spheroid core, confirming the excellent PDT effect of **PdL** in 3D tumor

spheroids. Remarkably, the complex is non-toxic in the dark but highly phototoxic to cancer cells at 1 μM both in a 2D and 3D environment, and both in presence of high or low O_2 concentrations, suggesting that further *in vivo* testing in mice xenografts may be tried to assess the delivery and antitumor efficacy of this compound in a medically more relevant cancer model.

Melanoma is one of the most aggressive skin cancer types, which is attributed to cause 80% of deaths related to skin cancer worldwide, though it only represents 4% of diagnosed skin cancer patients.³⁴ Among the various methods used to treat melanoma, PDT represents one of the most promising alternatives due to the excellent accessibility of skin for light irradiation, and significant skin penetration of visible light.³⁵ However, A375 melanoma was also reported to be particularly prone to developing a hypoxic tumor microenvironment, which quenches PDT type II photosensitizers, but may represent no limitation to type I photosensitizers.³⁶ The *in vivo* PDT effect of **PdL** was hence evaluated on human A375 tumor xenografts in nude mice. After tail intravenous injection with **PdL** (2.1 $\mu\text{mol/kg}$, 0.9 mg/kg , 420 μM , 100 μL saline), the mice showed constant body weight (Figure 5.4d) compared with the control groups, which is a sign of low systemic toxicity. This result was confirmed by H&E staining analysis that demonstrated that at this dose **PdL** was not toxic to important organs such as the heart, liver, lung, and kidneys (Figure AIV.9). In the dark group, **PdL** showed a moderate tumor growth inhibition, matching with its modest dark cytotoxicity to cancer cells *in vitro*; after green light irradiation (520 nm, 100 mW/cm^2 , 10 min, 60 J/cm^2), tumor growth was significantly inhibited by **PdL** over 20 days (Figure 5.4e). H&E staining of the irradiated tumors revealed that the tumor tissues were dramatically damaged in the **PdL+light** group, while the other groups did not show any remarkable effect (Figure 5.4f); the TUNEL staining, an assay to evaluate the number of apoptotic cells in tissues, also demonstrated the dramatic decrease and damage of cancer cells in the irradiated tumor (Figure 5.4f), while the control groups showed no effect. These experiments demonstrated that **PdL** not only shows excellent antitumor efficacy in the A375 melanoma mice model, but that this compound also shows very low cytotoxicity to healthy organs, highlighting the high potential of **PdL** for anticancer PDT application.

Table 1. Half-maximal effective concentration (EC_{50} in μM) of **PdL** for A549, A5431 and A375 cancer cells in normoxic, hypoxic or 3D-normoxic and 3D-hypoxic spheroids conditions under dark or green light irradiation. 95% confidence interval (CI in μM) and photoindex ($PI = EC_{50, dark}/EC_{50, light}$) are also indicated.

Cell line		EC ₅₀ Values (μM)							
	Condition	2D Normoxic		2D Hypoxic		3D Normoxic		3D Hypoxic	
A549	dark	12	+1 -1	17.2	+1.5 -1.3	>25			
	light	0.18	+0.02 -0.02	0.47	+0.04 -0.03	0.26	+0.01 -0.01	N.D	
	PI	68		37		>96			
	dark	20.3	+1.1 -1.1	15.6	+1.7 -1.6				
A431	light	0.45	+0.06 -0.05	0.9	+0.1 -0.1	N.D		N.D	
	PI	45		17					
	dark	12.3	+1.3 -1.4	15.9	+1.6 -1.4	9.19	+2.1 -1.8	14.3	+4.9 -2.7
A375	light	0.17	+0.01 -0.01	0.49	+0.09 -0.07	0.17	+0.01 -0.02	0.20	+0.01 -0.01
	PI	72		32		54		72	

Irradiation condition: normoxic 520 nm, 20 min, 10.9 mW/cm², 13 J/cm²; hypoxic 520 nm, 30 min, 7.22 mW/cm², 13 J/cm²; 3D-normoxic 520 nm, 32 min, 6.90 mW/cm², 13 J/cm²; 3D-hypoxic 520 nm, 55 min, 3.99 mW/cm², 13.2 J/cm². Data is the mean over three independent experiments. N.D means not determined.

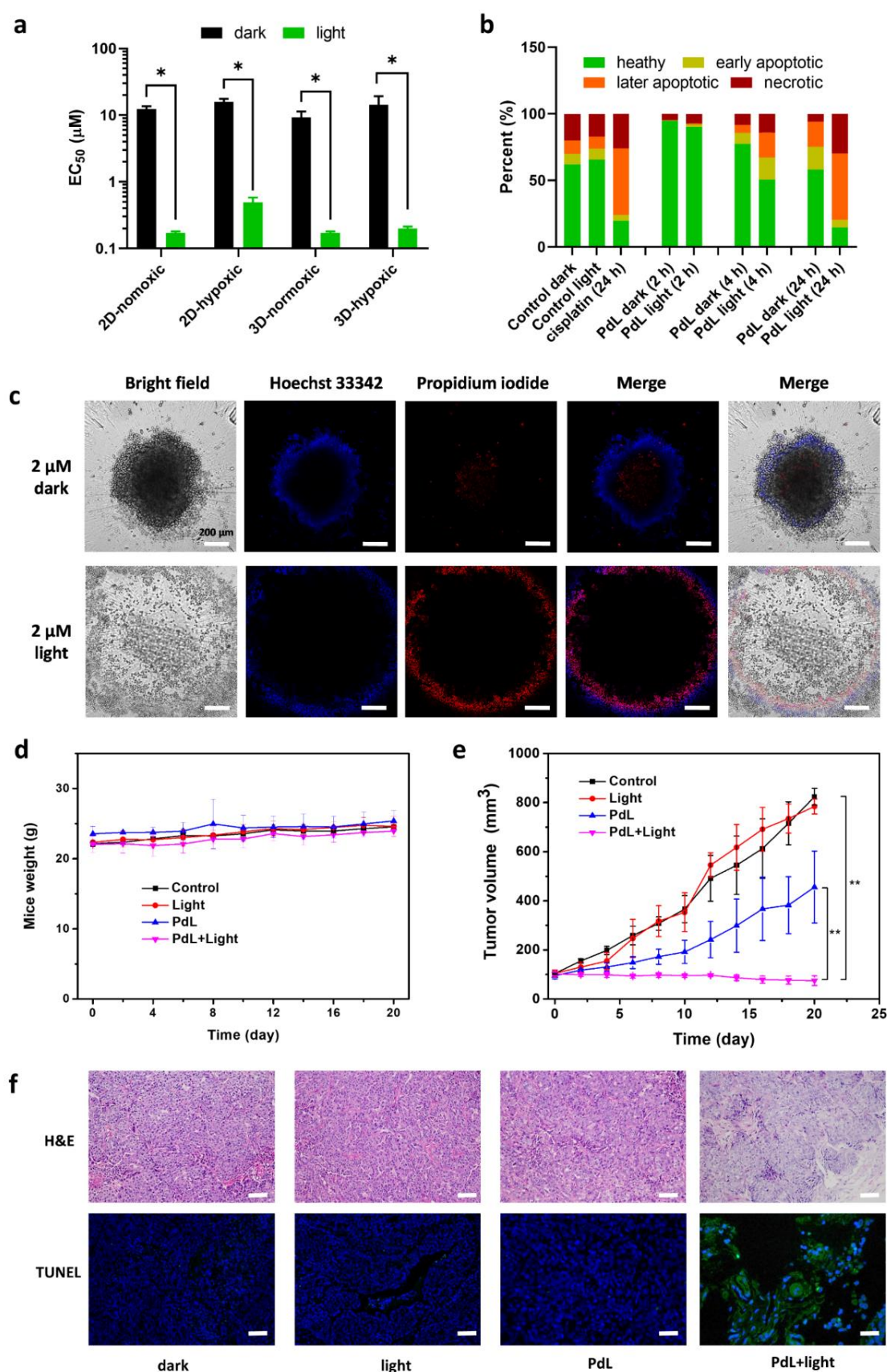


Figure 5.4 (a) EC_{50} values of **PdL** to A375 2D-monolayer and 3D-spheroid cancer cells incubated, either in the dark or upon green light irradiation (13 J/cm^2), and in normoxic or

hypoxic conditions; statistical significance was set to $p < 0.05$ (). (b) Flow cytometry quantification of healthy, early apoptotic, later apoptotic and necrotic A375 cells after treatment with **PdL** (2 μ M) in the dark or with green light irradiation in a time gradient (2 h, 4 h, 24 h). Cisplatin (7.5 μ M, 24 h) is used as positive control (c) Confocal images of 3D-normoxic A375 spheroids (scale bar 200 nm) in the dark or green light irradiation, with Hoechst 33342/Propidium iodide double staining after treated with **PdL** (2 μ M) for 72 h. (d) Time evolution of the mice weight 20 days post-treatment. (e) A375 tumor growth inhibition in different mice groups treated by tail intravenous injection; $N=3$, statistical significance was set to $p < 0.01$ (**). Light irradiation condition: 520 nm, 100 mW/cm², 10 min, 60 J/cm². Dose: 2.1 μ mol/kg, 0.9 mg/kg, 420 μ M, 100 μ L saline. (f) H&E and TUNEL staining assay to tumor slices of mice in different groups at day 5.*

5.2.5 Uptake and biodistribution of PdL nanoparticles *in vitro* and *in vivo*. The low systemic dark toxicity and high antitumor PDT efficacy of **PdL** stimulated us to check the drug uptake *in vitro* and *in vivo*. ICP-MS was hence used to determine the Pd content in A375 cells. The Pd content in A375 cell monolayers was 29 ng Pd/million cells 2 h after treatment with **PdL** (2 μ M, Figure 5.5a); after 24 h treatment, the Pd content was increased about 6-fold to 172 ng per million cells, with an uptake efficiency up to 34% (uptake efficiency (%) = total Pd mass in cells/total Pd mass in working solution \times 100%). When A375 cells were incubated with **PdL** (5 μ M) for 2 h at 4 °C, the cellular uptake was significantly reduced to 19 ng/million cells, compared to the 37 °C control (44 ng/million cells, Figure 5.5b). This result suggests that 57% of the cellular uptake of **PdL** is energy-dependent, while 43% of internalization takes place *via* passive diffusion or energy-independent channels. A possible interpretation of this combined active/passive uptake is that **PdL** probably is present in cell medium both as nanoparticles and isolated molecules, which are taken up by different mechanisms. Active transport was definitively demonstrated by the lower Pd content found in cells co-incubated with **PdL** and either NaN₃, pitstop, or wortmannin, while nocodazole and dynasore did not show any inhibition of the **PdL** uptake (Figure 5.5b). These data showed that active internalization probably occurred *via* clathrin-mediated endocytosis and micropinocytosis, while phagocytosis and dynamin-dependent endocytosis can be excluded. Overall, it appears that **PdL** mainly passes through the cell membrane *via* both energy-independent transport and endocytosis, which is consistent with the hypothesis of **PdL** being taken up both as mononuclear molecules, and as nanoparticles.

An essential question at this stage is to understand whether the nanoparticles formed by **PdL** *in vitro* would also form in living mice and may explain the antitumor selectivity observed in mice tumor xenografts. The presence and morphology of these nanostructures were tested in living mice. First, a blood sample was taken 5 min after intravenous tail injection of **PdL** (2.1 $\mu\text{mol/kg}$, 0.9 mg/kg, 420 μM , 100 μL saline). As shown in Figure AIV.10, the blood sample showed roughly spherical high-contrast nanoparticles with an average size of 181 ± 75 nm, which were not found in the blood samples of Pd-free mice, and matched very well with the nanoparticle average diameter observed for **PdL** *in vitro*. This important result suggested that **PdL** can keep self-assembling as nanoparticles in the blood. In a second step, 12 h after tail injection with **PdL** the A375 tumor of mice xenografts was sectioned using an ultramicrotome and the slices were imaged with EM. The EM images (Figure 5.5c, 1 and 0.5 μm scale, pointed out by red arrows) showed dark nano-sized spots in the cytoplasm of the cancer cells with an average diameter at 260 ± 75 nm, slightly larger than the diameter of nanoparticles in the cell medium and blood. These dark spots are characteristic for heavy-metal containing nanoparticles, and altogether strongly suggest that **PdL** accumulated at least partly as nanoparticles in the cytoplasm of tumor cells. The larger nanoparticle size in the tumor indicated that upon accumulating in the tumor tissue and entering the cells, the self-assembly of **PdL** present in the blood may be labile enough to rearrange into other shapes and sizes, which highlights the supramolecular nature of the Pd...Pd interaction. Interestingly, in the large scale EM image of the tumor slice, several long nanofibers were detected as well (width around 150 nm, Figure 5.5c, 10 μm scale), which might be attributed to **PdL**. These fibers are reminiscent of the nanofibers found when **PdL** was dissolved in THF/H₂O mixtures, which were characterized by a 100 nm width (Figure AIV.1). Overall, the presence of nanoparticles both in the blood and in the tumor tissue of mice treated with **PdL** is a proof-of-concept that self-assembly of the Pd sensitizer in blood leads to delivery of the prodrug to the tumor, which lies at the core of MoPSAN.

In order to assess whether this tumor delivery was selective or not, the biodistribution of **PdL** was determined in mice xenografts. Several hours (2, 6, 12, 20, 24 h) after intravenous tail injection of **PdL** (2.1 $\mu\text{mol/kg}$, 0.9 mg/kg, 420 μM , 100 μL saline), the Pd content of several healthy organs as well as that of the tumor, were determined with ICP-OES. As shown in Figure 5.5d, the complex showed low accumulation (below 0.27 $\mu\text{g/g}$ tissue) in the heart, kidney, and lung, while the liver showed significantly higher accumulation (above 1.0 $\mu\text{g/g}$ per gram tissue), as expected considering its role in detoxification and metabolism of exogenous substances.

Noticeably, the accumulation level of **PdL** in the liver gradually decreased in time, from 3.5 $\mu\text{g/g}$ tissue 2 h after injection to 1.0 $\mu\text{g/g}$ tissue 24 h after injection. Meanwhile, the tumor tissue showed an increased Pd accumulation from 0.17 to 0.87 $\mu\text{g/g}$ tissue during the first 12 h, and further decreased to 0.17 $\mu\text{g/g}$ per gram tissue at 20 h and 24 h. These data suggest that **PdL** nanostructures either withstand initial rapid accumulation in the liver, to relocate at the tumor site, or that they accumulate in parallel in the tumor site and liver, but at different rates. In any case, they show a metabolic cycle around 12-20 h. Besides, **PdL** shows a comparatively extraordinary efficient tumor accumulation efficacy, that culminates to 10.2 %ID/g [percent injected dose per gram of tissue (%ID/g) = (Pd content of tumor/Pd content of injection solution) \times 100%/mass of measured organs] at 12 h post-injection (Figure 5.5e). This exceptional drug delivery efficacy, which can probably be attributed to the EPR effect, confirms the high *in vivo* potential of the DSDS principle, here applied to a PDT type I photosensitizer. Critically, the high drug accumulation in the liver is not an issue because of the much lower toxicity of **PdL** when it is not irradiated by light. The specific application of drug self-delivery system for the photosensitizer **PdL** makes this MoPSAN approach very advantageous, compared to traditional nanoconjugates chemotherapy.

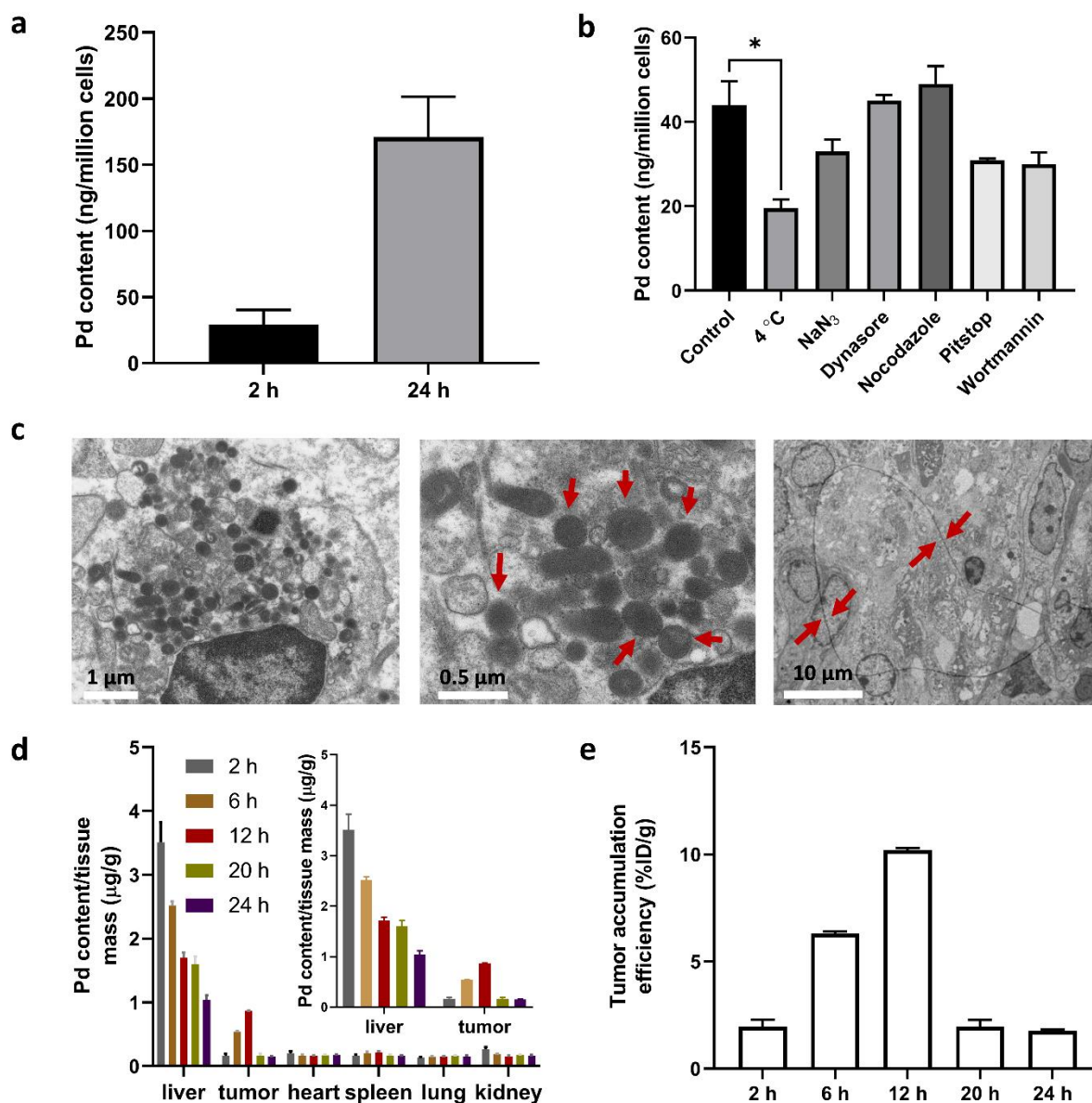


Figure 5.5 The Pd content (ICP-MS) of A375 skin melanoma cell monolayers treated with **PdL** (a) at 2 μ M after 2 or 24 h, and (b) at 5 μ M after 2 h in combination with different uptake inhibition pretreatment. (c) EM images at a different magnification of slices of A375 tumor xenografts in mice 12 h after intravenous tail injection of **PdL**. Nanoparticles and nanofibers are indicated by red arrows. (d) Biodistribution of palladium (ICP-MS) in different organs of mice at different time points after intravenous tail injection of **PdL**. (e) Tumor palladium accumulation efficiency in mice at different time points after intravenous tail injection by **PdL**. %ID/g = (Pd content of tumor/Pd content of injection solution) \times 100%/mass of measured organs). In vivo injection conditions: 420 μ M, 100 μ L saline.

5.3 Discussion

PDT offers an alternative to chemotherapy, with the potential to inhibit tumor proliferation while minimizing side-effects.¹⁷ In principle, the physical selectivity offered by light irradiation of the tumor tissue ensures antitumor selectivity. However, photosensitizer molecules taken up in healthy tissues lead to undesired photosensitivity (*e.g.* skin) for the patient, a typical side-effect of PDT with Photofrin for example.³⁷ It is hence essential that the photosensitizer is delivered with high efficacy to the tumor tissue. Many reports have demonstrated that nanoconjugates enable to increase the tumor accumulation of molecular drugs, including PDT photosensitizers.^{38, 39} However, a recent report has revealed the low average drug-loading capacity (typical 20 wt%) and tumor accumulation efficacy (medium 0.7 %ID) of classical drug delivery nanosystems,¹⁰ indicating the urgency to develop new nanosystems to solve the drug-loading and nanoparticle delivery problem. In this work, the drug-loading issue of the nanoparticle is overcome by the self-assembly of photosensitizer **PdL**. This self-assembly provides long circulation times (12-20 h) and a drug accumulation in the tumor tissue that is much higher (up to 10.2 %ID/g) than for traditional nanoconjugates, giving a strong indication that Pd...Pd interactions can be used to deliver anticancer (pro)drugs to tumors with high efficacy.

The other challenges relevant to PDT compounds are hypoxia and light penetration, which severely limit their photodynamic effect. Several innovative solutions have been proposed to solve the hypoxia problem. Nanoparticle-based drug delivery systems that evolve O₂, for example, can improve the local O₂ concentration in hypoxic tumor tissues before irradiation of the sensitizer, which recovers the photodynamic activity of photosensitizers observed in normoxic regions.^{40, 41} Others have combined photosensitizers and chemotherapy *via* hypoxia-activated linkers.⁴² Still, the complexity and low reproducibility of multicomponent nanoparticles endanger the clinical application of these systems.⁴³ By contrast, MoPSAN relies on a simple PDT type I molecular sensitizer, **PdL**, that can be reproducibly synthesized and self-assemble spontaneously in the blood into well-characterized nanoparticles. In this work, we choose A375 skin melanoma cancer models to test the PDT effect of MoPSAN because of the suitable skin penetration of visible light⁴⁴ and the highly hypoxic microenvironment of skin melanoma tumor.⁴⁵ Besides, melanoma is the most dangerous form of skin cancer and resistant to several PDT agents, probably due to the optical interference of highly-pigmented melanin.³⁵ Nevertheless, the *in vitro* and *in vivo* results demonstrate the significant green light-activated PDT effect of **PdL** even in presence of low dioxygen concentrations, suggesting the MoPSAN

may be a feasible strategy to overcome PDT resistance in skin melanoma. One remaining question is whether MoPSAN would stimulate T-cell activation and generate antitumor immune memory and systemic response after PDT treatment, which could not be investigated here to the immunoincompetent character of the mice used.⁴⁶

5.4 Conclusion

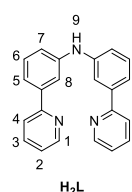
The new MoPSAN strategy, which consists of a molecular photosensitizer that self-assembles into long-circulating nanoparticles in blood, generates a very powerful PDT agent. As an isolated molecule, this palladium complex shows significant $O_2^{\bullet-}$ generation upon green light irradiation, making it a good PDT type I sensitizer. In addition, the strong supramolecular Pd...Pd interaction lets this complex self-assembly in biological medium such as blood, where the molecule is present as soluble nanoparticles. This spontaneous aggregation provokes, within 12 h, drug accumulation in the tumor *via* the EPR effect, and cellular uptake by a combination of passive and active transport. Importantly, these palladium nanoaggregates conserve the PDT type I properties of the monomer. This observation makes **PdL** to be a fundamentally different sensitizer compared with many porphyrin-based ones, which typically lose their photodynamic properties upon aggregation. With these results in hand, we conclude that the metallophilic Pd...Pd interaction has a high potential 1) to build supramolecular nanocarriers with improved tumor accumulation *via* the EPR effect, and 2) to generate PDT photosensitizers that conserve their phototoxic properties under hypoxia. With both properties combined, the MoPSAN demonstrate promising anti-tumor properties, here in skin melanoma xenograft models.

5.5 Experimental section

The DFT calculation, photophysical spectra, TEM, Cryo-EM, cell culture, photocytotoxicity, cell uptake and apoptosis experiments were carried out according to the description in chapter 3 and 4.

5.5.1 Synthesis and NMR characterization of ligands and metal complexes.

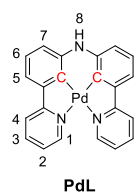
H₂L, (bis(3-(pyridin-2-yl)phenyl)amine)



A mixture of 2-(3-bromophenyl)pyridine (329 mg, 1.41 mmol), Pd(dba)₂ (81 mg, 0.14 mmol), racemic BINAP (106 mg, 0.17 mmol) and KO^t-Bu (1574 mg, 14 mmol) was partially dissolved in dry toluene (28 mL) under N₂ atmosphere. The mixture was stirred for 10 min, then 3-(2-Pyridyl)aniline (230 mg, 1.35 mmol) was added, followed by heating the reaction mixture to 95 °C. After 3 days of stirring, the brown mixture

was cooled down. Demi water (75.0 mL) was added and the mixture was stirred for 1 h. The H₂O layer was separated from the toluene layer. Extracted the H₂O layer with EtOAc (100 mL) for three times and combined the toluene and EtOAc layers, followed by rotary evaporation of the solvents. The crude product was purified by silica chromatography using pentane-EtOAc mixtures (2:1, $R_f = 0.3$) as eluent, to afford 290 mg of the target compound **H₂L**¹ (yield: 0.90 mmol, 67%). **ESI-MS** (cation): m/z calcd 324.2 (C₂₂H₁₇N₃ + H⁺), found 324.7. **¹H NMR** (300 MHz, DMSO-*d*₆): δ 8.65 (dt, $J = 4.7, 1.4$ Hz, 2H, H¹), 8.49 (s, 1H, H⁹), 7.97 – 7.81 (m, 6H, H⁵, H⁸, H³), 7.53 (dt, $J = 7.8, 1.3$ Hz, 2H, H⁴), 7.42 – 7.30 (m, 4H, H⁶, H²), 7.20 (dd, $J = 7.8, 2.3$ Hz, 2H, H⁷). **¹³C-APT NMR** (75 MHz, DMSO-*d*₆): δ 156.1, 149.5, 143.8, 139.7, 129.6, 122.6, 120.2, 120.2, 118.1, 117.4, 115.1.

PdL



A mixture of **H₂L** (90 mg, 0.28 mmol) and Pd(OAc)₂ (63 mg, 0.28 mmol) in a glacial acetic acid was refluxed for 24 h at 135 °C under N₂ atmosphere to give a yellowish green solution. Then the solvent was rotary evaporated. The crude product obtained was purified by silica chromatography using DCM/MeOH mixtures (v/v = 100:1.5, $R_f = 0.3$) as eluent, to afford 67 mg of target complex **PdL** (yield: 0.15 mmol, 56%). **ESI-MS** (cation): m/z calcd 428.0379 (C₂₂H₁₅N₃Pd + H⁺), found 428.0374. **¹H NMR** (300 MHz, DMSO-*d*₆) δ 9.20 (s, 1H, H⁸), 8.94 (d, $J = 5.4$ Hz, 2H, H¹), 8.20 (d, $J = 8.1$ Hz, 2H, H⁴), 8.10 – 8.00 (m, 2H, H³), 7.49 (ddd, $J = 7.1, 5.5, 1.3$ Hz, 2H, H²), 7.46 – 7.37 (m, 2H, H⁵), 7.14 (t, $J = 7.6$ Hz, 2H, H⁶), 7.00 (dd, $J = 7.9, 1.1$ Hz, 2H, H⁷). **¹³C NMR** (75 MHz, DMSO-*d*₆) δ 163.77, 148.75, 146.55, 139.56, 138.71, 137.87, 124.64, 122.74, 119.50, 115.14, 114.52. **Elemental analysis** calcd for **PdL**: C 61.77, H 3.53, N 9.82; found: C 61.93, H 3.64, N 9.60.

5.5.2 In vivo tumor inhibition experiments. Female BALB/c mice with 3 weeks old were originally purchased from Vital River Laboratory Animal Center (Beijing, China). The mice were kept under specific pathogen-free conditions with free access to standard food and water for 2 weeks, to let the mice weight around 20 g. This study was conducted following the Guide for the Care and Use of Laboratory Animals published by the US National Institutes of Health (8th edition, 2011). All protocols for animal studies conformed to the Guide for the Care and Use of Laboratory Animals. All animal experiments were performed under guidelines approved by the ethics committee of Peking University. The tumor model was established by inoculating 5×10^7 of A375 melanoma cells suspended in 100 μ L of PBS at the right flank region of each mouse, to obtain mouse A375 melanoma implant. 3 weeks later, the tumor volumes were

around 100 mm³. Tumor volume (V) can be calculated by formula $V = L/2 \times W^2$ after measuring the tumor length (L) and width (W).⁴⁷ The mice were then randomly divided into 4 groups (vehicle control, 520 nm light, **PdL**, **PdL**+520 nm light groups, each group 4 mice). The mice were treated through tail intravenous injection with saline for vehicle control and 520 nm light groups, or **PdL** (2.1 μmol/kg, 0.9 mg/kg, 420 μM, 100 μL saline) for **PdL** and **PdL**+520 nm light groups. After 12 h injection, 520 nm irradiation (100 mW/cm², 5 min) was then carried out twice, with an interval of 5 min for the light groups. Thus, the total light dose for each treatment was 100 mW/cm², 10 min, 60 J/cm². These treatment and irradiation steps were replicated at day 0, day 7 and day 14, respectively. On day 5, one mouse in each group was sacrificed and the tumor was taken up and fixed with paraformaldehyde (10% v/v), then sectioned into slices and analyzed *via* H&E or TUNEL protocols, to evaluate the tumor cell damage and apoptosis conditions. The tumor volume and body weight of left mice (N=3) were measured and recorded and the average tumor volume and body weight were calculated over 20 days. At last, the mice were sacrificed, and the healthy organs were taken up, fixed with paraformaldehyde (10% v/v), then sectioned into slices and analyzed *via* H&E protocol, to determine side effect of **PdL** after treatment.

5.5.3 Mice blood EM imaging experiments. The tumor-bearing mouse was treated with **PdL** (2.1 μmol/kg, 0.9 mg/kg, 420 μM, 100 μL saline) through intravenous tail injection. After 5 min, 1 mL of blood was taken up from the eye socket and diluted to 5 mL by PBS. After centrifugation (1500 rpm, 10 min), the supernatant was collected, and the left part was washed by PBS (5 mL) and centrifuged (1500 rpm, 10 min) again twice more, to obtain the supernatant PBS solution. These PBS solutions were then combined and centrifuged at a speed of 10000 rpm for 10 min. After removing the supernatant, 200 uL PBS were added and mixed well. Then the solutions were transferred to the TEM grids. For the preparation of TEM samples, a drop (15 μL) of the solution was added to the grids (formvar/carbon 200 Mesh, copper) and kept for 2 min, then the excess liquid on the grid was removed by filter paper, and dried for 2 h for TEM measurement. The TEM measurements were carried out in vacuum conditions (HITACHI H-7650).

5.5.4 Mice tumor EM imaging experiments. One tumor-bearing mouse was treated with **PdL** (2.1 μmol/kg, 0.9 mg/kg, 420 μM, 100 μL saline) through intravenous tail injection. After 12 h, the mouse was sacrificed, the tumor tissue was collected and then fixed by a biological TEM fixation solution (Wuhan Servicebio). After that, the tumor tissue was split into small pieces with volume around 1 mm³, and fixed again using 1 % osmic acid PB solution for 2 h, following

with dehydration by ethanol (v/v = 30 %, 50 %, 70 %, 80 %, 95 %, 100 %, each group 20 min) and acetone for two times (15 min). The prepared samples were then treated with acetone/epon-812 embedding medium in the ratio 1:1 for 2 h, 1:2 for 12 h, and pure epon-812 solution for another 5 h at 37 °C. After that, the tissue-containing embedding medium was filled in the embedding mold for 24 h at 37 °C, and another 60 °C for 48 h. The obtained tissue-containing resins were then sectioned into slices with thickness around 60-80 nm via ultramicrotome (Leica EM UC7), and moved to the copper grid (150 mesh). The obtained grids were stained by 2 % uranyl acetate ethanol solution for 8 min, and 2.6 % lead citrate solution for another 8 min. After that, the grids were dried at room temperature and observed using JEOL JEM2100 TEM (Japan).

5.5.5 Pd distribution determination on mice organs. The mice were treated with **PdL** (2.1 $\mu\text{mol/kg}$, 0.9 mg/kg, 420 μM , 100 μL saline) through intravenous tail injection. Then, the mice were sacrificed at 2 h, 6 h, 12 h, or 20 h, or 24 h, and their heart, liver, spleen, kidney, lung, and tumor were taken. Then, around 1 g of each organ were lysed overnight in a mixture solution of 65% HNO_3 (5 mL) and 30% H_2O_2 (2 mL) at 100 °C. Afterward, each sample was evaporated and another 5 mL HNO_3 solution (2%) was added. The Pd content in each organ or tumor was detected *via* ICP-OES (JY-Horiba ICP-OES Ultima 2).

5.6 References

1. R. L. Siegel, K. D. Miller and A. Jemal, *CA Cancer J. Clin.*, 2020, **70**, 7-30.
2. B. A. Chabner and T. G. Roberts, *Nat. Rev. Cancer*, 2005, **5**, 65-72.
3. Z. G. Chen, *Trends Mol. Med.*, 2010, **16**, 594-602.
4. M. Zeinali, S. Abbaspour-Ravasjani, M. Ghorbani, A. Babazadeh, T. Soltanfam, A. C. Santos, H. Hamishehkar and M. R. Hamblin, *Drug Discov. Today*, 2020, **25**, 1416-1430.
5. J. Nam, S. Son, K. S. Park, W. Zou, L. D. Shea and J. J. Moon, *Nat. Rev. Mater.*, 2019, **4**, 398-414.
6. S. Pottanam Chali and B. J. Ravoo, *Angew. Chem. Int. Ed.*, 2020, **59**, 2962-2972.
7. M. Chidambaram, R. Manavalan and K. Kathiresan, *J. Pharm. Pharm. Sci.*, 2011, **14**, 67-77.
8. V. P. Chauhan, T. Stylianopoulos, J. D. Martin, Z. Popovic, O. Chen, W. S. Kamoun, M. G. Bawendi, D. Fukumura and R. K. Jain, *Nat. Nanotechnol.*, 2012, **7**, 383-388.
9. R. B. Greenwald, Y. H. Choe, J. McGuire and C. D. Conover, *Adv. Drug Deliv. Rev.*, 2003, **55**, 217-250.
10. S. Wilhelm, A. J. Tavares, Q. Dai, S. Ohta, J. Audet, H. F. Dvorak and W. C. Chan, *Nat. Rev. Mater.*, 2016, **1**, 1-12.
11. Q. Dai, S. Wilhelm, D. Ding, A. M. Syed, S. Sindhwani, Y. Zhang, Y. Y. Chen, P. MacMillan and W. C. W. Chan, *ACS Nano*, 2018, **12**, 8423-8435.
12. S. Y. Qin, A. Q. Zhang, S. X. Cheng, L. Rong and X. Z. Zhang, *Biomaterials*, 2017, **112**, 234-247.
13. S. B. Brown, E. A. Brown and I. Walker, *Lancet Oncol.*, 2004, **5**, 497-508.
14. H. Huang, S. Banerjee, K. Qiu, P. Zhang, O. Blacque, T. Malcomson, M. J. Paterson, G. J. Clarkson, M. Staniforth, V. G. Stavros, G. Gasser, H. Chao and P. J. Sadler, *Nat. Chem.*, 2019, **11**, 1041-1048.
15. J. Karges, S. Kuang, F. Maschietto, O. Blacque, I. Ciofini, H. Chao and G. Gasser, *Nat. Commun.*, 2020, **11**, 3262.
16. N. Kotagiri, G. P. Sudlow, W. J. Akers and S. Achilefu, *Nat. Nanotechnol.*, 2015, **10**, 370-379.

17. S. A. McFarland, A. Mandel, R. Dumoulin-White and G. Gasser, *Curr. Opin. Chem. Biol.*, 2020, **56**, 23-27.
18. L. Larue, B. Myrzakhmetov, A. Ben-Mihoub, A. Moussaron, N. Thomas, P. Arnoux, F. Baros, R. Vanderesse, S. Acherar and C. Frochot, *Pharmaceuticals*, 2019, **12**.
19. A. P. Castano, T. N. Demidova and M. R. Hamblin, *Photodiagnosis Photodyn. Ther.*, 2004, **1**, 279-293.
20. M. S. Baptista, J. Cadet, P. Di Mascio, A. A. Ghogare, A. Greer, M. R. Hamblin, C. Lorente, S. C. Nunez, M. S. Ribeiro, A. H. Thomas, M. Vignoni and T. M. Yoshimura, *Photochem. Photobiol.*, 2017, **93**, 912-919.
21. A.-R. Azzouzi, S. Vincendeau, E. Barret, A. Cicco, F. Kleinclauss, H. G. van der Poel, C. G. Stief, J. Rassweiler, G. Salomon, E. Solsona, A. Alcaraz, T. T. Tammela, D. J. Rosario, F. Gomez-Veiga, G. Ahlgren, F. Benzaghrou, B. Gaillac, B. Amzal, F. M. J. Debruyne, G. Fromont, C. Gratzke and M. Emberton, *Lancet Oncol.*, 2017, **18**, 181-191.
22. A. Aliprandi, M. Mauro and L. De Cola, *Nat. Chem.*, 2016, **8**, 10-15.
23. D. A. K. Vezzu, J. C. Deaton, J. S. Jones, L. Bartolotti, C. F. Harris, A. P. Marchett, M. Kondakova, R. D. Pike, and S. Huo, *Inorg. Chem.*, 2010, **49**, 5107-5119.
24. X. Q. Zhou, M. Xiao, V. Ramu, J. Hilgendorf, X. Li, P. Papadopoulou, M. A. Siegler, A. Kros, W. Sun and S. Bonnet, *J. Am. Chem. Soc.*, 2020, **142**, 10383-10399.
25. M. Mauro, A. Aliprandi, D. Septiadi, N. S. Kehr and L. De Cola, *Chem. Soc. Rev.*, 2014, **43**, 4144-4166.
26. Q. Wan, W. P. To, C. Yang and C. M. Che, *Angew. Chem. Int. Ed.*, 2018, **57**, 3089-3093.
27. X. Q. Zhou, A. Busemann, M. S. Meijer, M. A. Siegler and S. Bonnet, *Chem. Commun.*, 2019, **55**, 4695-4698.
28. C. Zou, J. Lin, S. Suo, M. Xie, X. Chang and W. Lu, *Chem. Commun.*, 2018, **54**, 5319-5322.
29. J. Karges, F. Heinemann, M. Jakubaszek, F. Maschietto, C. Subecz, M. Dotou, R. Vinck, O. Blacque, M. Tharaud, B. Goud, E. Viñuelas Zahinos, B. Spingler, I. Ciofini and G. Gasser, *J. Am. Chem. Soc.*, 2020, **142**, 6578-6587.
30. S. Monro, K. L. Colon, H. Yin, J. Roque, 3rd, P. Konda, S. Gujar, R. P. Thummel, L. Lilge, C. G. Cameron and S. A. McFarland, *Chem. Rev.*, 2019, **119**, 797-828.
31. H. M. Peshavariya, G. J. Disting and S. Selemidis, *Free Radic. Res.*, 2007, **41**, 699-712.
32. V. Vichai and K. Kirtikara, *Nat. Protoc.*, 2006, **1**, 1112-1116.
33. J. Friedrich, C. Seidel, R. Ebner and L. A. Kunz-Schughart, *Nat. Protoc.*, 2009, **4**, 309-324.
34. S. Kuphal and A. Bosserhoff, *J. Pathol.*, 2009, **219**, 400-409.
35. Y. Y. Huang, D. Vecchio, P. Avci, R. Yin, M. Garcia-Diaz and M. R. Hamblin, *Biol. Chem.*, 2013, **394**, 239-250.
36. M. P. O'Connell, K. Marchbank, M. R. Webster, A. A. Valiga, A. Kaur, A. Vultur, L. Li, M. Herlyn, J. Villanueva, Q. Liu, X. Yin, S. Widura, J. Nelson, N. Ruiz, T. C. Camilli, F. E. Indig, K. T. Flaherty, J. A. Wargo, D. T. Frederick, Z. A. Cooper, S. Nair, R. K. Amaravadi, L. M. Schuchter, G. C. Karakousis, W. Xu, X. Xu and A. T. Weeraratna, *Cancer Discov.*, 2013, **3**, 1378-1393.
37. S. I. Moriwaki, J. Misawa, Y. Yoshinari, I. Yamada, M. Takigawa and Y. Tokura, *Photodermatol. Photoimmunol. Photomed.*, 2001, **17**, 241-243.
38. L. Salvioni, M. A. Rizzuto, J. A. Bertolini, L. Pandolfi, M. Colombo and D. Prosperi, *Cancers*, 2019, **11**.
39. Z. Yu, P. Zhou, W. Pan, N. Li and B. Tang, *Nat. Commun.*, 2018, **9**, 5044.
40. J. Kim, H. R. Cho, H. Jeon, D. Kim, C. Song, N. Lee, S. H. Choi and T. Hyeon, *J. Am. Chem. Soc.*, 2017, **139**, 10992-10995.
41. W. Fan, W. Bu, B. Shen, Q. He, Z. Cui, Y. Liu, X. Zheng, K. Zhao and J. Shi, *Adv. Mater.*, 2015, **27**, 4155-4161.
42. D. Cui, J. Huang, X. Zhen, J. Li, Y. Jiang and K. Pu, *Angew. Chem. Int. Ed.*, 2019, **58**, 5920-5924.
43. D. R. Baer, *Front. Chem.*, 2018, **6**, 145.
44. C. Ash, M. Dubec, K. Donne and T. Bashford, *Lasers Med. Sci.*, 2017, **32**, 1909-1918.
45. O. Distler, J. H. Distler, A. Scheid, T. Acker, A. Hirth, J. Rethage, B. A. Michel, R. E. Gay, U. Muller-Ladner, M. Matucci-Cerinic, K. H. Plate, M. Gassmann and S. Gay, *Circ. Res.*, 2004, **95**, 109-116.
46. J. M. Dabrowski and L. G. Arnaut, *Photochem. Photobiol. Sci.*, 2015, **14**, 1765-1780.
47. W. Sun, J. Fan, S. Wang, Y. Kang, J. Du and X. Peng, *ACS Appl. Mater. Interfaces*, 2018, **10**, 7832-7840.

6

Nitrogen coordination vs. rollover cyclometalation in tetrapyridyl anticancer gold(III) complexes

*In this work, a pair of gold(III) complexes derived from the analogous tetrapyridyl ligands **H₂biqbpy1** and **H₂biqbpy2** have been synthesized, i.e., the bis-cyclometalated complex [Au(**biqbpy1**)Cl] (**[1]Cl**) and its isomer [Au(**biqbpy2**)Cl] (**[2]Cl**). In **[1]**⁺, two of the four pyridyl rings are coordinated to the metal via a Au-C bond (“rollover” coordination mode, C[^]N[^]N[^]C) and the two non-coordinated amine bridges of the **biqbpy1**²⁻ ligand remain protonated, while in **[2]**⁺ the four pyridyl rings of the **biqbpy2**²⁻ ligand are coordinated to the metal via an Au-N bond (coordination mode N[^]N[^]N[^]N), but both non-coordinated amine bridges are deprotonated. As a result, both **[1]Cl** and **[2]Cl** are monocationic, making it possible to compare the effect of bis-cyclometalation on the chemical reactivity, anticancer properties, and protein interactions of these gold(III) compounds, without a change of their overall charge. The rollover cyclometalation resulted in **[1]Cl** being coordinatively stable in biomimetic conditions, while **[2]Cl** was reduced by millimolar concentration of GSH into metastable Au(I) species ultimately releasing the free ligand **H₂biqbpy2** and Au⁺ ions. On the other hand, **[1]Cl** made nanoparticles in cell-growing medium that resulted in very efficient cellular uptake. The chemical stability of **[1]Cl** in reducing conditions led to decreased thioredoxin reductase (TrxR) inhibition properties, compared to **[2]Cl**, which released the known TrxR-inhibiting Au⁺ ions. On the other hand, **[1]Cl** had more selective anticancer properties, i.e. it was almost 10 times more cytotoxic to human cancer cell lines (A549, A431, A375, MCF7) than to a non-cancerous cells line (MRC5). Both complexes **[1]Cl** and **[2]Cl** displaced reference radioligand [³H]dofetilide equally well from cell membranes expressing the K_v11.1 (hERG) potassium channel, and more so than the tetrapyridyl ligands **H₂biqbpy1** and **H₂biqbpy2**. Overall, these results suggested that bis-cyclometallation is an appealing method to improve the redox stability of Au(III) compounds. Such stability improves their selectivity against cancerous vs. non-cancerous cells, possibly due to their interaction with the K_v11.1 potassium channel.*

This chapter will be submitted as a full paper: X.-Q Zhou, I. Carbó-Bagué, M. A. Siegler, J. Hilgendorf, U. Basu, R. Liu, A. P. IJzerman, I. Ott and S. Bonnet*, *JACS Au*.

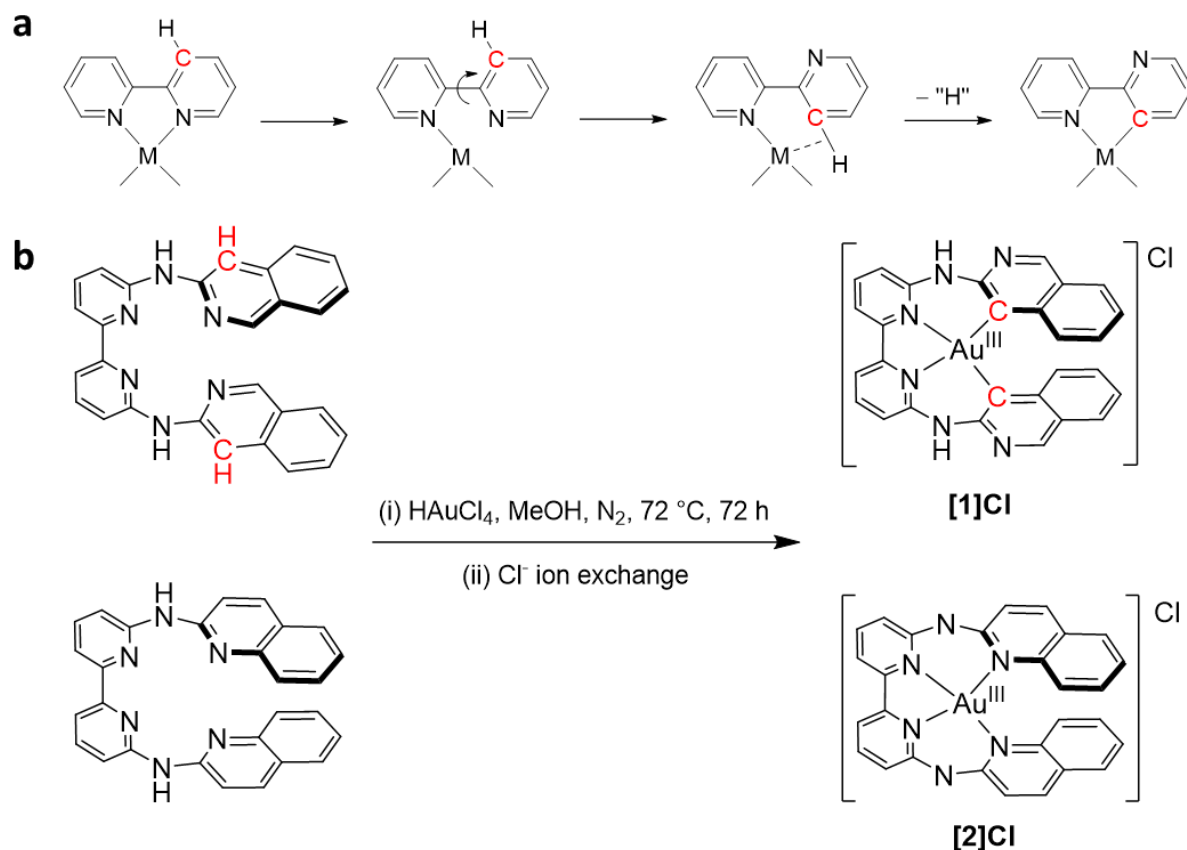
6.1 Introduction

The discovery of cisplatin's anticancer activity has brought a new era for the bioinorganic and medicinal chemistry communities.¹ Nowadays, cisplatin is one of the main chemotherapeutic drugs for the treatment of various cancers. However, the corresponding *trans* isomer, *trans*-[Pt(NH₃)₂Cl₂] is clinically inefficient, which is attributed to its much lower efficiency to form cross-link DNA adducts.² Overall, the anticancer properties of a metal compound can be strongly influenced by the intrinsic (stereo)chemical differences between two isomers.³ Recently, establishing structure-activity relationship between isomers of the same molecule has emerged as a new frontier in bioinorganic medicinal chemistry.^{4, 5}

Next to platinum itself, many heavy metal complexes are being investigated for their potential anticancer properties. They may show different modes of action (MOA), such as DNA binding, disruption of membranes, enzyme inhibition, or reactive oxygen species generation, which allows in many cases to overcome the resistance of tumors to cisplatin.⁶⁻⁸ In particular, gold complexes have been considered as an alternative to platinum because of the specific affinity of gold(I) ions for the thiol groups present in many biomolecules, especially thioredoxin reductase (TrxR) and glutathione (GSH).⁸⁻¹⁰ The TrxR/GSH system and its different components have been reported as the major cellular line of defense against increased oxidative stress and the accumulation of reactive oxygen species (ROS); when it works properly, it helps the cell to stay alive. Meanwhile, the expression of these two biomolecules is known to be higher in cancer cells than in normal cells, as the former need to sustain higher metabolism than the latter.^{11, 12} Altogether, the TrxR/GSH system has been recognized as a good target for anticancer therapy, notably for gold prodrug candidates. For example, Auranofin, an Au(I) compound characterized by the coordination of a phosphine and a thiol ligand in a linear arrangement, has been clinically approved for the treatment of rheumatoid arthritis for years. More recently, it has been thoroughly investigated as an anticancer drug, for its significant inhibition properties towards TrxR.¹³ Next to Au(I), many Au(III) compounds have been evaluated as anticancer drugs,¹⁴ many of them based on polypyridyl ligands. Interestingly, polypyridyl Au(III) complexes are typically reduced to Au(I) species upon cellular uptake, which is often accompanied by the release of the polypyridyl ligand(s).^{10, 14} Some Au(III) polypyridyl complexes are also reactive to the thiol residue of human serum albumin, leading to the dissociation of the complex before it reaches cancer tissues. By contrast, cyclometalated Au(III) complexes, *i.e.* compounds that have at least one metal-carbon σ bond, have been considered because of their higher redox stability in physiological conditions.¹⁰ On the other

hand, cyclometalation typically reduces the positive charge of Au(III) complex, which can strongly modify its biological properties, notably its cellular uptake and/or interaction with serum proteins.¹⁵

Most cytotoxic, cyclometalated Au(III) complexes known to date are based on the combination of a bipyridine or terpyridine ligand and monodentate ligand(s),^{14, 15} while cyclometalated Au(III) complexes based on tetradentate ligands are rare.¹⁵ Among the different reactions available to prepare cyclometalated complexes, an unconventional one called “rollover” has been identified in recent years, in particular in catalysis where the uncoordinated nitrogen atoms can play an important role.¹⁶ Rollover cyclometalation is a specific reversal of the coordination mode of a pyridyl moiety, from the expected metal-nitrogen bonding mode to a cyclometalated coordination mode where a meta CH group in the same heterocyclic ring is deprotonated to generate a metal-carbon bond (Scheme 6.1a).¹⁶ Rollover compounds have been predominantly described for bipyridine ligands coordinated to heavy atoms such as Pt(II) or Ir(III),^{16, 17} and were extensively developed by the Zucca group.^{18, 19} Recently, Hartinger et al. evaluated the anticancer abilities of a series of rollover cyclometalated bipyridine Pt(II) complexes, which appeared to be significantly influenced by the ancillary ligands.²⁰ Though Au(III) is isoelectronic to Pt(II) and shares the same popularity regarding cyclometalation, the synthesis of rollover cyclometalated Au(III) complexes have been rarely reported,^{21, 22} and none of them have been studied in a biological context. In this work, we studied the coordination of two isomers of a tetrapyridyl ligand, *i.e.* (N6,N6'-di(isoquinolin-3-yl)-[2,2'-bipyridine]-6,6'-diamine (**H₂biqbpy1**) and N6,N6'-di(quinolin-2-yl)-[2,2'-bipyridine]-6,6'-diamine (**H₂biqbpy2**), to Au(III). Unexpectedly, in the same reaction conditions the former ligand led to the formation of the rollover bis-cyclometalated monocationic Au(III) complex **[1]Cl**, while the latter led to the tetrapyridyl coordination isomer, **[2]Cl**, which is characterized by deprotonated NH bridges and hence also a single positive charge (Scheme 6.1b). Both monocationic complexes were fully characterized, the reason for rollover was studied by DFT calculations, and the biological activities of the two compounds were compared. Our results demonstrate that rollover cyclometalation dramatically influenced the reactivity of the gold complex towards thiol groups, the selectivity of its cytotoxic properties, and its protein interactions.



Scheme 6.1 (a) Scheme for rollover cyclometalation.¹⁹ (b) Synthesis route of isomer gold complexes **[1]Cl** and **[2]Cl**. Yields: 13% for **[1]Cl**, 18% for **[2]Cl**.

6.2 Results and discussion

6.2.1 Synthesis. The ligands **H2biqbpy1** and **H2biqbpy2** were prepared according to the literature.²³ Upon refluxing for 3 days under N₂ a mixture of each ligand with one equivalent of HAuCl₄ in methanol, the gold complexes **[Au(biqbpy1)]⁺** (**[1]⁺**) and **[Au(biqbpy2)]⁺** (**[2]⁺**) were obtained after purification by silica column chromatography (Scheme 6.1b). The complexation of gold(III) to the ligands was confirmed via NMR. The ¹H NMR peak at 11.70 ppm (400 MHz, DMSO-*d*₆) demonstrated the protonation of the two secondary amine bridges of the ligand in **[1]⁺**. By contrast, similar high-chemical shift peaks were not observed for **[2]⁺**, suggesting at least partial deprotonation of the amine bridges. Next to these differences, the 2D-NMR analysis also provided strong evidence that **[1]⁺** and **[2]⁺** were coordinated following a different pattern. The ¹³C-APT NMR showed that **[1]⁺** had two quaternary carbon atoms more than **[2]⁺**, indicating that **[1]⁺** had two more Au-C bonds. It should be noticed that at that stage the ¹H NMR and ESI mass spectrometry did not yield insight in the nature of the counterion of these Au(III) complexes; probably, these samples had mixed counterions, *i.e.* AuCl₄⁻, AuCl₂⁻, and/or Cl⁻.²⁴ Thus a chloride-loaded ion exchange resin was used to better define the nature of

the counter anion. **[1]Cl** was insoluble in water, while **[2]Cl** was quite hydrosoluble. Full characterization of the two compounds is given in the ESI.

6.2.2 X-ray crystallography and structure determination. Slow vapor diffusion of ethyl acetate into a methanol/DCM solution containing **[1]⁺** or **[2]⁺** gave red and black single crystals, respectively, suitable for X-ray crystal structure determination. The selected bond distances and angles are shown in Table AV1. The two crystal structures showed to contain different counter anions: one chloride anion per gold center for **[1]⁺**, and one **AuCl₄⁻** complex anion per cationic gold complex for **[2]⁺**. The compound **[1]Cl** crystallized in a monoclinic *P2₁/c* space group, while **[2](AuCl₄)** crystallized in a monoclinic *P2₁* space group. The cation of the two complexes showed a similar butterfly structure. The crystal structure of **[1]⁺** showed that it was a double “rollover” cyclometalated complex, characterized by a C^NN^C coordination mode, while **[2]⁺** was a classical tetrapyridyl complex, characterized by a N^NN^N coordination mode (Figure 6.1a). The M-C bond distances in **[1]⁺** (2.030(7)-2.060(5) Å) were similar to the M-N bond distances in **[2]⁺** (1.995(18)-2.081(18) Å). The two complexes exhibited distorted square-planar coordination spheres, as confirmed by the moderate tetradentate τ distortion values, *i.e.* $\tau = 0.19$ for **[1]Cl** and $\tau = 0.21$ for **[2](AuCl₄)** ($\tau = [360 - (\alpha + \beta)]/141$, where α and β are the two greatest coordination angles of the tetradentate coordination sphere; $\tau = 0$ reflects perfect planar coordination, $\tau = 1$ indicates perfect tetrahedral coordination). Besides showing different coordination spheres, the two complexes were also characterized by significant differences in the geometry of their amine bridges. Clearly, in **[1]⁺**, the bond distances in the bridge C9-N2, N2-C10, C19-N5 and N5-C20 fell within 1.348(10)-1.415(14) Å, indicative of a single bond character for both C-NH bonds. On the contrary, the amine-carbon bonds in **[2]⁺** were shorter, 1.331(7) and 1.40(3) Å, suggesting a higher double bond character for both amine-carbon bonds (C=N-C). This result suggested that the amine bridge in **[1]⁺** was protonated, while that in **[2]⁺** was deprotonated, thus generating conjugation between the lone pairs on the nitrogen bridges with the π system of the polypyridyl ligand. Last but not least, the highly distorted coordination sphere in both complexes generated a strongly helical structure, with both enantiomers being present as a 1:1 mixture in the crystal lattice because of the centrosymmetric space groups. In **[1]⁺** the quite similar helical structure, compared with **[2]⁺**, was obtained due to the rollover cyclometallation. It was accompanied by a short centroid-centroid distance between rings A and I of the quinoline groups (Figure 6.1a, 3.982 Å for **[1]⁺**, 3.343 Å for **[2]⁺**), which is close to the typical π - π stacking distance of aromatic rings (3.4 Å),²⁵

indicative of intramolecular π - π stacking between the two quinoline moieties in both complexes.

The prototypical molecular helices, helicenes, are organic compounds.^{26, 27} However, metal-based molecular helices have been described by Lehn, Sauvage, and Hannon, for example.^{28, 29} In this work, the helical structures of the gold complexes **[1]**⁺ and **[2]**⁺ indicate that gold complexation can be a new strategy to develop helical systems from planar ligands. In **[1]**⁺ the perpendicular distances between the centroids of the terminal ring A and I to the least-squares plane defined by the central two pyridyl rings D and F (red characters in Figure 6.1a), was $d_{A-DF} = 1.946$ Å and $d_{I-DF} = 1.586$ Å, while in **[2]**⁺ they were $d_{A-DF} = 1.984$ Å and $d_{I-DF} = 1.040$ Å (Figure 6.1b). The sum of the two values in **[1]**⁺ ($\Sigma d_{A/I-DF} = 3.532$) is about 17% larger than that in **[2]**⁺ ($\Sigma d_{A/I-DF} = 3.024$), indicating a more helical geometry for the bis-cyclometalated complex **[1]**⁺, possibly as a consequence of the repulsion between the terminal negatively charged carbon atoms. A difference in helical distortion was also found in the angle of the centroids of ring A and I with the Au(III) center (θ_{Au-AI}). The θ_{Au-AI} of **[1]**⁺ was 54.16°, which was larger than that in **[2]**⁺ ($\theta_{Au-AI} = 46.66^\circ$), demonstrating again the larger distortion in **[1]**⁺ than in **[2]**⁺. Some gold(III) complexes have been shown to interact via supramolecular Au...Au bonds.³⁰ However, in the crystal lattice of **[1]Cl** and **[2](AuCl₄)**, the metal centers were too far from each other ($d(\text{Au}...\text{Au}) \sim 4.2\text{-}5.5$ Å) to suggest any aurophilic interactions. On the other hand, intermolecular π - π stacking occurs between the quinoline rings of two adjacent molecules (π - π distance around 3.9 Å in **[1]Cl**, Figure AV1), leading to an interesting supramolecular packing of the helices (Figure 6.1c). The crystal structure of **[2](AuCl₄)** showed slightly different supramolecular helical arrangements cut by the larger AuCl₄[−] counter anions, placed at a relatively short Au...Au distance (around 4.27 Å, Figure 6.1c). These packing differences are a probable consequence of the higher distortion of the coordination sphere in **[1]**⁺ combined with the smaller size of chloride counter-anions, which leads to the generation of tighter intermolecular π - π stacking.

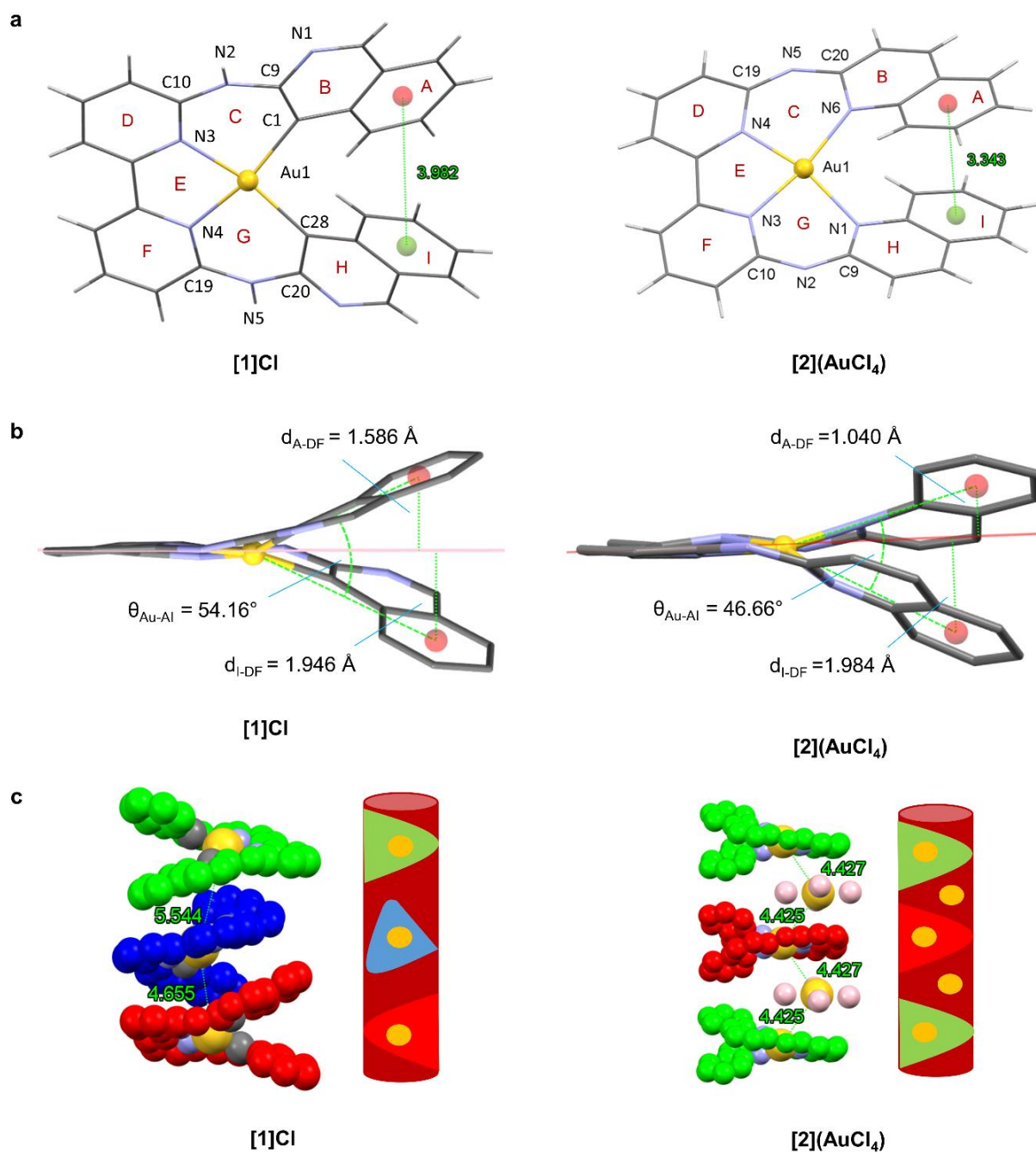


Figure 6.1 (a) Cationic part and ring numbers (red characters) in the crystal structures (wireframe style) of gold complexes **[1]Cl** and **[2](AuCl₄)**. The counterions were omitted for clarity. (b) Selected angles (°) and distances (Å) in **[1]Cl** and **[2](AuCl₄)**. The least-squares plane defined by the rings D and F is shown as a red line. (c) Spacefill construction and schematic pictures of the supramolecular helices in the crystal structure of **[1]Cl** and **[2](AuCl₄)**. The Au atoms label in yellow color, Cl in pink, and the coordinated N in pale blue, coordinated C in grey, and non-coordinated C in green, dark blue, and red.

6.2.3 DFT calculation of the classical and rollover complexes.

Considering the structural similarity between both ligands **H₂biqbpy1** and **H₂biqbpy2** and the different coordination modes obtained in **[1]⁺** and **[2]⁺** using identical reaction conditions, we investigated by DFT calculations what was the influence of rollover cyclometallation on the frontier orbitals of **[1]⁺** and the cause(s) of the rollover observed for **[1]⁺**. As shown in Figure 6.2, both **[1]⁺** and **[2]⁺** show similar highly distorted coordination structures in the DFT minimized structures, with a short π - π distance on the centroid of the terminal ring of the quinoline groups (4.55 and 4.06 Å for **[1]⁺** and **[2]⁺**, respectively, Table 6.1). The HOMO orbitals of both **[1]⁺** and **[2]⁺** have similar π symmetry, similar energies (-6.028 eV for **[1]⁺**, -6.118 eV for **[2]⁺**), and are both centered on the ligand with a negligible contribution of the Au(III) center (2.2% for **[1]⁺**, 0% for **[2]⁺**). By contrast, they show significantly different LUMO orbitals. The LUMO of **[1]⁺** was found centered on the bipyridine part of the ligand, while that of **[2]⁺** was essentially the expected anti-bonding combination of the Au(III) $d_{x^2-y^2}$ orbitals (33%) and the p orbitals of the coordinated nitrogen atoms, which altogether results in drastically different LUMO energies (-2.520 eV for **[1]⁺** vs. -3.267 for **[2]⁺**). Consequently, **[1]⁺** is predicted to be much more difficult to reduce than **[2]⁺**, as expected for cyclometalated complexes. Besides, the HOMO-LUMO energy gaps of **[1]⁺** and **[2]⁺** is very different, *i.e.* 3.508 eV in **[1]⁺** and 2.611 eV in **[2]⁺**, suggesting that both isomers should have different absorbance spectra. This hypothesis was further confirmed by time-dependent density functional theory calculations (TDDFT) in water, using COSMO to simulate solvent effects. As shown in Figure AV2, the classical N-bonded **[2]⁺** exhibited a red-shifted lowest-energy transition (694 nm), compared with that of the cyclometalated **[1]⁺** (451 nm).

To understand the reason for rollover cyclometallation we also simulated by DFT the tetrapyridyl coordination mode of **biqbpy1²⁻** (the isomer of **[1]⁺** called **[1a]⁺**, Figure 6.2a) and the rollover cyclometalated binding mode of **biqbpy2²⁻** (the isomer of **[2]⁺** called **[2a]⁺**, Figure 6.2b). In the rollover cyclometalated binding mode **[1]⁺** and **[2a]⁺**, the HOMO and LUMO orbitals showed similar metal-independent π -symmetry and a LUMO located on the bipyridine ligand. The tetrapyridyl molecules **[2]⁺** and **[1a]⁺** shared similar metal-independent, π -symmetry HOMO orbitals; however, their LUMO orbitals was centered on the Au-N₄ antibonding $d_{x^2-y^2} - p_{x,y}$ interaction, suggesting that upon reduction, coordination of the tetrapyridyl ligand to the metal might be weakened. Interestingly, the relative total binding energy of both cyclometalated molecules **[1]⁺** and **[2a]⁺** were found significantly lower than that of **[1a]⁺** and **[2]⁺** (Table 6.1). This result suggested that the thermodynamic stability of **[1]⁺**

and $[2]^+$ might not be the only factor influencing which isomer is obtained in the reaction conditions, hence that both reactions were under kinetic control. However, it should also be noted that both hypothetical structures $[1a]^+$ and $[2a]^+$ show much longer centroid-centroid distances (6.70 and 7.29 Å, respectively) between the terminal rings of the quinolines, compared with that in the isomers obtained experimentally $[1]^+$ and $[2]^+$ (4.55 and 4.06 Å, respectively). This difference also suggests that intramolecular π - π stacking of the quinoline moieties may play an important role in the mechanism leading to the final structures, and hence in the occurrence of rollover cyclometalation for $[1]^+$.¹⁹ Overall, a probable mechanism for the C-H activation of rollover $[1]^+$ is described in Figure 6.2c. Firstly, the precursor HAuCl_4 reacts with $\text{H}_2\text{biqbpy1}$ to generate the first intermediate $[\text{Au}(\text{H}_2\text{biqbpy1})\text{Cl}_2]\text{Cl}$, in which the Au(III) center binds with the bipyridine part and two chloride ligands. In a second step, intramolecular C-H...Cl hydrogen bond weakens the C-H bond, which triggers the generation of the first M-C bond and the second intermediate $[\text{Au}(\text{Hbiqbpy1})\text{Cl}]\text{Cl}$. Repeating this process a second time finally results in the rollover bis-cyclometalated $[1]\text{Cl}$.

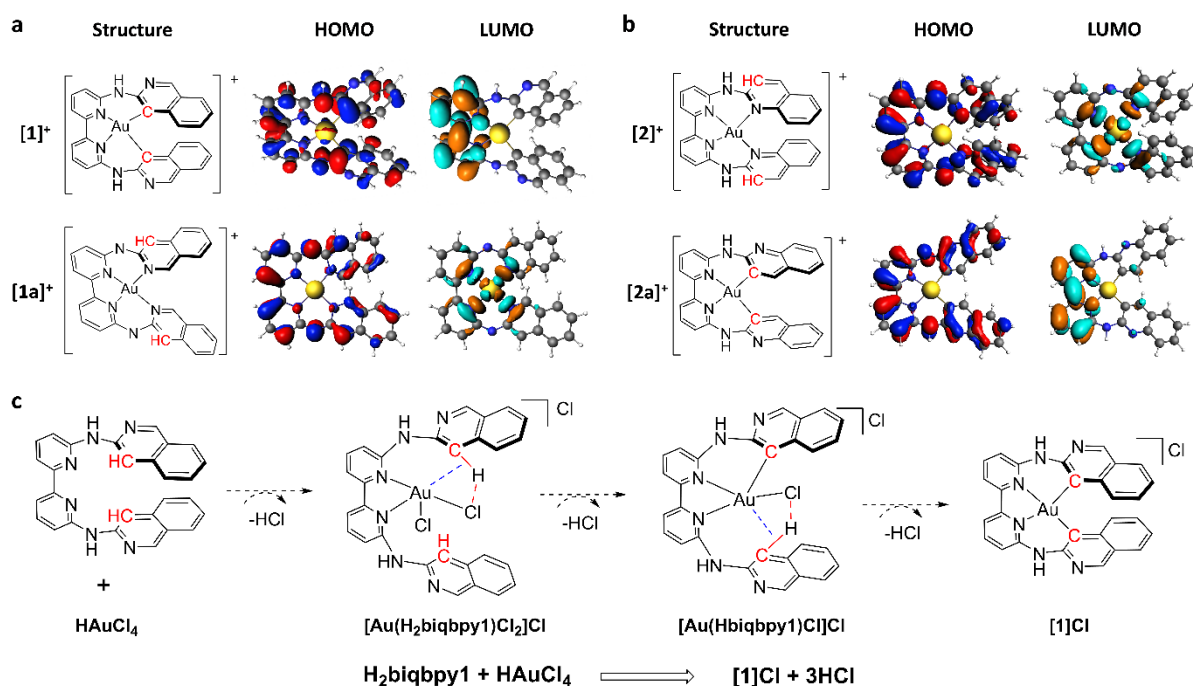


Figure 6.2 Structure, calculated geometry, and frontier orbitals (HOMO, LUMO) of (a) $[1]^+$ and $[1a]^+$, (b) $[2]^+$ and $[2a]^+$. (c) Proposed mechanism for the C-H activation and cyclometalation of $\text{H}_2\text{biqbpy1}$ to form $[1]\text{Cl}$.

Table 6.1. The calculated information of complexes $[1]^+$, $[2]^+$, $[1a]^+$ and $[2a]^+$.

Complex	HOMO (eV)	LUMO (eV)	ΔE (eV)	Relative total bind energy (eV)	End ring π - π distance (Å)
$[1]^+$	-6.028	-2.520	3.508	0	4.55
$[2]^+$	-6.118	-3.267	2.851	+0.8790	4.06
$[1a]^+$	-5.707	-3.096	2.611	+0.7726	6.70
$[2a]^+$	-6.332	-2.586	3.746	-0.6004	7.29

6.2.4 Behavior in solution. The absorbance spectra of both complexes in PBS solution at 310 K presented no significant changes over 24 h (Figure AV3), suggesting that they were thermally stable in aqueous solutions. $[2]Cl$ had a significant intense metal-to-ligand charge transfer (MLCT) absorbance band around 450-500 nm, while that of $[1]Cl$ was not remarkable, matching well with the trend observed by DFT and TDDFT calculation. However, when dissolving the complexes (50 μM) in PBS containing GSH (100 μM), the two complexes showed completely different behavior. The absorbance spectra of $[2]Cl$ rapidly changed (in < 30 s), with a significant decrease of the absorption band in the visible region of the spectrum, which hereafter remained stable (for 25 min), while the spectrum of $[1]Cl$ remained constant in these conditions (Figure 6.3a). The fast reaction of $[2]Cl$ with GSH suggested that reduction of Au(III) to Au(I) might take place.³¹ In order to check this, 1H NMR was used to monitor the reaction between $[2]Cl$ and GSH in D_2O , using a complex: GSH ratio of 1:2. After mixing GSH with $[2]Cl$, the 1H NMR peaks of $[2]Cl$ showed a dramatic change, accompanied by the generation of a peak for GSSG in the aliphatic region (2.98 and 3.26 ppm, blue star in Figure 6.3b). Although the peaks in the aromatic region can be split into two different Au(I) species involving the **H₂biqbpy2** ligand (indicated as yellow circle or green triangle in Figure 6.3b), their interpretation is difficult. After 24 h a precipitate was formed, which after filtration and 1H NMR analysis was found to be the free tetrapyridyl ligand (Figure AV4). These UV-vis and NMR spectroscopy experiments demonstrate that $[2]Cl$ is easily reduced by GSH, while $[1]Cl$ is much more stable in the presence of GSH, suggesting that the rollover cyclometalation stabilizes the gold complexes in thiol-containing solutions.

The stability of both complexes in cell-growing medium Opti-MEM complete (containing 2.5% fetal calf serum (FCS)) was also studied for 24 h using absorption spectroscopy (Figure 6.3c). For $[1]Cl$ only the baseline of the spectrum increased gradually, suggesting the formation of nanoparticles might occur, but there was no obvious reaction nor isosbestic point. Nanoparticle

formation was confirmed by dynamic light scattering measurements (DLS, Figure 6.3d): the Opti-MEM solution of **[1]Cl** showed a significant signature of nanoparticles in the range 100-500 nm and much higher particle numbers than the Opti-MEM control group. By contrast, the absorbance band of **[2]Cl** in the visible region exhibited a rapid decrease during the first 10 min and finally disappeared, suggesting that a chemical reaction occurred in medium leading to a change of the Au coordination sphere. Considering the results above, reduction by thiol species present in the medium, like GSH, is the most likely explanation to the reaction of the Au(III) complex **[2]Cl** in medium. In summary, both experiments suggested that the Au(III) center in **[1]Cl** is stable to reduction by thiol groups such as GSH or FCS, proving that bis-cyclometalation results in the stabilization of gold(III), even if rollover cyclometallation is also accompanied by the formation of nanoparticles. By contrast, the gold(III) center in **[2]Cl** is very sensitive to reduction by thiol groups, which is a direct consequence of the high electronegativity and charge of the Au(III) center. In cell-growing medium, reduction of **[2]Cl** into Au(I) was followed by slow release of the insoluble tetrapyridyl ligand, with the concomitant formation of unidentified gold(I) species probably involving GSH.³²

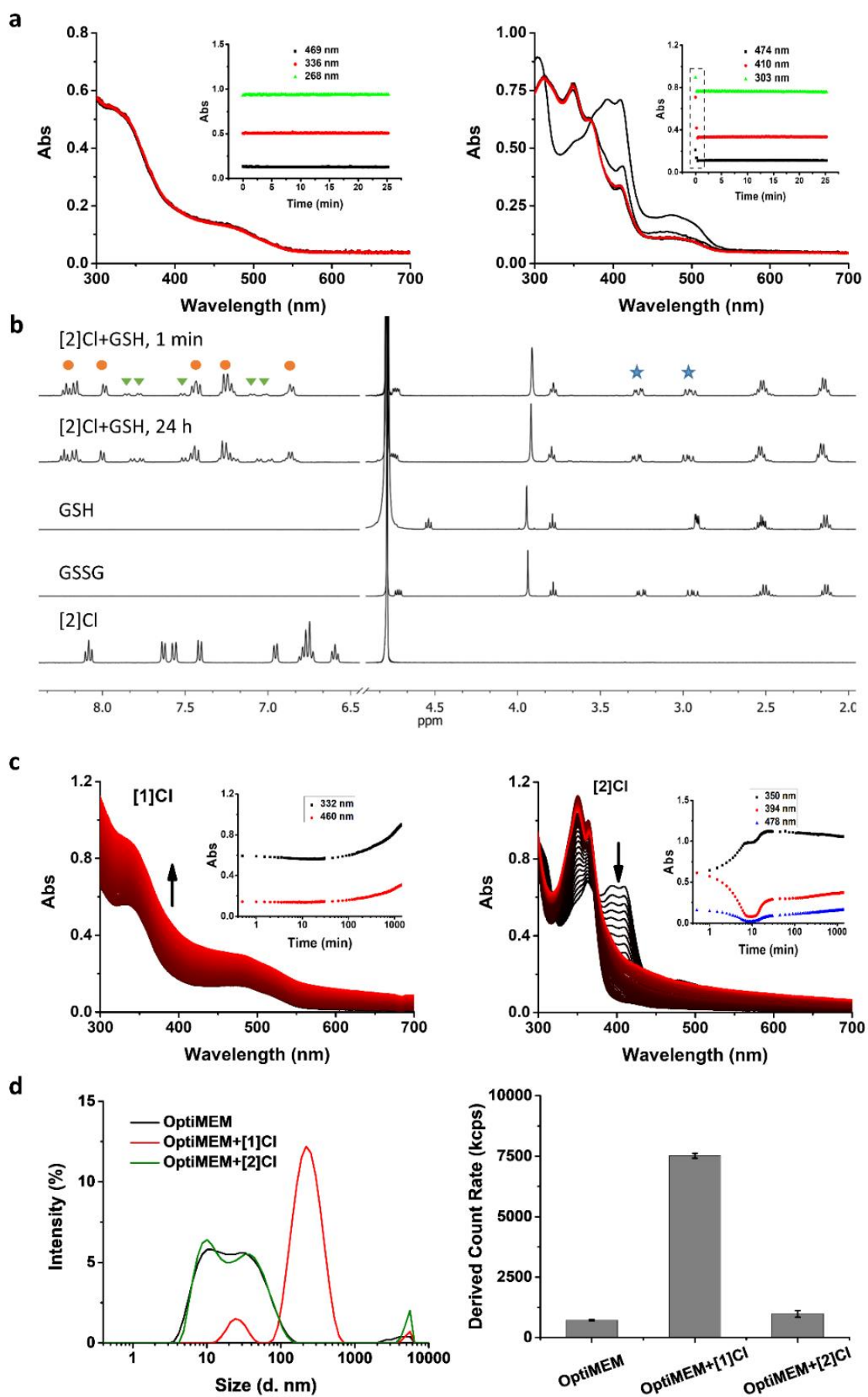


Figure 6.3 (a) Time evolution of the absorbance spectrum of [1]Cl and [2]Cl (50 μ M) in PBS solution containing GSH (100 μ M) for 25 min; measurement interval 12 s, color changes from black (0 s) to red (25 min). (b) ^1H NRM monitoring of a [2]Cl/GSH mixture in D_2O (concentration ratio 3 mM/6 mM). Yellow pie and green triangle indicate different Au(I) species. (c) Time evolution of the absorbance spectrum of [1]Cl and [2]Cl (50 μ M) in Opti-MEM medium solution containing FCS (2.5% v/v) for 24 h; measurement interval: first 30 min every 0.5 min, the left 23.5 h every 15 min; color changes from black (0 s) to red (25 min). (d) DLS size distribution and derived count rate of [1]Cl and [2]Cl (50 μ M) in Opti-MEM medium solution containing FCS (2.5% v/v).

6.2.5 Anticancer properties. The cytotoxicity of both gold complexes [1]Cl and [2]Cl to 2D monolayers of four human cancer cell lines (lung cancer A549, skin cancer A431, melanoma cancer A375, and breast cancer MCF7) and one non-cancerous cell line (MRC5) was determined using a reported SRB assay, both in normoxic and hypoxic conditions.³³ The half-maximal effective concentrations (EC_{50} in μM), defined as the concentration necessary to kill 50% of the cells, compared to the untreated control, are shown in Table 6.2. The dose-response curves of gold complexes and cisplatin for these cells are shown in Figure AV5-7. Similar to cisplatin, [1]Cl showed a broad-spectrum anticancer ability to all cancer cells with EC_{50} in the range of 3.3–16 μM , both in normoxic and hypoxic conditions. Interestingly, [1]Cl exhibited a relatively higher EC_{50} (27 and 28 μM in normoxic and hypoxic conditions, respectively) to non-cancerous MRC5 cells, suggesting some form of selectivity towards cancer cells for [1]Cl. By comparison, [2]Cl showed generally lower EC_{50} values to cancer cells, *i.e.* higher cytotoxicity, with significant antiproliferative properties against A375 and MCF7 cancer cells (EC_{50} = 0.7 and 0.3 μM , respectively, in normoxic conditions). However, [2]Cl also showed high cytotoxicity to healthy MRC5 cells (3.3 and 1.5 μM in normoxic and hypoxic conditions, respectively), which might limit further applications in cancer treatment.

Apoptosis is a form of programmed cell death that can be induced by some metallodrugs. Here, the Annexin V/propidium iodide double staining was used to demonstrate if these two complexes kill cancer cells via the apoptosis or necrosis pathway. The different fluorescence states of both dyes in each cell indicates its status, *i.e.* healthy (-/-), early apoptotic (+/-), later apoptotic (+/+) or necrotic (-/+). As shown in Figure 6.4a, after treatment with complex [1]Cl or [2]Cl (10 μM) to A549 cells for 24 h, the percentage of cells in the early and late apoptotic quadrants increased with compound concentration compared with the control group, suggesting that [1]Cl and [2]Cl kill A549 cells *via* stimulating the cell apoptosis process. Drug uptake

efficiency is highly relevant to the cytotoxicity of many metallodrugs. ICP-MS was hence used to determine the Au content in A549 cells. 24 h after treatment with these two complexes (1 μM), the Au content in A549 cells were 51 ng Au/million cells for **[1]Cl**, 8-fold higher than that of **[2]Cl** (6 ng Au/million cells, Figure 6.4b), demonstrating unambiguously the more efficient cellular uptake of cyclometalated rollover complex **[1]Cl** in A549 cells. Considering the identical charges of **[1]**⁺ and **[2]**⁺, this difference cannot be due here to increased passive uptake for **[1]Cl**, as usually hypothesized for cyclometalated complexes.³⁴ It might be due on the one hand to the formation of nanoparticles of **[1]Cl** in the cell medium, which may help to trigger energy-dependent endocytosis-related transport pathways. On the other hand, the lower uptake of **[2]Cl** might be linked to its decomposition in the cell culture into Au⁺ ions that cannot be taken up efficiently, which also suggests that the toxicity of this complex might be that of the ligand **H₂biqbp₂**.

In humans, cancer appears as a 3D tumor characterized by a complicated microenvironment, which greatly influences the permeability, uptake, and cytotoxicity of anticancer drugs.³⁵ In recent years, *in vitro* 3D tumor spheroids have been developing as a more suitable model for the pre-screening of anticancer drugs, as they provide better mimicry of nutrient and drug penetration of *in vivo* tumors. Thus, the cytotoxicity of both gold complexes was also determined in 3D tumor spheroids, using the final spheroid diameter as well as a fluorescence-based Cell Titer Glo 3D end-point assay quantifying ATP (Figure 6.4c-e).³⁶ As shown in Figure 6.4c, **[1]Cl** showed good anti-proliferation properties in ~1000 μm diameter A549 tumor spheroids ($\text{EC}_{50} = 7 \mu\text{M}$), while **[2]Cl** exhibited slightly higher cytotoxicity ($\text{EC}_{50} = 4 \mu\text{M}$). Both were found less toxic than cisplatin ($\text{EC}_{50} = 0.6 \mu\text{M}$). Notably, the spheroid diameter was found not to be a good measure of the effect of these compounds, as the dose-diameter curves were found very different from the dose-response curves using the Cell TiterGlo3D assay. In summary, the cytotoxicity of the two gold complexes remained high in a 3D tumor model, where **[2]Cl** kept the higher cytotoxicity observed in a 2D model.

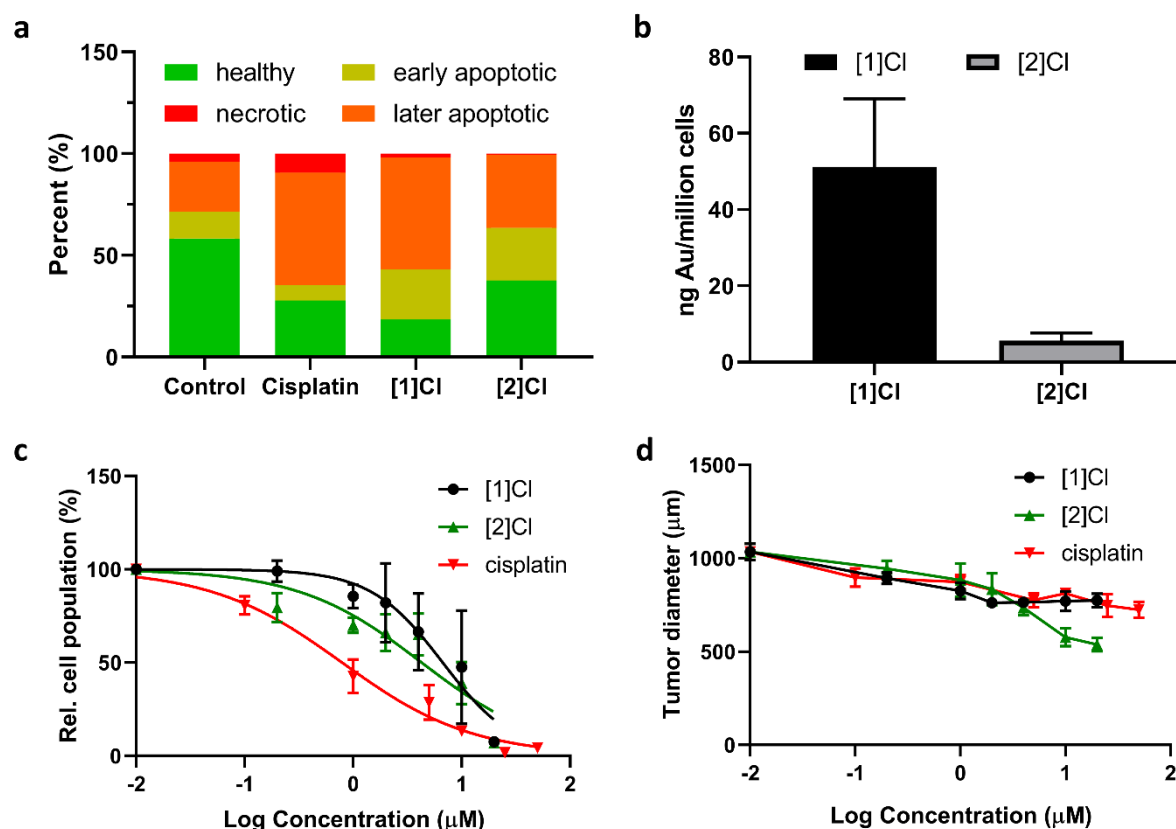


Figure 6.4 (a) Flow cytometry quantification of healthy, early apoptotic, later apoptotic and necrotic A549 cells after treatment with cisplatin (15 μM), [1]Cl (10 μM) or [2]Cl (10 μM) for 24 h. (b) The Au content (ICP-MS) of A549 cells after treatment with [1]Cl and [2]Cl (1 μM) for 24 h. (c) 3D-tumor EC_{50} values of gold complexes and cisplatin based on a 3D CellTiterGlo ATP end-point assay. (d) Evolution of the tumor spheroid diameter after treatment with different concentrations of the gold complexes [1]Cl and [2]Cl or cisplatin.

Table 6.2. Half-maximal effective concentrations (EC_{50} in μM) of gold complexes [1]Cl and [2]Cl and cisplatin towards 2D cancer cell and healthy cell monolayers in normoxic (21% O_2) and hypoxic (1% O_2) conditions. 95% confidence interval (CI in μM over three independent biological experiments) are also indicated.

Complex		EC_{50} (μM)											
		Cell line											
		A549	$\pm\text{CI}$	A431	$\pm\text{CI}$	A375	$\pm\text{CI}$	MCF7	$\pm\text{CI}$	MRC5	$\pm\text{CI}$	A549-3D	$\pm\text{CI}$
[1]Cl ₂	Normoxic	3.3	+0.7 -0.6	4	+1 -1	5	+1 -1	4	+1 -1	27	+16 -9	7	+4 -2
	Hypoxic	5	+2 -2	16	+7 -5	6	+3 -2	9	+2 -1	28	+9 -6	N.D.	
[2]Cl	Normoxic	3.1	+0.3	3.5	+0.6	0.7	+0.2	0.3	+0.1	3.3	+0.8	4	+3

			-0.3		-0.5		-0.1		-0.1		-0.7		-2
	Hypoxic	3.9	+0.7 -0.6	2.9	+0.8 -0.5	4	+4 -2	2.1	+0.1 -0.1	1.5	+0.2 -0.2	N.D.	
cisplatin	Normoxic	4.5	+0.7 -0.6	1.8	+0.5 -0.4	1.2	+0.1 -0.1	3.6	+1.2 -0.9	5.8	+1.5 -1.2	0.8	+0.3 -0.2
	Hypoxic	24	+11 -5	13	+4 -3	3.4	+0.8 -0.7	N.D.		9.4	+5.7 -3.6	N.D.	

6.2.6 Proteins binding and inhibition properties. Several gold complexes have been demonstrated to show significant binding and inhibition properties to several proteins, such as urease,³⁷ aquaporin,³⁸ and particularly TrxR.^{9, 32} To determine the inhibition properties of **[1]Cl** and **[2]Cl** towards mammalian TrxR, a spectrophotometric assay was realized using commercially available rat-liver TrxR. As shown in Table 6.3, **[1]Cl** did not show any inhibition activity to TrxR at the tested concentration. This low inhibition property might be attributed to the weak reactivity of **[1]Cl** with biological thiols (see above). By contrast, **[2]Cl** showed significant TrxR inhibition activity with a submicromolar IC₅₀ ($0.13 \pm 0.02 \mu\text{M}$), which may be attributed to its high reactivity with reducing thiols, which generate Au⁺ ions that are known inhibitors of TrxR. The significant difference between **[1]Cl** and **[2]Cl** indicates that rollover cyclometalation might represent a promising design strategy to generate anticancer gold compounds that show a target different from TrxR, and do not release polypyridyl ligands upon reacting with cell medium or intracellular GSH.

Indeed, next to releasing Au⁺ ions, reduction of **[2]Cl** by biological thiols also leads to the release of the free polypyridyl ligand **H₂biqbpy2**, which might have unselective toxicity. This hypothesis stimulated us to look into the biological activity of the two polypyridyl ligands **H₂biqbpy1** and **H₂biqbpy2**. N-heterocyclic ligands are found in roughly 60% of FDA-approved drugs, and pyridine ring systems are prominent examples of such fragments.³⁹ Many N-heterocyclic ligands have been considered as potential inhibitors of potassium channels in the cell membrane or mitochondrial membrane.⁴⁰⁻⁴² Potassium channels have been proposed as emerging targets in cancer therapy, for their overexpression in several cancer cell lines, and their specific functions in cell proliferation as they control cell cycle progression.^{43, 44} On the other hand, a classical safety issue in medicinal chemistry is K⁺ channel inhibition, in particular the broad-substrate K_v11.1 (hERG) potassium channel, which is known to generate cardiac toxicity *in vivo*.^{45, 46} Here, we evaluated the K_v11.1 channel interaction of the two gold complexes **[1]Cl** and **[2]Cl** and their ligands **H₂biqbpy1** and **H₂biqbpy2** at a single

concentration (10 μM) in a [^3H]dofetilide displacement assay.⁴⁷ When a compound binds to the K_v11.1 channel, the binding of reference hERG blocker [^3H]dofetilide is decreased, which is used to quantify the K_v11.1 binding efficiency of the tested compounds. As shown in Table 3, all four compounds displaced [^3H]dofetilide from the channel albeit to different degrees. While **H₂biqbpy1** was a poor binder, **H₂biqbpy2** displaced 84% of [^3H]dofetilide binding. The gold complexes showed a (slightly) higher effect, *i.e.* 91% displacement for the rollover compound **[1]Cl** and 92% displacement for **[2]Cl**. Such good K⁺-channel binding properties of both metal complexes are probably due to the high similarity, both in terms of shape and positive charge, of these molecules. Altogether, both **[1]Cl** and **[2]Cl** efficiently bind to the K_v11.1 channel. The higher toxicity of **[2]Cl** might be related to a combination between K⁺ channel inhibition by the released ligand, and TrxR inhibition by the released Au⁺ ions.

Table 6.3. Binding of tetrapyridyl ligands and their gold(III) complexes to TrxR and K_v11.1 proteins.

Compound	TrxR inhibition IC ₅₀ (μM)	[^3H]dofetilide binding remaining (%) ^b	K _v 11.1 binding (%) ^c
H₂biqbpy1	N.D. ^a	64 \pm 4	36 \pm 4
[1]Cl	>5	8.7 \pm 0.1	91.3 \pm 0.1
H₂biqbpy2	N.D.	16 \pm 4	84 \pm 4
[2]Cl	0.13 \pm 0.02	7.9 \pm 0.2	92.1 \pm 0.2

^a N.D. = not determined. ^b tested concentration = 10 μM ; ^c K_v11.1 binding (%) = 100% - [^3H]dofetilide binding remain (%).

6.3 Discussion and Conclusion

Many gold(III) compounds have been demonstrated to be potential anticancer metallodrugs due to their easy reduction to gold(I) upon intracellular uptake. Gold(I) species always show strong binding affinity to the thiol groups of many key biomolecules and enzymes inside a cell, notably to glutathione (GSH) or thioredoxin reductase (TrxR), which are overexpressed in cancer cells because they control the redox balance of cells.^{10, 48, 49} However, several cyclometalated gold(III) complexes have been shown to withstand reduction by biological thiols while keeping anticancer properties, indicating that a different anticancer mechanism may be operative.⁵⁰ Very limited research has focused on the comparison of cyclometalated vs. classical nitrogen-coordinated gold compounds, both from the chemical structure point of view to that of the biological activities. In this work, we synthesized two gold(III) isomers, *i.e.* the rollover cyclometalated **[1]Cl** (C[^]N[^]N[^]C) and the classically nitrogen-coordinated **[2]Cl** (N[^]N[^]N[^]N). The two complexes show strikingly similar helical molecular structures, but they exhibited dramatically different reactivity to GSH and TrxR proteins: **[1]Cl** shows no reaction to thiol

groups and no TxrR inhibition, while **[2]Cl** reacts with thiol groups rather quickly, which is accompanied with the release of the tetradentate ligand and TxrR-inhibiting Au^+ ions. The low thiol group susceptibility of **[1]Cl** should be attributed to the high stability of the M-C bond and localization of the LUMO of this complex on the bipyridine group, without the involvement of metal.

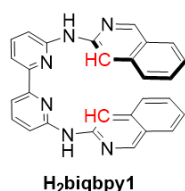
In biological terms, both compounds were found anticancer active, but in a quite different manner. On the one hand, **[2]Cl** is an interesting cytotoxic compound that upon reduction releases both a TxrR-inhibiting Au^+ ion and a good K^+ -channel blocker ligand **H₂biqbpy2**, which may act synergistically. However, cellular uptake is limited by thiol-induced decomposition outside the cells, and toxicity to non-cancerous cells is also high. On the other hand, **[1]Cl** is more promising in several aspects: it shows much higher toxicity in cancerous vs. non-cancerous cell lines, and a high cellular uptake probably in the form of nanoparticles. Cellular uptake provides intact Au(III) complexes inside the cell that have excellent redox stability in presence of biological thiols, and improved K^+ channel binding, compared to the ligand **H₂biqbpy1**. It is unclear at present if K^+ channel inhibition is the reason for the higher toxicity to cancer cells. However, bis-cyclometalation appears as an appealing strategy to generate Au(III) anticancer compounds that enter the cell efficiently and inhibit proteins that are different from TxrR.

6.4 Experimental section

The DFT calculation, cell culture, cytotoxicity, cell uptake, apoptosis and 3D tumor spheroids inhibition experiments were carried out according to the description in chapters 3 and 4.

6.4.1 Synthesis and analytical data for ligands and gold complexes

H₂biqbpy1.

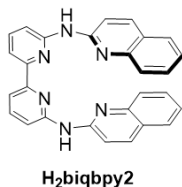


This ligand was synthesized according to a literature procedure.¹ A mixture of 6,6'-dibromo-2,2'-bipyridine (1004 mg, 3.18 mmol), Pd(dba)₂ (296 mg, 0.32 mmol), racemic BINAP (395 mg, 0.64 mmol) and cesium carbonate (4145 mg, 12.14 mmol) was partially dissolved in dry toluene (50 mL) under N₂

atmosphere. The mixture was stirred for 10 min, then 3-aminoisoquinoline (919 mg, 6.37 mmol) was added, followed by heating the reaction mixture to 85 °C. After 3 days of stirring, the brown mixture was cooled down. Demi water (75.0 mL) was added and the mixture was stirred for 1 h. The mixture was then filtered, and dry in a vacuum to obtain the light green product (1288 mg, 91% yield). **ESI-MS** (cation): *m/z* calcd 441.2 (C₂₈H₂₀N₆ + H⁺), found

441.2. **^1H NMR** (300 MHz, $\text{DMSO}-d_6$): δ 10.00 (s, 2H), 9.13 (s, 2H), 8.80 (s, 2H), 8.08 – 7.98 (m, 4H), 7.94 (t, J = 7.8 Hz, 2H), 7.83 (t, J = 8.4 Hz, 2H), 7.67 (t, J = 7.4 Hz, 2H), 7.43 (t, J = 7.3 Hz, 2H), 7.35 (d, J = 7.9 Hz, 2H).

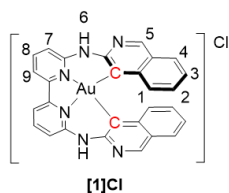
H₂biqbpy2.



The synthesis of H₂biqbpy2 is similar to that of H₂biqbpy1, except that 2-aminoquinoline was used to replace 3-aminoisoquinoline. The yield is 943 mg, 2.14 mmol, 67%. **ESI-MS** (cation): m/z calcd 441.2 ($\text{C}_{28}\text{H}_{20}\text{N}_6 + \text{H}^+$), found

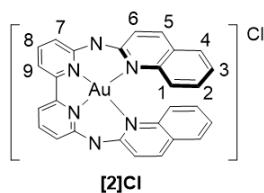
441.2. **^1H NMR** (300 MHz, DMSO): δ 10.15 (s, 2H), 8.46 (dd, J = 7.5, 1.7 Hz, 2H), 8.22 (d, J = 9.0 Hz, 2H), 8.04 – 7.90 (m, 4H), 7.80 (td, J = 9.1, 8.7, 1.8 Hz, 6H), 7.64 (ddd, J = 8.4, 6.9, 1.5 Hz, 2H), 7.38 (ddd, J = 8.1, 6.9, 1.3 Hz, 2H).

[Au(biqbpy1)]Cl ([1]Cl).



A mixture of H₂biqbpy1 (100 mg, 0.23 mmol) and HAuCl_4 (85 mg, 0.25 mmol) was dissolved in MeOH (30 mL), and stirred under N_2 atmosphere at 75 °C for 3 days. Then the solvent was rotary evaporated. The crude product obtained was purified by silica chromatography using dichloromethane-MeOH mixtures (10:2, R_f = 0.35) as eluent to afford the target compound. Then the complex was dissolved in the MeOH and across the Cl^- ion exchange resin to unify the counterion as Cl^- . The yield of final product [1]Cl was 25 mg, 0.03 mmol, 13%. **HRMS** (cation): m/z calcd 635.1258 ($[\text{C}_{28}\text{H}_{18}\text{AuN}_6]^+$), found 635.1244. **^1H NMR** (400 MHz, $\text{DMSO}-d_6$): δ 11.70 (s, 2H, H^6), 9.08 (d, J = 0.7 Hz, 2H, H^5), 8.25 (dd, J = 8.4, 7.5 Hz, 2H, H^8), 8.19 (dd, J = 7.6, 1.1 Hz, 2H, H^9), 7.87 (dd, J = 8.4, 1.1 Hz, 2H, H^7), 7.78 (dt, J = 8.0, 1.0 Hz, 2H, H^4), 7.29 (dd, J = 8.6, 1.0 Hz, 2H, H^1), 7.09 (ddd, J = 8.0, 6.8, 1.1 Hz, 2H, H^3), 6.84 (ddd, J = 8.4, 6.9, 1.4 Hz, 2H, H^2). **^{13}C NMR** (101 MHz, $\text{DMSO}-d_6$): δ 153.10, 151.91, 148.04, 141.22, 140.81, 139.21, 129.38, 128.91, 127.24, 126.25, 125.28, 116.34, 115.44, 113.03. **Elemental analysis**: calcd for [1]Cl + 4 H_2O : C 45.27, H 3.53, N 11.31; found C 45.49, H 3.63, N 11.29.

[Au(biqbpy2)]Cl ([2]Cl).



A mixture of H₂biqbpy2 (100 mg, 0.23 mmol) and HAuCl_4 (85 mg, 0.25 mmol) was dissolved in MeOH (30 mL), and stirred under N_2 atmosphere at 75 °C for 72 h. Then the solvent was rotary evaporated.

The crude product obtained was purified by silica chromatography using dichloromethane-MeOH mixtures (10:1, R_f = 0.3) as eluent to afford the target compound. Then the complex was dissolved in the MeOH and across the Cl^- ion exchange resin to unify the

counterion as Cl^- . The yield of final product **[2]Cl** was 27 mg, 0.04 mmol, 18%. **HRMS** (cation): m/z calcd 635.1258 ($[\text{C}_{28}\text{H}_{18}\text{AuN}_6]^+$), found 635.1236. **^1H NMR** (400 MHz, $\text{DMSO-}d_6$): δ 8.21 (dd, $J = 8.4, 7.4$ Hz, 2H, H^8), 8.10 (dd, $J = 7.5, 1.3$ Hz, 2H, H^7), 7.96 (d, $J = 8.9$ Hz, 2H, H^5), 7.63 (dd, $J = 8.4, 1.2$ Hz, 2H, H^9), 7.59 – 7.52 (m, 2H, H^2), 7.41 – 7.34 (m, 2H, H^4), 7.28 (d, $J = 8.9$ Hz, 2H, H^6), 6.98 – 6.88 (m, 4H, H^3, H^1). **^1H NMR** (400 MHz, D_2O): δ 7.99 (t, $J = 8.4, 7.4$ Hz, 2H, H^8), 7.49 (d, $J = 7.7, 1.2$ Hz, 2H, H^7), 7.45 (d, $J = 8.9$ Hz, 2H, H^6), 7.30 (d, $J = 8.3, 1.1$ Hz, 2H, H^9), 6.83 (d, 2H, H^3), 6.70 – 6.54 (m, 6H, $\text{H}^4, \text{H}^5, \text{H}^1$), 6.47 (t, $J = 7.3$ Hz, 2H, H^2). **^{13}C NMR**, (101 MHz, D_2O): 175.78, 152.50, 149.51, 142.01, 140.66, 139.92, 129.11, 128.65, 126.46, 125.70, 125.57, 122.93, 118.65, 116.89. **Elemental analysis**: calcd for **[2]Cl** + $4\text{H}_2\text{O}$: C 45.27, H 3.53, N 11.31; found C 45.26, H 3.51, N 11.30.

6.4.2 Proteins binding and inhibition properties of gold complexes

TrxR inhibition property determination. To determine the inhibition of mammalian thioredoxin reductase (TrxR), a spectrophotometric assay was done using commercially available rat liver TrxR (Sigma-Aldrich). The enzyme was diluted with distilled water to achieve a concentration of 2.5 U/mL. The gold complexes were freshly dissolved DMF to get a stock solution of 10 mM. To a 25 μL aliquot of the enzyme solution, 25 μL of potassium phosphate buffer, pH 7.0, containing the complexes at different concentrations or vehicle (DMF) without compounds (control probe) was added, and the resulting solutions (final concentration of DMF: max. 0.5% v/v) were incubated with moderate shaking for 75 min at 37 $^\circ\text{C}$ in a 96-well plate. Subsequently, to each well, 225 μL of the reaction mixture (1000 μL of reaction mixture consisted of 500 μL of potassium phosphate buffer, pH 7.0, 80 μL of EDTA solution (100 mM, pH 7.5), 20 μL of BSA solution (0.2%), 100 μL of NADPH solution (20 mM), and 300 μL of distilled water) was added. The reaction was started by the addition of 25 μL of an ethanolic 5,5'-Dithiobis 2-nitrobenzoic solution (DTNB, 20 mM). After proper mixing, the formation of 5-TNB was monitored with a microplate reader (Perkin-Elmer Victor X4) at 405 nm in 10 s intervals for 10 min. The increase in 5-TNB concentration over time followed a linear trend ($R^2 \geq 0.99$), and the enzymatic activities were calculated as the slopes (increase in absorbance per second) thereof. For each tested compound, the noninterference with the assay components was confirmed by a negative control experiment using an enzyme-free solution. The IC_{50} values were calculated as the concentration of complexes decreasing the enzymatic activity of the untreated control by 50% and are given as the means and standard deviations of two independent experiments.

Kv11.1 potassium channel binding affinity. This experiment was carried out according to a literature procedure.⁴² Briefly, the cell membrane of HEK293Kv 11.1 cells was collected. Then the loading of [³H]dofetilide on the cell membrane was performed by mixing membrane aliquots containing 30 µg protein with 2 nM [³H]dofetilide in a total volume of 100 µL incubation buffer at 15 °C for 90 min. After loading, a single point dissociation assay was initiated by the addition of 10 µM dofetilide in the absence (control) or presence of 10 µM of gold complexes and corresponding ligands. After 10 min of incubation, samples were separated by rapid filtration through a 96-well GF/B filter plate using a Perkin Elmer Filtermate-harvester (Perkin Elmer, Groningen, The Netherlands). Filters were subsequently washed with ice-cold wash buffer two times. Then the filter-bound radioactivity was determined by scintillation spectrometry *via* the 1450 Microbeta Wallac Trilux scintillation counter (Perkin Elmer) after the addition of 37.5 µL Microscint and for another 2 h extraction. The binding of [³H]astemizole in the control was set as 100%.

6.5 References

1. F. M. Muggia, A. Bonetti, J. D. Hoeschele, M. Rozenzweig and S. B. Howell, *J. Clin. Oncol.*, 2015, **33**, 4219-4226.
2. Y. R. Liu, C. Ji, H. Y. Zhang, S. X. Dou, P. Xie, W. C. Wang and P. Y. Wang, *Arch. Biochem. Biophys.*, 2013, **536**, 12-24.
3. S. Nafisi and N. Zeinab, *DNA Cell Biol.*, 2009, **28**, 469-477.
4. M. Pandrala, M. K. Sundaraneedi, A. J. Ammit, C. E. Woodward, L. Wallace, F. R. Keene and J. G. Collins, *Eur. J. Inorg. Chem.*, 2015, **34**, 5694-5701.
5. S. M. Meier-Menches, C. Gerner, W. Berger, C. G. Hartinger and B. K. Keppler, *Chem. Soc. Rev.*, 2018, **47**, 909-928.
6. S. Thota, D. A. Rodrigues, D. C. Crans and E. J. Barreiro, *J. Med. Chem.*, 2018, **61**, 5805-5821.
7. T. Lazarević, A. Rilak and Ž. D. Bugarčić, *Eur. J. Med. Chem.*, 2017, **142**, 8-31.
8. N. Cutillas, G. S. Yellol, C. de Haro, C. Vicente, V. Rodríguez and J. Ruiz, *Coord. Chem. Rev.*, 2013, **257**, 2784-2797.
9. M. Mora, M. C. Gimeno and R. Visbal, *Chem. Soc. Rev.*, 2019, **48**, 447-462.
10. T. Zou, C. T. Lum, C.-N. Lok, J.-J. Zhang and C.-M. Che, *Chem. Soc. Rev.*, 2015, **44**, 8786-8801.
11. J.-J. Jia, W.-S. Geng, Z.-Q. Wang, L. Chen and X.-S. Zeng, *Cancer Chemother. Pharmacol.*, 2019, **84**, 453-470.
12. M. P. Gamcsik, M. S. Kasibhatla, S. D. Teeter and O. M. Colvin, *Biomarkers*, 2012, **17**, 671-691.
13. F. Angelucci, A. A. Sayed, D. L. Williams, G. Boumis, M. Brunori, D. Dimastrogiovanni, A. E. Miele, F. Pauly and A. Bellelli, *J. Biol. Chem.*, 2009, **284**, 28977-28985.
14. I. Ott, *Coord. Chem. Rev.*, 2009, **253**, 1670-1681.
15. R. Kumar and C. Nevado, *Angew. Chem. Int. Ed.*, 2017, **56**, 1994-2015.
16. B. Butschke and H. Schwarz, *Chem. Sci.*, 2012, **3**, 308-326.
17. M. Leist, C. Kerner, L. T. Ghoochany, S. Farsadpour, A. Fizia, J. P. Neu, F. Schön, Y. Sun, B. Oelkers, J. Lang, F. Menges, G. Niedner-Schatteburg, K. S. M. Salih and W. R. Thiel, *J. Organomet. Chem.*, 2018, **863**, 30-43.
18. A. Zucca, G. L. Petretto, S. Stoccoro, M. A. Cinellu, M. Manassero, C. Manassero and G. Minghetti, *Organometallics*, 2009, **28**, 2150-2159.
19. L. Maidich, G. Dettori, S. Stoccoro, M. A. Cinellu, J. P. Rourke and A. Zucca, *Organometallics*, 2015, **34**, 817-828.
20. M. V. Babak, M. Pfaffeneder-Kmen, S. M. Meier-Menches, M. S. Legina, S. Theiner, C. Licon, C. Orvain, M. Hejl,

- M. Hanif, M. A. Jakupc, B. K. Keppler, C. Gaidon and C. G. Hartinger, *Inorg. Chem.*, 2018, **57**, 2851-2864.
21. L. Maidich, M. A. Cinellu, F. Cocco, S. Stoccoro, M. Sedda, S. Galli and A. Zucca, *J. Organomet. Chem.*, 2016, **819**, 76-86.
22. F. Cocco, M. A. Cinellu, G. Minghetti, A. Zucca, S. Stoccoro, L. Maiore and M. Manassero, *Organometallics*, 2010, **29**, 1064-1066.
23. V. H. S. van Rixel, B. Siewert, S. L. Hopkins, S. H. C. Askes, A. Busemann, M. A. Siegler and S. Bonnet, *Chem. Sci.*, 2016, **7**, 4922-4929.
24. Y. Simonov, O. Bologa, P. Bourosh, N. Gerbelev, J. Lipkowski and M. Gdaniec, *Inorg. Chim. Acta*, 2006, **359**, 721-725.
25. C. Janiak, *Dalton Trans.*, 2000, **21**, 3885-3896.
26. Y. Nakakuki, T. Hirose and K. Matsuda, *J. Am. Chem. Soc.*, 2018, **140**, 15461-15469.
27. N. Saleh, C. Shen and J. Crassous, *Chem. Sci.*, 2014, **5**, 3680-3694.
28. G. W. Coates, P. D. Hustad and S. Reinartz, *Angew. Chem. Int. Ed.*, 2002, **41**, 2236-2257.
29. R. Kramer, J. M. Lehn and A. Marquis-Rigault, *Proc. Natl. Acad. Sci. U.S.A.*, 1993, **90**, 5394-5398.
30. Q. Wan, J. Xia, W. Lu, J. Yang and C.-M. Che, *J. Am. Chem. Soc.*, 2019, **141**, 11572-11582.
31. K. K. Kung, H. M. Ko, J. F. Cui, H. C. Chong, Y. C. Leung and M. K. Wong, *Chem. Commun.*, 2014, **50**, 11899-11902.
32. T. Zou, C. T. Lum, S. S. Chui and C. M. Che, *Angew. Chem. Int. Ed.*, 2013, **52**, 2930-2933.
33. X. Q. Zhou, A. Busemann, M. S. Meijer, M. A. Siegler and S. Bonnet, *Chem. Commun.*, 2019, **55**, 4695-4698.
34. H. Huang, P. Zhang, H. Chen, L. Ji and H. Chao, *Chem. Eur. J.*, 2015, **21**, 715-725.
35. J. Karges, S. Kuang, F. Maschietto, O. Blacque, I. Ciofini, H. Chao and G. Gasser, *Nat. Commun.*, 2020, **11**, 3262.
36. X. Q. Zhou, M. Xiao, V. Ramu, J. Hilgendorf, X. Li, P. Papadopolou, M. A. Siegler, A. Kros, W. Sun and S. Bonnet, *J. Am. Chem. Soc.*, 2020, **142**, 10383-10399.
37. L. Mazzei, M. N. Wenzel, M. Cianci, M. Palombo, A. Casini and S. Ciurli, *ACS Med. Chem. Lett.*, 2019, **10**, 564-570.
38. A. de Almeida, A. F. Mosca, D. Wragg, M. Wenzel, P. Kavanagh, G. Barone, S. Leoni, G. Soveral and A. Casini, *Chem. Commun.*, 2017, **53**, 3830-3833.
39. M. Meanwell, M. B. Nodwell, R. E. Martin and R. Britton, *Angew. Chem. Int. Ed.*, 2016, **55**, 13244-13248.
40. L. P. Du, K. C. Tsai, M. Y. Li, Q. D. You and L. Xia, *Bioorg. Med. Chem. Lett.*, 2004, **14**, 4771-4777.
41. J. F. Carvalho, J. Louvel, M. L. Doornbos, E. Klaasse, Z. Yu, J. Brussee and I. J. AP, *J. Med. Chem.*, 2013, **56**, 2828-2840.
42. Z. Yu, J. P. van Veldhoven, J. Louvel, I. M. t Hart, M. B. Rook, M. A. van der Heyden, L. H. Heitman and I. J. AP, *J. Med. Chem.*, 2015, **58**, 5916-5929.
43. A. Felipe, R. Vicente, N. Villalonga, M. Roura-Ferrer, R. Martinez-Marmol, L. Sole, J. C. Ferreres and E. Condom, *Cancer Detect. Prev.*, 2006, **30**, 375-385.
44. L. A. Pardo and W. Stuhmer, *Nat. Rev. Cancer*, 2014, **14**, 39-48.
45. P. Feng, L. Zhao, F. Guo, B. Zhang, L. Fang, G. Zhan, X. Xu, Q. Fang, Z. Liang and B. Li, *Chem. Biol. Interact.*, 2018, **293**, 115-123.
46. K. Jeevaratnam, K. R. Chadda, C. L. Huang and A. J. Camm, *J. Cardiovasc. Pharmacol. Ther.*, 2018, **23**, 119-129.
47. Z. Yu, J. P. D. van Veldhoven, I. M. E. t Hart, A. H. Kopf, L. H. Heitman and A. P. Ijzerman, *Eur. J. Med. Chem.*, 2015, **106**, 50-59.
48. K. Nakao, N. Minato and S. Uemoto, *Innovative medicine: basic research and development*, Springer Nature, 2015.
49. A. Ilari, P. Baiocco, L. Messori, A. Fiorillo, A. Boffi, M. Gramiccia, T. Di Muccio and G. Colotti, *Amino Acids*, 2012, **42**, 803-811.
50. S. Gukathasan, S. Parkin and S. G. Awuah, *Inorg. Chem.*, 2019, **58**, 9326-9340.

7

Summary & General discussion & Outlook

7.1 Summary of this PhD thesis

Cancer is a leading cause of death worldwide. Chemotherapy based on small-molecule drugs is considered as one of the main treatments to fight cancers, though it is accompanied by severe side effects. Nanomedicine and photodynamic therapy (PDT), in this respect, represent emerging alternatives aimed at reducing the side effects of small-molecule drugs. Through rational design, nanocarriers have the reputation to help increasing drug accumulation in the tumor site *via* the enhanced permeability and retention (EPR) effect, which lowers the systemic cytotoxicity of nanoformulated drugs. PDT is a form of light-activated anticancer treatment involving a photosensitizer (usually small molecules), photons, and O₂. This method can selectively activate the drugs in the tumor site to induce cell death, avoiding damage to non-irradiated healthy tissues. However, small-molecule photosensitizers still show some of the drawbacks of chemotherapy, such as low tumor accumulation and rapid blood clearance. For example, padeliporfin (Tookad[®], a clinical approved palladium-based photosensitizer) reaches its highest plasma concentration in the human body at as fast as 5 min, and it is then rapidly metabolized by kidneys.¹ In this thesis, PDT and nanomedicine were combined in order to achieve efficient accumulation of photosensitizers within cancer cells (*in vitro*) or at the tumor site (*in vivo*), before being selectively activated by light irradiation. We propose an alternative to the complicated synthesis and challenging reproducibility of multi-components nanocarriers, which often lead to low drug loading efficiencies and dramatically restrict clinical applications of nano-sized drug delivery systems that, in pre-clinical tests, had appeared as promising. In the research described in this thesis, we focused on the design and preparation of small-molecule photosensitizers based on tetradentate ligands cyclometalated to *d*⁸ transition metal centers. We realized that these molecules can be used to develop a molecular photosensitizer self-assembly nanosystem (MoPSAN) based on the supramolecular assembly of these molecules *via* the metallophilic metal...metal (M...M) interaction. These nanosystems achieve high drug-loading, high cellular uptake *in vitro* and high tumor accumulation efficiency *in vivo*, and excellent anticancer PDT effects, both *in vitro* and *in vivo*.

In **chapter 2**, we describe the two isomers of a cyclometalated palladium(II) complex and compared their anticancer PDT properties *via* several photophysical and photobiological methods. The first isomer **PdL¹**, which shows an N[^]N[^]C[^]N coordination mode, showed excellent singlet oxygen generation quantum yield (0.89) under blue light irradiation, resulting in high blue-light-activated photoindexes in human cancer cells. By contrast, the second isomer **PdL²**, characterized by an N[^]N[^]N[^]C coordination mode, had both low blue light absorption

and low singlet oxygen quantum yield (0.38), giving a negligible activation by blue light *in vitro*. DFT calculation showed that the higher absorption in the blue region of **PdL¹**, and thus its lower HOMO-LOMO energy gap, was due to the closer proximity between the electron-rich cyclometalated aromatic cycle and the nitrogen bridge of the ligand, while in **PdL²** both aromatic rings adjacent to the amine bridge are electron-poor pyridine rings, which lowers the HOMO energy. These results demonstrate that changing the position of the carbon-metal bond in the coordination sphere of photoactive organometallic prodrugs can be used to tune the energy gap between their frontier orbitals, and hence their absorption in the visible region of the spectrum, which is essential in PDT applications.

The deprotonation of the non-coordinated NH bridge in the palladium complexes described in **chapter 2** resulted in water-insoluble neutral metal complexes, thus limiting their application for cancer treatment *in vivo*. In **chapter 3**, we describe the results of methylation of the amine bridge to avoid this problem. Three water-soluble analogous palladium complexes were successfully synthesized: two cyclometalated isomers [**PdMeL¹**]**OAc** (N[^]N[^]C[^]N coordination) and [**PdMeL²**]**OAc** (N[^]N[^]N[^]C coordination), and a reference tetrapyrrolyl complex [**Pd(Mebppy)**](**OAc**)₂ (N[^]N[^]N[^]N coordination). All complexes are soluble in pure water. [**PdMeL¹**]**OAc** has similar photophysical and photobiological properties compared with **PdL¹**, and even showed good blue-light activated PDT effect in a mice tumor xenograft, suggesting the promising potential of palladium-based photosensitizers for PDT application. Critically, in this work we found that cyclometalation of a palladium complex triggers the self-assembly of the complex into nanorods *via* the metallophilic Pd...Pd interaction, which also depends on the presence of proteins in the cell medium used to dissolve the compounds. Importantly, endocytosis plays a critical role in the cellular uptake of these aggregates, and it promotes much higher cellular uptake of the cyclopalladated complexes than conventional non-cyclometalated tetrapyrrolyl analogue [**Pd(Mebppy)**](**OAc**)₂. The role of the protein corona in drug delivery systems is actively debated for several years, but the nanoscale, protein-dependent self-aggregation of a self-assembling drug molecule, had not been documented before. Overall, this work shows that (pro)drugs that self-assemble into nanorods can lead to excellent drug penetration in 3D tumor models, which suggests a new strategy to combine metallodrugs with nanomedicine, further discussed in **chapter 5**.

In the research described in **chapter 4**, using the same ligands described in **chapter 3**, but changing the metal, we demonstrated that platinum(II) complexes [**PtMeL¹**]**OAc** and [**PtMeL²**]**OAc** both showed strong metallophilic interactions, which also resulted in the self-

assembly of nanoaggregates in cell-growing medium. However, although both series of complexes (with Pd^{2+} or Pt^{2+}) showed self-assembly *via* metallophilic interactions and cell-dependent cytotoxicity in the dark, their photochemical properties were found to be dramatically different. The excellent PDT properties and negligible emission of the palladium aggregates were replaced, in the platinum series, by poor PDT properties but red-shifted absorption and deep-red emission properties, which allows for using these aggregates in cell imaging rather than for phototherapy. The different photochemical properties of the platinum *vs.* palladium complexes must originate from their different relative rates of excited state deactivation, both in the self-assembled and monomeric forms. Phosphorescence and non-radiative deactivation to the ground singlet state are quantum-chemically forbidden processes that strongly depend on spin-orbit coupling, which is stronger for platinum(II) than for palladium(II) ions. Generally, Pt(II) $5d_z^2$ orbital is higher in energy than the Pd(II) $4d_z^2$ orbital, which leads to Pt(II) showing a stronger influence than Pd(II) in the frontier molecular orbitals, inter-system crossing efficiency and the $T_1 \rightarrow S_0$ radiative decay, altogether giving platinum complexes a more intense phosphorescence.² This phosphorescence, located in the deep-red region of the spectrum, allowed us to study the uptake and localization of these supramolecular nanoparticles in cells; in A549 cells the deep-red emissive nanoaggregates of $[\text{PtMeL}^2]\text{OAc}$ were located in the mitochondria, which was also confirmed by cell electron microscopy due to the high electron density of platinum compounds. Overall, this set of polypyridyl platinum complexes demonstrated new perspectives in using the metallophilic interactions to build supramolecular nanosystems that, at high concentration, can kill cancer cells, but at low concentration, may be used as deep-red trackers for different organelles – here the mitochondria.

In **chapter 5**, we describe a bis-cyclometalated palladium complex, **PdL³**, which allowed on the one hand for further shifting the absorption of the complex towards longer wavelengths, and on the other hand, for further decreasing the charge to form a neutral complex and generating strong Pd...Pd interactions. **PdL³** was indeed demonstrated to self-assemble as nanoaggregates in cell-growing medium, but also to have improved PDT properties compared to the mono-cyclometalated complex **PdL¹**: next to being activated with green light instead of blue light due to the further destabilization of the HOMO by the second Pd-C bond, it was also particularly cytotoxic under hypoxic conditions, with photoindexes of up to 70 in skin melanoma cell lines. This excellent reactivity was due to a PDT type I mechanism, which is notoriously less dependent on the O_2 concentration than PDT type II. **PdL³** served as a proof-of-concept for the MoPSAN concept, where a PDT photosensitizer self-assembles into

nanostructures for tumor targeting *in vivo* using the EPR effect. Dense nanoparticles were found by electron microscopy (EM) in plasma following intravenous injection of the compound in mice, which demonstrates self-assembly in biological conditions. Then, ICP-MS measurements demonstrated the significant accumulation of **PdL³** in the tumor, with exceptional drug delivery efficacy of up to 10.2% ID/g. EM images of tumor slices proved again the accumulation of self-aggregated nanoparticles of **PdL³** in the solid tumor. With these results in hand, we advocate that the supramolecular metallophilic Pd...Pd interaction has a high potential 1) to build supramolecular nanocarriers with improved tumor accumulation *via* the EPR effect, and 2) to generate PDT photosensitizers that conserve their phototoxic properties under hypoxia.

Finally, in **chapter 6** we report the chemistry of cyclometalated Au(III) compounds. Although Au(III) is isoelectronic to Pt(II), it has significantly different properties due to its higher charge and electronegativity (2.4 for Au and 2.2 for Pt). In general, cyclometalation in polypyridyl metal complexes decreases their molecular charge, compared with conventional nitrogen coordination, which significantly influences their lipophilicity as well. As discussed in **chapter 2**, many reports claim that the higher lipophilicity of cyclometalated complexes stimulates their cellular uptake *via* passive transport through the cell membrane, which potentially may lead to better therapeutic effects with lower doses of a compound, but at the cost of cancer selectivity. On the other hand, cyclometalation stabilizes the Au(III) oxidation state, which lowers the propensity of cyclometallagold compounds to be reduced by biological thiol groups once they have reached the cytosol. We investigated the coordination of a pair of tetrapyridyl ligands to gold(III) ions and in **chapter 6** describe the serendipitous discovery that one of these ligands preferentially binds the Au(III) center *via* “rollover cyclometalation” to form a bis-cyclometalated gold(III) complex **[Au(biqbpy1)]Cl** ($C^{\wedge}N^{\wedge}N^{\wedge}C$), while the other ligand coordinates with its four nitrogen atoms to afford the traditional tetrapyridyl complex **[Au(biqbpy2)]Cl** ($N^{\wedge}N^{\wedge}N^{\wedge}N$). Interestingly, both cationic complexes bear the same +1 charge due to the deprotonation of the amine bridges in **[Au(biqbpy2)]⁺**, while the bis-cyclometalated analogue **[Au(biqbpy1)]⁺** keeps its amine bridges protonated. These two isomers offer hence the unique opportunity to compare cyclometalated *vs.* non-cyclometalated Au(III) complexes without a change of the overall charge of the complex. We found that the roll-over cyclometalated **[Au(biqbpy1)]Cl** is highly stable in reducing biological conditions, but that it also forms nanoparticles in cell medium, which led to a 6-fold more efficient uptake in A549 cancer cells, compared with the tetrapyridyl analogue **[Au(biqbpy2)]Cl** that does not form nanoparticles but is much more prone to decomposition by reduction in cell-growing medium.

The identical charge, but different aggregation properties of **[Au(biqbpy1)]Cl** vs. **[Au(biqbpy2)]Cl**, give a new perspective on the enhanced cellular uptake of cyclometalated gold complexes. As unambiguously demonstrated for Pd(II) and Pt(II) cyclometalated complexes reported in previous **chapters** of this thesis, these nano-aggregates may trigger active transport such as endocytosis, which is typically more efficient than passive transport. Moreover, **[Au(biqbpy1)]Cl** is more stable in biological conditions and hence showed decreased TrxR inhibition, compared with **[Au(biqbpy2)]Cl** which upon intracellular reduction released the known TrxR-inhibiting Au⁺ as free ions. The resulting cytotoxicity to cancer cells was lowered for **[Au(biqbpy1)]Cl** compared with **[Au(biqbpy2)]Cl**, but its toxicity to non-cancerous cells was also comparatively much lower, i.e., its selectivity to cancer cells was higher than that of **[Au(biqbpy2)]Cl**. Meanwhile, both complexes exhibited similarly high potassium channel binding ability, which might be due to their identical charge and similar molecular shape. Their potassium channel binding ability was also higher than that of the tetrapyrrolyl ligands they were made of, suggesting that metal complexation might be an alternative method to regulate the potassium channel activity of small molecules. Altogether, the comparison of these isomers, from a chemical and biological point of view, provided new insights on the use of cyclometalation as a drug design principle to modify the balance between stability, aggregation, toxicity, and protein inhibition properties of gold(III) anticancer complexes.

7.2 General discussion

7.2.1 Cyclometalation reactions

Overall, we have reported in this thesis several cyclometalated polypyridyl complexes based on palladium(II), platinum(II) and gold(III), and compared their chemical and biological properties with that of their classical nitrogen-coordinated analogues. cyclometalated C-H activation in cyclopalladation reactions usually involve either tetrachloridopalladate salts in presence of a base, or palladium acetate in acetic acid or benzene.³ All the cyclometalated palladium complexes reported in this thesis have been obtained by the reaction of palladium acetate and the corresponding ligands in refluxing acetic acid. A similar method also was successful for most cyclometalated platinum complexes, which were mostly obtained by using bis(acetylacetonate)platinum(II) as a precursor. However, three unexpected cyclometalated Ru(III), Au(III) Pd(II) and Pt(II) complexes were also obtained, which are shown in Figure 7.1 but have not been described in this thesis. The compounds **[Ru(MeL¹)Cl₂]**, **[Au(HL²)Cl](AuCl₄)**, **[PdL⁴OAc]** and **[Pt(L⁵)Cl]**, were obtained *via* the reaction of

dichloro(*p*-cymene)ruthenium(II) dimer, NaAuCl_4 , $\text{Pd}(\text{OAc})_2$, and K_2PtCl_4 , respectively, with the corresponding ligands in refluxing acetic acid. It should be noticed that the Ru(II) precursor was oxidized to Ru(III) in the cyclometalation process, even under argon, indicating that the thermodynamic stability of cyclometalated Ru(III) complexes might be high enough, at least in such conditions, to hinder the synthesis of cyclometalated Ru(II) complexes based on this ligands. In the three complexes $[\text{Au}(\text{HL}^2)\text{Cl}](\text{AuCl}_4)$, $[\text{PdL}^4\text{OAc}]$ and $[\text{Pt}(\text{L}^5)\text{Cl}]$, the compound obtained was not the expected one but the oxidation state of the metal did not change during cyclometalation (Figure 7.1). In that regard, these cases are similar to the rollover cyclometalated $[\text{Au}(\text{biqbpy1})]\text{Cl}$ described in **chapter 6**: upon reacting HAuCl_4 with **H₂biqbpy1** in refluxing methanol, the obtained cyclometalated compound did not correspond to the expected tetrapyridyl coordination mode.

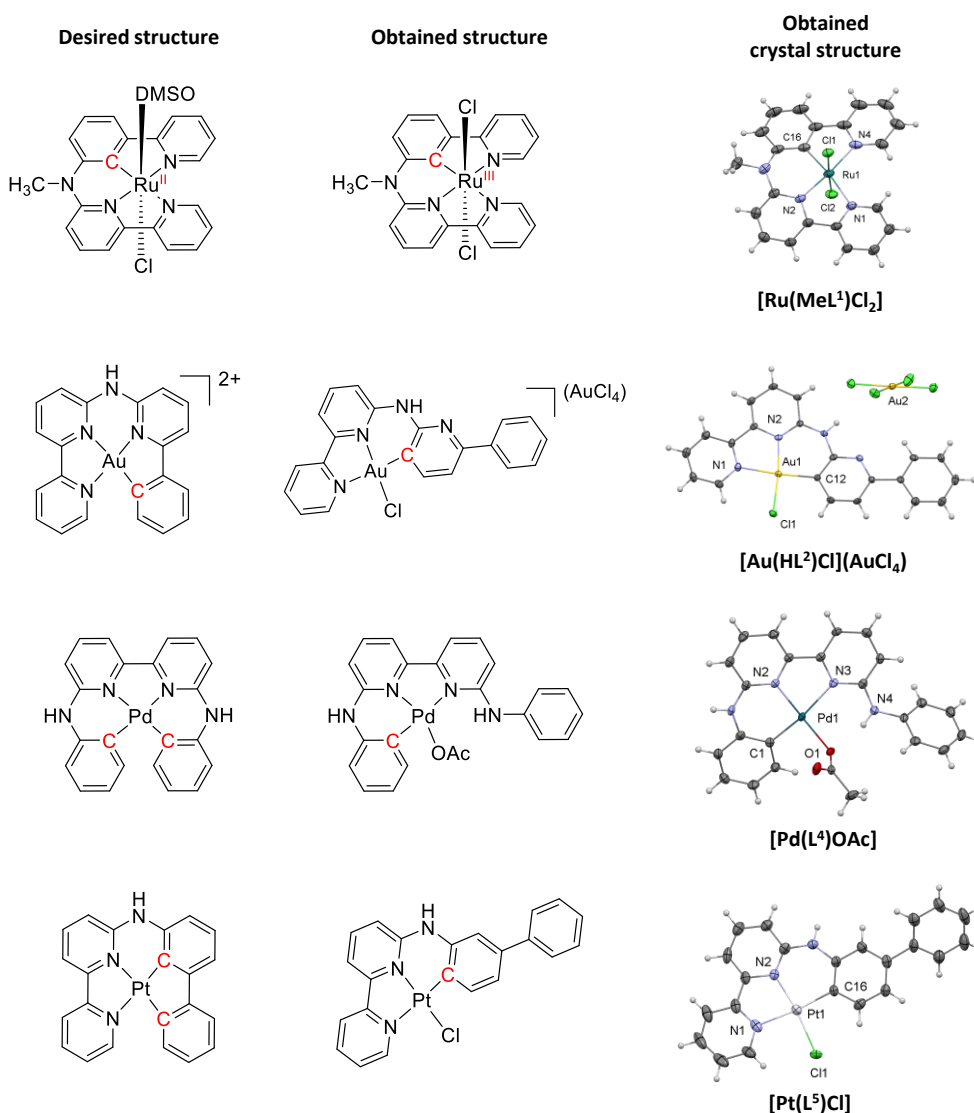


Figure 7.1 The chemical and crystal structures of unexpected cyclometalated complexes obtained in our research, but not described in great details in this thesis.

It is hence particularly interesting to illustrate the different possible outcomes of a cyclometalation reaction, with a tetradentate ligand, by comparing the structures of **[PdL²]** described in **chapter 2** and **[Au(HL²)Cl](AuCl₄)** (Figure 7.1). The ligand is the same, but different metal precursors resulted in different cyclometalated products. As shown in Figure 7.2, the acetate or chloride anions are also potential ligands, which may play a blocking role towards binding of the expected nitrogen ligands to the metal center. On the other hand, these same ligands may activate a C-H on the same pyridine ring *via* intramolecular O...H or Cl...H hydrogen bond, ultimately promoting the formation of Pd-C or Au-C bonds. The Pd(OAc)₂ precursor in particular was prone to such C-H activation of phenyl groups, as acetates are rather basic and weak ligands (Figure 7.2a). For the gold precursor NaAuCl₄, the chloride ligand is probably a better ligand than acetate, while the C-H...Cl intramolecular hydrogen bond may be less strong due to the lower basicity of chloride, compared to acetate; hence coordination of the pyridine ring and C-H activation of the terminal phenyl group was slower, compared to the activation of the more acidic pyridine C-H bond, which further triggered a “rollover” (Figure 7.2b) similar to that described in **chapter 6**. The proposed intermediates for the rollover cyclometalation observed for **[Au(HL²)Cl]⁺** are shown in Figure 7.2c. Interestingly, when reacting PtCl₄²⁻ with **HL⁵** the complex **[Pt(L⁵)]⁺** shown in Figure 7.1 was obtained, which is very similar to **[Au(HL²)Cl]⁺**. This result suggested that the nature of the ancillary ligand on the metal precursor (acetate *vs.* chloride), and notably its basicity and ability to bind to the metal, play a more essential role on the final outcome of the cyclometalation reaction, that played by the electron-richness of the aromatic cycle that finally becomes cyclometalated (pyridine *vs.* phenyl group).

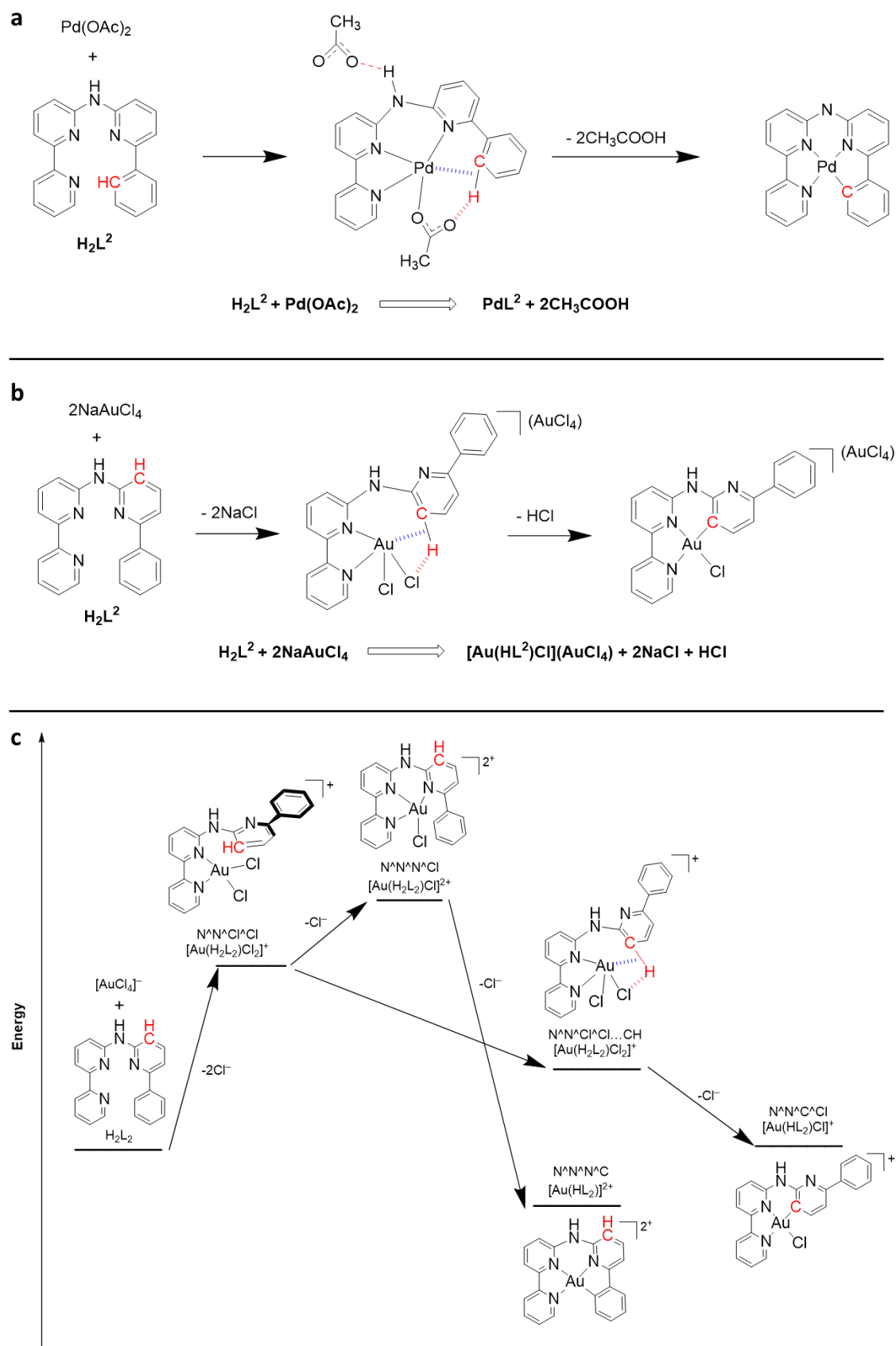


Figure 7.2 Proposed cyclometalation mechanism for PdL^2 (a), $[\text{Au}(\text{HL}^2)\text{Cl}](\text{AuCl}_4)$ (b) and proposed reaction intermediates towards the preparation of $[\text{Au}(\text{HL}^2)]^{2+}$ (c).

7.2.2 Supramolecular aggregation of cyclometalated complexes in a biological context

In this thesis it is reported that cyclometalated polypyridyl metal complexes always showed better cellular uptake than their tetrapyridyl analogues, which is usually attributed, in the recent literature, to the higher lipophilicity of the former and their enhanced ability to cross membranes by passive diffusion. However, we demonstrated that actually the nanoaggregation of cyclometalated complexes triggers efficient active endocytic transport of the compound, rather than passive transport through the cell membrane. This research indicates the critical importance of understanding the supramolecular behavior of anticancer compounds in cell-growing medium, *i.e.* before they interact with living cells. Gasser' group recently reported the nanoaggregation of several ruthenium complexes in aqueous solutions,⁴ and also emphasized that understanding the nature of the actual metal species entering cancer cells is critical. We envision that the present work has clearly demonstrated that nanoaggregation in cell medium and in blood has impressive consequences on the cellular uptake mechanism and efficiency of drug penetration into tumors *in vivo*. With this knowledge, the formation of nanoaggregates should be taken into serious consideration, and even consciously applied for the future development of metallodrugs.

7.3 About the strength of the metallophilic interaction

We demonstrated that cyclometalation is a convincing method to stimulate supramolecular metallophilic M...M interactions of Pd(II) and Pt(II) complexes and their subsequent self-assembly to nanoaggregates in biological media. The M-C bond of cyclometalated complexes decreases the positive charge of the complex, which combined with the strong π - π stacking interactions of planar tetradentate aromatic ligands allows these metal centers to overcome their electrostatic repulsion, resulting in overlapping of metal-based d_z^2 orbitals and ligand-based π orbitals with those of nearby complexes. The metallophilic interaction was initially described for Au(I) species, and was therefore called an aurophilic interaction.⁵ However, in recent literature it was revealed that also Au(III), Pt(II), and Pd(II) complexes may show metallophilic M...M interactions.⁶ Although the torsion of the **biqbpy1**²⁻ and **biqbpy2**²⁻ ligands described in **chapter 6** appeared too large to generate a short Au...Au distance, it may be interesting to compare the influence of the nature of the d^8 metal on the strength of the metallophilic interaction. In order to do so, we calculated the structures of dimers of two series of analogous Pd(II), Pt(II), and Au(III) complexes. In the first series, the ligand **HMeL**¹ was used, which is a phenyl derivative of the tetrapyridyl ligand **Mebbpya**. It should be noted that **[Pd(MeL¹)]⁺**, **[Pt(MeL¹)]⁺**, and **[PdMebbpya]²⁺** were all synthesized and are described in this thesis

(**chapter 3**), while $[\text{Au}(\text{MeL}^1)]^{2+}$ has not been synthesized yet. DFT models of these dimers and their monomer were minimized in vacuum using PBE0 as functional and the dDsC correction to take into account dispersion effects. As shown in Figure 7.3a, dimers of the monocationic complexes $[\text{Pd}(\text{MeL}^1)]^+$ and $[\text{Pt}(\text{MeL}^1)]^+$ exhibit short M...M distances (around 3.18-3.34 Å), while for the bicationic analogues $[\text{Au}(\text{MeL}^1)]^{2+}$ and $[\text{Pd}(\text{Mebppy})]^{2+}$ the minimization jobs diverged to Au...Au and Pd...Pd distances longer than 5 Å, at which no metallophilic interaction can be considered anymore. This theoretical result indicated that the reduction of the charge of Pd(II), Pt(II) or Au(III) complexes by cyclometalation is one of the main reasons why the metallophilic interaction may arise: cationic metal complexes repulse each other by electrostatic effects, and this charge repulsion must be overcome to trigger self-assembly *via* the metallophilic M...M interactions.

To further study the influence of the charge of the monomer on the formation of dimers, and exclude the influence of a particular ligands, DFT calculations were also carried out for the biscyclometalated analogues of the complexes described in the previous paragraph, *i.e.* neutral $[\text{Pd}(\text{MeL}^3)]$, $[\text{Pt}(\text{MeL}^3)]$, and monocationic $[\text{Au}(\text{MeL}^3)]^+$. As shown in Figure 7.3b, calculations of the dimer $\{[\text{Au}(\text{MeL}^3)]\}^{2+}$ did converge this time, with a short Au...Au distance (3.45 Å) demonstrating the importance of charge control for the generation of M...M interactions. The neutral dimers $[\text{Pd}(\text{MeL}^3)]_2$ and $[\text{Pt}(\text{MeL}^3)]_2$ also showed short M...M distances (3.17 and 3.20 Å, respectively), suggesting that experimentally these three complexes may generate metallophilic M...M interactions (see also **chapter 5** for an example with palladium and **HL**³). We also calculated the stabilization energy $\Delta E_{\text{M}...M}$ of all three M...M dimers, defined as $\Delta E_{\text{M}...M} = \text{total bonding energy of the dimer} - 2 \times \text{total bonding energy of monomer}$. $\Delta E_{\text{M}...M}$ was the highest for $[\text{Pt}(\text{MeL}^3)]$ ($\Delta E_{\text{Pt}...Pt} = -126.0$ kJ/mol), very closely followed by $[\text{Pd}(\text{MeL}^3)]$ ($\Delta E_{\text{Pd}...Pd} = -123.6$ kJ/mol). Both values are of the same order of magnitude compared to hydrogen bonds, as the strongest hydrogen bond $\text{FH}...F^-$ is -169 kJ/mol.⁷ By contrast, the gold(III) dimer was found to be higher in energy than the two monomers, with $\Delta E_{\text{Au}...Au} = +68.34$ kJ/mol, highlighting again the destabilizing effect brought by the higher charge of the trivalent gold(III) center, compared to divalent metal centers (Figure 7.3c). These data suggest that the metallophilic Pd...Pd and Pt...Pt interactions help to stabilize these dimers, while the aurophilic Au...Au interaction (at least in this complex) is not strong enough to stabilize the dimer $\{[\text{Au}(\text{MeL}^3)]\}^{2+}$. For such a molecule supramolecular aggregates based on the aurophilic interaction would require some additional attracting interaction, for example with counter anions or proteins from the medium, which have not been introduced in this model.

Altogether, according to DFT calculations the charge of d^8 metal complexes based on Pd(II), Pt(II) and Au(III) strongly influence the generation of metallophilic M...M interaction, and in both series the Pt(II)...Pt(II) and Pd(II)...Pd(II) interactions were comparable in energy, while the Au(III)...Au(III) interaction was found the weakest. This result also matches well with the popularity of the metallophilic M...M interaction in the scientific literature, where studies on metallophilic interaction of Pt(II) and Pd(II) compounds are rather common, while those related to Au(III) complexes remain scarce.^{6, 8}

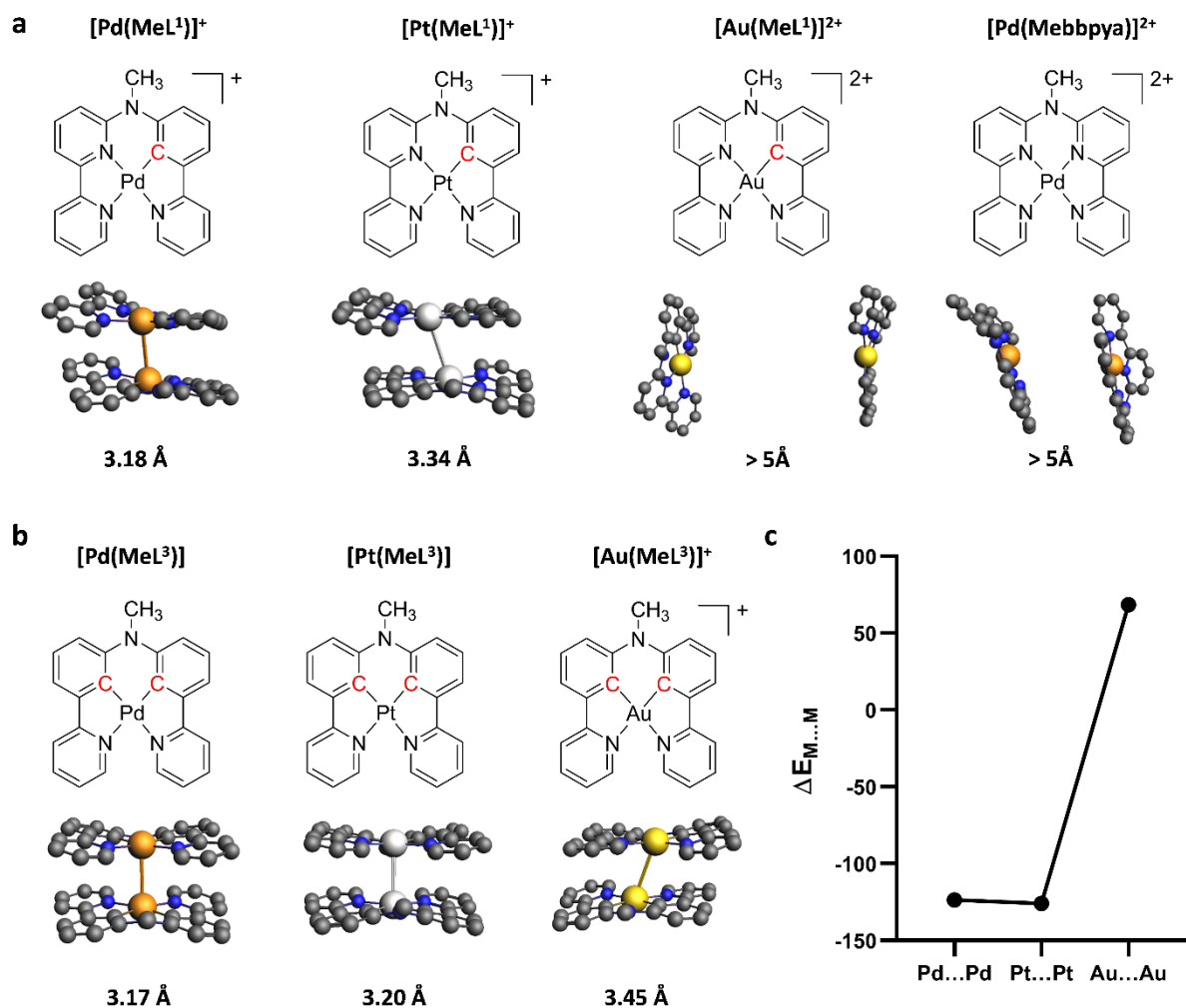


Figure 7.3 (a) DFT structures and M...M distances (Å) for the minimized dimers of $[\text{Pd}(\text{MeL}^1)]^+$, and $[\text{Pt}(\text{MeL}^1)]^+$. For $[\text{Au}(\text{MeL}^1)]^{2+}$ and $[\text{Pd}(\text{Mebbpys})]^{2+}$ the M...M distances diverged above 5 Å. (b) Chemical formulae, DFT-minimized structures, and M...M distances (Å) for the dimers of $[\text{Pd}(\text{MeL}^3)]$, $[\text{Pt}(\text{MeL}^3)]$ and $[\text{Au}(\text{MeL}^3)]^+$. (c) DFT-calculated stabilization energy $\Delta E_{\text{M} \dots \text{M}}$ for the M...M interaction in $[\text{Pd}(\text{MeL}^3)]_2$, $[\text{Pt}(\text{MeL}^3)]_2$ and $[\text{Au}(\text{MeL}^3)]^{2+}$. Level of theory: ADF/PBE0-dDsC/TZP in vacuum with scalar (ZORA) relativistic effects.

7.3 Outlook

In this thesis, we describe that cyclometalated palladium complexes can be made that have interesting PDT efficiency following type I or type II mechanisms as supramolecular aggregates, while analogous cyclometalated platinum complexes also aggregate strongly via the metallophilic Pt...Pt interaction, but show poor photodynamic properties. Instead, aggregation makes them strongly emissive in the photodynamic window of the spectrum, thus allowing deep-red bioimaging application. To combine the PDT properties of cyclopalladated complexes and the bioimaging potential of cycloplatinated complexes, it might be possible to foresee the use of mixtures of both molecules, to generate self-assemblies *via* heterometallic Pd...Pt...Pt interactions. With such mixtures new theranostic nanoplateforms capable of PDT and cell imaging are around the corner for fighting cancer, in which the Pd species play the role of a PDT agent, while the Pt...Pt species emerge as deep-red trackers.

We also demonstrated the stability of these supramolecular metallophilic M...M interactions in solution, in living cells, and even in living mice. The resulting nanostructures with both types of cyclometalated complexes are strongly dependent on the proteins contained in the aqueous solution transporting the compound, whether it is cell-growing medium or circulating blood in mice. We found that the nanoparticles formed *via* Pd...Pd interaction show an extraordinary tumor accumulation efficiency, suggesting the promising potential of such aggregated metal complexes to develop nanocarrier systems based on the metallophilic M...M interaction. For example, it would be possible to conjugate some tumor-microenvironment-sensitive medicinal components to the bridging amine group of palladium or platinum cyclometalated complexes, and let the metallophilic M...M interaction drive nanoparticle formation in the living body and target these nanoparticles to the tumor. Following tumor uptake, the medicinal components would be released or activated, to achieve the targeted treatment.

In this thesis, we have reported the influence of the nature of the metal center on the photochemical and photobiological properties of metal complexes based on one tetradentate ligand structure. Next to the compounds reported in **chapters 2-6**, we also synthesized two biscyclometalated palladium and platinum complexes [**PdL⁶**] and [**PtL⁶**] (Figure 7.4), the detailed study of which has not been included in this thesis. These compounds showed intricate phosphorescence properties that are also tuned by the metal center, the ligand, and the self-assembly of the molecule. When dissolving [**PdL⁶**] or [**PtL⁶**] in pure DMSO, deep-blue or green

emission was observed, respectively, which were attributed to the monomers. However, upon increasing the water fraction in DMSO (f_w = volume of water/total volume) from 0.0 to 0.9, the two complexes aggregated, to generate the metal...metal interaction, as demonstrated by a significant red-shift of the emission. These complexes hence show interesting properties as luminescent materials, though time was too short to evaluate them comprehensively.

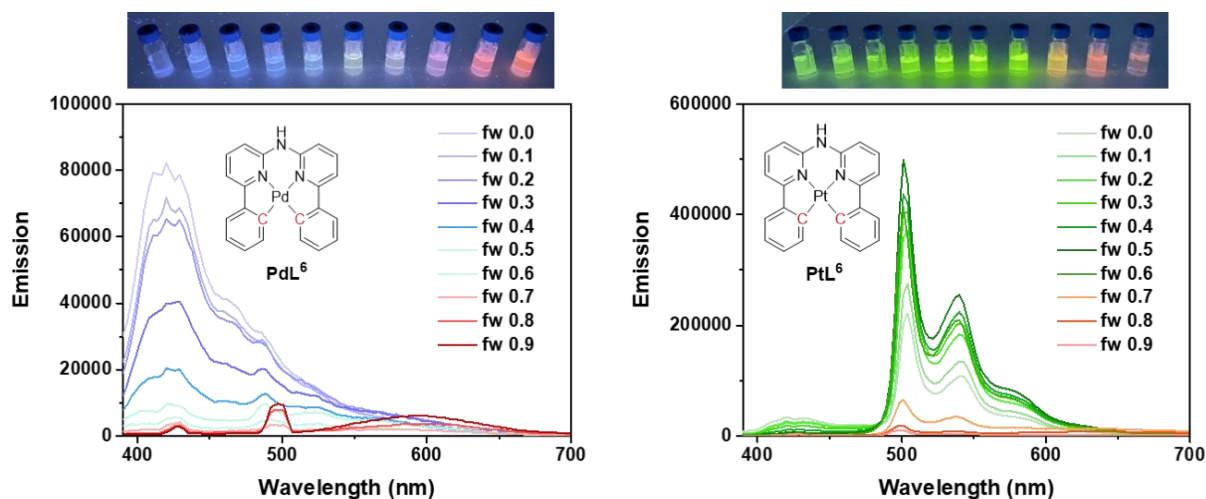


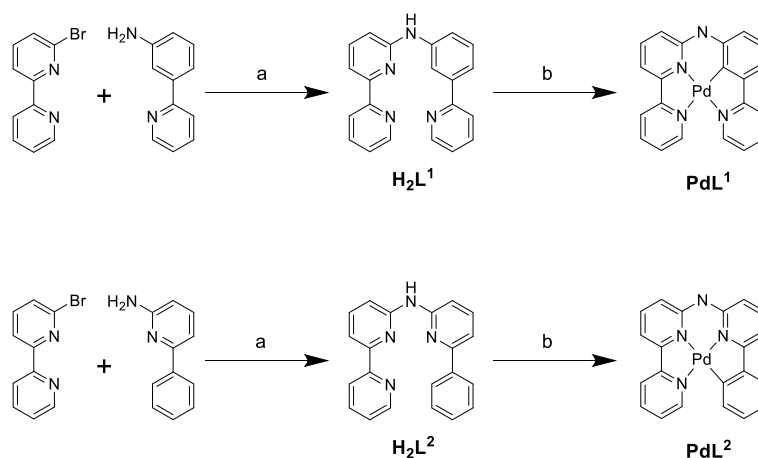
Figure 7.4 Visual impression and emission spectra of $[PdL^6]$ and $[PtL^6]$ in water/DMSO mixtures (f_w change from 0.0 to 0.9).

In conclusion, the results described in this thesis bridge the fields of anticancer metallodrugs, photodynamic therapy, cell imaging, luminescent materials, and nanomedicine. By using cyclometalation and the supramolecular metallophilic M...M interaction, it was possible to show the fantastic impact that metal complexes may have on the development of future anticancer drugs and nanomaterials.

7.4 References

1. J. Trachtenberg, A. Bogaards, R. A. Weersink, M. A. Haider, A. Evans, S. A. McCluskey, A. Scherz, M. R. Gertner, C. Yue, S. Appu, A. Aprikian, J. Savard, B. C. Wilson and M. Elhilali, *J. Urol.*, 2007, **178**, 1974-1979.
2. Q. Wan, W.-P. To, X. Chang and C.-M. Che, *Chem*, 2020, **6**, 945-967.
3. J. Dupont, C. S. Consorti and J. Spencer, *Chem. Rev.*, 2005, **105**, 2527-2572.
4. A. Notaro, G. Gasser and A. Castonguay, *ChemMedChem*, 2020, **15**, 345-348.
5. Z. Wu, Y. Du, J. Liu, Q. Yao, T. Chen, Y. Cao, H. Zhang and J. Xie, *Angew. Chem. Int. Ed.*, 2019, **58**, 8139-8144.
6. Q. Wan, J. Xia, W. Lu, J. Yang and C. M. Che, *J. Am. Chem. Soc.*, 2019, **141**, 11572-11582.
7. J. Emsley, *Chem. Soc. Rev.*, 1980, **9**, 91-124.
8. C. Zou, J. Lin, S. Suo, M. Xie, X. Chang and W. Lu, *Chem. Commun.*, 2018, **54**, 5319-5322.

APPENDIX I SUPPORTING INFORMATION FOR CHAPTER 2



Scheme AI.1 (a) Toluene, BINAP, $Pd(dba)_2$, $KOt-Bu$, 85 °C, N_2 , 3 days; (b) CH_3COOH , N_2 , 135 °C, 12 h.

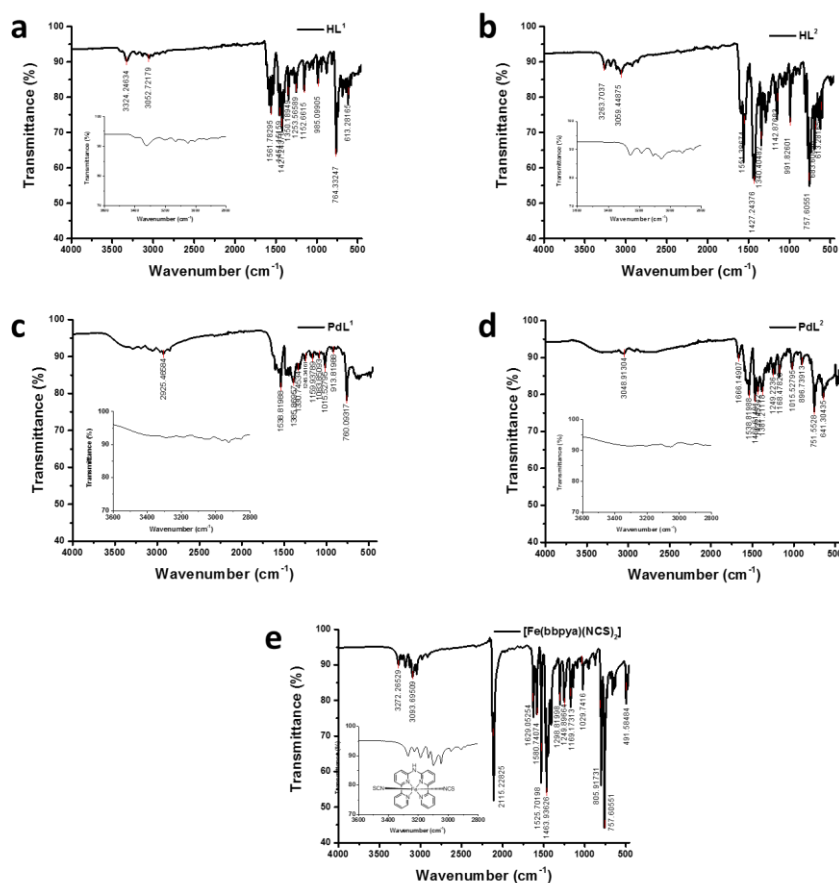


Figure AI.1 IR spectra of ligands HL^1 (a), HL^2 (b), palladium complexes PdL^1 (c), PdL^2 (d), and the reference complex $[Fe(bbpya)(NCS)_2]$ (e).

Table AI.1 Crystallographic Data for **PdL²**

Complex	PdL²
Crystal data	
Chemical formula	C ₂₁ H ₁₄ N ₄ Pd
<i>M_r</i>	428.76
Crystal system, space group	Monoclinic, <i>P</i> 2 ₁ / <i>n</i>
Temperature (K)	110
<i>a</i> , <i>b</i> , <i>c</i> (Å)	10.3734 (3), 7.2412 (2), 20.6547 (6)
β (°)	100.020 (3)
<i>V</i> (Å ³)	1527.83 (8)
<i>Z</i>	4
Radiation type	Mo <i>K</i> α
μ (mm ⁻¹)	1.23
Crystal size (mm)	0.23 × 0.11 × 0.04
Data collection	
Diffractometer	SuperNova, Dual, Cu at zero, Atlas
Absorption correction	Gaussian <i>CrysAlis PRO</i> 1.171.39.29c (Rigaku Oxford Diffraction, 2017) Numerical absorption correction based on gaussian integration over a multifaceted crystal model Empirical absorption correction using spherical harmonics, implemented in SCALE3 ABSPACK scaling algorithm.
<i>T_{min}</i> , <i>T_{max}</i>	0.625, 1.000
No. of measured, independent and observed [<i>I</i> > 2σ(<i>I</i>)] reflections	20278, 3517, 3063
<i>R_{int}</i>	0.036
(sin θ/λ) _{max} (Å ⁻¹)	0.650
Refinement	
<i>R</i> [<i>F</i> ² > 2σ(<i>F</i> ²)], 0.025, 0.060, 1.07 <i>wR</i> (<i>F</i> ²), <i>S</i>	
No. of reflections	3517
No. of parameters	320
No. of restraints	581
H-atom treatment	H-atom parameters constrained
Δρ _{max} , Δρ _{min} (e Å ⁻³)	0.88, -0.79

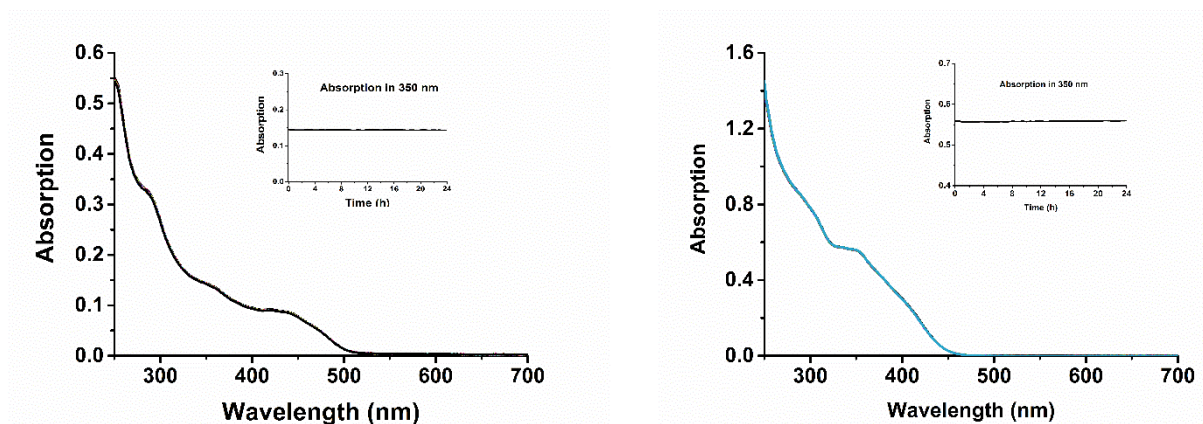


Figure AI.2 Time-evolution of the absorption spectra of **PdL¹** (left) and **PdL²** (right) in PBS: DMSO (50 μ m, 1:1) solution at 310 K for 24 hours. The spectra were measured every 30 min.

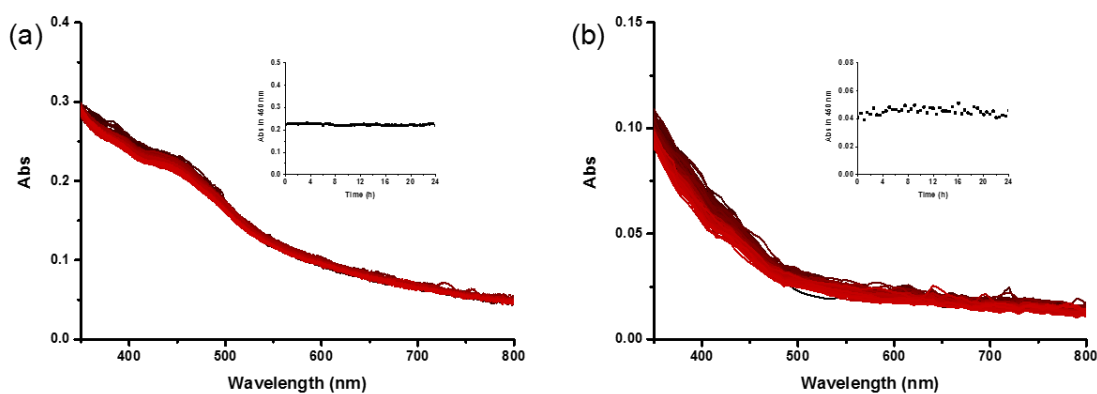


Figure AI.3 Evolution of the absorption spectrum of complexes **PdL¹** (a) and **PdL²** (b) when incubated in Opti-MEM containing 2.5% FCS at 310 K for 24 hours. The spectra were measured every 30 min. Inset: time evolution of the absorbance at 450 nm. The color of spectra change from black (0 h) to red (24 h).

Table AI.2 Octanol-water partition coefficients ($\log P_{ow}$) of the two palladium complexes.

Complex	$\log P_{ow}$
PdL¹	-0.64
PdL²	0.046

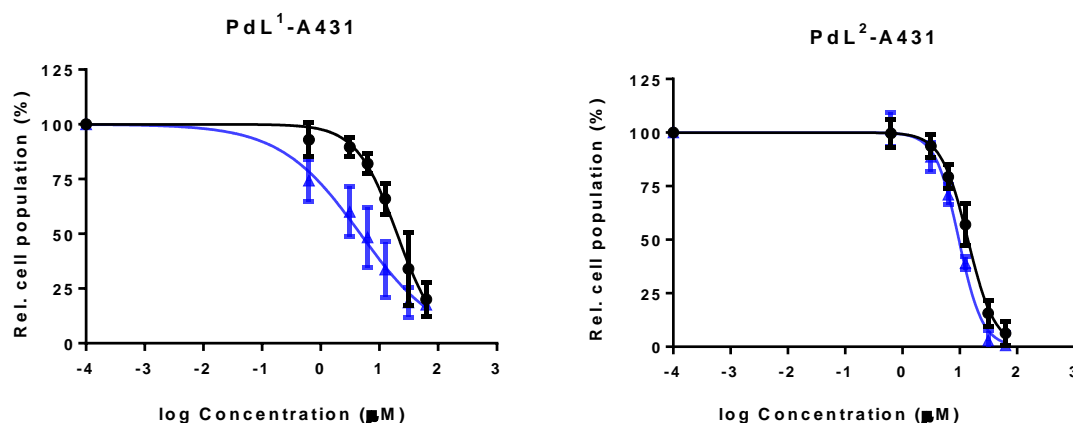


Figure AI.4 Dose-response curves for A431 cells incubated with palladium complexes and irradiated 5 min with blue light (blue data points), or left in the dark (black data points). Photocytotoxicity assay outline: cells seeded at 5×10^3 cells/well at $t = 0$ h; treated with **PdL¹** or **PdL²** at $t = 24$ h; irradiated at $t = 48$ h, blue light (455 nm, 5 min, 10.5 mW cm^{-2} , 3.2 J cm^{-2}); SRB assay performed at $t = 96$ h. Incubation conditions: 37°C , 21% O_2 , 7% CO_2 .

Table AI.3 Photophysical data for **PdL¹** and **PdL²**

Complex	λ_{abs} , nm ($\epsilon \times 10^3 \text{ M}^{-1} \text{ cm}^{-1}$) ^a	λ_{em} (nm) ^b	ϕ_{P} ^b	ϕ_{Δ} ^b	Lifetime (ns) ^{a,c}	
					τ_1	τ_2
PdL¹	251 (26.8), 286 (17.1), 422 (4.3)	539	0.0017	0.89	0.271 ± 0.002 (97%)	6.4 ± 0.3 (3%)
PdL²	283 (16.7), 347 (11.7)	604	0.00084	0.38	0.333 ± 0.005 (96%)	5.3 ± 0.5 (4%)

^a Measurements were carried out in methanol. ^b Measurements were carried out at 450 nm excitation wavelength and in a solution of deuterated methanol in air atmosphere according to literature. The absorption of complexes at 450 nm were set below 0.1 to avoid the generation of excimer. A solution of $[\text{Ru}(\text{bpy})_3]\text{Cl}_2$ (Tris(2,2'-bipyridyl)dichlororuthenium(II)) in deuterated methanol (photoluminescence quantum yield $\phi_{\text{P}} = 0.015$, singlet oxygen quantum yield $\phi_{\Delta} = 0.73$) was used as reference. ^c Excitation source 375 nm. Biexponential model: $y = y_0 + A_1 \cdot \exp(-(x-x_0)/\tau_1) + A_2 \cdot \exp(-(x-x_0)/\tau_2)$

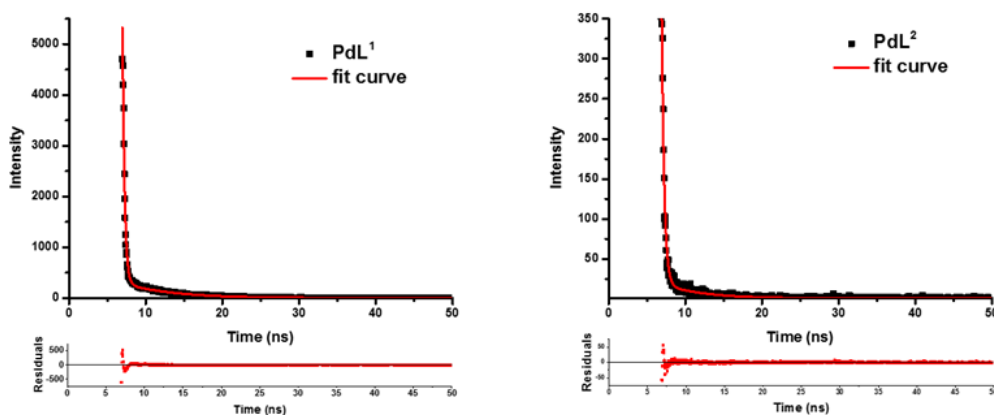


Figure AI.5 The phosphorescence lifetime spectra and fit curve of palladium complexes in methanol. Fit equation: $y = y_0 + A_1 \cdot \exp(-(x-x_0)/\tau_1) + A_2 \cdot \exp(-(x-x_0)/\tau_2)$.

Table AI.4 HOMO and LUMO energies, Energy gap (ΔE) of **PdL¹** and **PdL²**

Complex	LUMO/eV	HOMO/eV	ΔE /eV
PdL¹	-2.048	-5.258	3.21
PdL²	-2.114	-5.644	3.53

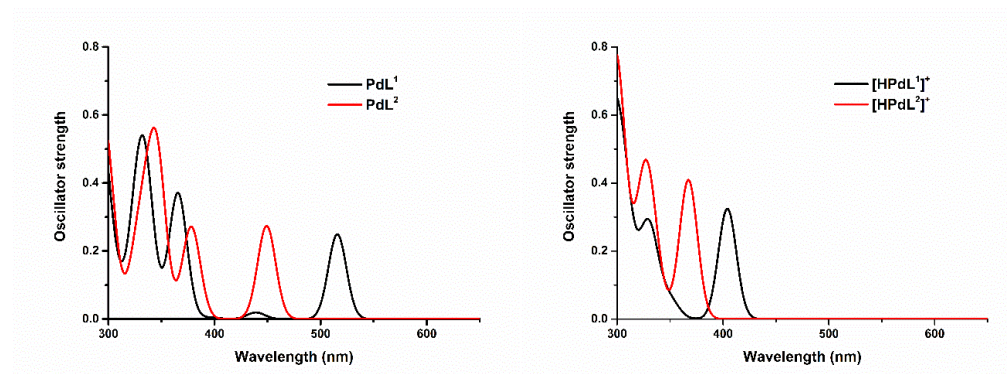
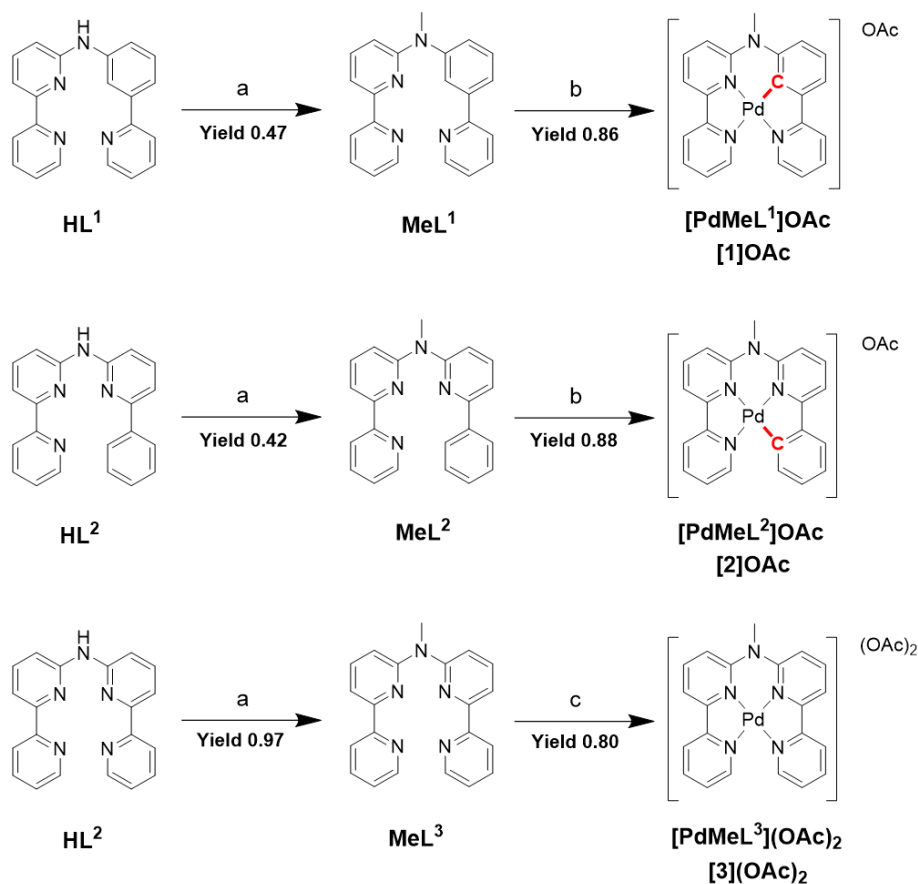


Figure AI.6 TDDFT-calculated spectra for **PdL¹**, **PdL²** (left) and **[PdHL¹]⁺**, **[PdHL²]⁺** (right) at the TZP/COSMO level in methanol. The theoretical curves were calculated and plotted in ADF with Gaussian Fixed Oscillator Strengths. Scaling factor = 1.0, peak width = 30 nm.

APPENDIX II SUPPORTING INFORMATION FOR CHAPTER 3



Scheme AII.1 Synthesis of ligands MeL¹-MeL³ and of their palladium complexes. Reaction condition: (a) CH₃I, KO^t-Bu, DMF, room temperature, 24 h; (b) palladium(II) acetate, CH₃COOH, N₂, 135 °C, 24 h; (c) Palladium(II) acetate, MeOH, 65 °C, 24 h.

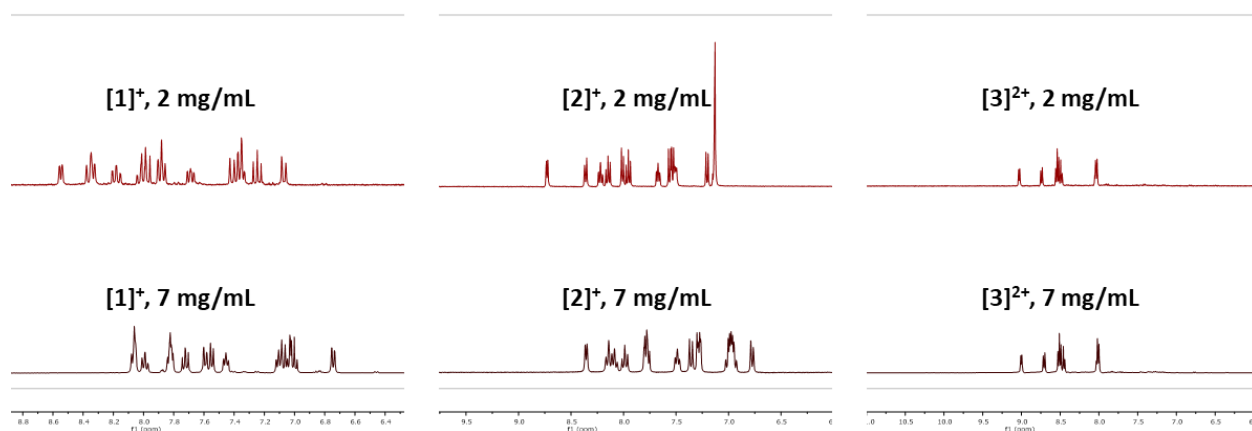


Figure AII.1 The aromatic region of the ¹H NMR spectrum of complexes [1]⁺-[3]²⁺ at low (2 mg/mL) and high (7 mg/mL) concentration. Solvent: CD₃OD.

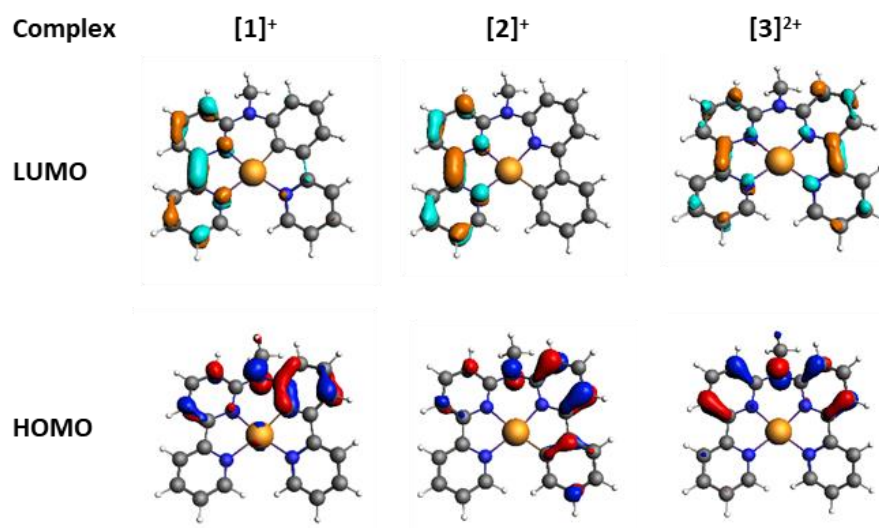


Figure AII.2 DFT calculation of HOMOs (bottom) and LUMOs (top) orbitals of $[1]^+$ - $[3]^{2+}$; occupied orbitals (HOMO) have red and blue lobes, and unoccupied orbitals (LUMO) brown and cyan lobes. Element color code: grey = C; orange = Pd; blue = N; white = H. Level of theory: ADF/DFT/PBE0/TZP/COSMO(water).

Table AII.2 HOMO and LUMO energies, energy gap (ΔE) of complexes $[1]^+$ - $[3]^{2+}$.

Complex	HOMO /eV	LUMO/eV	ΔE /eV
$[1]^+$	-6.24	-2.41	3.83
$[2]^+$	-6.58	-2.46	4.11
$[3]^{2+}$	-6.95	-2.82	4.13

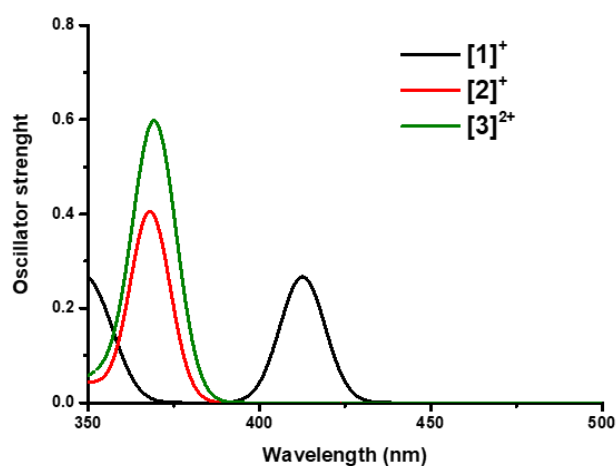


Figure AII.3 TDDFT-calculated spectra for palladium complexes $[1]^+$ - $[3]^{2+}$. Level of theory: ADF/TDDFT/PBE0/TZP/COSMO (water).

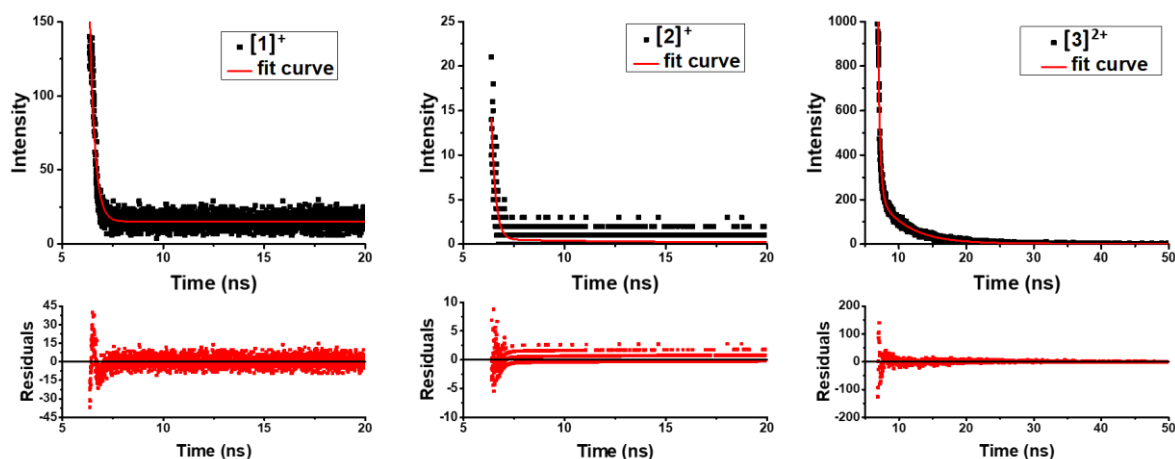


Figure AII.4 The phosphorescence lifetime spectra and fit curve of complexes $[1]^+$ - $[3]^{2+}$ in water under air atmosphere at room temperature. Fit equation: $y = y_0 + A_1 \cdot \exp(-(x-x_0)/\tau_1)$ ($[1]^+$ and $[2]^+$), $y = y_0 + A_1 \cdot \exp(-(x-x_0)/\tau_1) + A_2 \cdot \exp(-(x-x_0)/\tau_2)$ ($[3]^{2+}$). Excitation wavelength: 375 nm. The data were analyzed via OriginPro 9.1.

Table AII.5 The derived countrate (kcps) values of complexes in different solutions and different concentrations.

complex	H ₂ O	PBS	Opti-MEM with FCS	Opti-MEM without BSA
Solution only	54	40	894	107
$[1]^+$ 5 μ M	37	65	2268	1936
$[1]^+$ 50 μ M	146	187	19144	18970
$[2]^+$ 5 μ M	30	58	2775	5657
$[2]^+$ 50 μ M	67	61	22311	25377
$[3]^{2+}$ 5 μ M	56	60	927	136
$[3]^{2+}$ 50 μ M	79	21	930	101

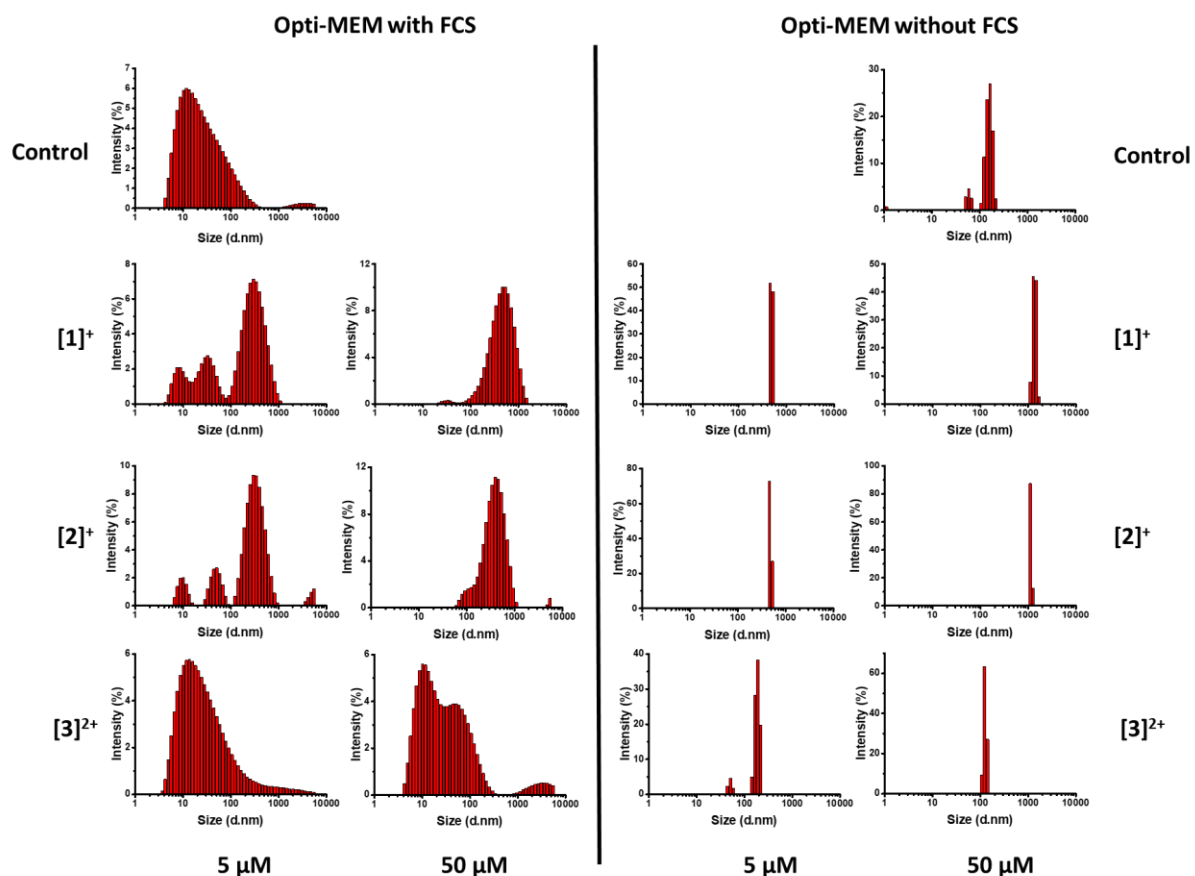


Figure AII.5 Size distributions according to DLS of solution of [1]OAc-[3]OAc at 5 or 50 μM in different solvents.

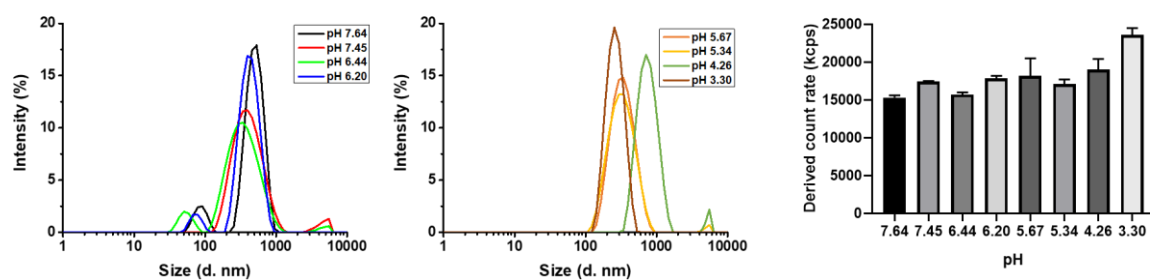


Figure AII.6 DLS size distribution (left and middle) and derived count rate (right) of [1]OAc (50 μM) in Opti-MEM complete medium at different pH.

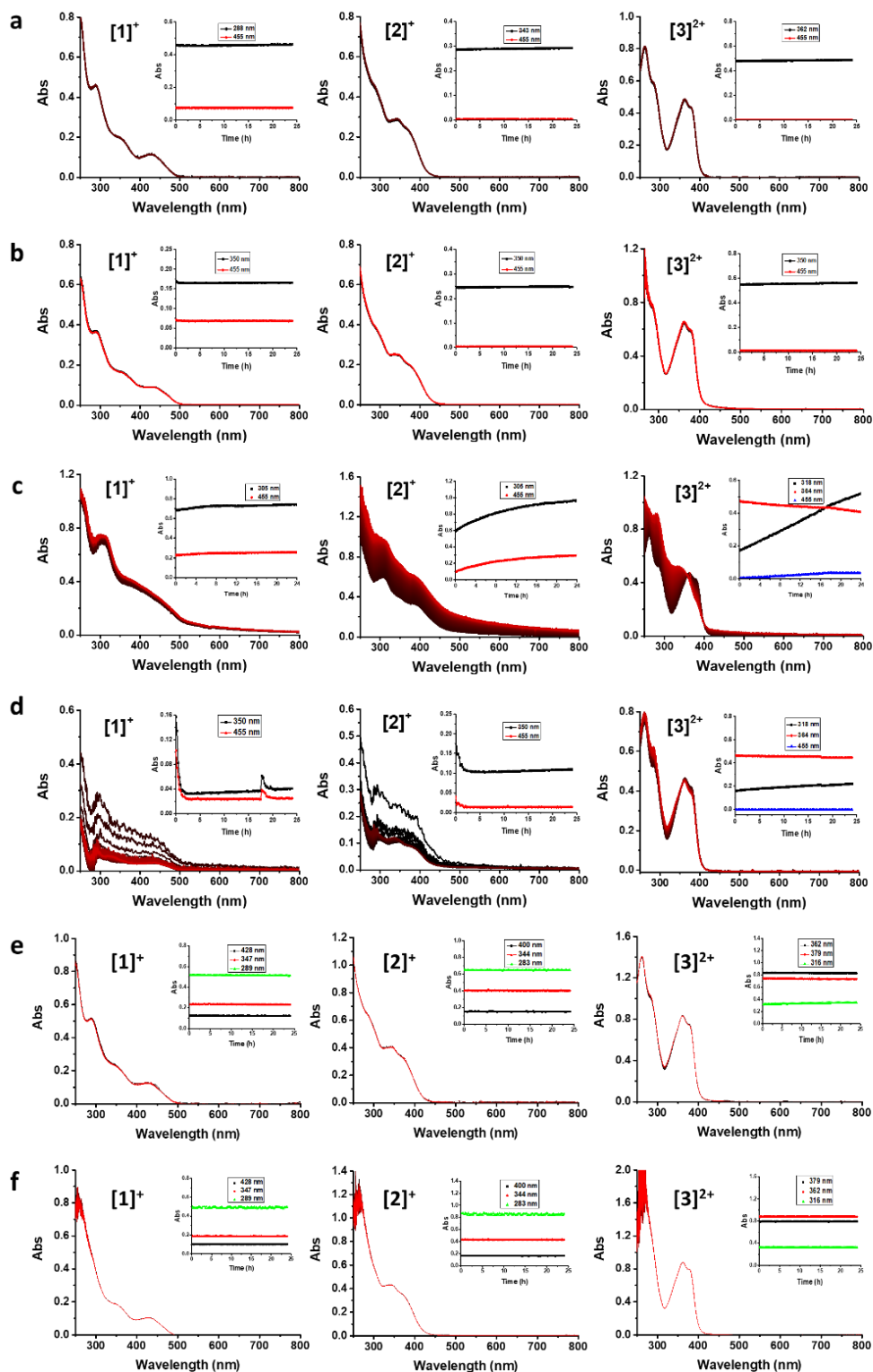


Figure AII.7 Time evolution of the absorbance spectra of solutions of $[1]^+$ - $[3]^{2+}$ in H_2O (a), PBS (b), cell medium with FCS (c), cell medium without FCS (d), H_2O with GSH (200 μM , e) and H_2O with ascorbic acid (200 μM , f) at 310 K. Concentration 50 μM . The color change of the spectra indicates the time, with black corresponding to the first curve (0 h) and red to the last one (24 h).

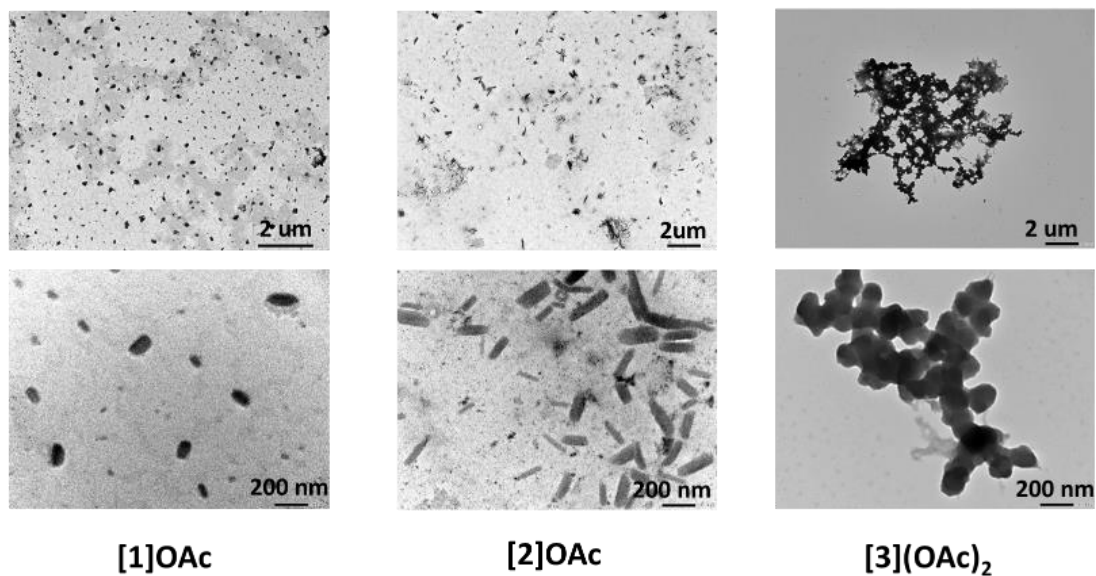


Figure AII.8 TEM images of samples prepared from evaporated MilliQ water solutions of [1]OAc, [2]OAc, and [3](OAc)₂ (50 μM). Scale bar: 2 μm (top) and 200 nm (bottom).

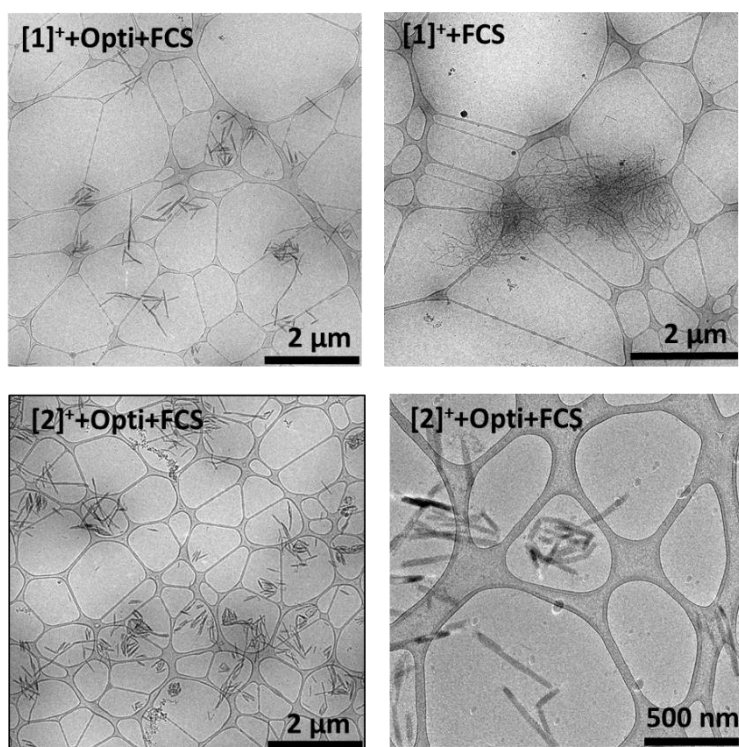


Figure AII.9 The Cryo-TEM images of complexes [1]⁺-[2]⁺ (50 μM) in the Opti-MEM medium with or without FCS.

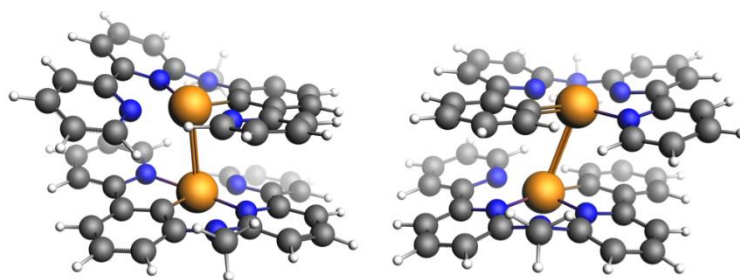


Figure AII.10 Structures of the DFT-optimized dimers $\{[1]^+\}_2$ (left) and $\{[2]^+\}_2$ (right).

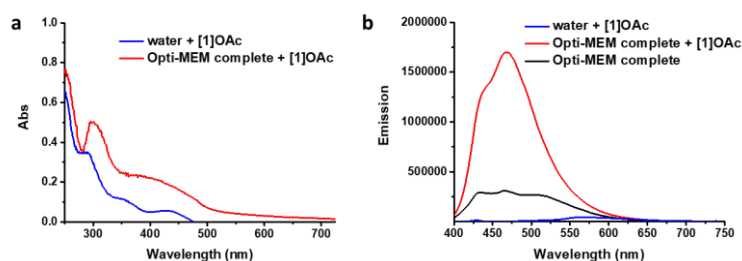


Figure AII.11 The absorbance (a) and emission spectra (b) of $[1]\text{OAc}$ ($50\ \mu\text{M}$) in water and Opti-MEM complete medium.

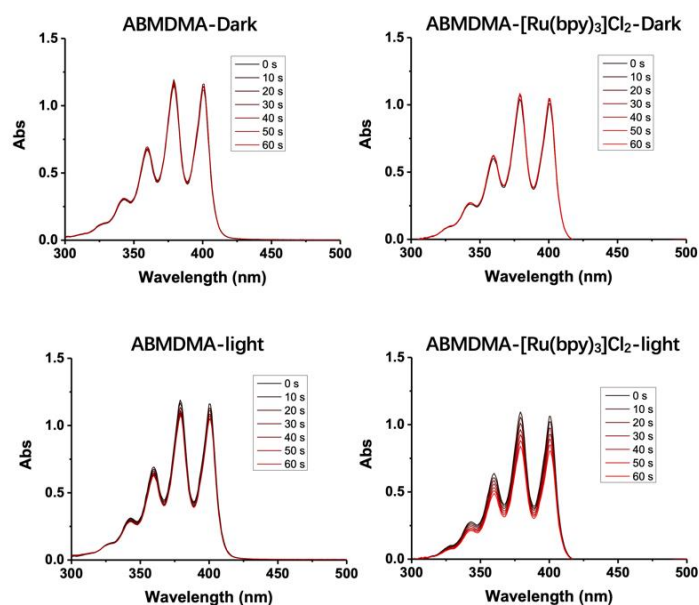


Figure AII.12 The absorbance of ABMDMA Opti-MEM complete solution ($100\ \mu\text{M}$) in the absence or presence of $[\text{Ru}(\text{bpy})_3]\text{Cl}_2$ ($50\ \mu\text{M}$) under dark or blue light ($450\ \text{nm}$) irradiation. (b) Absorbance time evolution and linear fit curve at $378\ \text{nm}$ of ABMDMA Opti-MEM complete solution ($100\ \mu\text{M}$) in the absence or presence of $[1]\text{OAc}$ ($50\ \mu\text{M}$), $[\text{Ru}(\text{bpy})_3]\text{Cl}_2$ ($50\ \mu\text{M}$) under blue light irradiation. The baseline for these spectra was a solution of $[1]\text{OAc}$ ($50\ \mu\text{M}$) or $[\text{Ru}(\text{bpy})_3]\text{Cl}_2$ ($50\ \mu\text{M}$) in Opti-MEM medium without ABMDMA.

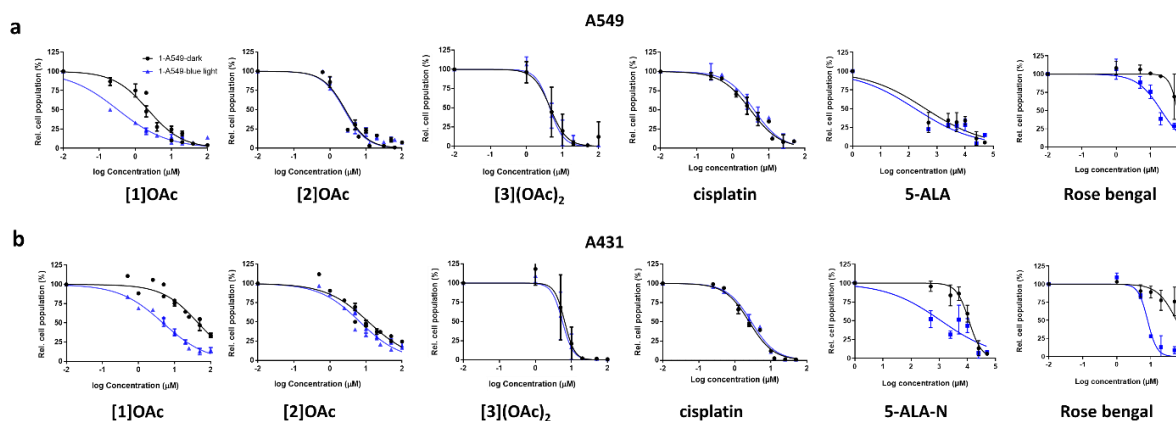


Figure AII.13 Dose-response curves for A549 and A431 cancer cells incubated with complexes [1]OAc-[3](OAc)₂ and cisplatin, either in the dark (black data points) or upon blue light irradiation (5 minutes, 5.66 mW cm⁻², 1.7 J cm⁻², blue data points), under normoxic condition (37 °C atmosphere, 21% O₂ and 7.0% CO₂).

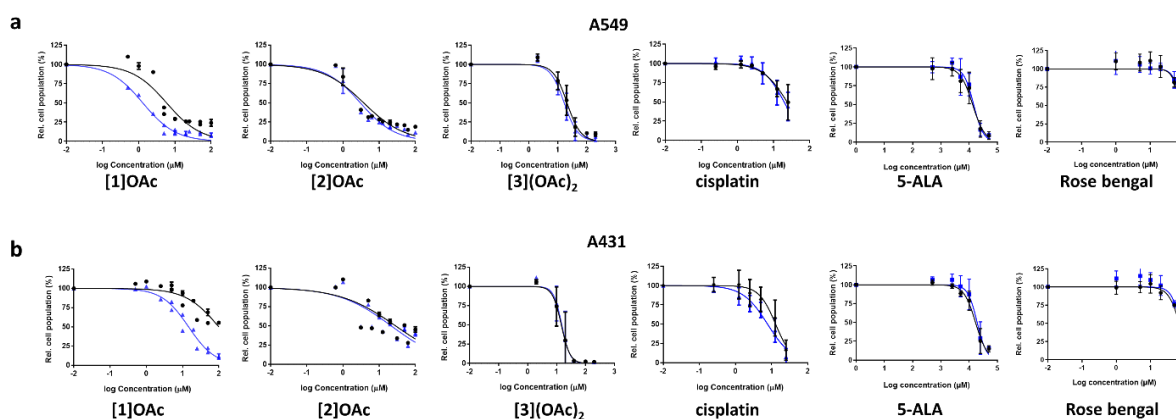


Figure AII.14 Dose-response curves for A549 and A431 cancer cells incubated with complexes [1]OAc-[3](OAc)₂, cisplatin, 5-ALA and Rose bengal either in the dark (black data points) or upon blue light irradiation (455 nm, 8 min, 3.54 mW cm⁻², 1.7 J cm⁻², blue data points) under hypoxic condition (37 °C atmosphere, 1% O₂ and 7.0% CO₂).

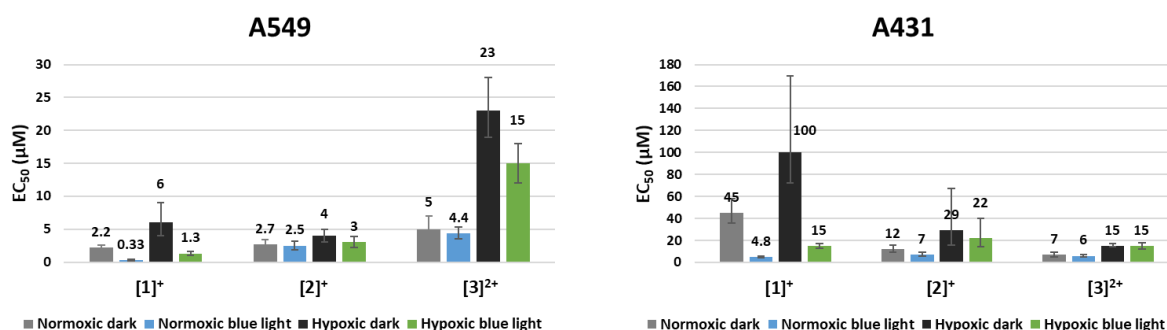


Figure AII.15 Graphical representation of the EC₅₀ values of complexes [1]OAc-[3](OAc)₂ in A549 and A431 in the dark or upon blue light irradiation, in normoxic vs. hypoxic conditions. (irradiation condition: normoxic 455 nm, 5 minutes, 5.66 mW cm⁻², 1.7 J cm⁻², hypoxic 455 nm, 8 min, 3.54 mW cm⁻², 1.7 J cm⁻²).

Table AII.7 Palladium cellular uptake according to ICP-MS analysis in the different fractions of A549 cells treated with [1]OAc-[3](OAc)₂ (1 μ M) in the dark after 24 h.

Complex	Treatment (ng Pd)	Metal uptake (ng Pd/million cells)	Metal uptake efficiency (%)	Fractions	Metal distribution (ng Pd/million cells)	Relative metal distribution (%)
[1]OAc	212.84	19 \pm 7	5.2	cytosol	0.7 \pm 0.1	3.5
				membranes	0.23 \pm 0.03	1.1
				nucleus	0.23 \pm 0.03	1.1
				cytoskeleton	17 \pm 3	94.3
[2]OAc	212.84	14 \pm 4	9.8	cytosol	0.45 \pm 0.05	3.3
				membranes	0.68 \pm 0.09	5.1
				nucleus	0.34 \pm 0.04	2.5
				cytoskeleton	12 \pm 2	89.1
[3](OAc) ₂	212.84	1.7 \pm 0.2	0.8	cytosol	0.42 \pm 0.09	23.3
				membranes	0.28 \pm 0.06	15.6
				nucleus	0	0
				cytoskeleton	1.1 \pm 0.2	61.1

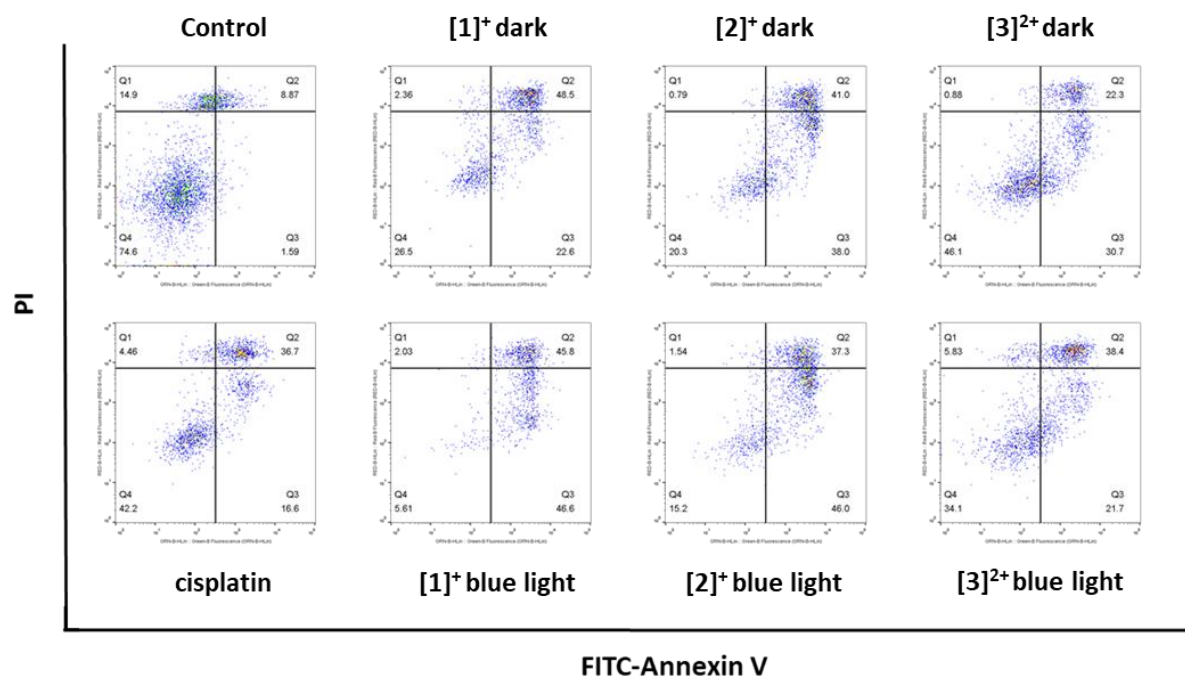
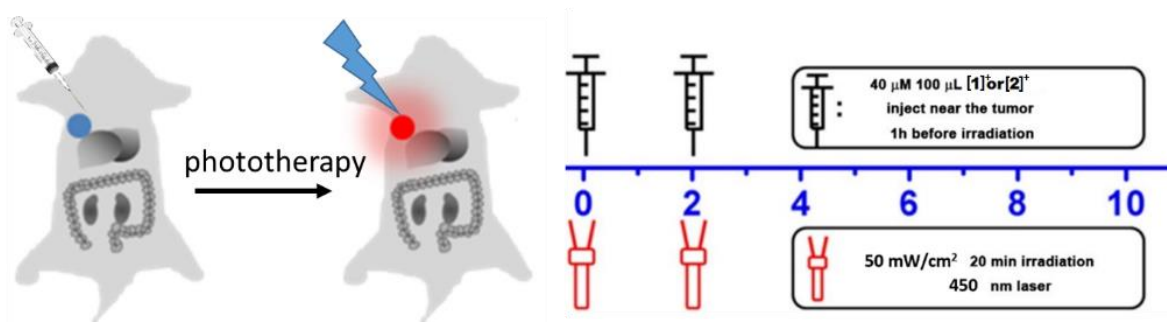


Figure AII.16 Annexin V/propidium iodide double staining FACS data for A549 cells after treatment with cisplatin (15 μ M) and complexes [1]OAc-[3](OAc)₂ (15 μ M) in the dark or upon blue light irradiation (455 nm, 5 minutes, 5.66 mW cm⁻², 1.7 J cm⁻²).



Scheme AII.2 The sketch of *in vivo* experiments for complexes [1]⁺ and [2]⁺.

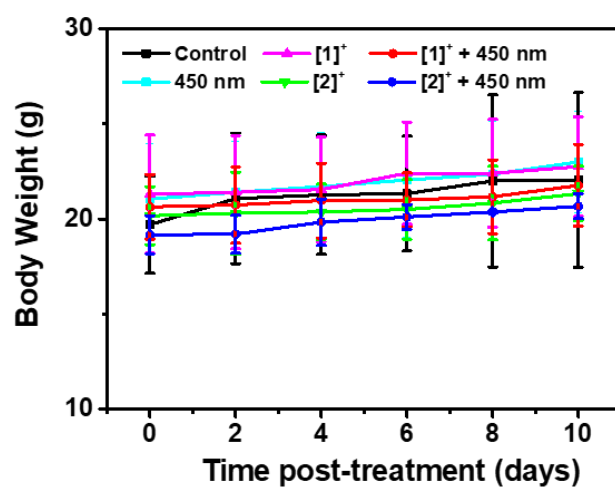


Figure AII.17. Bodyweight of mice treated with [1]OAc and [2]OAc and control groups.

APPENDIX III SUPPORTING INFORMATION FOR CHAPTER 4

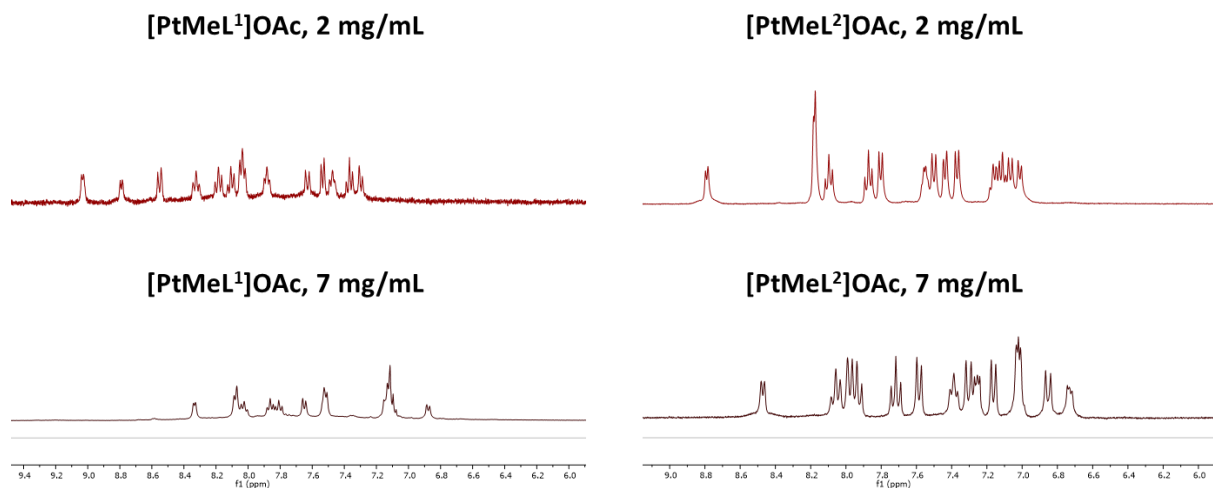


Figure AIII.1 ^1H NMR of complexes $[\text{PtMeL}^1]\text{OAc}$ and $[\text{PtMeL}^2]\text{OAc}$ at low (2 mg/mL MeOD) and high (7 mg/mL MeOD) concentration.

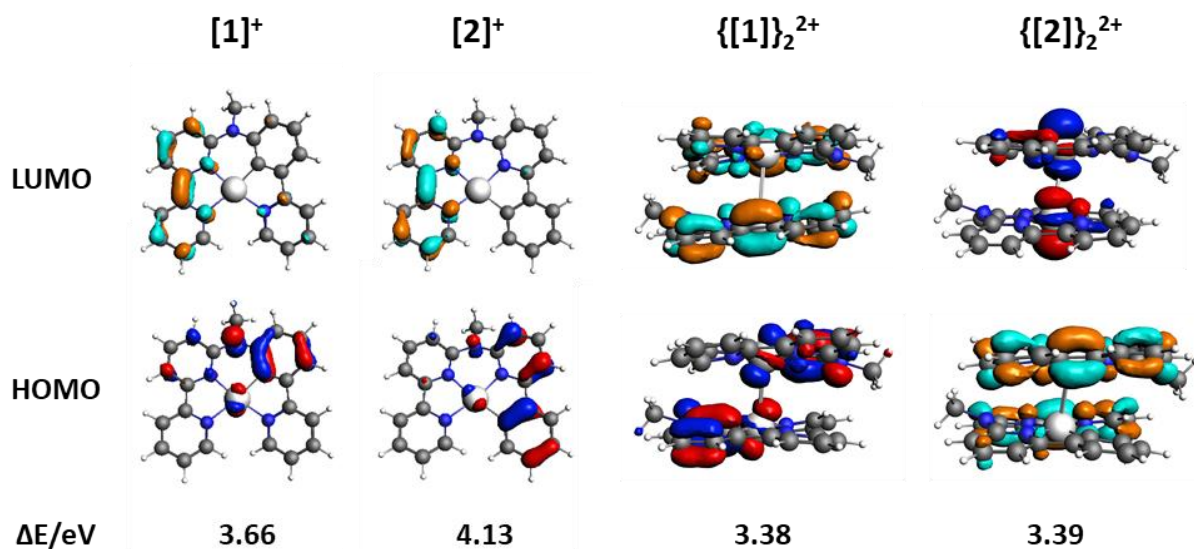
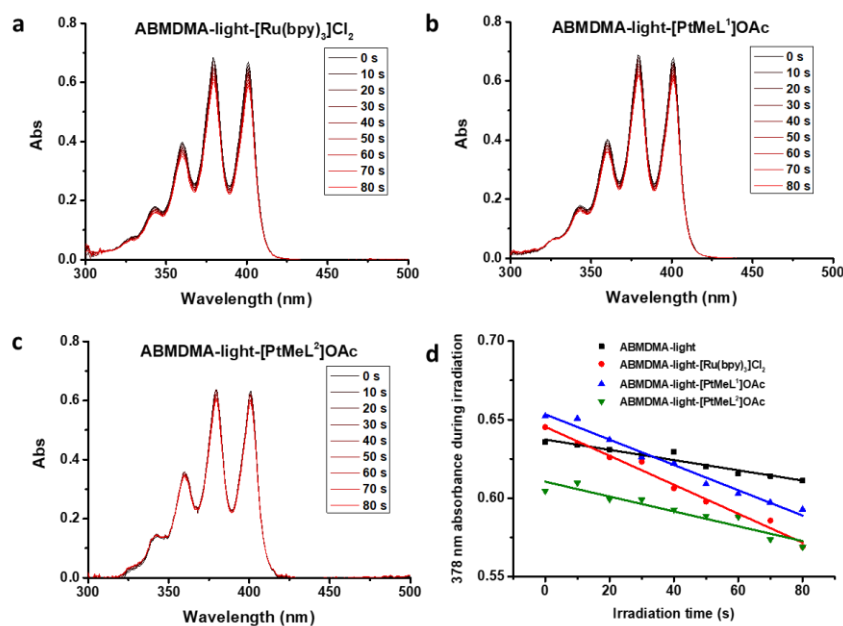


Figure AIII.2 (a) DFT calculation of HOMOs (bottom) and LUMOs (top) orbitals of $[1]^+$ and $[2]^+$ in monomer and dimer states. Occupied orbitals (HOMO) have red and blue lobes, and unoccupied orbitals (LUMO) brown and cyan lobes. Element color code: blue = N, grey = C, white = Pt and H.

Table AIII.1 The lowest ($\lambda > 350$ nm) and most intense ($f > 0.01$) TDDFT singlet-singlet transitions calculation information of platinum complexes in monomer and dimer states.

Complex	Energy (nm)	Energy (eV)	Oscillator strength (f)	Orbital transition contribution
[1] ⁺	370.3522	3.3477	0.3260	65.1% HOMO-1→LUMO 26.0% HOMO→LUMO+1
	441.1625	2.8104	0.2223	96.8% HOMO→LUMO
[2] ⁺	375.1118	3.3053	0.4247	61.0% HOMO-1→LUMO 35.7% HOMO→LUMO
[[1] ₂] ²⁺	518.4094	2.3916	0.0188	78.3% HOMO→LUMO
	471.8107	2.6278	0.0996	93.8% HOMO→LUMO
	454.6116	2.7273	0.0203	15.3% HOMO-2→LUMO 11.9% HOMO-1→LUMO+1
[[2] ₂] ²⁺	473.1412	2.6204	0.0163	83.3% HOMO→LUMO
	447.1158	2.7730	0.0697	93.5% HOMO→LUMO
	413.8552	2.9958	0.0506	91.8% HOMO-1→LUMO

**Figure AIII.3** Singlet oxygen generation of aggregates of [1]OAc-[2]OAc and reference [Ru(bpy)₃]Cl₂ in Opti-MEM complete medium. (a-c) The absorbance change of ABMDMA (100 μM) in Opti-MEM complete medium in presence of [1]OAc-[2]OAc or reference [Ru(bpy)₃]Cl₂ (50 μM) upon blue light irradiation (d) Evolution of the absorbance at 378 nm vs. irradiation time of ABMDMA (100 μM) in Opti-MEM complete medium in the absence or presence of [1]OAc-[2]OAc or reference [Ru(bpy)₃]Cl₂ (50 μM) under blue light irradiation. Irradiation conditions: 298 K, 450 nm, 5.23 mW cm⁻², 80 s.

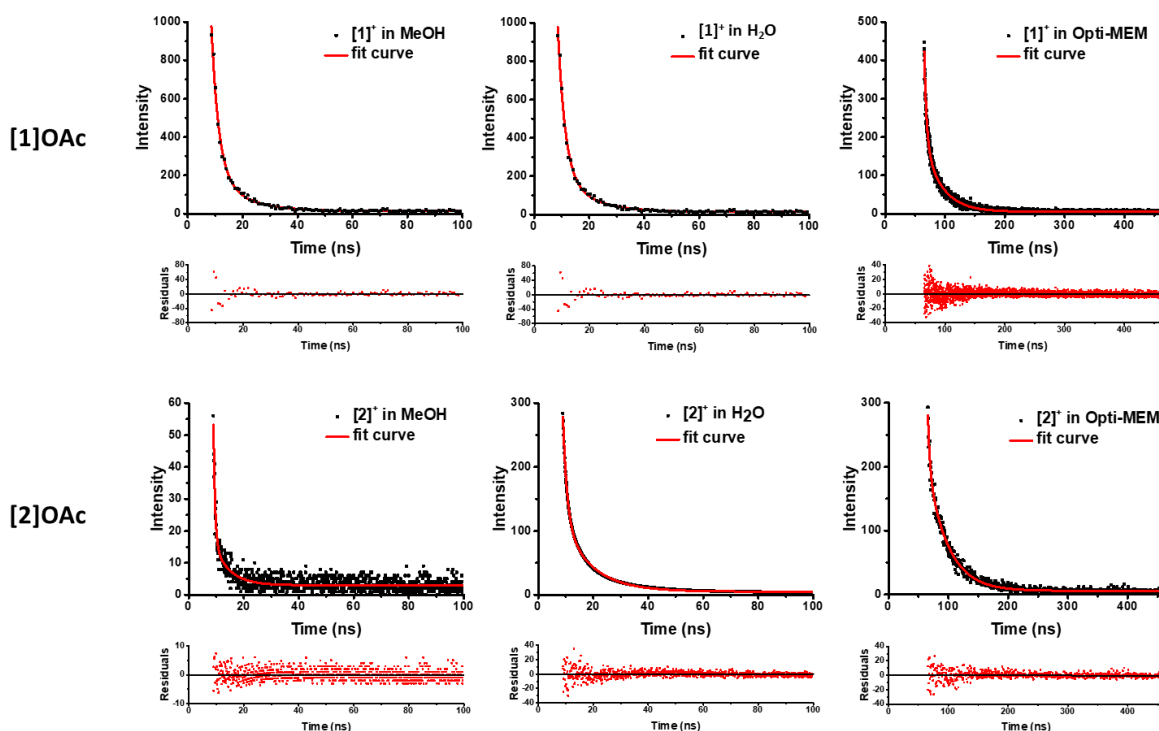


Figure AIII.4 The phosphorescence lifetime spectra and fitting curves for platinum complexes [1]OAc and [2]OAc in aerated methanol, water and Opti-MEM. Fit equation: $y = y_0 + A_1 \cdot \exp(-(x-x_0)/\tau_1) + A_2 \cdot \exp(-(x-x_0)/\tau_2)$.

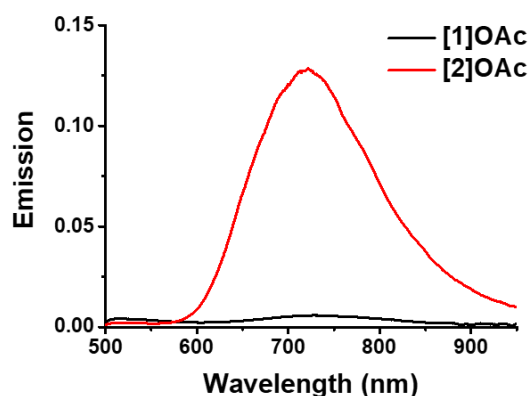


Figure AIII.5 The solid emission spectra of complexes [1]OAc and [2]OAc (excitation 450 nm, laser intensity 50 mW cm⁻², Edmund optics high-pass filter was used to filter the spectra below 500 nm).

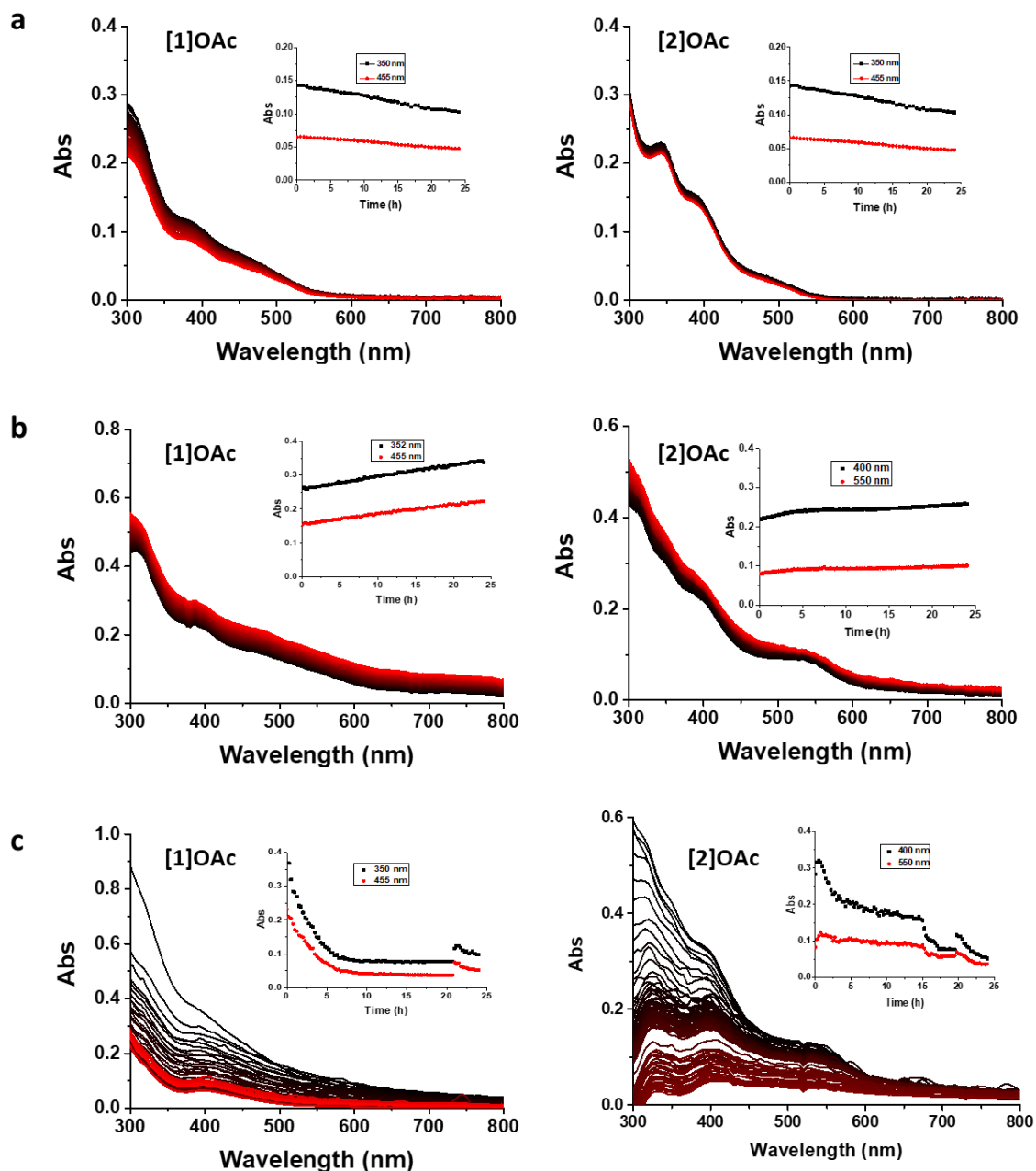


Figure AIII.6 Time evolution for 24 h of the absorbance spectra of solutions of [1]OAc and [2]OAc (50 μM) in PBS (a), OptiMEM with (b) or without (c) FCS medium (2.5 % v/v). Interval: 15 min, from black (0 h) to red (24 h).

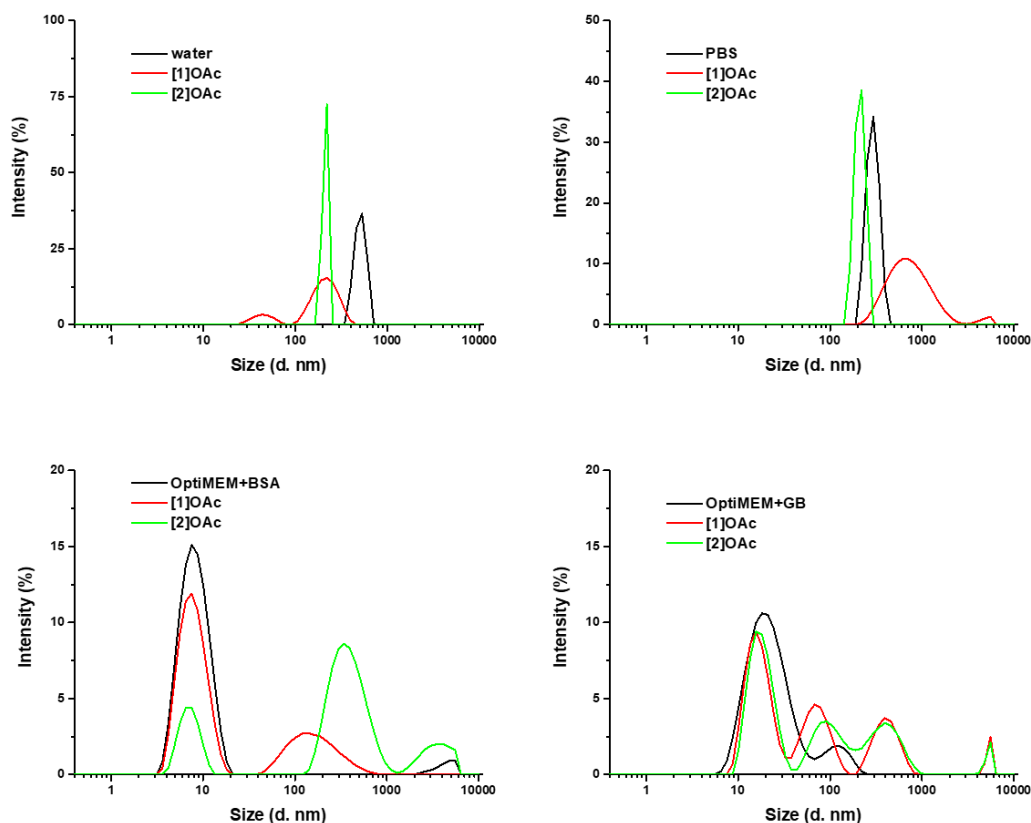


Figure AIII.7 Size distribution observed by Dynamic Light Scattering (DLS) for [1]OAc and [2]OAc (50 μ M) dissolved in different buffers. PBS = phosphate buffer saline; BSA = bovine serum albumin (50 g/L in Opti-MEM medium); GB = globulin (30 g/L in Opti-MEM medium).

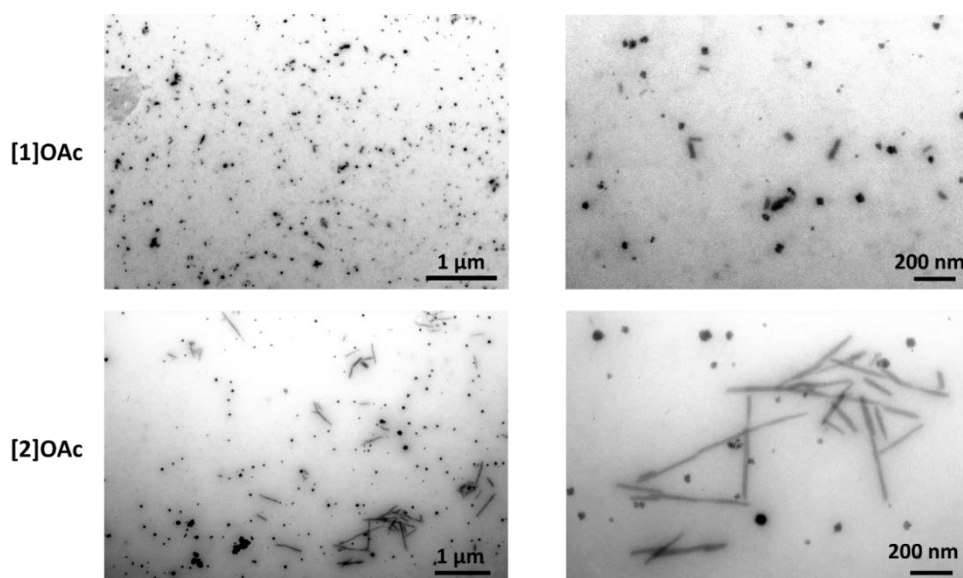


Figure AIII.8 TEM images of [1]OAc and [2]OAc (50 μ M) in Opti-MEM with FCS (2.5 % v/v).

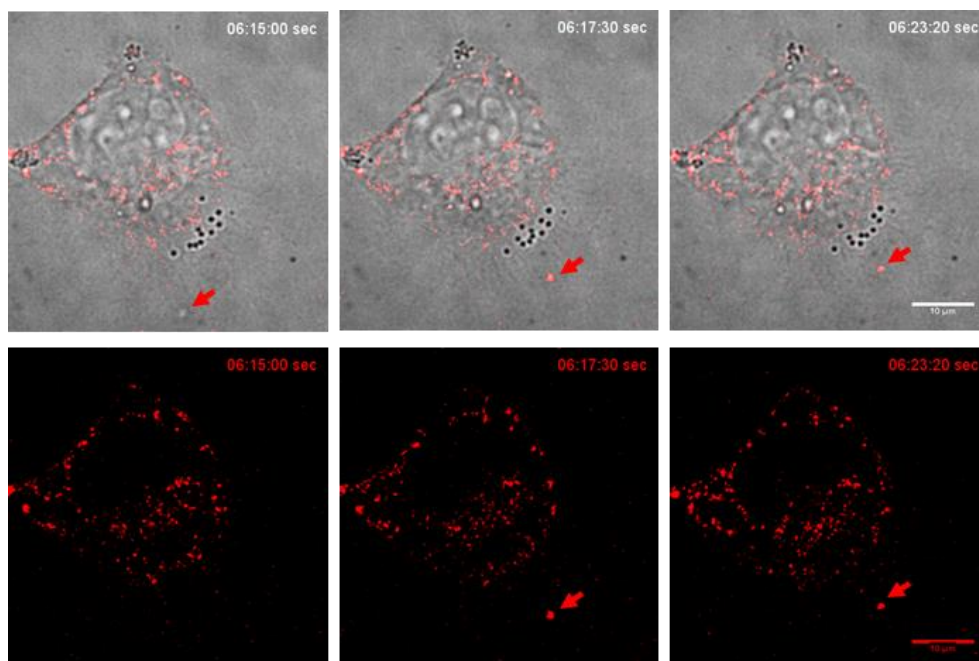


Figure AIII.9 Selected timepoints from 16-h time-lapse confocal fluorescence live-cell imaging of [1]OAc uptake by A549 cells. The complex was added in the dish 15 min before initiation of the measurement ($t=0$). The top row shows overlaid bright field and [1]OAc fluorescence images. The bottom row shows [1]OAc fluorescence images. Red arrows indicate [1]OAc uptake by the cell. Brightfield and fluorescence (561 nm excitation) images were acquired every 50 s. Time is indicated in hours:minutes:seconds format. The selected time points are extracted from [Video S1](#).

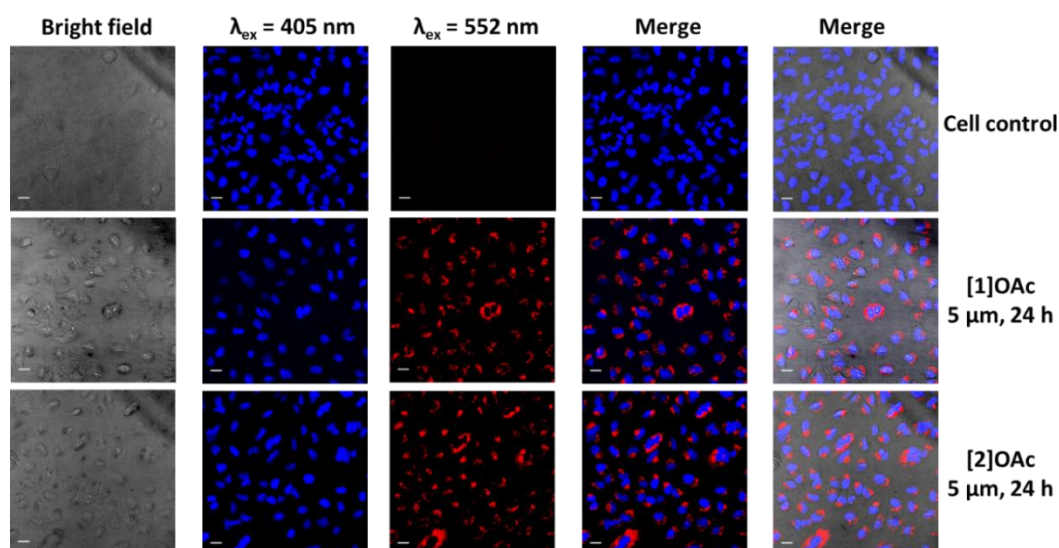


Figure AIII.10 Confocal images of A549 cells treated with or without complexes [1]OAc and [2]OAc (red, 650-750 nm, $\lambda_{\text{ex}} = 552$ nm), and staining with Hoechst 33342 (blue, 420-480 nm, $\lambda_{\text{ex}} = 405$ nm). Scale bar: 20 μm . complex concentration 5 μM , Pearson coefficients -1.

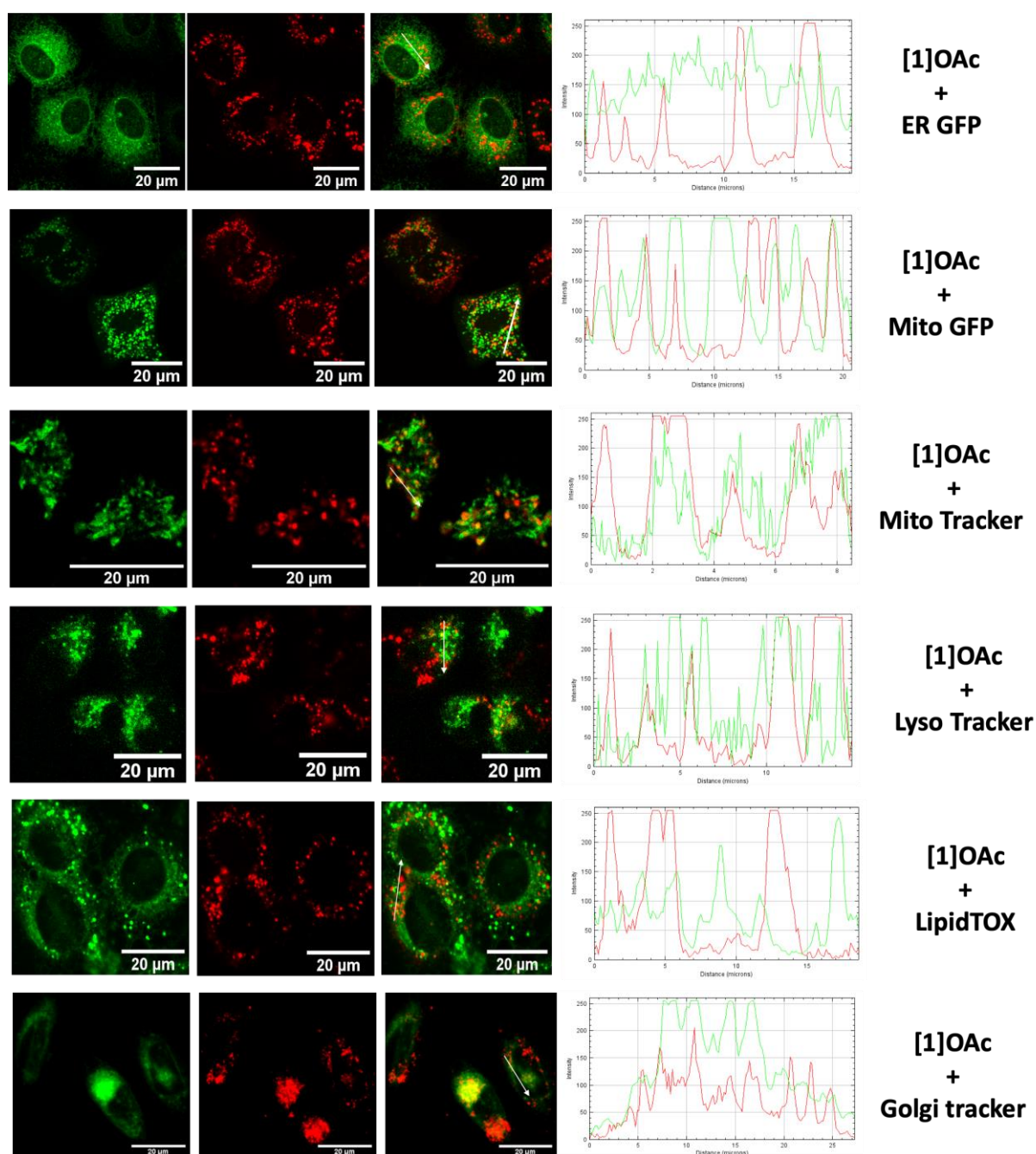


Figure AIII.11 Confocal microscopy overlapping images and pixel intensity curves for A549 cells co-treated with complexes **[1]OAc** (red, 5 μM) and (green) dyes Endoplasmic reticulum Green Fluorescent Protein (GFP), Mitochondria GFP, MitoTracker Green FM, LysoTracker™ Green DND-26, HCS LipidTOX™ Green Neutral Lipid Stain and BODIPY™ FL C5-Ceramide complexed to BSA Golgi. Green channel ($\lambda_{\text{ex}} = 488 \text{ nm}$, $\lambda_{\text{em}} = 500\text{-}530 \text{ nm}$). Red channel ($\lambda_{\text{ex}} = 552 \text{ nm}$, $\lambda_{\text{em}} = 650\text{-}750 \text{ nm}$).

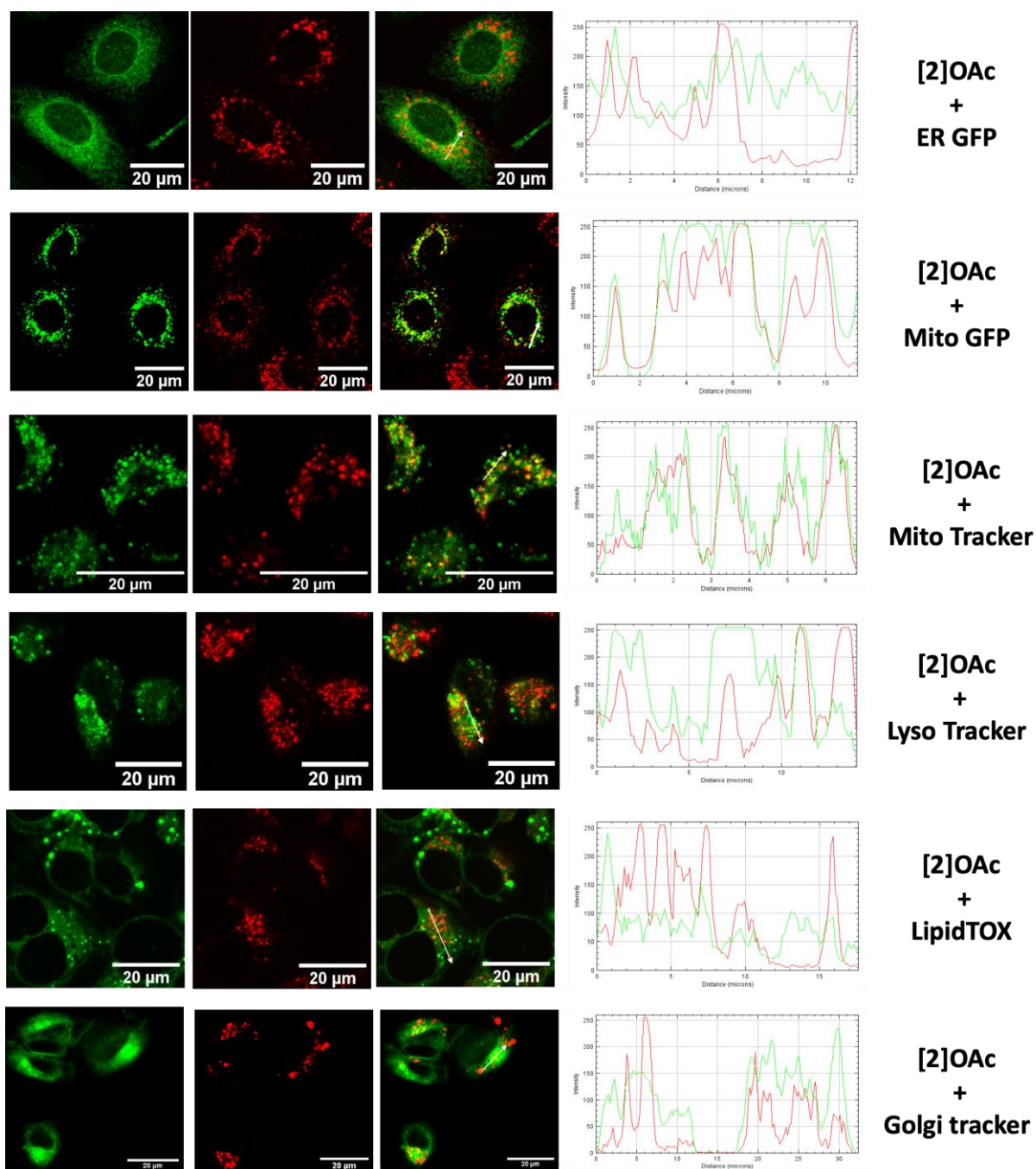


Figure AIII.12 Confocal microscopy overlapping images and pixel intensity curves for A549 cells co-treated with complex **[2]OAc** (red, 5 μM) and (green) dyes Endoplasmic reticulum Green Fluorescent Protein (GFP), Mitochondria GFP, MitoTracker Green FM, LysoTracker™ Green DND-26, HCS LipidTOX™ Green Neutral Lipid Stain and BODIPY™ FL C5-Ceramide complexed to BSA Golgi. Green channel ($\lambda_{\text{ex}} = 488 \text{ nm}$, $\lambda_{\text{em}} = 500 - 530 \text{ nm}$). Red channel ($\lambda_{\text{ex}} = 552 \text{ nm}$, $\lambda_{\text{em}} = 650 - 750 \text{ nm}$).

Table AIII.2 Pearson's correlation coefficients measured for co-localization studies of complexes [1]OAc or [2]OAc and different organelle-staining dyes in confocal cell imaging shown in Figure S15 and S16.

Dye	Complex	
	[1]OAc	[2]OAc
Endoplasmic reticulum GFP	-0.1 to 0.2	-0.1 to 0.2
Mitochondria GFP	-0.2 to 0.4	0.3 to 0.6
MitoTracker Green FM	0.2 to 0.4	0.3 to 0.5
LysoTracker™ Green DND-26	-0.3 to 0.1	0.0 to 0.3
HCS LipidTOX™ Green Neutral Lipid Stain	0.0 to 0.1	-0.1 to 0.1
BODIPY™ FL C5-Ceramide complexed to BSA golgi Dye	0.5 to 0.7	-0.4 to 0.6

Table AIII.3 Platinum cellular uptake according to ICP-MS analysis in A549 cells treated with [1]OAc and [2]OAc (5 μ M, 1 mL) in combination with different inhibition conditions after 2 h.

Complex	inhibitor	uptake (ng Pd/million cells)	Inhibition percent ^a
[1]OAc	control	111 \pm 25	0%
	dynasore	84 \pm 7	24%
	4 °C	52 \pm 2	53%
[2]OAc	control	159 \pm 5	0%
	dynasore	58 \pm 7	64%
	4 °C	66 \pm 8	58%

^a Inhibition percent = (uptake_{control} - uptake_{inhibitor}) / uptake_{control} \times 100%.

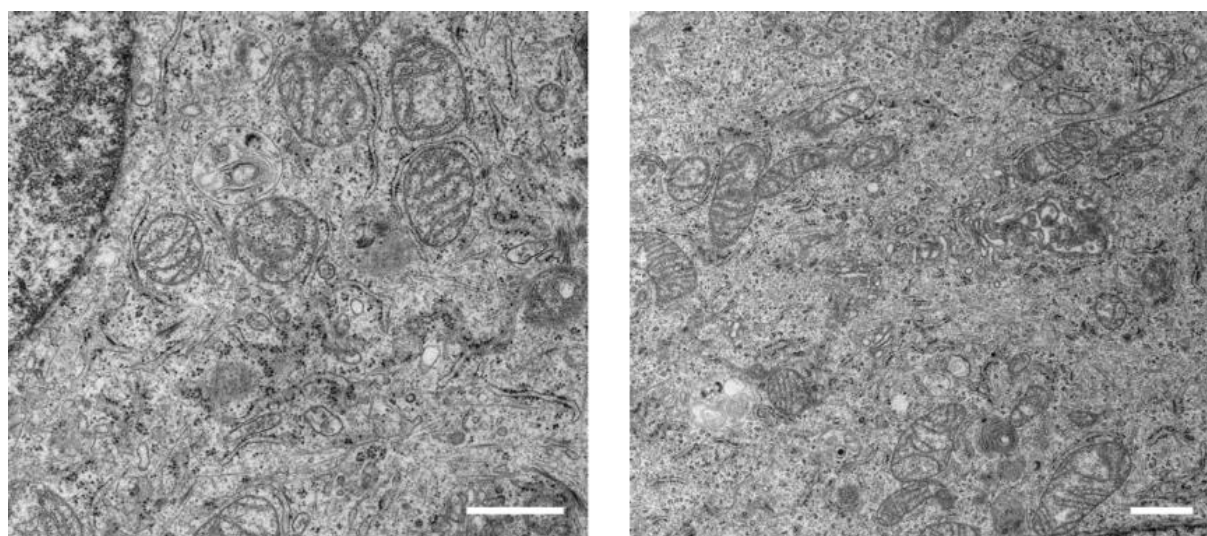


Figure AIII.13 Electron Microscopy imaging of control A549 cells without platinum treatment (scale bar 1 μ M).

APPENDIX IV SUPPORTING INFORMATION FOR CHAPTER 5

Table AIV.1 Selected bond distances (Å) and angels (degree) in the crystal structure of **PdL**.

Distance (Å)		Angel (°)	
Pd-N1	2.144(3)	C11-Pd1-C17	92.09(12)
Pd-C11	1.969(3)	C11-Pd1-N1	80.17(11)
Pd-C17	1.972(3)	C17-Pd1-N1	171.99(11)
Pd-N3	2.163(3)	C17-Pd1-N3	80.24(11)°
Pd-Pd	3.518	N1-Pd1-N3	107.42(10)

Table AIV.2 TDDFT singlet-singlet transitions calculation information of **PdL** in monomeric or dimeric state.

State	Energy (nm)	Energy (eV)	Oscillator strength (f)	Orbital contribution	transition
Monomer	383.0	4.0697	0.1262	HOMO→LUMO	89.9%
	335.2	3.6989	0.3642	HOMO→LUMO+1	84.7%
	304.65	3.2369	0.7603	HOMO-1→LUMO	70.9%
Dimer	540.1232	2.2955	0.0043	HOMO→LUMO	100%
	501.6673	2.4714	0.0484	HOMO→LUMO	96%
	450.6614	2.7512	0.0168	HOMO→LUMO	47.3%
				HOMO-1→LUMO	36.9%
	400.7565	3.0938	0.0819	HOMO→LUMO+1	86.4%

Table AIV.3 The photophysical properties of **PdL** in monomeric state.

Solvent	λ_{abs} , nm ($\epsilon \times 10^3 \text{ M}^{-1} \text{ cm}^{-1}$) ^a	λ_{em} (nm) ^{a,b}	lifetime (ns) ^{a,d}	ϕ_{p} ^c	ϕ_{Δ} ^c
DMSO	343 (25.8), 405 (5.2), 481 (3.7)	564	0.406 ± 0.004	0.0008	0.09
THF	347 (22.5), 410 (4.3), 480 (2.9)	540	0.432 ± 0.005		

^a measurement were carried out in aerated DMSO or THF^b excitation and concentration: 419 nm, 100 μM .^c measurement was carried out in MeOD.^d excitation source : 340 nm. Monoexponential model: $y = y_0 + A_1 \cdot \exp[-(x-x_0)\tau_1]$

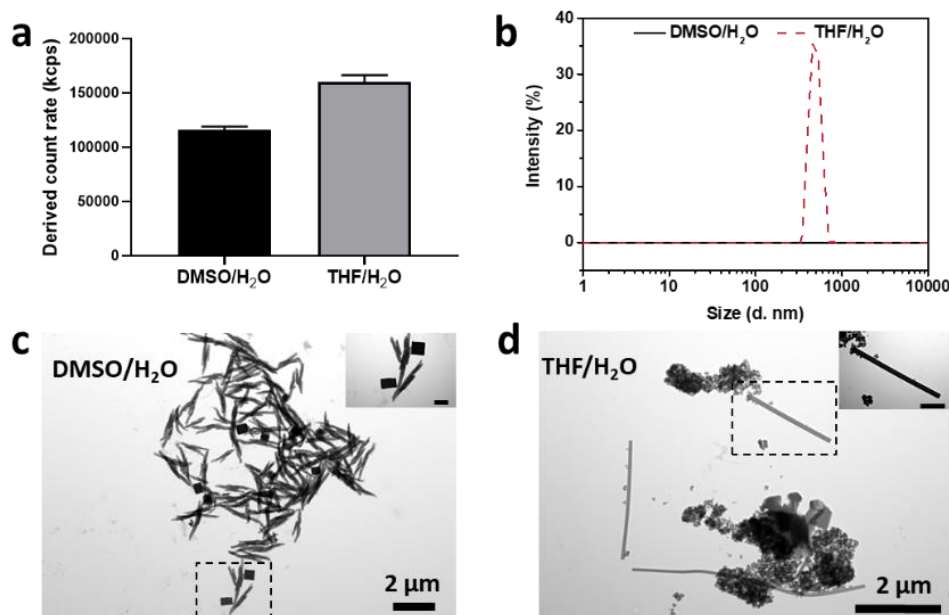


Figure AIV.1 (a) DLS derived count rate in the DMSO/H₂O or THF/H₂O system of **PdL** (100 μ M) after 30 min self-assembly; (b) Size distribution of the DLS analysis in the DMSO/H₂O or THF/H₂O system of **PdL** (100 μ M) after 30 min self-assembly; TEM images of samples prepared from the DMSO/H₂O (c) or THF/H₂O (d) system of **PdL** (100 μ M) after 30 min self-assembly. Inset picture scale bar: 500 nm.

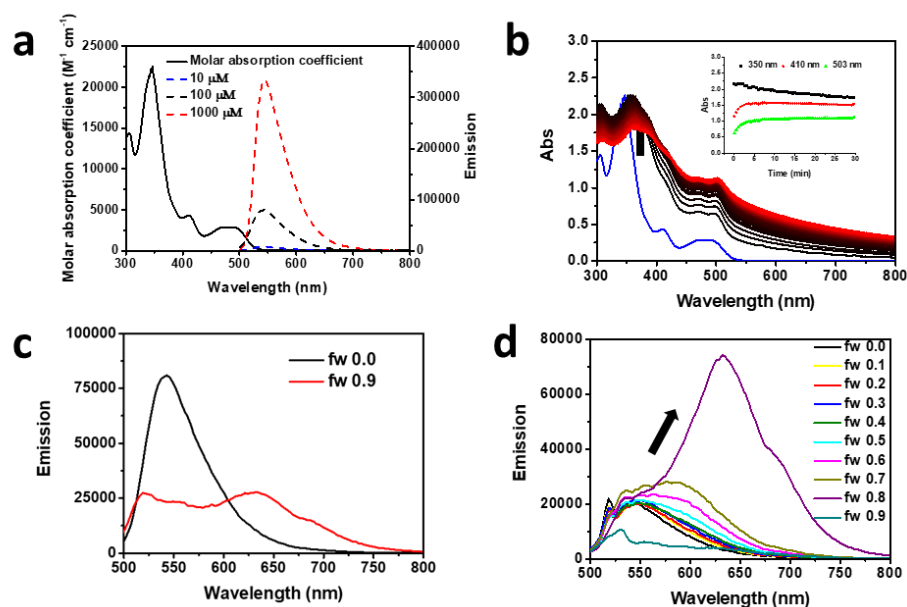


Figure AIV.2 (a) The molar absorption coefficient (black solid line) and emission spectra of **PdL** in tetrahydrofuran (THF) solution at different concentrations (blue dash line 10 μ M; black dash line 100 μ M, red dash line 1000 μ M). (b) Time evolution of the absorption spectra of H₂O/THF solution (100 μ M, 9:1, v/v) of **PdL** at 298 K for 30 min (30 s interval, the color of

spectra change from black (0 min) to red (30 min); the blue line is the absorbance spectra of **PdL** (100 μM) in pure THF). Inset: time evolution of the absorption at 350 nm (black square), 480 nm (red dot), 504 nm (green triangle) of the solution. (d) Emission spectra of **PdL** (100 μM) in pure THF (fw ($V_{\text{water}}/V_{\text{total}}$) = 0.0) and water/THF mixture (9:1, v/v, fw = 0.9); excitation 419 nm. (d) Emission spectra of **PdL** (20 μM) in different THF/water ratio (from v/v = 10/0 to 1/9, excitation 450 nm).

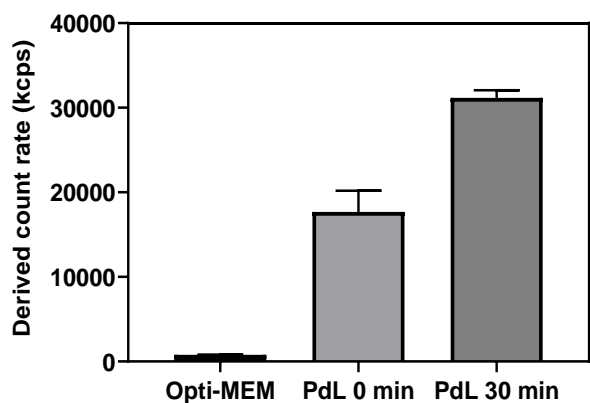


Figure AIV.3 DLS scattering-derived count rate of **PdL** in Opti-MEM complete medium at 0 and 30 min under room temperature.

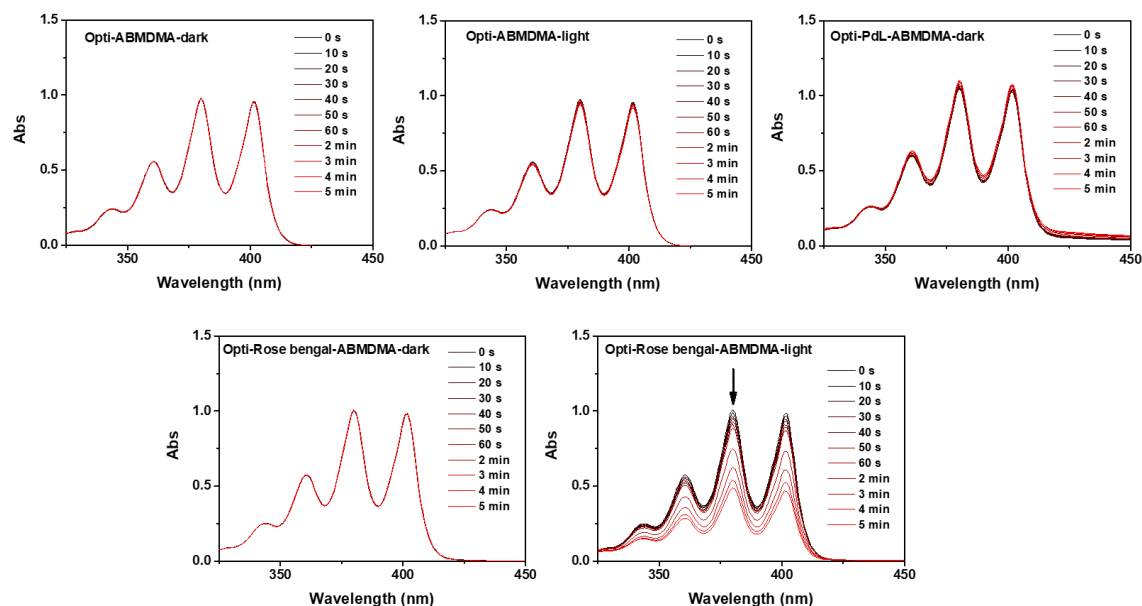


Figure AIV.4 Time evolution of the absorption spectrum of an Opti-MEM complete solution of 9,10-anthracenediyl-bis(methylene)-dimalonic acid (ABMDMA, 100 μM) in the absence or presence of **PdL** (25 μM) or rose Bengal, under green light irradiation (515 nm).

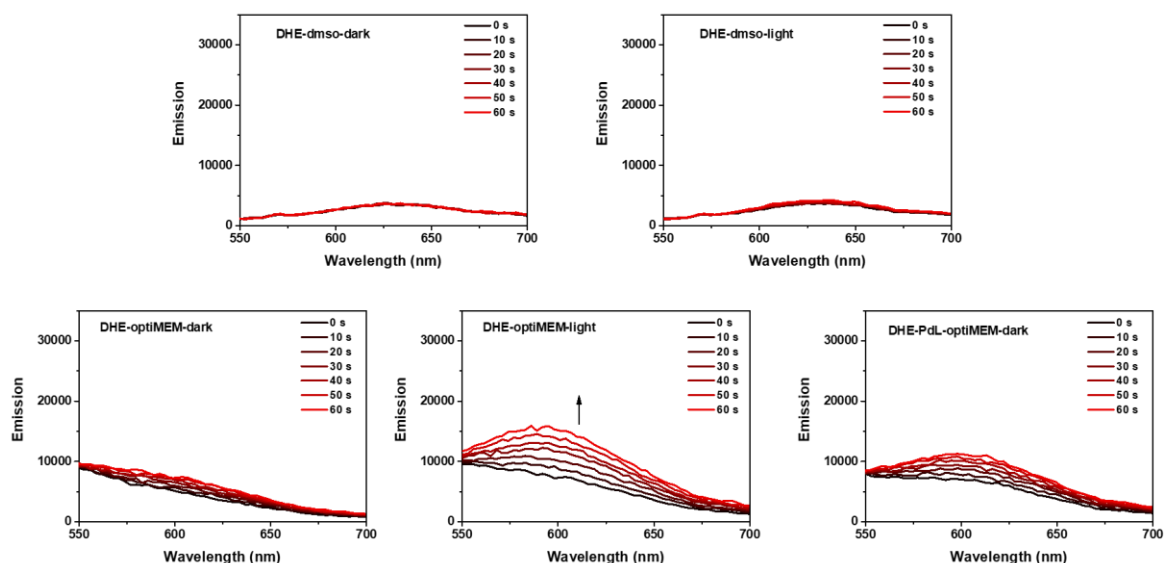


Figure AIV.5 The emission spectra of dihydroethidium (DHE) solution (DMSO or Opti-MEM complete) in the absence or presence of **PdL** (25 μM) under green light irradiation (520 nm) or in the dark, over 60 s.

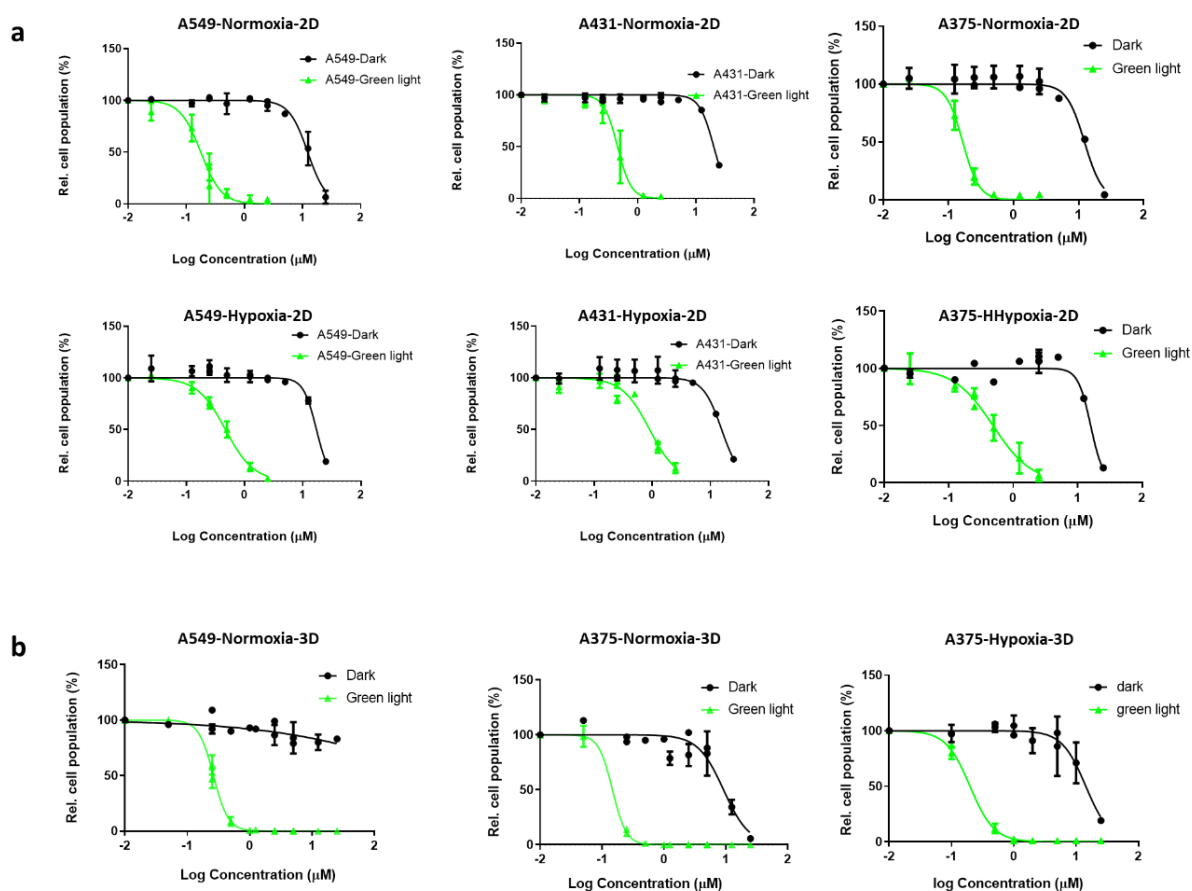


Figure AIV.6 Dose-response curves for 2D-monolayer (a) or 3D-spheroid (b) for different human cancer cell lines incubated with **PdL**, either in the dark (black data points) or upon green

light irradiation (green data points) under normoxic-2D (520 nm, 20 min, 10.92 mW/cm², 13 J/cm²), hypoxic-2D (520 nm, 32 min, 6.90 mW/cm², 13 J/cm²), normoxia-3D spheroid condition (520 nm, 32 min, 6.90 mW/cm², 13 J/cm²), or hypoxia-3D spheroid condition (520 nm, 55 min, 3.99 mW/cm², 13 J/cm²).

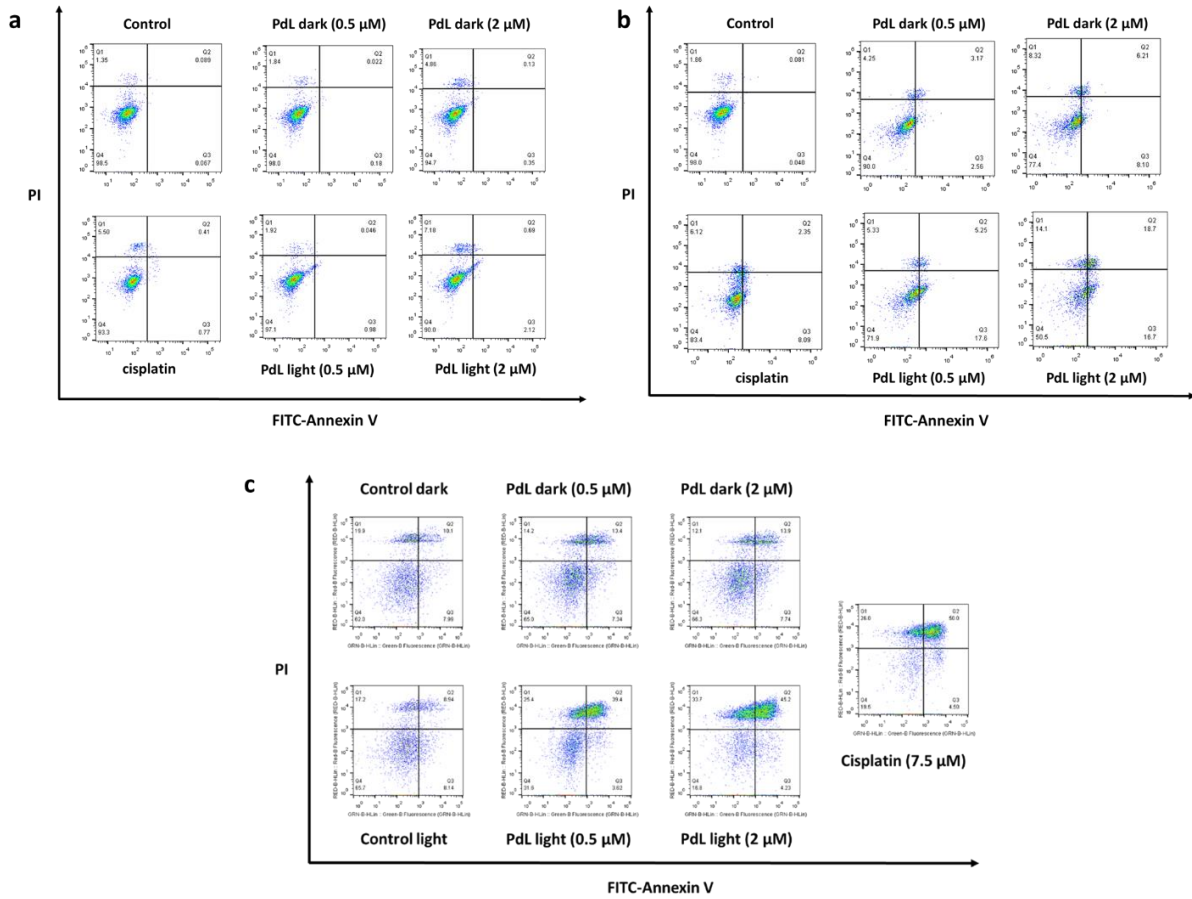


Figure AIV.7 Annexin V/Propidium iodide double staining FACS data for A375 cells after treatment with cisplatin (7.5 μM) or **PdL** (0.5 μM or 2 μM) in the dark or upon green light irradiation (normoxic 520 nm, 20 min, 10.9 mW/cm², 13 J/cm²) after 2 (a), 4 (b) and 24 h (c)

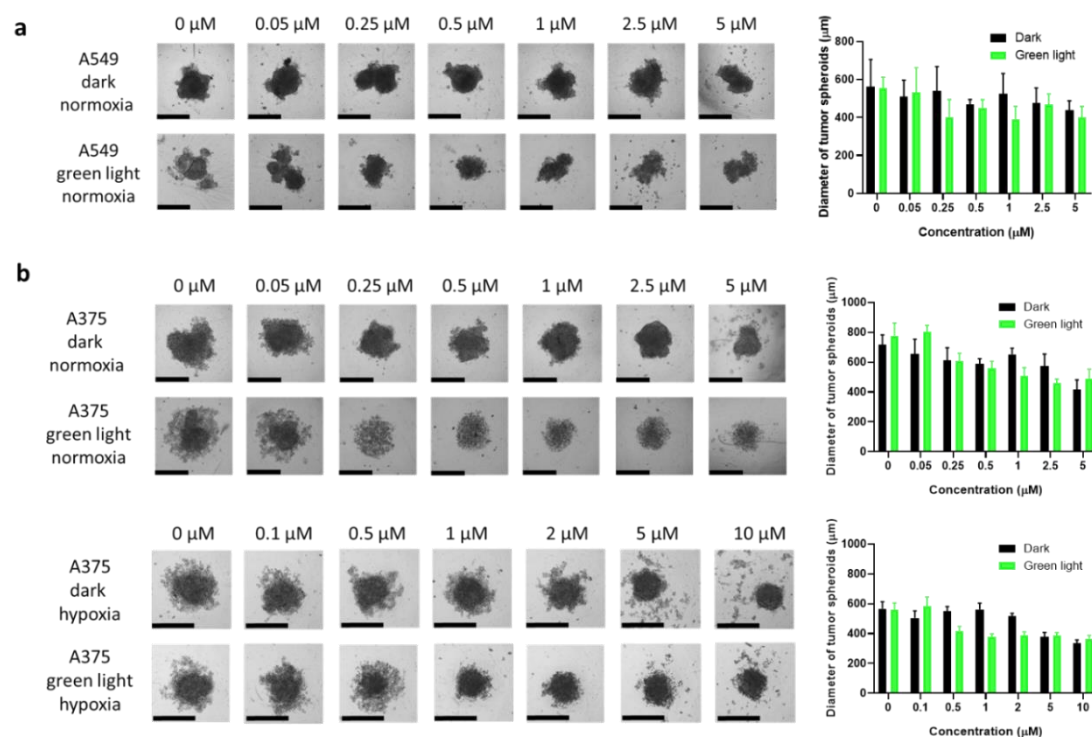


Figure AIV.8 Bright field images (left) and diameter (right, μm) for A549 (a) and A375 (b) 3D tumor spheroids kept in the dark (black bars) or irradiated with green light (green bars, 520 nm, 13 J/cm²). Scar bar 500 μm .

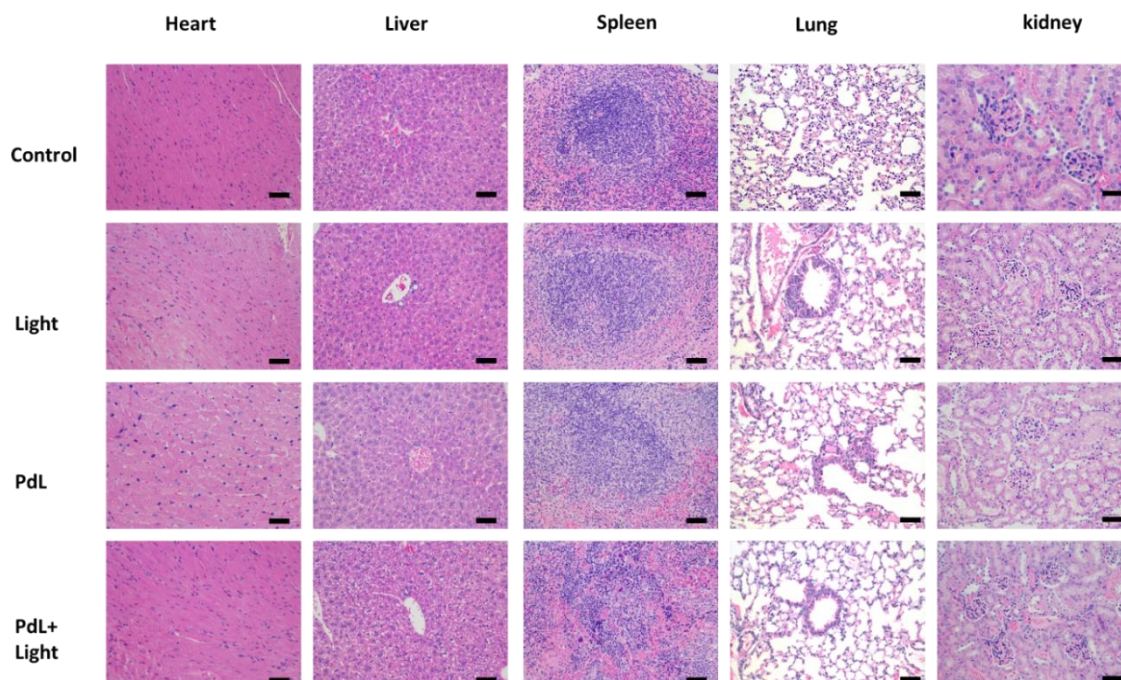


Figure AIV.9 The H&E staining of different mice organs after treatment with vehicle control or **PdL**, and either without or with green light irradiation (100 mW/cm², 10 min, 60 J/cm²). Scale bar 200 μm .

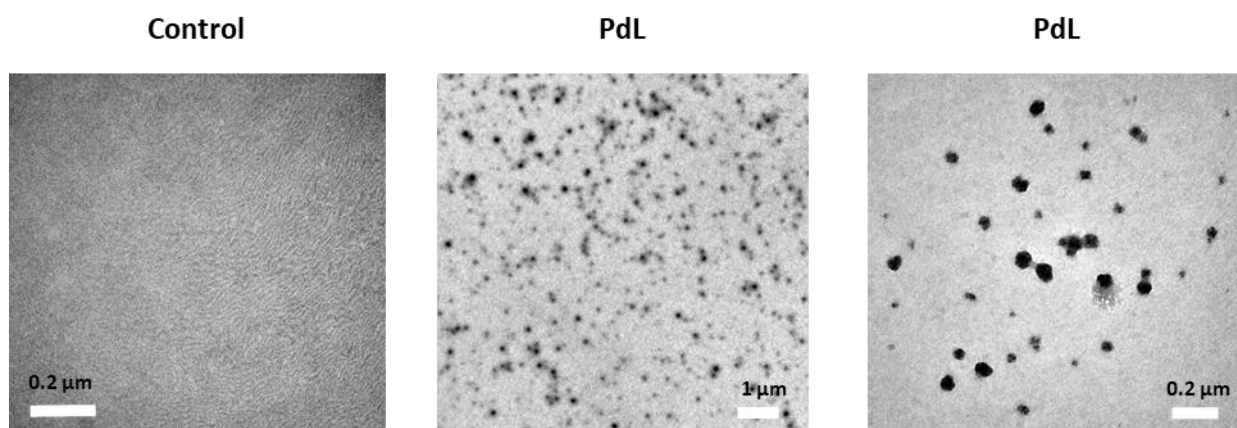
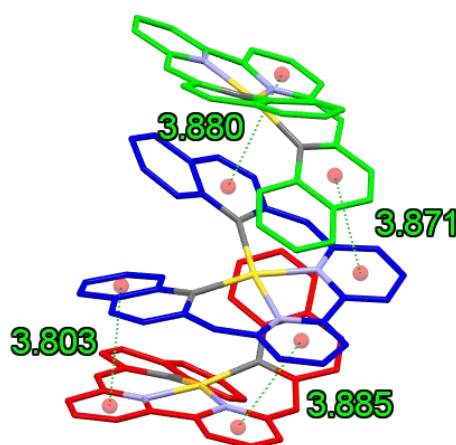


Figure AIV.10 EM images showing the morphology of nanoparticles found in the blood of mice 12 h after intravenous tail injection of **PdL** (middle and right images), or in an untreated control mice (left image). Injection dose: 2.1 μmol/kg, 0.9 mg/kg, 420 μM, 100 μL saline.

APPENDIX V SUPPORTING INFORMATION FOR CHAPTER 6

Table AV1. The selected bond distances (Å) and angels (°) of [1]Cl and [2]AuCl₄.

[1]Cl		[2]AuCl ₄	
Au-C28	2.030(7)	Au-N3	1.995(18)
Au-N3	2.046(6)	Au-N6	2.00(2)
Au-N4	2.050(6)	Au-N4	2.002(16)
Au-C1	2.060(5)	Au-N1	2.081(18)
C28-Au-N3	166.6(6)	N3-Au-N6	167.2(13)
C28-Au-N4	92.7(3)	N3-Au-N4	81.4(6)
N3A Au-N4A	81.5(3)	N6-Au-N4	93.2(9)
C28-Au-C1	96.5(3)	N3-Au-N1	88.8(9)
N3-Au-C1	91.3(3)	N6-Au-N1	99.0(7)
N4-Au-C1	166.9(4)	N4-Au-N1	163.0(13)

**Figure AV1.** The crystal packing structure of [1]Cl with the intermolecular π - π stacking distance. The H and counterions were omitted for clarity.**Table AV2.** The TDDFT singlet-singlet transitions calculation information of gold complexes.

Complex	Energy (nm)	Energy (eV)	Oscillator strength (f)	Orbital transition contribution
[1] ⁺	451	2.7451	0.2282	97.4% HOMO→LUMO
	370	3.3471	0.1146	95.6% HOMO-1→LUMO
	694	1.7863	0.0074	97.8% HOMO→LUMO
[2] ⁺	531	2.3334	0.0066	98.1% HOMO-1→LUMO
	469	2.6413	0.1915	95.9% HOMO→LUMO+1

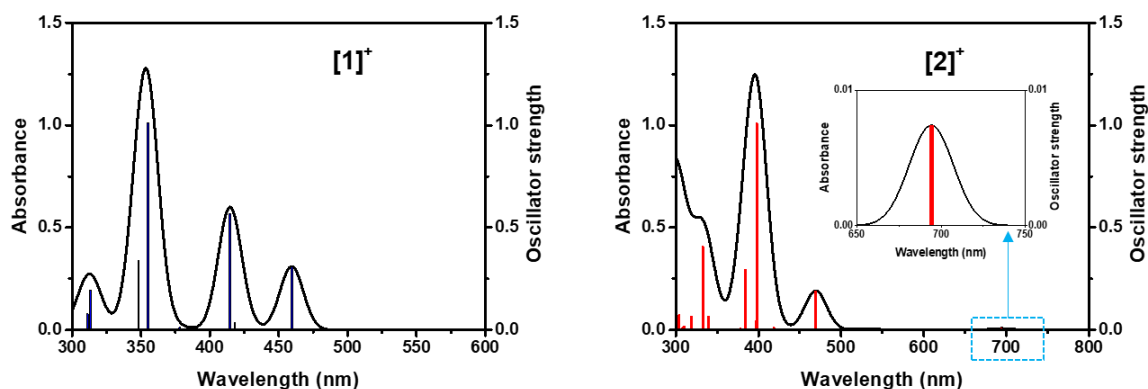


Figure AV2. The TDDFT absorbance peaks and spectra of $[1]^+$ and $[2]^+$.

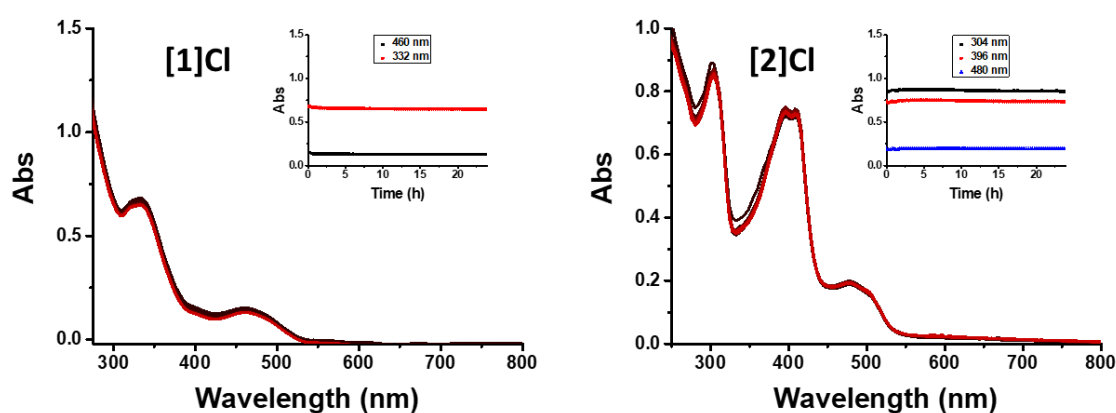


Figure AV3. Time evolution of the absorbance spectrum of $[1]Cl$ and $[2]Cl$ (50 μM) in PBS solution (100 μM) for 24 hours at 37 $^{\circ}C$; measurement interval 15 min, color changes from black (0 s) to red (24 h).

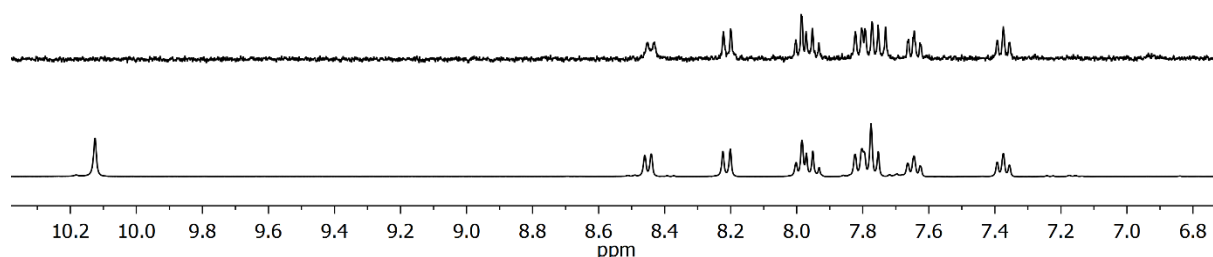


Figure AV4. 1H NMR of the precipitate formed after 24 h of incubation of compound $[2]Cl$ (3.0 mM) and GSH (6.0 mM) at a ratio of 1:2 (top) and spectra of $H_2biqbpy_2$ (bottom) added as a reference for peak identification. All spectra were measured in $DMSO-d_6$ at 25 $^{\circ}C$.

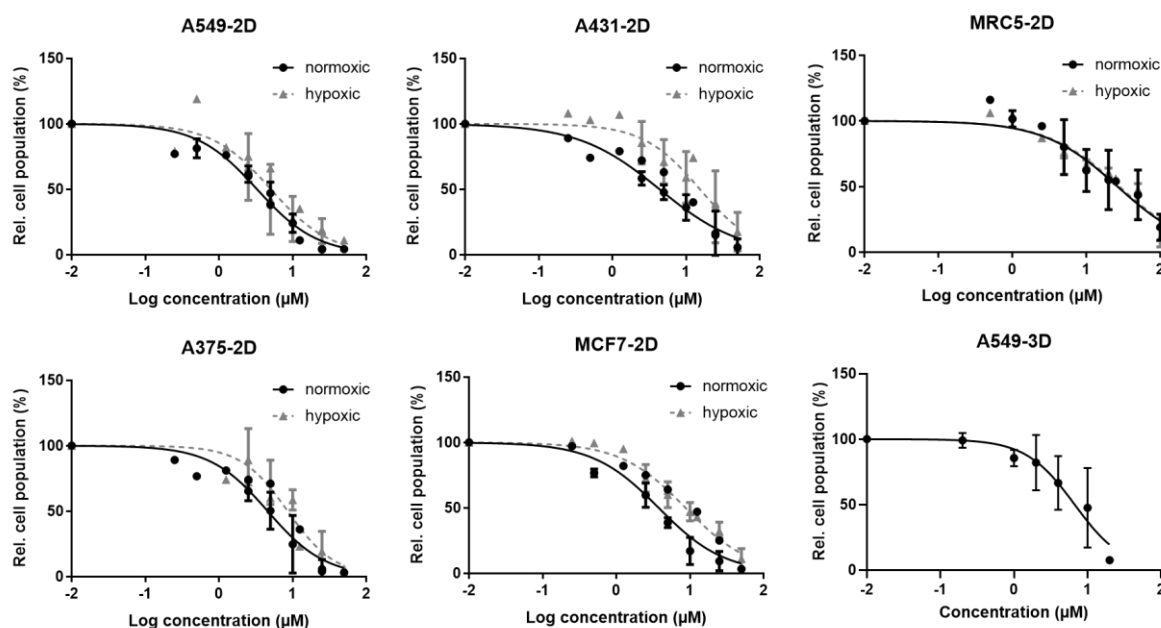


Figure AV5. Dose-response curves for four cancer cells and one healthy skin cells incubated with [1]Cl under normoxic or hypoxic conditions, in the 2D-monolayer or 3D-spheroid model.

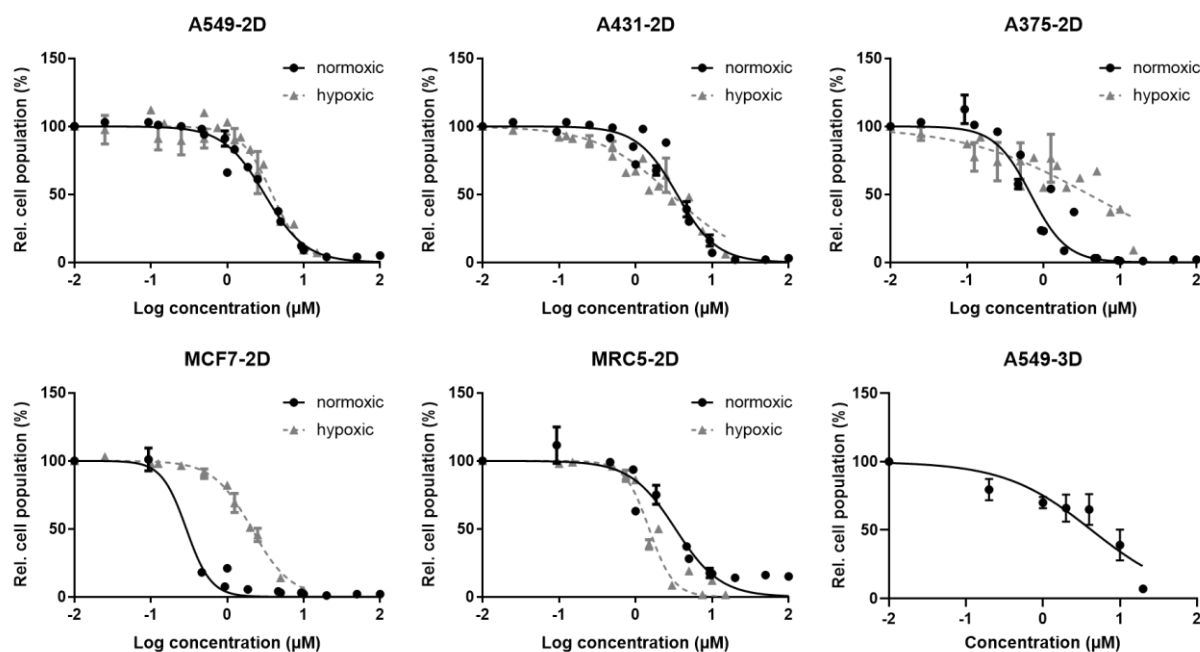


Figure AV6. Dose-response curves for four cancer cells and one healthy skin cells incubated with [2]Cl under normoxic or hypoxic conditions, in the 2D-monolayer or 3D-spheroid model.

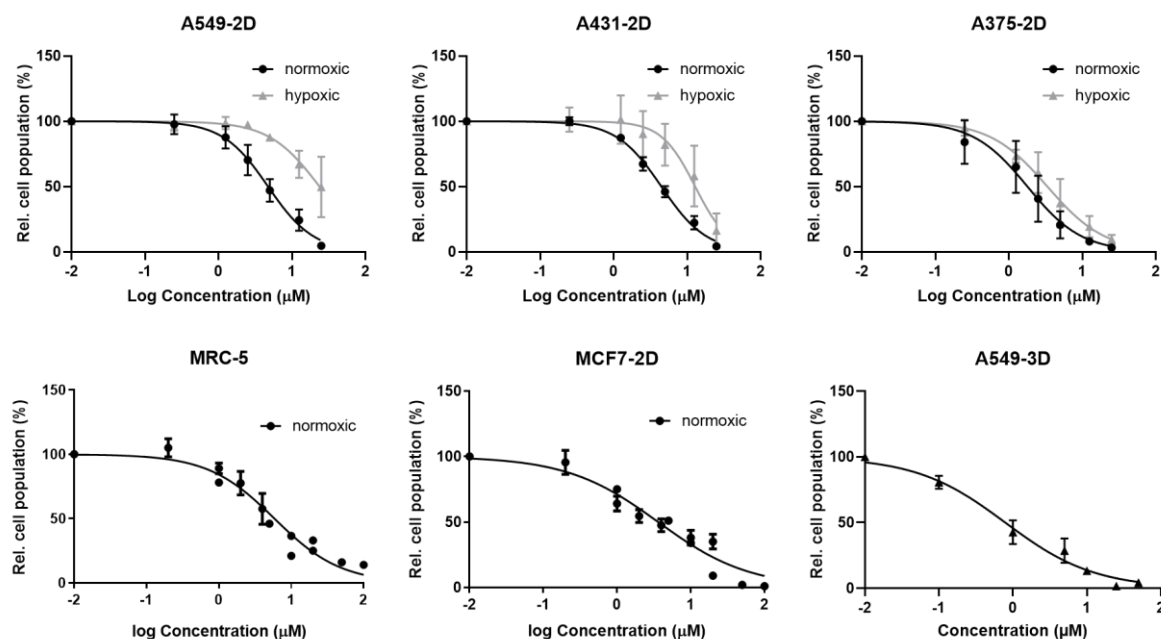


Figure AV7. Dose-response curves for four cancer cells and one healthy skin cells incubated with cisplatin under normoxic or hypoxic conditions, in the 2D-monolayer or 3D-spheroid model.

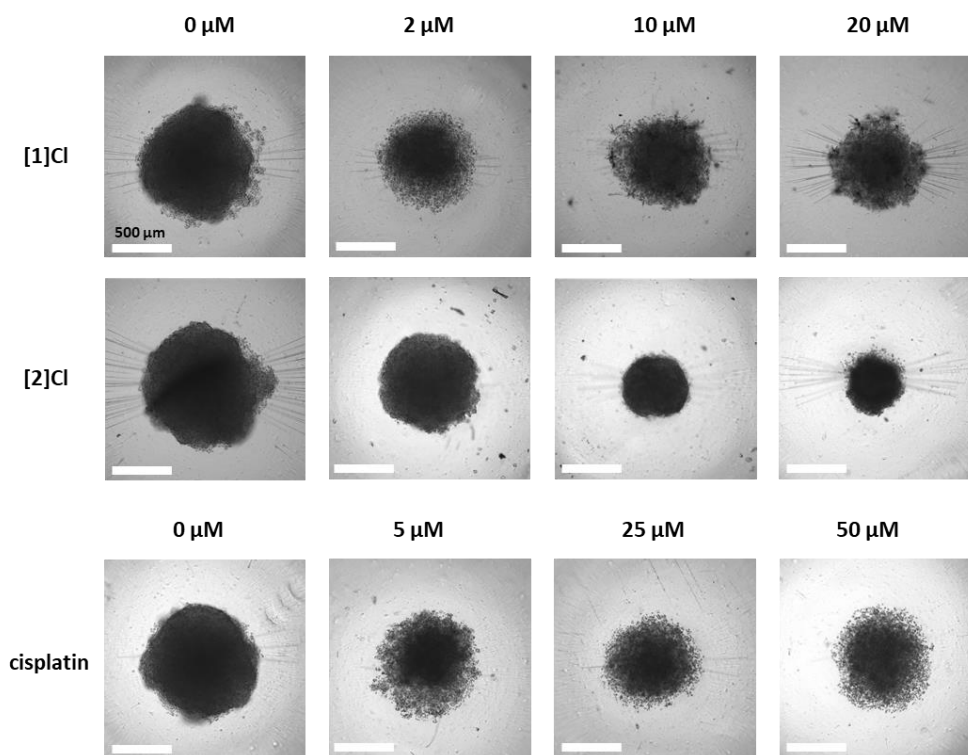


Figure AV8. Bright-field imaging of 3D tumor spheroids treated with gold complexes or vehicle control (DMSO); scale bar is 500 μm . The cells were seeded at $t=0$ (500 cells per well), treated at $t=4$ days, measured (diameter) at $t=7$ days.

SAMENVATTING VAN DIT PROEFSCHRIFT

Wereldwijd is kanker een belangrijke doodsoorzaak. Chemotherapie gebaseerd op kleine moleculen wordt beschouwd als een van de belangrijkste behandelingen om kanker te bestrijden, alhoewel chemotherapeutische behandelingen vaak gepaard gaan met ernstige bijwerkingen. Nanogeneeskunde en fotodynamische therapie (PDT) vertegenwoordigen in dit opzicht opkomende alternatieven, die gericht zijn op het verminderen van de bijwerkingen van de behandeling. Door een rationeel ontwerp kunnen nanodragers de eigenschap hebben om de accumulatie van geneesmiddelen op de locatie van de tumor te verhogen via een verbeterde permeabiliteit- en retentie-effect (EPR), die de systemische cytotoxiciteit van nanogeformuleerde geneesmiddelen verlaagt. PDT is een vorm van door licht geactiveerde antikankerbehandeling met een fotosensibilisator (meestal kleine moleculen), fotonen en molecuulair zuurstof. Deze methode kan selectief de medicijnen in de tumor activeren en zo celdood induceren, terwijl er geen schade wordt aangericht aan de omliggende gezonde, niet bestraalde cellen. Fotosensibilisatoren die bestaan uit kleine moleculen vertonen echter nog steeds enkele van de nadelen van chemotherapie, zoals een lage ophoping in de tumor en snelle verwijdering uit het bloed. Padeliporfin (Tookad®, een klinisch goedgekeurde fotosensibilisator op palladiumbasis) bereikt bijvoorbeeld zijn hoogste plasmaconcentratie in het menselijk lichaam in slechts 5 minuten en wordt vervolgens snel door de nieren afgebroken en afgevoerd. In dit proefschrift zijn PDT en nanogeneeskunde gecombineerd om efficiënte ophoping van fotosensibilisatoren in kankercellen (*in vitro*) of op de tumorplaats (*in vivo*) te bereiken, voordat ze selectief worden geactiveerd doormiddel van bestraling met licht. Wij bieden een alternatief voor de compliceerde synthese en lage reproduceerbaarheid van nanodragers die bestaan uit meerdere componenten, wiens eigenschappen vaak leiden tot lage lading-efficiëntie van geneesmiddelen. Hierdoor kunnen de klinische toepassingen dramatisch beperkt worden, terwijl de verbindingen in preklinische tests veelbelovend leken te zijn. Binnen het onderzoek dat beschreven wordt in dit proefschrift hebben we ons gericht op het ontwerp en de synthese van kleine, moleculaire fotosensibilisatoren op basis van d^8 overgangsmetaalverbindingen van gecyclometalleerde, tetradentate liganden. Verder ontdekten we dat deze moleculen kunnen worden gebruikt om een moleculaire fotosensibilisator-zelfassemblage-nanosysteem (MoPSAN) te ontwikkelen, op basis van de supramoleculaire samenstelling van deze moleculen via metallofiele metaal...metaal (M...M) interacties. Deze nanosystemen vertonen een hoge medicijnbelading, hoge cellulaire opname *in vitro* en hoge

accumulatie in de tumor *in vivo*, en uitstekende anti-kanker PDT effecten zowel *in vitro* als *in vivo*.

In **hoofdstuk 2** beschrijven we twee isomeren van een gecyclometalleerd palladium(II)verbinding en hebben we hun antikanker PDT eigenschappen via verschillende fotofysische en fotobiologische methoden vergeleken. Het eerste isomeer **PdL¹**, met een N[^]N[^]C[^]N-coördinatie, vertoonde een uitstekende kwantumopbrengst van de productie van singletzuurstof (0.89) bij bestraling met blauw licht, wat ook resulteerde in hoge foto-indices bij blauw lichtactivatie van het isomeer in menselijke kankercellen. Daarentegen had het tweede isomeer **PdL²**, gekenmerkt door een N[^]N[^]N[^]C-coördinatie, zowel een lage absorptie-efficiëntie van blauw licht alsook een lage kwantumopbrengst van de vorming van singletzuurstof (0.38), wat *in vitro* een verwaarloosbare activering van **PdL²** door blauw licht opleverde. DFT-berekeningen toonden aan dat de hogere lichtabsorptie in het blauwe gebied van **PdL¹**, en dus de lagere HOMO-LUMO energiekloof, veroorzaakt werd door de kleinere afstand tussen de elektronenrijke, gecyclometalleerde aromatische ring en de stikstofbrug van het ligand, terwijl in **PdL²** beide aromatische ringen naast de aminebrug elektronenarm zijn, waardoor de HOMO-energie lager uitvalt. Deze resultaten tonen aan dat de positie van de koolstof-metaalbinding in de coördinatiesfeer van fotoactieve organometaalprogeneesmiddelen kan worden gebruikt om de energiekloof tussen hun grensorbitalen af te stemmen, en daarmee ook de absorptie in het zichtbare gebied van het spectrum, wat essentieel is in PDT-toepassingen.

De deprotonering van de niet-gecoördineerde NH-brug in de palladiumcomplexen beschreven in **hoofdstuk 2** resulteerde in neutrale metaalcomplexen die onoplosbaar zijn in water, waardoor hun toepassing voor kankerbehandeling *in vivo* beperkt was. In **hoofdstuk 3** beschrijven we de resultaten van methylering van deze aminebrug om dit probleem te vermijden. Drie in water oplosbare analoge palladiumcomplexen werden met succes gesynthetiseerd: twee gecyclometalleerde isomeren [**PdMeL¹**]**OAc** (N[^]N[^]C[^]N coördinatie) en [**PdMeL²**]**OAc** (N[^]N[^]N[^]C coördinatie), en een referentie-tetrapyridylcomplex [**Pd(Mebbpya)**](**OAc**)₂ (N[^]N[^]N[^]N coördinatie). Alle complexen zijn oplosbaar in water. [**PdMeL¹**]**OAc** heeft vergelijkbare fotofysische en fotobiologische eigenschappen als **PdL¹**, maar daarnaast ookeen sterk blauw licht geactiveerd PDT-effect in een muizen-tumor xenotransplantaat, hetgeen een veelbelovend resultaat is voor een palladium-gebaseerde fotosensibilisator voor toepassing in PDT. Opmerkelijk in dit werk is de ontdekking dat cyclometallering van een palladiumcomplex de zelfassemblage van het complex tot nanostaafjes mogelijk maakt via metallofiele Pd...Pd

interacties. Dit proces is verder afhankelijk van de eiwitten in het celmedium waarin de verbindingen opgelost worden. Een belangrijke waarneming is dat endocytose een cruciale rol speelt bij de cellulaire opname van deze aggregaten, wat een hogere cellulaire opname van de gecyclometallegeerde complexen veroorzaakt in vergelijking met conventionele niet-gecyclometallegeerde tetrapyridylverbinding $[\text{Pd}(\text{Mebppy})](\text{OAc})_2$. Er wordt al jaren gedebatteerd over de rol van de eiwitcorona in medicijnafgiftesystemen, maar de eiwitafhankelijke zelfaggregatie van een zelfassemblerend medicijn was nog niet eerder gedocumenteerd. Dit werk laat verder zien dat geneesmiddelen die zichzelf assembleren tot nanostaafjes een uitstekende medicijnpenetratie in 3D-tumormodellen hebben, wat een nieuwe strategie kan opleveren door metallodrugs te combineren met nanogeneeskunde, zoals verder is besproken in **hoofdstuk 5**.

In het onderzoek beschreven in **hoofdstuk 4** is gebruik gemaakt van dezelfde liganden als beschreven in **hoofdstuk 3**, maar is het palladium vervangen door platina. Hierdoor konden we aantonen dat de platina(II)-complexen $[\text{PtMeL}^1]\text{OAc}$ en $[\text{PtMeL}^2]\text{OAc}$ beide sterke metallofile interacties vertoonden, wat ook hier resulteerde in de zelfassemblage van nanoaggregaten in celweekmedium. Hoewel allebei de Pd^{2+} - en de Pt^{2+} -reeksen zelfassemblage vertoonden via metallofile interacties en celafhankelijke cytotoxiciteit vertoonden in het donker, bleken hun fotochemische eigenschappen dramatisch te verschillen. De uitstekende PDT-eigenschappen en verwaarloosbare emissie van de palladiumaggregaten werden in de platinaserie vervangen door slechte PDT-eigenschappen maar wel een naar rood-verschoven absorptie- en dieprode emissie-eigenschappen, waardoor deze aggregaten kunnen worden gebruikt in microscopie in plaats van fototherapie. De verschillende fotochemische eigenschappen van de platina- en de palladiumcomplexen moeten afkomstig zijn vanuit hun verschillende relatieve deactiveringssnelheden van de aangeslagen toestand, zowel in de aggregaten als in de monomere vormen. Fosforescentie en stralingsloze interne conversie naar de singlet grondtoestand zijn kwantumchemisch verboden processen die sterk afhankelijk zijn van spin-baan koppeling, die sterker is voor platina(II)- dan voor palladium(II)-ionen. Over het algemeen is de Pt(II) $5d_z^2$ -orbitaal hoger in energie dan de Pd(II) $4d_z^2$ -orbitaal, wat ertoe leidt dat Pt(II) een sterkere invloed vertoont dan Pd(II) op de moleculaire grensorbitalen, de efficiëntie van intersysteemovergang, en de $T^1 \rightarrow S^0$ stralingsverval, waardoor de platinacomplexen een intensere fosforescentie krijgen. Deze fosforescentie, gelegen in het dieprode gebied van het spectrum, stelde ons in staat de opname en lokalisatie van deze supramoleculaire nanodeeltjes in cellen te bestuderen. Zo werd er gevonden dat in A549-cellen

de dieproud-emitterende nanoaggregaten van **[PtMeL₂]OAc** zich in de mitochondriën ophopen, wat ook werd bevestigd door elektronenmicroscopie vanwege de hoge elektronendichtheid van platinaverbindingen. Over het geheel genomen toonde deze reeks polypyridyl-platinacomplexen nieuwe perspectieven bij het gebruik van de metallofiele interacties om supramoleculaire nanosystemen te bouwen die, bij hoge concentratie, kankercellen kunnen doden, maar bij lage concentratie kunnen worden gebruikt als dieprode kleurstoffen voor verschillende organellen, in dit geval de mitochondriën.

In **hoofdstuk 5** beschrijven we een bis-gecyclometalleerd palladiumcomplex, **PdL³**, dat het niet alleen mogelijk maakte om de absorptie van het complex verder te verschuiven naar langere golflengten, maar ook om de lading verder te verlagen zodat er een neutraal complex gevormd wordt met sterke Pd...Pd interacties. Er werd verder aangetoond dat **PdL³** zichzelf assembleert als nanoaggregaten in celkweekmedium, maar ook verbeterde PDT-eigenschappen heeft in vergelijking met het mono-gecyclometalleerde complex **PdL¹**. Naast het feit dat deze verbinding geactiveerd kan worden met groen licht in plaats van blauw licht, als gevolg van de verdere destabilisatie van de HOMO door de tweede Pd-C binding, bleek het ook bijzonder cytotoxisch onder zuurstofarme omstandigheden, met fotoindices tot en met 70 in huidmelanoomcellijnen.

Deze uitstekende reactiviteit was te danken aan een PDT type I mechanisme, dat minder afhankelijk is van de zuurstofconcentratie dan PDT type II. **PdL³** diende als een “proof-of-concept” voor het MoPSAN-concept, waarbij een PDT-fotosensibilisator zichzelf assembleert tot tumorgerichte nanostructuren *in vivo* met behulp van het EPR-effect. Dicht opelkaarzittende nanodeeltjes werden gevonden met elektronenmicroscopie (EM) in plasma na intraveneuze injectie van het complex in muizen, wat aantoont dat zelfassemblage in biologische omstandigheden optreedt. Vervolgens toonden ICP-OES metingen significante ophoping van **PdL³** in de tumor aan, met een uitzonderlijke hoge medicijnafgifte tot 10.2% ID/g. EM-beelden van tumorplakjes bewezen opnieuw de accumulatie van zelf-geaggregeerde nanodeeltjes van **PdL³** in de solide tumor. Op basis van deze resultaten concluderen we dat de supramoleculaire metallofiele Pd...Pd interactie een hoog potentieel heeft om 1) supramoleculaire nanodragers te bouwen met verbeterde ophoping in de tumor via het EPR-effect, en 2) PDT-fotosensibilisatoren te genereren die hun fototoxische eigenschappen behouden onder zuurstofarme omstandigheden.

Ten slotte rapporteren we in **hoofdstuk 6** de chemie van gecyclometalleerde Au(III)-verbindingen. Hoewel Au(III) en Pt(II) iso-elektronisch zijn, hebben ze verschillende

eigenschappen vanwege de hogere lading en elektronegativiteit van Au(III) (2.4 voor Au en 2.2 voor Pt). Over het algemeen verlaagt cyclometallering in polypyridyl-metaalcomplexen hun moleculaire lading in vergelijking met conventionele stikstofcoördinatie, hierdoor wordt de lipofiliciteit van deze verbindingen danook aanzienlijk beïnvloedt. Zoals besproken is in **hoofdstuk 2**, beweren veel publicaties dat de hogere lipofiliciteit van gecyclometallegeerde complexen de cellulaire opname stimuleert via passieve transportatie door het celmembraan, wat kan leiden tot betere therapeutische effecten bij lagere doses van een verbinding, maar dat dit ten koste gaat van de kankerselectiviteit. Verder stabiliseert cyclometallering de Au(III)-oxidatietoestand, waardoor deze goudverbindingen minder snel worden gereduceerd door biologische thiolgroepen als ze het cytosol hebben bereikt. We onderzochten de coördinatie van een aantal tetrapyridylliganden met goud(III)-ionen en in **hoofdstuk 6** beschrijven we de toevallige ontdekking dat een van deze liganden bij voorkeur aan het Au(III)-centrum bindt via 'rollover cyclometallation' waarbij een bisgecyclometallegeerd goud(III)-complex **[Au(biqbpy1)]Cl** ($C^+N^+N^+C$) gevormd wordt, terwijl het andere ligand coördineert met vier stikstofatomen om het traditionele tetrapyridylcomplex **[Au(biqbpy2)]Cl** ($N^+N^+N^+N$) te vormen. Interessant is dat beide kationische complexen een lading van 1+ hebben, wat veroorzaakt wordt doordat de bruggende amines in **[Au(biqbpy2)]⁺** gedeprotoneerd zijn, in tegenstelling tot de bisgecyclometallegeerd verbinding **[Au(biqbpy1)]⁺** waarin de aminebruggen geprotoneerd bleven. Deze twee verbindingen bieden daarom de unieke mogelijkheid om gecyclometallegeerde versus niet-gecyclometallegeerde Au(III)-complexen te vergelijken zonder de algehele lading van het complex te veranderen. We ontdekten dat de roll-over gecyclometallegeerde verbinding **[Au(biqbpy1)]Cl** zeer stabiel is in reducerende biologische omstandigheden, maar dat het ook nanodeeltjes vormt in celmedium, waardoor het een 6-voudige efficiëntere opname in A549-kankercellen had dan de tetrapyridylverbinding **[Au(biqbpy2)]Cl**, die geen nanodeeltjes vormde maar eerder reductie ondergaat in celweekmedium.

De identieke lading maar verschillende aggregatie-eigenschappen van **[Au(biqbpy1)]Cl** en **[Au(biqbpy2)]Cl** bieden een nieuw perspectief op de verbeterde cellulaire opname van gecyclometallegeerde goudcomplexen. Zoals duidelijk is aangetoond voor de Pd(II)- en Pt(II)-gecyclometallegeerde complexen beschreven in eerdere hoofdstukken van dit proefschrift, kunnen deze nano-aggregaten actief transport activeren, zoals endocytose, wat doorgaans efficiënter is dan passief transport. Bovendien is **[Au(biqbpy1)]Cl** stabiel in biologische omstandigheden en vertoonde het daarom een verminderde TrxR-remming in vergelijking met

[Au(biqbpy2)]Cl, die bij intracellulaire reductie de bekende TxrR-remmende Au^+ als vrije ionen vrijgaf. De resulterende cytotoxiciteit in kankercellen was lager voor **[Au(biqbpy1)]Cl** dan voor **[Au(biqbpy2)]Cl**, maar de toxiciteit bij niet-kankercellen was ook relatief veel lager, waardoor de selectiviteit voor kankercellen hoger was dan **[Au(biqbpy2)]Cl**. Ondertussen vertoonden beide complexen een vergelijkbaar hoog kaliumkanaalbindend vermogen, wat mogelijk toegeschreven zou kunnen worden aan hun identieke lading en vergelijkbare moleculaire vorm. Hun kaliumkanaalbindingsvermogen was ook hoger dan dat van de losse tetrapyridyliganden, wat suggereert dat metaalcomplexering een alternatieve methode zou kunnen zijn om de kaliumkanaalactiviteit met behulp van kleine moleculen te reguleren. Al met al leverde de vergelijking van deze isomeren, vanuit chemisch en biologisch oogpunt, nieuwe inzichten op met betrekking tot het gebruik van cyclometallering bij het ontwerp voor geneesmiddelen om de balans tussen stabiliteit, aggregatie, toxiciteit en eiwitremming van goud(III) antikanker complexen te verbeteren.

In het kort, de resultaten die in dit proefschrift worden beschreven overbruggen de gebieden van metallomedicijnen tegen kanker, fotodynamische therapie, celbeeldvorming, luminescerende materialen en nanogeneeskunde. Door gebruik te maken van cyclometallering en de supramoleculaire metallofiele M...M interactie, was het mogelijk om de fantastische impact aan te tonen die metaalcomplexen kunnen hebben op de ontwikkeling van toekomstige antikankermedicijnen en nanomaterialen.

总结

金属配合物 (metal complex) 用于疾病治疗由来已久。其中, 顺铂作为第一代金属基抗癌药物 (anticancer metallodrug) 已经被临床应用于治疗众多类型的癌症。但是其较强的副作用和体内不稳定性等缺点, 促使科学工作者进一步开发低毒副作用、高治疗效果的新型金属基抗癌药物。近些年来, 光动力疗法 (photodynamic therapy, PDT) 与光敏剂 (photosensitizer, PS) 的结合为这一方向带来了大量新的突破。简而言之, 光可以激发金属配合物, 使其达到三线态激发态, 从而与基态氧气反应生成单线态氧 ($^1\text{O}_2$), 或者与细胞内的生物大分子反应生成一些活性氧物种 (reactive oxygen species), 这两类物质都对细胞有巨大毒性。通过控制光照的位置, 实现黑暗条件下的低毒性以及光照后的高毒性, 可以达成物理层面的靶向性, 从而定点杀伤肿瘤部位。

本篇毕业论文第二章, 即设计合成了两个钯金属配合物异构体 (PdL^1 , PdL^2)。它们的特点在于两者都为环金属化合物 (cyclometalated complex), 即具有一个钯-碳键 (Pd-C), 可以使得金属配合物在生理条件下更加稳定, 不易被降解。研究发现它们产生单线态氧的能力大不相同, 导致只有 PdL^1 有较好的蓝光激发的 PDT 效果。这一差异可归结于 Pd-C 键位置的不同导致其吸收光谱的变化。本章节建立了钯金属配合物光敏剂的基本结构框架, 推动了后续章节的发展。

第三章, 我们对第二章所述的两个钯配合物进行了甲基化, 稳定其价态在+1, 配以羧酸根, 得到两个具有良好的水溶性的环钯金属配合物异构体 $[\text{PdMeL}^1]\text{OAc}$ 和 $[\text{PdMeL}^2]\text{OAc}$ 。与此同时, 我们设计合成出它们的多吡啶配位的类似物 $[\text{PdMebbpya}](\text{OAc})_2$ 。比较发现, $[\text{PdMeL}^1]\text{OAc}$ 和 $[\text{PdMeL}^2]\text{OAc}$ 具有超分子钯-钯相互作用 (Pd...Pd interaction), 即它们分子间的钯与钯之间的距离较短 (小于 0.4 纳米), 可发生 d_z^2 轨道间的重叠, 而 $[\text{PdMebbpya}](\text{OAc})_2$ 没有这一特性。进一步研究发现, 在细胞培养液中, 前两者可以发生自组装 (self-assembly) 生成纳米棒并被血清蛋白稳定住, 而后者只能以单分子的形式在溶液中存在。生成的纳米棒进一步刺激了细胞以更高效的内吞作用摄入两个环钯金属配合物, 而 $[\text{PdMebbpya}](\text{OAc})_2$ 只能以比较低效的扩散作用的形式进入细胞。细胞实验证实, $[\text{PdMeL}^1]\text{OAc}$ 依旧具有可被蓝光激发的光动力抗癌疗效, 在小鼠实验中也具有良好的抗肿瘤活性。本章首次证实环钯配合物可以通过自组装形式促进其被细胞吸收, 并结合光动力疗法, 获得在小鼠层面的较好抗癌效果。

在第四章中，我们使用与第三章相同的配体（ligand），合成了两个环铂金属配合物 $[\text{PtMeL}^1]\text{OAc}$ 和 $[\text{PtMeL}^2]\text{OAc}$ 。它们同样具有铂-铂相互作用（Pt...Pt interaction），可在细胞培养液中发生自组装行为并通过内吞作用高效进入癌细胞中。有趣的在于，这两个铂配合物并不具备光动力疗效，却有长寿命的深红区细胞成像（long-time deep-red cell imaging）的功能。通过共聚焦显微镜（confocal microscopy），我们证实 $[\text{PtMeL}^2]\text{OAc}$ 可用于线粒体染色剂。细胞电镜（cell-TEM）实验直观证实了 $[\text{PtMeL}^2]\text{OAc}$ 可在线粒体中以纳米粒的形式存在。结合各类细胞摄入抑制实验，暗示了 $[\text{PtMeL}^2]\text{OAc}$ 是以一种不同寻常的内吞途径进入线粒体的。一般而言，纳米粒通过内吞作用跨过细胞膜后，会进入溶酶体中，然后通过溶酶体逃逸再进入细胞质，随后进入特定的细胞器中。然而 $[\text{PtMeL}^2]\text{OAc}$ 却是通过发动蛋白通道进入细胞形成囊泡，此囊泡可直接进入线粒体，并不需要溶酶体的帮助。于此，本章开发出一个基于铂-铂相互作用的深红区线粒染色剂，并首次明确证明铂-铂相互作用可以让金属配合物以纳米粒的形式存在于细胞，从而将纳米医学、配位化学与细胞成像一同联系起来。

我们基于第二章的工作，在第五章进一步优化，合成出具有两个钯-碳键的环钯金属配合物 PdL^3 。该配合物同样有由钯-钯相互作用诱导的自组装行为，在常氧、厌氧、3D 肿瘤与活体实验上均表现出优异的绿光激发的光动力疗效。与此同时，我们分析了 PdL^3 在小鼠中的脏器分布情况和肿瘤处的摄入效率与形貌。研究发现 12 小时后，该药物在肿瘤有很好的富集率（10.2% ID/g），远高于目前的纳米药物递送系统的平均效率（0.7% ID/g）。生物电镜实验也进一步证实它以纳米粒的形式存在于小鼠肿瘤部位。我们认为，分子光敏剂容易合成，结构确定，使得其具有良好的可重复性。与此同时，由其自组装形成的纳米粒可认为有近乎 100% 的药物负载率（传统纳米药物递送系统负载率低于 20%），再加上光敏剂的光动力疗效，三者结合，我们提出一个简单易操作的纳米概念，即分子光敏剂自组装纳米体系（molecular photosensitizer self-assemble nanosystems, MoPSAN）。

第六章，不同于前五章，我们开发出两个金配合物异构体 $[\text{Au}(\text{biqbpy}1)]\text{Cl}$ 和 $[\text{Au}(\text{biqbpy}2)]\text{Cl}$ 。前者为环金配合物，有两个金-碳（Au-C）键和两个金-氮（Au-N）键。后者是多吡啶金配合物，有四个金-氮（Au-N）键。研究表明， $[\text{Au}(\text{biqbpy}1)]\text{Cl}$ 在生理条件下高度稳定，对含硫生物分子不敏感，在细胞培养液中可生成纳米粒。而 $[\text{Au}(\text{biqbpy}2)]\text{Cl}$ 容易被含硫生物分子还原，解离生成 Au^+ 离子和单独的配体。蛋白层

面的实验表明，两个金属配合物及其配体均可作为钾离子通道的锁定剂， $[\text{Au}(\text{biqbpy}2)]\text{Cl}$ 还可以作为硫氧还蛋白还原酶的抑制剂。细胞毒性实验表明， $[\text{Au}(\text{biqbpy}1)]\text{Cl}$ 可选择性的杀伤癌细胞，对正常细胞的毒性较低；而 $[\text{Au}(\text{biqbpy}2)]\text{Cl}$ 对癌细胞和正常细胞均具有较强的毒性。本章通过比较具有近似结构的同分异构体，探讨它们在蛋白层面和细胞层面的生物活性，拓展了金配合物的生物学应用。

总而言之，本篇毕业论文通过合理设计，开发出一系列金属基药物，并将它们成功应用在癌症治疗和细胞成像上。与此同时，通过引入了金属-金属相互作用，将配位化学、生物无机化学、超分子化学、纳米医学和光动力疗法有机结合起来，提出了分子光敏剂自组装纳米体系（MoPSAN）这一概念，有待后续的研究和发展。

LIST OF PUBLICATIONS

Published:

1. **Xue-Quan Zhou**, M. Xiao, V. Ramu, J. Hilgendorf, X. Li, P. Papadopolou, M. A Siegler, A. Kros, Wen Sun*, Sylvestre Bonnet*, “The self-assembly of a cyclometalated palladium photosensitizer into proteins-stabilized nanorods triggered drug uptake *in vitro* and *in vivo*.” *J. Am. Chem. Soc.* 142.23 (2020): 10383–10399. (*Front cover*)
2. **Xue-Quan Zhou**, A. Busemann, M. S Meijer, M. A Siegler, Sylvestre Bonnet*, “The two isomers of a cyclometalated palladium sensitizer show different photodynamic properties in cancer cells.” *Chem. Comm.* 55.32 (2019): 4695-4698.
3. **Xue-Quan Zhou**, Y. Li, D.-Y. Zhang, Y. Nie, Z.-J. Li, W. Gu, X. Liu, Jin-Lei Tian*, S.-P. Yan, “Copper complexes based on chiral Schiff-base ligands: DNA/BSA binding ability, DNA cleavage activity, cytotoxicity and mechanism of apoptosis.” *Eur. J. Med. Chem.* 114 (2016): 244-256.
4. **Xue-Quan Zhou**, Q. Sun, J.-L. Tian, S.-P. Yan, “The synthesis and application of mononuclear copper complexes.” P.R. China, Patent, CN103788118A, 2016. (in Chinese)
5. **Xue-Quan Zhou**, Q. Sun, L. Jiang, S.-T. Li, W. Gu, Jin-Lei Tian*, X. Liu, S.-P. Yan, “Synthesis, characterization, DNA/BSA interactions and anticancer activity of achiral and chiral copper complexes.” *Dalton Trans.* 44.20 (2015): 9516-9527.
6. Yue Liu, **Xue-Quan Zhou***, J. Lu, S.-T. Li, Y. Nie, Jin-Lei Tian*, X. Liu, S.-P. Yan, “Biological evaluation of rare earth complexes bearing 1H-imidazo [4,5-f]-1,10-phenanthroline moiety as promising anticancer chemotherapeutics.” *Appl. Organomet. Chem.* 32.12 (2018): e4617.
7. Anja Busemann, C. Araman, I. Flaspohler, A. Pratesi, **Xue-Quan Zhou**, V. HS van Rixel, M. A Siegler, L. Messori, S. I van Kasteren, S. Bonnet*, “Alkyne functionalization of a photoactivated ruthenium polypyridyl complex for click-enabled serum albumin interaction studies.” *Inorg. Chem.* 59.11 (2020): 7710–7720.
8. Quanchi Chen, V. Ramu, Y. Aydar, A. Groenewoud, **Xue-Quan Zhou**, M. J Jager, H. Cole, C. G Cameron, Sherri A McFarland*, Sylvestre Bonnet*, B Ewa Snaar-Jagalska*, “TLD1433 photosensitizer inhibits conjunctival melanoma cells in zebrafish ectopic and orthotopic tumour models.” *Cancers*, 12.3 (2020): 587.

Under review:

1. **Xue-Quan Zhou**, I. Carbó-Bagué, M. A. Siegler, J. Hilgendorf, U. Basu, I. Ott, R. Liu, L. Zhang, V. Ramu, A. P. IJzerman, Sylvestre Bonnet*, “Rollover cyclometalation vs. nitrogen coordination in tetrapyridyl anticancer gold(III) complexes: effect on protein interaction and toxicity.” *JACS Au*.
2. **Xue-Quan Zhou**, M. Mytiliniou, J. Hilgendorf, Y. Zeng, P. Papadopoulou, Y. Shao, E. Bos, M. A. Siegler, F. Buda, A. Kros, R. I. Koning, D. Heinrich, Sylvestre Bonnet*, “Intracellular dynamic assembly of deep-red emitting supramolecular nanostructures based on the Pt...Pt metallophilic interaction”, *Advanced Materials*.

Manuscript in preparation:

1. **Xue-Quan Zhou**, Wen Sun*, P. Wang, V. Ramu, S. Jiang, S. Abyar, P. Papadopoulou, Y. Shao, M. A. Siegler, F. Buda, A. Kros, Sylvestre Bonnet*, “Self-assembling cyclopalladated photosensitizers for photodynamic therapy: aggregation, tumor accumulation, and anti-tumor activity in a skin melanoma xenograft”.
2. **Xue-Quan Zhou**, I. Carbó-Bagué, M. A. Siegler, G. Bigliardi, O. King, U. Basu, I. Ott, R. Liu, A. P. IJzerman, Sylvestre Bonnet*, “Thiol-activated anticancer tetrapyridyl gold(III) complexes for lysosome imaging and protein regulation”.
3. **Xue-Quan Zhou**, M. A. Siegler, Sylvestre Bonnet*, “Tuning emission spectra of biscyclometalated platinum complexes by changing the position of metal-carbon bond”.
4. **Xue-Quan Zhou**, L. Roeleveld, M. A. Siegler, Sylvestre Bonnet*, “The anticancer activity and mechanism of tetrapyridyl palladium complexes”.

CURRICULUM VITAE

Xuequan Zhou was born in Xianning, Hubei Province, China on 11th February 1992. However, the registered birthday is 1st February 1990 for a historical reason. In 2009, he graduated from Xianning High School and was admitted to Nankai University located at Tianjin. He received his Bachelor (2013) and Master (2016) degree in Chemistry from Nankai University. His master thesis was entitled: “Studies on the synthesis and anticancer ability of metal complexes with Schiff-base and acylhydrazone ligands”. During his MSc studies, he obtained the awards of “Excellent Graduate in Nankai University”, “Excellent Thesis in Nankai University” and “China National Scholarship for Postgraduate”.

With a scholarship from the Chinese Scholarship Council (CSC), he started his PhD studies in September 2016, under the supervision of Prof. Sylvestre Bonnet and Prof. Elisabeth Bouwman in the group of Metals in Catalysis, Biomimetics & Inorganic Materials (MCBIM) at the Leiden Institute of Chemistry, Leiden University. During his PhD studies, he collaborated with Dr. Wen Sun (Dalian University of Technology), Dr. Maxime A. Siegler (Johns Hopkins University), Prof. Ingo Ott (Technische Universität Braunschweig), Prof. Alexander Kros (Leiden Institute of Chemistry), Dr. Roman I. Koning (Leiden University Medical Center), Prof. Doris Heinrich (Fraunhofer Institute for Silicate Research ISC) and Prof. Adriaan P. IJzerman (Leiden Academic Centre for Drug Research). In total, he supervised three MSc and two BSc students and one first-year chemistry lab course. During his PhD research, he followed the two courses “HRSMC Physical Methods in Inorganic Chemistry” and “Graduate School Course of Leiden University: Scientific Conduct”, as well as the autumn school on “HRSMC Advanced Metal-Organic Chemistry and Catalysis”.

He presented parts of the research described in this PhD thesis at the following conferences:

Poster presentations

- Chemistry as Innovating Science (CHAINS), 2016, Veldhoven, The Netherlands
- Chemistry as Innovating Science (CHAINS), 2017, Veldhoven, The Netherlands
- Holland Research School of Molecular Chemistry (HRSMC) Symposium, 2018, Leiden, The Netherlands
- Reedijk Symposium, 2018, Leiden, The Netherlands

Oral presentations

- 25th Anniversary Symposium of the Holland Research School of Molecular Chemistry (HRSMC), 2019, Amsterdam, The Netherlands

- 8th International Meeting of the Institute of Metal in Biology of Grenoble, 2019, Grenoble, France
- 2020 Chemistry as Innovating Science online conference (CHAINS), The Netherlands

ACKNOWLEDGMENT

First of all, the Chinese Scholarship Council (CSC) is acknowledged for a personal grant (No. 201606200045). Dr. Anja Busemann (Leiden Institute of Chemistry) is thanked for her training me on cell culture (Chapter 2). Dr. Michael S Meijer (Leiden Institute of Chemistry) is thanked for singlet oxygen quantum yield measurements (Chapter 2). Dr. Maxime A Siegler (Johns Hopkins University) is kindly thanked for the resolution of all X-ray crystal structures shown in this work (Chapter 2-6). Ming Xiao, Dr. Xuezhao Li and Dr. Wen Sun (Dalian University of Technology) are gratefully acknowledged for performing the *in vivo* experiments presented in this thesis (Chapter 2 and 5). Dr. Vadde Ramu (Leiden Institute of Chemistry) is thanked for part of *in vitro* works (Chapter 2 and 5). Panagiota Papadopoulou and Prof. Alexander Kros (Leiden Institute of Chemistry) are kindly thanked for cryogenic electron microscopy (Cryo-EM) measurements (Chapter 2-4). Maria Mytiliniou and Prof. Doris Heinrich (Leiden Institute of Physics) are thanked for real-time confocal cell imaging (Chapter 4). Ye Zeng (Leiden Institute of Chemistry) is thanked for cellular uptake inhibition experiment (Chapter 4). Yang Shao and Dr. Francesco Buda (Leiden Institute of Chemistry) are thanked for computational modeling (Chapter 4-5). Erik Bos and Dr. Roman I. Koning (Leiden University Medical Center) are acknowledged for cell-EM imaging (Chapter 4). Suhua Jiang and Dr. Peiyuan Wang (Fujian Institute of Research on the Structure of Matter, Chinese Academy of Sciences) are thanked for biological EM in tissues (Chapter 5). Selda Abyar is thanked for performing FACS experiments (Chapter 5). Dr. Uttara Basu and Prof. Ingo Ott (Technische Universität Braunschweig) are thanked for TrxR protein inhibition experiments (Chapter 6). Liyan Zhang (Leiden Institute of Chemistry) is thanked for part of *in vitro* experiments (Chapter 6). Dr. Rongfang Liu and Prof. Adriaan P. IJzerman (Leiden Academic Centre for Drug Research) are acknowledged for potassium channel binding assays. Dr. Karthick Sai Sankar Gupta and Fons Lefeber (Leiden Institute of Chemistry) are gratefully thanked for their assistance with NMR measurements. Hans van der Elst (Leiden Institute of Chemistry) is thanked for HR-MS measurements. Dr. Sipeng Zheng is kindly thanked for the ESI-MS and ICP-MS measurements. Corjan van de Griend is kindly thanked for his help in writing the Dutch summary. Supervised students Imma Carbó-Bagué, Jonathan Hilgendorf, Oliver King, Giulia Bigliardi and Lucas Roeleveld are gratefully thanked for their contributions to this thesis. Chengyu Liu, Shengxiang Yang, Liyan Zhang, Mengjie Shen, Yang Shao, Chunmiao Ye, Ye Zeng, Wanbin Hu, Selda Abyar, Yurong Chen, Dr. Feng Jiang, Dr. Lin Jiang, Dr. Vadde Ramu, Dr. Anja Busemann, Dr. Vincent

van Rixel, Dr. Andrea Pannwitz, Dr. Michael S Meijer and the whole MCBIM group members are gratefully acknowledged for the general and scientific discussion. The Leiden China Science (LSC) Community and Ms. Yun Tian are greatly thanked for their contribution in integrating CSC grantees in Leiden. The roommates at Olivabank (Mengmeng Sun, Min He, Wenxi Chen, Li Zeng, Yiling Li, An Wang, Jing Zhang, Hongxia Shen, Yi Ding) are warmly thanked for the comfortable living environment. Prof. Sylvestre Bonnet and Prof. Elisabeth Bouwman are gratefully acknowledged for supervision, scientific discussion, and support. Finally, I would like to thank my family for their great support to help me overcome the pressure during my PhD career, especially in the corona lockdown period of 2020.

